

IGT x ImNO JOINT SYMPOSIUM

**March 5-6, 2025
The Westin Harbour Castle, Toronto**

A platform for Canada's next generation of medical imaging and therapeutics researchers

PROCEEDINGS

Table of Contents

IGT x ImNO 2025 Co-Chairs	4
Organizing Committee	4
Scientific Committee	4
Planning Committee.....	4
Student Committee	5
Abstract Reviewers	5
Oral and Pitch/Poster Judges & Session Chairs	5
Welcome Letter	6
Code of Conduct	7
Supporting Organizations	8
INOVAIT.....	8
Ontario Institute for Cancer Research Imaging Program	8
3D Ultrasound and Multi-Modality Imaging for Personalized Medicine	9
Boston Scientific	9
Machine Learning in Medical Imaging Consortium (MaLMIC)	10
Sunnybrook Health Sciences Centre.....	10
GE HealthCare	10
Toronto Metropolitan University.....	10
Exact Imaging	11
Scintica	11
Siemens Healthineers	11
ClaroNav	12
Daxsonics	12
FUJIFILM VisualSonics	12
NDI	12
Keynote Speakers	13
Birgit Ertl-Wagner.....	13
Amir Manbachi.....	14
Panel Session: Lessons Learned from First-Time Founders and Leaders	15
Carla du Toit.....	15
Ananth Ravi	15
Tali Rosman	16
Nardin Samuel.....	16

Panel Session: Career Pathways for Graduates: Academic and Industry Advice on Talent Development	17
Padina Pezeshki	17
Terry Peters	17
Graham A. Wright	18
Cari Whyne	18
Alla Reznik.....	18
Program at a Glance	19
2025 IGT x ImNO Joint Symposium Program.....	20
Talk and Pitch Abstracts (in order of the talks).....	28
Oral Presentations 1: Cancer 1	29
Oral Presentations 2: MRI & Neuroimaging	34
Pitches 1: Cancer 1	39
Pitches 2: MRI & Neuroimaging.....	52
Oral Presentations 3: Device, Systems, and Robotic Development	60
Oral Presentations 4: Deep Learning/Machine Learning Methodology 1.....	65
Pitches 3: Device, Systems, and Robotic Development.....	70
Pitches 4: Deep Learning/Machine Learning Methodology 1	80
Oral Presentations 5: General 1	91
Oral Presentations 6: Image Guided Intervention and Surgery 1	96
Oral Presentations 7: Deep Learning/Machine Learning Methodology 2.....	101
Oral Presentations 8: Image Guided Intervention and Surgery 2	106
Pitches 5: Deep Learning/Machine Learning Methodology 2	111
Pitches 6: Image Guided Intervention and Surgery.....	120
Oral Presentations 9: Cancer 2	130
Oral Presentations 10: Cardiac, Lung, and Musculoskeletal Imaging	135
Oral Presentations 11: Optical Imaging & Ultrasound Imaging.....	140
Oral Presentations 12: General 2	145
Pitches 7: Optical Imaging & Ultrasound Imaging	150
Pitches 8: General.....	162
Author Index.....	170

IGT x ImNO 2025 Co-Chairs



Ali Tavallaei
Toronto Metropolitan University



Dafna Sussman
Toronto Metropolitan University

Organizing Committee

Scientific Committee

Michael Daly, Princess Margaret Cancer Centre
Michael Hardisty, University of Toronto
Brandon Helfield, Concordia University
Eno Hysi, University of Toronto

Elodie Lugez, Toronto Metropolitan University
Meaghan O'Reilly, Sunnybrook Research Institute
Jessica Rodgers, University of Manitoba
Ali Tavallaei, Toronto Metropolitan University

Planning Committee

Clara MacKinnon-Cabral, INOVAIT / Sunnybrook Research Institute
Carol Richardson, OICR Imaging Program
Bobbi Hoffman, Gemstone Event Management
Ahmed Nasef, INOVAIT / Sunnybrook Research Institute
Shaina Scrimgeour, Gemstone Event Management
Kitty Wong, Robarts Research Institute

Student Committee

Jessica de Kort, University of Manitoba
 Flora Diep, Queen's University
 Sean D'Mello, University of Waterloo

Sina Keshavarz, Toronto Metropolitan University
 Elahe Memari, Concordia University
 Rachel Theriault, Queen's University

Abstract Reviewers

Faranak Akbarifar
 Viktoriia Batarchuk
 Elvis Chen
 Mark Chiew
 Laura Connolly
 Gabriella d'Albenzio
 Michael Daly
 Razieh Enjilela
 Mohammad Farahmand
 Aaron Fenster
 Gabor Fichtinger
 Nancy Ford
 Stewart Gaede
 Donna Goldhawk
 Maged Goubran
 Amanda Hamilton
 Michael Hardisty

Mohamed Harmanani
 Justin Hicks
 Rebecca Hisey
 Matthew Holden
 Eno Hysi
 Amoon Jamzad
 Miranda Kirby
 Ivan Kosik
 Manuela Kunz
 Angus Lau
 M. Louis Lauzon
 Elodie Lugez
 Chris Macgowan
 Nooshin Maghsoodi
 James Mainprize
 Stewart McLachlin
 Elka Miller

Lucas Narciso
 Jamie Near
 Terry Peters
 Mihaela Pop
 Jessica Rodgers
 Benjamin Rotstein
 Dafna Sussman
 Sarah Svenningsen
 Jesse Tanguay
 Ali Tavallaei
 Junchao Tong
 Joseph Umoh
 Tamas Ungi
 Justin Wan
 Jill Weyers
 Chris Yeung

Oral and Pitch/Poster Judges & Session Chairs

Ryan Au
 Amal Aziz
 Joeana Cambranis-Romero
 Patrick Carnahan
 Laura Connelly
 Gabriella d'Albenzio
 Michael Daly
 Celine Dubroy-McArdle
 Razieh Enjilela
 Maged Goubran
 Michael Hardisty
 Rebecca Hisey
 Megan Hutter
 Eno Hysi

Amoon Jamzad
 Fatemeh Rastegar Jooyl
 Sule Karagulleoglu Sina
 Keshavarz
 April Khademi
 Carla Kulcsar
 Andras Lasso
 Daniel Louie
 Elodie Lugez
 Sarah Mattonen
 Azin Mirzajavadkhan
 Nika Momeni
 Gerald Moran
 Adnan Munawar

Meaghan O'Reilly
 Terry Peters
 Sara Rezvanjou
 Jessica Rodgers
 Siddarth Sadanand
 Saba Sadatamin
 Dafna Sussman
 Mahdi Tahmasebi
 Ali Tavallaei
 Joseph Umoh
 Edward Wang
 Cari Whyne
 Sydney Wilson
 Dylan Young

Welcome Letter

Dear IGT x ImNO Joint Symposium Attendees:

On behalf of the 2025 Organizing Committee, we are excited to welcome you to the 2025 Image-Guided Therapeutics (IGT) x Imaging Network Ontario (ImNO) Joint Symposium. We are delighted to be in-person in Toronto, ON this year and are looking forward to reconnecting with this exceptional community as we come together once again. The first two-day Joint Symposium, hosted by INOVAIT and ImNO, will be a joint medical imaging, image-guided therapy, and artificial intelligence symposium bringing in the next generation of researchers and industry experts.

This rendezvous of researchers promotes collaborations, broadcasts career opportunities, informs trainees on diverse imaging applications, and fosters a greater understanding of the commercialization process. The symposium features world-renowned keynote speakers and sessions that bring our trainees together with imaging scientists, clinicians, patient groups, and industry representatives.

Highlights for this year's program include two keynote speakers, Birgit Ertl-Wagner and Amir Manbachi, as well as two lunch-and-learn panel session on the lessons learned from first-time founders and leaders and career pathways for graduates, including academic and industry advice on talent development. The Symposium will feature 120 accepted presentations split between 48 oral presentations, 62 pitch-and-poster presentations, and 10 poster-only presentations. There will also be plenty of opportunities for you to network with your imaging colleagues, including a reception and trainee social games.



We are pleased to thank the following groups for their support of the 2025 Joint Symposium:

In closing, we would like to thank our reviewers who provided feedback on the proffered abstracts and acknowledge the significant contributions made by members of the Scientific, Student, and Planning Committees. These teams have worked very hard to bring us this year's Symposium.

We hope you enjoy this year's program of keynotes, discussion, oral talks, and pitch-and-poster presentations.

Sincerely,

Ali Tavallaei and Dafna Sussman

IGT x ImNO Joint Symposium 2025 Co-Chairs

Code of Conduct

All attendees, speakers, sponsors and volunteers at the IGT x ImNO Joint Symposium are required to agree with the following code of conduct. Organisers will enforce this code throughout the event. We expect cooperation from all participants to help ensure a safe environment for everybody.

Overview

INOVAIT and the ImNO are committed to providing a harassment-free symposium experience for everyone, regardless of gender, gender identity and expression, age, sexual orientation, disability, physical appearance, body size, race, ethnicity, religion (or lack thereof), or technology choices. We do not tolerate harassment of symposium participants in any form. Use of sexualised language and imagery that does not convey a scientific message is not appropriate. We expect participants and sponsors to follow these rules for the duration of the symposium in any symposium venue or platform, including talks, social media and events, and other online media. Symposium participants violating these rules may be sanctioned or expelled from the symposium without a refund at the discretion of the symposium organisers.

Details

Harassment includes offensive verbal comments related to gender, gender identity and expression, age, sexual orientation, disability, physical appearance, body size, race, ethnicity, religion, technology choices, sexual images in public spaces, deliberate intimidation, stalking, following, harassing photography or recording, sustained disruption of talks or other events, inappropriate contact, and unwelcome sexual attention. Use of images, activities, uniforms/costumes or other materials that create a sexualised environment will not be tolerated.

Anyone asked to stop any harassing behavior is expected to comply immediately. If anyone engages in harassing behavior, the symposium organisers may take any action they deem appropriate, including warning the offender or expulsion from the symposium with no refund.

Need Help?

If you are being harassed, notice that someone else is being harassed, or have any other concerns, contact the Symposium Manager at info@IGTxImNO.ca or send an email to IGT x ImNO ombudsperson, Dr. Michael Hardisty, at ombudsperson@IGTxImNO.ca or reach out to the IGT x ImNO 2025 Chairs, Drs. Ali Tavallaei and Dafna Sussman, at chairs@IGTxImNO.ca.

Conference staff will be happy to help participants contact hotel/venue security or local law enforcement, provide escorts, or otherwise assist those experiencing harassment to feel safe for the duration of the conference. We value your attendance.

We expect everyone to follow these rules for the duration of the symposium within and outside symposium venues and platforms, including but not limited to symposium-related talks, workshops, and social events involving IGT x ImNO symposium attendees, and in all symposium related communications, including social media.

Supporting Organizations

INOVAIT and the ImNO are grateful for the support of our sponsors and partners, and their dedication to imaging research. Without their support, the continuation of this important event wouldn't be possible.



INOVAIT is Canada's network dedicated to supporting Canadian companies advancing image-guided therapy (IGT) technologies with artificial intelligence. The INOVAIT network invests strategically in collaborative partnerships that build upon Canada's strength in digital innovation and medical science research to create a critical mass of world-leading image-guided therapy companies.

The network brings together a wide range of companies, research organizations, post-secondary institutions, and not-for-profit organizations to foster robust relationships within the Canadian IGT community and advance the sector as a global leader in healthcare. The network is hosted at Sunnybrook Research Institute and supported by the Government of Canada's Strategic Innovation Fund through Innovation, Science, and Economic Development Canada.



Ontario Institute for Cancer Research Imaging Program
Co-Director: Drs. Aaron Fenster and Martin Yaffe – [Ontario Institute for Cancer Research](#)

The OICR Imaging Program accelerates the translation of research into the development of new imaging innovations for earlier cancer detection, diagnosis and treatment through four major projects: probe development and commercialization, medical imaging instrumentation and software, pathology validation, and imaging for clinical trials. The Imaging Program facilitates improved screening and treatment options for cancer patients by streamlining advances in medical imaging through the complex pipeline from discovery to clinical translation and ultimately to clinical use.



3D Ultrasound and Multi-Modality Imaging for Personalized Medicine

Lead Researchers: Drs. Aaron Fenster and Alla Reznik

Sponsor: [Ontario Research Fund \(ORF\)](#)

Continued developments of medical imaging systems have vastly improved our ability to visualize body tissues and processes, enabling more accurate detection of medical conditions.

However, recent trends for personalized or precision medicine, i.e., delivering “the right treatment to the right patient at the right time”, impose new requirements for imaging modalities in terms of diagnostic and predictive capabilities and change the emphasis from a nonspecific to an organ-specific imaging approach - a significant paradigm shift in medicine. Indeed, precision medicine often cannot be achieved with existing general purpose or whole-body imaging devices. Predictive and preventive precision medicine calls for new approaches where organ-specific imaging tools are customized for particular organs or diseases to obtain the highest efficacy and diagnostic capability.

Dual-modality imaging is an integral part of this approach as it provides complimentary visual and quantitative information that is based on aligned morphological and functional data. We have a long history of developing innovative imaging systems used to solve clinical unmet needs, some of which have been translated clinically and commercialized. Our efforts are driven by innovations resulting in improved diagnostic accuracy as well as increased patient comfort.

The overarching goal of the ORF is to develop effective new imaging-based systems that will use ultrasound imaging with radionuclide imaging to overcome the limitations of independent systems and meet the challenges of unmet clinical needs.



Boston Scientific (NYSE: BSX) is a worldwide developer, manufacturer and marketer of medical devices with approximately 24,000 employees and revenue of \$7.622 billion in 2011. For more than 40 years, Boston Scientific has advanced the practice of less-invasive medicine by providing a broad and deep portfolio of innovative products, technologies and services across a wide range of medical specialties. The Company’s products help physicians and other medical professionals improve their patients’ quality of life by providing alternatives to surgery. For more information, please visit www.bostonscientific.com.



Machine Learning in Medical Imaging Consortium (MaLMIC)
Working Group: Drs. Aaron Fenster, Anne Martel, Julia Publicover, Amber L. Simpson, Aaron Ward, Martin Yaffe –
Machine Learning for Medical Imaging

The Consortium was launched to accelerate research and development of machine learning solutions for unmet needs in medical imaging through collaborations between academic and clinical researchers, and with Canadian industry.



Sunnybrook Health Sciences Centre (SRI) is the research arm of Sunnybrook Health Sciences Centre, an internationally recognized academic health sciences centre fully affiliated with the University of Toronto. With well-established programs in basic and applied sciences which span across three scientific platforms and ten clinical programs, SRI is developing innovations in care for the more than 1.3 million patients the hospital cares for annually.



GE HealthCare is a leading global medical technology, pharmaceutical diagnostics, and digital solutions innovator, dedicated to providing integrated solutions, services and data analytics that clinicians more effective, therapies more precise, and patients healthier and happier. Serving patients and providers for more than 100 years, GE HealthCare is advancing connected and compassionate care, while simplifying the patient’s journey across the care pathway. Together, we’re creating a world where healthcare has no limits.



Toronto Metropolitan University is at the intersection of mind and action. What our students learn in the classroom is enhanced by real-world knowledge and experience. We champion diversity, entrepreneurship and innovation.



At **TMU**, we tackle real-world challenges in pursuit of positive change. This commitment is our defining characteristic — it makes us who we are as an institution and community. From our leading academics and cutting-edge research that meets evolving societal needs to our culture of inclusivity and the impact our students make, our determination to improve lives is the force that fuels our creativity and our passion for innovation.



Exact Imaging, based in Markham, Ontario, is the world's leader in high-resolution micro-ultrasound systems enabling real-time imaging and guided biopsies in the urological market for prostate cancer. Exact Imaging's ExactVu™ microUS platform operates at 29 MHz and enables a whole new level of resolution with the benefits of ease of use, affordability, and provides an extension of the current urological workflow. Using the Exact Imaging platform, urologists can visualize areas of interest in the prostate and specifically target biopsies at those areas. The platform has regulatory approval in jurisdictions worldwide including Europe, the United States, Japan, Brazil, and Canada.



Scintica is a leading supplier of preclinical research solutions and provides applications and technical support, and a platform for scientists to share their scientific findings. We carry a diverse portfolio of products, including imaging systems (MRI, PET, CT, Optical, DEXA and High-Frequency Ultrasound), intravital microscopy, lab equipment, workstations, incubators, tissue culture analysis, live cell imaging and much more. Our mission is to link scientists and researchers with the right precision tools to further research by providing high-value instrumentation and solutions to the preclinical research community. Scintica, Making the world brighter. www.scintica.com



Siemens Healthineers pioneers breakthroughs in healthcare. For everyone. Everywhere. Sustainably. The company is a global provider of healthcare equipment, solutions and services, with activities in more than 180 countries and direct representation in more than 70. The group comprises Siemens Healthineers AG, listed as SHL in Frankfurt, Germany, and its subsidiaries. As a leading medical technology company, Siemens Healthineers is committed to improving access to healthcare for underserved communities worldwide and is striving to overcome the most threatening diseases. The company is principally active in the areas of imaging, diagnostics, cancer care and minimally invasive therapies, augmented by digital technology and artificial intelligence.



ClaroNav (claronav.com) is dedicated to the development of surgical navigation and visualization solutions. Our rapidly growing, yet profitable, company is controlled by its founders and employees. We develop, test, manufacture, market, train, and support our products at our Toronto headquarters. Leveraging proprietary software, mechanical and electronics designs, we deliver products to the dental (Navident, MicronMapper), medical (Navient) and OEM (MicronTracker) markets. We are currently seeking software engineers with exceptional abilities, knowhow and passion for developing advanced 3D vision and visualization algorithms. If you are interested in joining us, please write us at jobs@claronav.com.



Daxsonics offers full-stack ultrasound product development for medical devices, taking ideas and concepts through prototyping, or complementing an existing product development team shorten the time to market. Daxsonics' services include Acoustic, Electrical, and Mechanical Engineering, Software and Systems Engineering, Prototyping and target manufacturing for ultrasound transducers and support for all stages of a medical device product life cycle.



FUJIFILM VisualSonics: Famous for ground-breaking ultra-high frequency ultrasound and photoacoustic technology, FUJIFILM VisualSonics has had a tremendous impact on translational research by allowing users to visualize the nature of a disease like never before. Our ultrasound technology operates at higher frequencies than those found in most conventional ultrasound systems, up to 70 MHz. With these high frequencies, our unique imaging platforms are able to generate images at resolutions that far exceed any other system available on the market – as small as 30 μm . This is ideal for acquiring high resolution images in small animals or for superficial imaging in the human body.



NDI is the world's leading innovator of optical and electromagnetic navigation technology. For 40+ years, we've helped medical device OEMs bring new surgical navigation applications—and clinical breakthroughs—to market.

Keynote Speakers

Wednesday, March 5, 2025, at 9:15am

Title: Pediatric Imaging – What We Need (and Don't Need) AI for

Birgit Ertl-Wagner, Hospital for Sick Children

Dr. Birgit Ertl-Wagner is Radiologist-in-Chief of the Department of Diagnostic & Interventional Radiology at the Hospital for Sick Children in Toronto, Canada. She holds the Derek Harwood-Nash Chair in Medical Imaging and is Senior Associate Scientist in the Neurosciences & Mental Health Program of the SickKids Research Institute. Dr. Ertl-Wagner is a Professor in the Department of Medical Imaging of the University of Toronto.



Dr. Ertl-Wagner's clinical interest lies in the field of pediatric neuroradiology, including tumor imaging, imaging of neuroinflammatory and metabolic disorders, neurovascular imaging, and pediatric head & neck imaging.

Her research is characterized by an interdisciplinary approach with a focus on magnetic resonance imaging research, imaging-based Artificial Intelligence, and translation of research into clinical settings. Dr. Ertl-Wagner is on the editorial board of several renowned scientific journals and serves on multiple committees of national and international scientific societies. She has received numerous awards for her research and teaching.

Thursday, March 6, 2025, at 4:15pm

Title: The Abundant Promise of Ultrasound in Neurosurgery

Amir Manbachi, Johns Hopkins University

Dr. Amir Manbachi is an accomplished and distinguished figure in the fields of neurosurgery, biomedical engineering, ultrasound and entrepreneurship. His impressive background includes a multitude of roles and accolades that reflect his commitment to advancing medical technology and innovation.



Academic and Professional Roles:

- Associate Professor at Johns Hopkins University in the departments of Neurosurgery, Biomedical Engineering, Mechanical Engineering, Electrical and Computer Engineering.
- Co-founder and director of HEPIUS Innovation Labs, focusing on cutting-edge wearables and implantable medical ultrasound devices for spinal cord injury patients.

Research Focus:

Pioneering work in applying sound and ultrasound technologies to various neurosurgical applications such as imaging, tumor ablation, and neuromodulation. Specific interests include ultrasound-guided spine surgery, detection of foreign bodies, and monitoring blood flow and tissue perfusion.

Publications and Intellectual Property:

- Authored numerous journal articles, conference proceedings, inventions, and books; notably publications in Nature Communications Medicine, IEEE Transactions on Biomedical Engineering (TBME), Ultrasonics, Microcirculation, Scientific Reports, etc.
- Recognized for significant contributions with over 20 inventions and several prestigious awards.

Teaching and Mentorship:

Extensive experience in teaching engineering design, medical imaging, and entrepreneurship at Johns Hopkins and the University of Toronto. Received teaching excellence awards from both institutions.

Dr. Manbachi's career exemplifies a profound dedication to interdisciplinary collaboration, innovation, and education. His impactful research and entrepreneurial ventures have significantly advanced the frontier of medical ultrasound technology, particularly in the realm of neurosurgery and biomedical engineering.

Panel Session: Lessons Learned from First-Time Founders and Leaders

Panelists:

- Carla du Toit, Dalhousie University's School of Medicine
- Ananth Ravi, Stryker
- Tali Rosman, Toronto Metropolitan University
- Nardin Samuel, University of Toronto

Carla du Toit, Dalhousie University's School of Medicine

Carla du Toit is a medical student at Dalhousie University's School of Medicine, and has a background in integrative bioscience research specializing in musculoskeletal health and three-dimensional ultrasound technology. Carla is a Co-founder of NovaSonix Healthcare Inc., a start-up developing cutting-edge three-dimensional ultrasound technology to improve clinical practice for the prevention, detection, and monitoring of musculoskeletal disease. Drawing on inspiration from a childhood spent in rural South Africa and Nova Scotia, Carla strives to develop portable advanced imaging technology for patients that face challenges in accessing these services across Canada. Within NovaSonix's first year of operation has: won the Bone and Joint Institutes | Morrisette Institute for Entrepreneurship Musculoskeletal Innovation Award; won Orthopedic Research Society Business Competition; placed in the top 15 for Synapse Life Sciences 2024; and garnered investor interests both within Canada and abroad.

Ananth Ravi, Stryker

In his thinking, innovation, and research, Ananth Ravi puts the patient first. He believes the patient's experience of treatment is just as important as the treatment itself. Growing up in Zambia, Ananth's early years were marked with loss due to cancers that were treatable in other parts of the world. He has dedicated his career to lowering barriers for treatment and developing innovations that help increase access to care.

Ananth is a co-inventor on numerous patents and has garnered several grants for medical device innovations. His commitment to improving the treatment process inspired him to develop the localization technology, MOLLI® that resulted in the creation of MOLLI Surgical.

Prior to MOLLI, he was a Medical Physicist at Sunnybrook's Odette Cancer Centre and Clinical Operations Lead, Brachytherapy. He is the only medical physicist to ever win the Human Touch Award, which recognizes his passion for improving the quality of care for cancer patients.

Tali Rosman, Toronto Metropolitan University

Tali Rosman is a seasoned business and M&A advisor to early-stage technology companies and investors. Rosman, coming from an M&A and Strategy background, has built and led Elem Additive, Xerox's advanced manufacturing subsidiary. Rosman commercialized the liquid metal jetting technology, taking it to market and signing partnerships with the likes of the US Navy and Siemens, resulting in the sale of Elem Additive in 2023. Since then, she has been serving as a business advisor to both startups and investors in deep-tech and industry 4.0 and has been leading small & medium cap M&A and investment transactions. Rosman also serves as an EIR (Entrepreneur in Residence) at Toronto Metropolitan University, collaborating with TMU's Business Development department to drive innovation, commercialization and impact.

Rosman is a passionate advocate for innovation and is a frequent speaker at industry events and has been featured in numerous publications.

Nardin Samuel, University of Toronto

Dr. Nardin Samuel is currently a resident physician and post-doctoral research scientist at the University of Toronto, specializing in Neuroscience. She is the CEO & Co-founder of Cove Neurosciences, a deep tech startup developing innovative software analytics for brain data. Dr. Nardin Samuel is one of the board members of the Clinician Investigator Trainee Association of Canada and an Advisory Board Member of iGan Partners. Meanwhile, she has taken part in multiple speaking engagements and is also taking an active part in undergraduate and graduate education at the Temerty Faculty of Medicine, University of Toronto. Dr. Nardin Samuel, an entrepreneur, scientist and physician, and has recently been awarded with the Leadership Award by the 2023 Women Empowerment Awards. She has also been placed in the Top 100 Most Powerful Women in Canada list by WXN.

Panel Session: Career Pathways for Graduates: Academic and Industry Advice on Talent Development

Panelists:

- Padina Pezeshki, Medtronic
- Terry Peters, Robarts Research Institute
- Graham A. Wright, Sunnybrook Research Institute
- Cari Whyne, Sunnybrook Health Sciences Centre
- Alla Reznik, Lakehead University

Padina Pezeshki, Medtronic

Padina Pezeshki is an engineering physics graduate and completed a masters, PhD and a postdoctoral fellowship in biomedical engineering. Her academic research has contributed to multiple medical device patents and several commercial products comprising Nanotite™ implant (Biomet 3i), RFA denervation probes (Baylis Medical) and OsteoCool™ bone ablation probe (Medtronic). Padina has authored over 40 journal and conference papers, served as a university lecturer, and presented at national and international meetings (including TED Talks). She has engaged in entrepreneurship through a startup and currently assumes the role of a Principal Medical Science Advisor and Clinical Research Specialist at Medtronic Canada, managing research and medical science activities for Canada's Medical Surgical portfolio.

Terry Peters, Robarts Research Institute

Prof. Terry Peters is a Scientist in the Imaging Research Laboratories at the Robarts Research Institute, London, On, Canada, and Professor Emeritus in the Departments of Medical Imaging and Medical Biophysics and the School of Biomedical Engineering at Western University in London, Ontario, Canada. He obtained his PhD in Electrical Engineering at the University of Canterbury in Christchurch, NZ, in image reconstruction for CT in 1974. In 1997, he joined the Imaging Research Labs at the Robarts Research Institute at Western University, where he established the Laboratory for Virtual Augmentation and Simulation for Surgery and Therapy. He has mentored over 100 trainees, authored over 370 peer-reviewed papers, books, and book chapters, and has been cited ~30,000 times. He is a Fellow of the Canadian College of Physicists in Medicine, the Australasian College of Physical Scientists and Engineers in Medicine, the Canadian Organization for Medical Physics, the Institute of Electrical and Electronics Engineers, the MICCAI Society, the Canadian Academy of Health Sciences, and the Royal Society of Canada. He has also been awarded the Enduring Impact Award from the MICCAI Society and the Gold Medal from the Canadian Organization of Medical Physics.

Graham A. Wright, Sunnybrook Research Institute

Graham A. Wright, PhD is a Senior Scientist at Sunnybrook Research Institute and a Professor in the Department of Medical Biophysics at the University of Toronto. The research focus of Dr. Wright's group is cardiovascular imaging, with an emphasis on MRI. This effort includes basic biophysics to characterize the relationship between MR signals and underlying pathophysiology in blood and tissue; engineering to develop more effective methods and devices to acquire, analyze, and visualize medical images; and application of these tools to assessment, treatment planning, and therapy guidance in ischemic and structural heart diseases, complex arrhythmias, and peripheral vascular diseases. Together with trainees and collaborators, he has published over 235 peer-reviewed papers and 545 conference abstracts, which have garnered numerous awards and resulted in 25 patents. Dr. Wright collaborates with a broad range of companies from start-ups to multi-nationals in translating research results toward clinical practice.

Cari Whyne, Sunnybrook Health Sciences Centre

Dr. Cari Whyne, PhD, FIOR, is the Susanne and William Holland Chair in Musculoskeletal Research at Sunnybrook Health Sciences Centre in Toronto. She is a Senior Scientist and the Director of the Holland Bone and Joint Research Program at Sunnybrook Research Institute and a Full Professor in the Department of Surgery, Institute of Biomedical Engineering and Institute of Medical Sciences at the University of Toronto. Dr. Whyne received her BSc. in Mechanical Engineering from Queen's University and her PhD from the University of California Berkeley / University of California San Francisco in Bioengineering. The focus of her work is clinically translational bioengineering research. Dr. Whyne's research integrates biomechanical analyses with basic science, preclinical and clinical investigations, including extensive work in computational image analysis, micro-imaging, machine learning and finite element modeling techniques. Her work also incorporates design, simulation, evaluation and clinical translation of novel less/minimally invasive surgical techniques and devices. The primary foci of Dr Whyne's research are cancer in bone, biomechanics and imaging (spinal, craniomaxillofacial, upper and lower extremity), rehabilitation, surgical optimization and fracture fixation/healing.

Alla Reznik, Lakehead University

Dr. Alla Reznik is a Tier 1 Canada Research Chair in Physics of Radiation Medical Imaging and a Professor in the Physics Department at Lakehead University. She also serves as a Senior Scientist at the Thunder Bay Regional Health Research Institute (TBRHRI). Dr. Reznik completed her Ph.D. in solid-state physics from the Technion - Israel Institute of Technology and has held positions at GE Medical Systems and Sunnybrook Health Sciences Centre.

Dr. Reznik's research specializes in photoconductive materials and technologies for radiation medical imaging, focusing on organ-targeted Positron Emission Tomography (PET) and low-dose x-ray imaging detectors. It aims to enhance patient outcomes and make advanced imaging technologies more accessible and affordable for healthcare systems. Her work on organ-targeted Positron Emission Tomography (PET) has led to the establishment of Radialis Inc, a Lakehead/TBRHRI spin-off company which produces a commercial version of the PET technology developed by her group for breast cancer detection.

Program at a Glance

Wednesday, March 5, 2025					
8:00 - 9:00	Breakfast (Foyer)				
9:00 - 9:15	Welcome & Opening Remarks (Centre)				
9:15 - 10:00	Keynote I: Pediatric Imaging – What We Need (and Don't Need) AI for <i>Birgit Ertl-Wagner, Hospital for Sick Children</i> (Centre)				
10:00 - 10:15	Coffee Break (East)				
10:15 - 11:15	<table border="1"> <tr> <td>Oral Presentations 1 Cancer 1 (Centre)</td> <td>Oral Presentations 2 MRI & Neuroimaging (East)</td> </tr> <tr> <td>Pitches 1 Cancer (Centre)</td> <td>Pitches 2 MRI & Neuroimaging (East)</td> </tr> </table>	Oral Presentations 1 Cancer 1 (Centre)	Oral Presentations 2 MRI & Neuroimaging (East)	Pitches 1 Cancer (Centre)	Pitches 2 MRI & Neuroimaging (East)
Oral Presentations 1 Cancer 1 (Centre)	Oral Presentations 2 MRI & Neuroimaging (East)				
Pitches 1 Cancer (Centre)	Pitches 2 MRI & Neuroimaging (East)				
11:15 - 11:45	Poster Viewing (Pitch Sessions 1 & 2 presenting) (Centre)				
11:45 - 12:45	Lunch Pickup (Foyer)				
12:45 - 14:00	Panel - Lessons Learned From First-Time Founders and Leaders (Centre)				
13:00 - 13:45	<table border="1"> <tr> <td>Oral Presentations 3 Device, Systems, and Robotic Development (Centre)</td> <td>Oral Presentations 4 Deep Learning/Machine Learning Methodology 1 (East)</td> </tr> <tr> <td>Pitches 3 Device, Systems, and Robotic Development (Centre)</td> <td>Pitches 4 Deep Learning/Machine Learning Methodology 1 (East)</td> </tr> </table>	Oral Presentations 3 Device, Systems, and Robotic Development (Centre)	Oral Presentations 4 Deep Learning/Machine Learning Methodology 1 (East)	Pitches 3 Device, Systems, and Robotic Development (Centre)	Pitches 4 Deep Learning/Machine Learning Methodology 1 (East)
Oral Presentations 3 Device, Systems, and Robotic Development (Centre)	Oral Presentations 4 Deep Learning/Machine Learning Methodology 1 (East)				
Pitches 3 Device, Systems, and Robotic Development (Centre)	Pitches 4 Deep Learning/Machine Learning Methodology 1 (East)				
14:00 - 15:00	Break & Poster Viewing (Pitch Sessions 3 & 4 presenting) (Centre / Exhibit Hall)				
15:00 - 15:30	<table border="1"> <tr> <td>Oral Presentations 5 General 1</td> <td>Oral Presentations 6 Image Guided Intervention and Surgery 1</td> </tr> </table>	Oral Presentations 5 General 1	Oral Presentations 6 Image Guided Intervention and Surgery 1		
Oral Presentations 5 General 1	Oral Presentations 6 Image Guided Intervention and Surgery 1				
15:30 - 16:30	Break & Poster Viewing (Pitch Sessions 3 & 4 presenting) (Centre / Exhibit Hall)				
16:30 - 17:30	<table border="1"> <tr> <td>Oral Presentations 5 General 1</td> <td>Oral Presentations 6 Image Guided Intervention and Surgery 1</td> </tr> </table>	Oral Presentations 5 General 1	Oral Presentations 6 Image Guided Intervention and Surgery 1		
Oral Presentations 5 General 1	Oral Presentations 6 Image Guided Intervention and Surgery 1				
17:30 - 19:00	Reception/Social Event (Centre & East)				

Thursday, March 6, 2025					
8:00 - 9:00	Breakfast (Foyer)				
9:00 - 10:00	<table border="1"> <tr> <td>Oral Presentations 7 Deep Learning/Machine Learning Methodology 2 (Centre)</td> <td>Oral Presentations 8 Image-guided Intervention and Surgery 2 (East)</td> </tr> <tr> <td>Pitches 5 Deep Learning/Machine Learning Methodology 2 (Centre)</td> <td>Pitch Presentations 6 Image-guided Intervention and Surgery (East)</td> </tr> </table>	Oral Presentations 7 Deep Learning/Machine Learning Methodology 2 (Centre)	Oral Presentations 8 Image-guided Intervention and Surgery 2 (East)	Pitches 5 Deep Learning/Machine Learning Methodology 2 (Centre)	Pitch Presentations 6 Image-guided Intervention and Surgery (East)
Oral Presentations 7 Deep Learning/Machine Learning Methodology 2 (Centre)	Oral Presentations 8 Image-guided Intervention and Surgery 2 (East)				
Pitches 5 Deep Learning/Machine Learning Methodology 2 (Centre)	Pitch Presentations 6 Image-guided Intervention and Surgery (East)				
10:00 - 10:30	Break & Poster Viewing (Pitch Sessions 5 & 6 presenting) (Centre / Exhibit Hall)				
10:30 - 11:30	<table border="1"> <tr> <td>Oral Presentations 9 Cancer 2 (Centre)</td> <td>Oral Presentations 10 Cardiac, Lung, and Musculoskeletal Imaging (East)</td> </tr> </table>	Oral Presentations 9 Cancer 2 (Centre)	Oral Presentations 10 Cardiac, Lung, and Musculoskeletal Imaging (East)		
Oral Presentations 9 Cancer 2 (Centre)	Oral Presentations 10 Cardiac, Lung, and Musculoskeletal Imaging (East)				
11:30 - 12:30	Lunch Pickup (Foyer)				
12:30 - 13:45	Panel - Career Pathways for Graduates: Academic and Industry Advice on Talent Development (Centre)				
12:45 - 13:30	<table border="1"> <tr> <td>Oral Presentations 11 Optical Imaging & Ultrasound Imaging (Centre)</td> <td>Oral Presentations 12 General 2 (East)</td> </tr> <tr> <td>Pitches 7 Optical Imaging & Ultrasound Imaging (Centre)</td> <td>Pitches 8 General (East)</td> </tr> </table>	Oral Presentations 11 Optical Imaging & Ultrasound Imaging (Centre)	Oral Presentations 12 General 2 (East)	Pitches 7 Optical Imaging & Ultrasound Imaging (Centre)	Pitches 8 General (East)
Oral Presentations 11 Optical Imaging & Ultrasound Imaging (Centre)	Oral Presentations 12 General 2 (East)				
Pitches 7 Optical Imaging & Ultrasound Imaging (Centre)	Pitches 8 General (East)				
13:45 - 14:45	Break & Poster Viewing (Pitch Sessions 7 & 8 presenting) (Centre / Exhibit Hall)				
14:45 - 15:15	<table border="1"> <tr> <td>Oral Presentations 11 Optical Imaging & Ultrasound Imaging (Centre)</td> <td>Oral Presentations 12 General 2 (East)</td> </tr> <tr> <td>Pitches 7 Optical Imaging & Ultrasound Imaging (Centre)</td> <td>Pitches 8 General (East)</td> </tr> </table>	Oral Presentations 11 Optical Imaging & Ultrasound Imaging (Centre)	Oral Presentations 12 General 2 (East)	Pitches 7 Optical Imaging & Ultrasound Imaging (Centre)	Pitches 8 General (East)
Oral Presentations 11 Optical Imaging & Ultrasound Imaging (Centre)	Oral Presentations 12 General 2 (East)				
Pitches 7 Optical Imaging & Ultrasound Imaging (Centre)	Pitches 8 General (East)				
15:15 - 16:15	Break & Poster Viewing (Pitch Sessions 7 & 8 presenting) (Centre / Exhibit Hall)				
16:15 - 17:00	Keynote II: Keynote: The Abundant Promise of Ultrasound in Neurosurgery <i>Amir Manbachi, Johns Hopkins University</i> (Centre)				
17:00 - 17:30	Closing Remarks & Awards (Centre)				

2025 IGT x ImNO Joint Symposium Program

Wednesday, March 5, 2025

8:00 – 9:00	Breakfast	Foyer
8:00 – 16:00	Registration	Foyer
9:00 – 9:15	Welcome & Opening Remarks <i>Dafna Sussman and Ali Tavallaei, Toronto Metropolitan University & Aaron Fenster, Robarts Research Institute and Raphael Ronen, INNOVAIT</i>	Metropolitan Ballroom – Centre
9:15 – 10:00	Keynote Session I <i>Chairs: Rebecca Hisey & Jessica Rodgers</i> Keynote: Pediatric Imaging – What We Need (and Don't Need) AI for Anne Martel, University of Toronto <i>Birgit Ertl-Wagner, Hospital for Sick Children</i>	Metropolitan Ballroom – Centre
9:15 – 15:30	Exhibits Open	Poster & Exhibit Hall
10:00 – 10:15	Coffee Break	Foyer
10:15 – 11:15	Oral Presentations 1: Cancer 1	Oral Presentations 2: MRI & Neuroimaging
	Metropolitan Ballroom – Centre	Metropolitan Ballroom – East
	<i>Chairs: Gabriella d'Albenzio & Sule Karagulleoglu</i>	<i>Chairs: Dafna Sussman & Celine Dubroy-McArdle</i>
	O1-1: The Role of Flow and Microbubble-Induced Shear Stress in Endothelial Cell Immunobiology <i>Elahe Memari, Concordia University</i>	O2-1: Fetoplacental Blood-Mimicking Phantoms for Optimizing Susceptibility Weighted Imaging <i>Dylan Young, Toronto Metropolitan University</i>
	O1-2: Using Computed Tomography perfusion (CTP) to Assess Changes in the Contrast Distribution Volume in Pancreatic Cancer Patients: a Potential Biomarker for Patient Response to Standard-of-care Therapy <i>Jin-Young Bang, Western University</i>	O2-2: A Pulse Sequence for Single Breath Hold Saturation Transfer Imaging of the Entire Gravid Abdomen <i>Siddharth Sadanand, Toronto Metropolitan University</i>
	O1-3: Advancing Treatment of Skeletal Metastases: Radiation-Induced Photodynamic Therapy (RadioPDT) with Novel Nanoparticles <i>Azin Mirzajavadkhan, University of Toronto</i>	O2-3: Laterally Oscillating Trajectory for Undersampling Slices (LOTUS) <i>Mayuri Sothynathan, Western University</i>
O1-4: Differences in Radiologist Search Patterns when Assessing mpMRI for Prostate Cancer <i>Ryan Au, Western University</i>	O2-4: The Effect of MRI RF Coil Selection on Spatial Trends in T1 Relaxation <i>Sandra Alexander, Toronto Metropolitan University</i>	
10:45 - 11:20	Pitches 1: Cancer	Pitches 2: MRI & Neuroimaging
	Metropolitan Ballroom – Centre	Metropolitan Ballroom – East
	<i>Chairs: Laura Connelly & Jessica Rodgers</i>	<i>Chairs: Razieh Enjilela & Fatemeh Rastegar Jooyl</i>
P1-01: Automatic Gleason Grading for Better Prognosis Prediction <i>Matthew McNeil, University of Toronto</i>	P2-01: Suppression of Lipid Contamination in Whole Brain Slice Magnetic Resonance Spectroscopic Imaging using Two-Dimensional Selective Excitation <i>Jason Rock, Sunnybrook Research Institute</i>	

	<p>P1-02: LLM-Based Prostate Cancer Grading Through Reasoning Segmentation <i>Emma Willis, Queen's University</i></p>	<p>P2-02: Deep-Learning Based Detection of Placenta Previa from Fetal MRI: A Cascaded CNN Approach <i>Nika Momeni, Toronto Metropolitan University</i></p>
	<p>P1-03: Evaluating the Synergistic Effects of Antiangiogenic Therapy and Stereotactic Body Radiation Therapy in Pancreatic Cancer using Multi-Modal Optical Coherence Tomography <i>Hector Alejandro Contreras-Sanchez, University of Toronto</i></p>	<p>P2-03: Accounting for Fat Contamination in Amine/Amide Concentration Independent Detection (AACID) CEST MRI of the Human Spinal Cord <i>Victoria Little, Western University</i></p>
	<p>P1-04: Characterization of Osteosarcopenia Quantified With AI-Enabled Musculoskeletal Imaging Biomarkers in Patients Undergoing Spine SBRT <i>Yessica Castano Sainz, Sunnybrook Research Institute</i></p>	<p>P2-04: Modelling 13C-Bicarbonate Signal Changes Due to Lactate Oxidation Pathways in Hyperpolarized MRI <i>Dylan Dingwell, University of Toronto</i></p>
	<p>P1-05: Assessing Diffuse Optical Spectroscopy and Magnetic Resonance Imaging for Quantification of Multimodal Gadolinium-Incorporated Porphysomes for Theranostic Guidance of Oral Cancer in Mice <i>Theodore Husby, University of Toronto</i></p>	<p>P2-05: Comparison of Lipid Suppression Techniques for in vivo Whole Brain MR Spectroscopic Imaging <i>Kaito Hara-Lee, Queen's University</i></p>
	<p>P1-06: Designing an Endometrial Pathology Slide Classification User Interface for Efficient Diagnostics <i>Matthew Lam, Toronto Metropolitan University</i></p>	<p>P2-06: Microscopic Fractional Anisotropy of the Hippocampus in Dementia Patients <i>Ricardo Rios-Carrillo, Western University</i></p>
	<p>P1-07: Evaluating Osteosarcopenia Progression in a Preclinical Model of Prostate Cancer Bone Metastases with Imaging Biomarkers <i>Leanna Abraham, University of Toronto</i></p>	
	<p>P1-08: Leveraging Transformers to Improve Dose Prediction in Complex Multi-lesion Lung SABR Plans <i>Edward Wang, Western University</i></p>	
	<p>P1-09: Precursor Droplet Extrusion for the Production of Size-Controlled Lipid-Stabilized Drug-Loaded Nanobubbles <i>Patrick Dong Min Chang, University of Toronto</i></p>	
	<p>P1-10: Photodynamic Therapy-Based Photochemical Immune Stimulation for the Treatment of Ovarian Cancer in a Xenograft Mouse Model <i>Breana Shehetila, University of Toronto</i></p>	
11:45 – 12:45	<p>Poster Viewing (Pitch Sessions 1 & 2 plus posters below presenting) P1-11: Automated Detection of Lymph Node Metastasis in Prostate Cancer Using Whole Slide Images <i>Kangdi Shi, University Health Network</i> P1-12: CollinsOral Epithelial Cell Quantification for Dysplasia Grading Using Histopathology Images <i>Kangdi Shi, University Health Network</i> P2-7: Preliminary PET Imaging Reveals Reduced Synaptic Density in Autistic vs Non-Autistic Youth <i>Christin Schifani, Centre for Addiction and Mental Health</i></p>	Posters & Exhibit Hall
12:45 – 14:00	Lunch Pickup	Foyer

13:00 - 13:45	Panel: Lessons Learned from First-Time Founders and Leaders Metropolitan Ballroom – Centre	
	<i>Carla du Toit, Dalhousie University's School of Medicine; Ananth Ravi, Stryker; Tali Rosman, Toronto Metropolitan University; Nardin Samuel, University of Toronto</i>	
14:00 – 15:00	Oral Presentations 3: Device, Systems, and Robotic Development	Oral Presentations 4: Deep Learning/Machine Learning Methodology 1
	Metropolitan Ballroom – Centre	Metropolitan Ballroom – East
	<i>Chairs: Ali Tavallaei & Sina Keshavarz</i>	<i>Chairs: Michael Daly & Edward Wang</i>
	O3-01: Generating and Measuring Flow for Hemodynamic Simulations of Interventional Vascular Procedures <i>David Ng, Robarts Research Institute</i>	O4-01: Foundation Models for Cancer Tissue Margin Assessment with Mass Spectrometry <i>Mohammad Farahmand, Queen's University</i>
	O3-02: Design and Testing of an MRI Phantom Faraday Cage using Rapid Prototyping Techniques <i>Alexander Dunn, Toronto Metropolitan University</i>	O4-02: From Text to Insight: Classifying Microcalcifications in Radiology Reports with AI <i>Zardar Khan, Sunnybrook Research Institute</i>
	O3-03: Resection Cavity Tracking Using a Bench-Top Robot and Electromagnetic Tracking <i>Kian Hashtrudi-Zaad, University of Toronto</i>	O4-03: Automatically Segmenting Curved Catheters in Prostate Brachytherapy Ultrasound Images with a Deep Learning and Feature Extraction Pipeline <i>Jessica de Kort, The University of Winnipeg & University of Manitoba</i>
	O3-04: Accurate Catheter Tracking for Image-Guided Therapy Applications using Fiber-Bragg Grating <i>Mahdi Tahmasebi, Toronto Metropolitan University</i>	O4-04: Evaluating the Use of Automatic Workflow Recognition for Central Venous Catheterization Training <i>Catherine Austin, Queen's University</i>
15:00 – 15:30	Pitches 3: Device, Systems, and Robotic Development	Pitches 4: Deep Learning/Machine Learning Methodology 1
	Metropolitan Ballroom – Centre	Metropolitan Ballroom – East
	<i>Chairs: Ali Tavallaei & Joeana Cambranis-Romero</i>	<i>Chairs: Michael Daly & Siddarth Sadanand</i>
	P3-01: Design and Ergonomic Assessment of Steerable Catheter Handles for the CathPilot System <i>Sina Keshavarz, Toronto Metropolitan University</i>	P4-01: Comparative Analysis of Deep Learning Approaches for Urethral Segmentation in High-Dose-Rate Prostate Brachytherapy Using Transrectal Ultrasound Images <i>Nicole Valencia, The University of Winnipeg</i>
	P3-02: Validation of 3D Ultrasound Musculoskeletal System <i>Clara Duquette Evans, Western University</i>	P4-02: Predicting Inspiratory Chest CT Image Viability using Deep Learning <i>Sara Rezvanjou, Toronto Metropolitan University</i>
	P3-03: Multi-Material Hand Fracture Model for Spatial Learning <i>Trinette Wright, Techna & University Health Network</i>	P4-03: Involvement-Aware Foundation Models for Prostate Cancer Detection in Ultrasound <i>Mohamed Harmanani, Queen's University</i>
	P3-04: A Preclinical SPECT System Using Ultrahigh Energy Resolution CZT Detectors for Alpha and Beta Emitter Radiopharmaceutical Therapy Imaging <i>Aileen Ouyang, MH3D Inc.</i>	P4-04: Automated CNN-based Segmentation of Carotid Atherosclerotic Plaque and Morphological Characterization of Carotid B-mode Ultrasound Images <i>Nahid Babazadeh Khameneh, McGill University & Research Institute of McGill University Health Centre</i>
	P3-05: Design Optimizations of an Expandable Cable-Driven Parallel Mechanism for Minimally Invasive Cardiovascular Interventions (CathPilot) <i>Sina Keshavarz, Toronto Metropolitan University</i>	P4-05: Automatic Prostate Segmentation in Micro-Ultrasound Imaging using the Segment Anything Model <i>Olivia Radcliffe, Queen's University</i>

	<p>P3-06: Developing Low-Cost 3D-Printed Prosthetics with a Functional Wrist for Patients Along the Thai-Myanmar Border <i>Emese Elkind, Queen's University</i></p>	<p>P4-06: Advancing Kidney Ablation Analysis in 3D CT Images: A Deep Learning Segmentation Framework <i>Maryam Rastegarpour, Western University</i></p>
	<p>P3-07: Validating and Iterating the TRU-VU Wrist Positioning Aid and Educational Training to Improve the Standardization of Wrist Radiography <i>Laura Vancer, Western University</i></p>	<p>P4-07: Performing Prostate Segmentation Using SAM-Med2D Across Multiple Ultrasound Modalities <i>Vivian Nguyen, Queen's University</i></p>
		<p>P4-08: Evaluating the Use Cases of 3D and 2D Segmentation in Fetal MRIs <i>Alejo Costanzo, Toronto Metropolitan University</i></p>
15:30 – 16:30	<p>Poster Viewing (Pitch Sessions 3 & 4 plus posters below presenting)</p> <p>P3-08: Bridging the Gap with Customizable Above-Elbow Prosthetic Designs to Balance Open-Source Models and Patient-Specific Needs <i>Emese Elkind, Queen's University</i></p> <p>P3-09: Miniaturized Gamma-Imaging Probe for Lung Cancer Detection <i>Alysha Prem, Toronto Metropolitan University</i></p> <p>P4-09: Risk stratification of early-stage non-small cell lung cancer using PET-based radiomics <i>Christine Santiago, Western University</i></p> <p>P4-10: Automatic Classification of Levator Ani Muscle Avulsion in 3D Transperineal Ultrasound Images <i>Mihir Gokal, Western University</i></p>	Posters & Exhibit Hall
16:30 – 17:30	<p style="text-align: center;">Oral Presentations 5: General 1</p> <p style="text-align: center;">Metropolitan Ballroom – Centre</p> <p><i>Chairs: Amal Aziz & Eno Hysi</i></p> <p>O5-01: A Sensorless Freehand 3D Ultrasound Solution with a Novel Coupling Pad <i>Libin Liang, Robarts Research Institute & Western University</i></p> <p>O5-02: A Motion Assessment and Image Quality Enhancement Technique using Retrospective Frame Averaging with Low-dose Volumetric 4D-CT for Radiation Therapy Simulation <i>Timothy Yau, Western University</i></p> <p>O5-03: A Dual-Camera Simulation of Markerless, Optical Head Pose Tracking Using Deep Learning for Motion Correction in Magnetic Resonance Imaging <i>Marina Silic, University of Toronto</i></p> <p>O5-04: Image Database Creation for Improved Imaging of Mitral Valve Surgery Training Phantoms <i>Emma Zhang, Western University</i></p>	<p style="text-align: center;">Oral Presentations 6: Image Guided Intervention and Surgery 1</p> <p style="text-align: center;">Metropolitan Ballroom – East</p> <p><i>Chairs: Michael Hardisty & Mahdi Tahmasebi</i></p> <p>O6-01: A Feasibility Study on Enhanced Navigation in Breast-Conserving Surgery through Haptic Feedback <i>Laura Connolly, Queen's University</i></p> <p>O6-02: Physical Replication and Validation of Mathematical Mitral Valve Models <i>Patrick Carnahan, Robarts Research Institute</i></p> <p>O6-03: Non-invasive Ablation of Intra-abdominal Fetal Rabbit Umbilicus using Magnetic Resonance Guided High Intensity Focused Ultrasound Therapy <i>Ava Danialy, University of Toronto</i></p> <p>O6-04: Radio-Ultrasound-Guided System for Real-Time Intraoperative Localization: A Phantom Study <i>Sydney Wilson, Western University</i></p>
17:30 – 17:45	Refresh Break	
17:30 – 19:00	Welcome Reception & Social Event	
		Metropolitan Ballroom – Centre & East

Thursday, March 6, 2025

8:00 – 15:00	Registration	Foyer
8:00 – 9:00	Breakfast	Foyer
9:00 – 10:00	Oral Presentations 7: Deep Learning/Machine Learning Methodology 2	Oral Presentations 8: Image-Guided Intervention and Surgery 2
	Metropolitan Ballroom – Centre	Metropolitan Ballroom – East
	<i>Chairs: Patrick Carnahan & Edward Wang</i>	<i>Chairs: Saba Sadatamin & Cari Whyne</i>
	O7-01: Micro-CT Anatomical Measurement of the Human Cadaveric Subaxial Cervical Vertebrae: Machine Learning Prediction of the Lamina Length <i>Joseph Umoh, Western University</i>	O8-01: Feasibility of Three-dimensional Ultrasound for Cervical Cancer Treatment Planning <i>Tiana Trumpour, Western University</i>
	O7-02: Automated Diaphragm Segmentation using Deep Learning from Chest CT Images <i>Mustansir Verdawala, Toronto Metropolitan University</i>	O8-02: First Demonstration of Functional Connectivity Mapping using a 1.5T MR-Linac in Glioblastoma <i>Eaman Almasri, University of Toronto & Sunnybrook Research Institute</i>
	O7-03: A Deep Learning Pipeline for 3D Brain-Wide Mapping of Local Neuronal Ensembles in Tera-Voxel Light Sheet Microscopy <i>Ahmadreza Attarpour, University of Toronto</i>	O8-03: Improving Success Rate of Navigated Breast-Conserving Surgery by Needle Stabilization <i>Chris Yeung, Queen's University</i>
O7-04: Evaluating Deep Learning Models to Classify Early-Stage Esophageal Cancer: A Preliminary Study <i>Marcus Milantoni, Western University</i>	O8-04: Assessment of a Mini Stereotactic Guidance System for Percutaneous Focal Liver Tumour Ablation <i>Joeana Cambranis-Romero, Western University</i>	
9:45 – 16:30	Exhibits Open	Posters & Exhibits Hall
10:00 – 10:30	Pitches 5: Deep Learning/Machine Learning Methodology 2	Pitches 6: Image-Guided Intervention and Surgery
	Metropolitan Ballroom – Centre	Metropolitan Ballroom – East
	<i>Chairs: Patrick Carnahan & Celine Dubroy-McArdle</i>	<i>Chairs: Saba Sadatamin & Cari Whyne</i>
	P5-01: Evaluating and Comparing the Surgical Tool Detection Performance of YOLO Object Detection Models in Simulated Central Venous Catheterization <i>Aden Wong, Queen's University</i>	P6-01: Validation of an Electroanatomic Map Conversion Tool for Registration to Radiation Treatment Planning Images <i>Sarah Konermann, McGill University</i>
	P5-02: Machine Learning-Based Prediction of Vertebral Fracture Risk in SBRT Patients using Quantitative Imaging Data <i>Dawit Gulta, Sunnybrook Research Institute</i>	P6-02: Thrombectomy Assist: Live Thrombus Detection <i>Lola Assad, Queen's University</i>
	P5-03: Predicting the Phase of Cataract Surgery with Deep Learning <i>Joshua Bierbrier, Queen's University</i>	P6-03: Development of a Novel System for Micro-Ultrasound-Guided Focal Low-Dose-Rate Prostate Brachytherapy <i>David Contella, Western University</i>
P5-04: Automated MRI-Based Segmentation of Multiple Fetal Brain Structures <i>Yasmin Modarai, Toronto Metropolitan University</i>	P6-04: 3D Calyx Segmentation for the Volumetric Detection of Hydronephrosis <i>Marina Music, Queen's University</i>	

	<p>P5-05: Leveraging Surgical Workflow Recognition for Skill Assessment in Simulated Cataract Surgery <i>Bining Long, Queen's University</i></p>	<p>P6-05: Predicting Patient-Specific Instantaneous Spatial Temperature Maps for MR-Guided Laser Interstitial Thermal Therapy for Epilepsy using a Physics-Informed Neural Network <i>Saba Sadatamin, University of Toronto</i></p>
	<p>P5-06: Leveraging Convolutional Embeddings for AFib Detection in the Intensive Care Unit Setting <i>Nooshin Maghsoodi, Queen's University</i></p>	<p>P6-06: Assessing the Impact of a Magnetic Field Generator on Fluoroscopic Image Quality <i>Mateen Mirzaei, Western University</i></p>
	<p>P5-07: Self-Supervised Parallel Transmit RF Pulse Design for 2D Spatially Selective Excitation <i>Yuliang Xiao, University of Toronto & Sunnybrook Research Institute</i></p>	<p>P6-07: Designing a 6-Axis Testbed for Accessible Image-Guided Robotics Research <i>Coleman Farvolden, Queen's University</i></p>
	<p>P5-08: Ultrasound Probe Segmentation for RGB-D Object Tracking in Central Line Insertion <i>Réna Hajjar, Queen's University</i></p>	
10:30 – 11:30	<p>Break & Poster Viewing (Pitches 5 & 6 plus posters below presenting)</p> <p>P6-08: Evaluating Sensitivity Differences of Healthy Spinal Cord and Intramedullary Spinal Cord F98 Glioma in Response to Focused Ultrasound and Microbubbles <i>Mahsa Mokhlesabadi, Sunnybrook Research Institute</i></p> <p>P6-09: The Impact of Propagation Pathways on Targeting Accuracy in Transspinal Ultrasound Focusing <i>David Martin, Sunnybrook Research Institute</i></p>	Posters & Exhibit Hall
11:30 – 12:30	<p>Oral Presentations 9: Cancer 2</p> <p>Metropolitan Ballroom – Centre</p> <p><i>Chairs: Ryan Au & Amoon Jamzad</i></p> <p>O9-01: Regional Predictors of Progression after Stereotactic Radiosurgery for Brain Metastases <i>Robert Policelli, Western University</i></p> <p>O9-02: Development of Cisplatin Prodrug-Loaded Microbubbles for Ultrasound-Aided Targeted Cancer Therapy <i>Sean McGrath, University of Toronto</i></p> <p>O9-03: Adaptive Resource-Efficient Federated Learning for Prostate MRI using PCA and Early Stopping - Negin Piran Nanekaran, University of Guelph</p> <p>O9-04: A Mechatronic Needle Guidance System for Prostate-Specific Positron Emission Tomography and 3D Transrectal Ultrasound-Guided Trans-perineal Prostate Biopsy <i>Sule Karagulleoglu Kunduraci, Western University</i></p>	<p>Oral Presentations 10: Cardiac, Lung, and Musculoskeletal Imaging</p> <p>Metropolitan Ballroom – East</p> <p><i>Chairs: Michael Hardisty & Nika Momeni</i></p> <p>O10-01: Ultrasound 3D Reconstruction of the Lower Spine for Facet Joint Injection <i>Gaurav Ranjit, Queen's University</i></p> <p>O10-02: Enhanced Cardiac Imaging using Fixed-Filter Spectral Imaging with Anti-Correlated Noise Correction <i>Lisa Garland, Robarts Research Institute</i></p> <p>O10-03: Development of a Tissue-Equivalent Lung Phantom Compatible for Proton Magnetic Resonance Imaging (MRI) for Evaluation of Airway Size <i>Razieh Enjilela, Toronto Metropolitan University</i></p> <p>O10-04: Examining the Bilateral Loading Relationship in Thumb Osteoarthritis <i>Jennifer Villeneuve, Western University</i></p>
12:30 – 13:45	Lunch Pickup	Foyer
12:45 - 13:30	<p>Panel: Career Pathways for Graduates: Academic and Industry Advice on Talent Development <i>Padina Pezeshki, Medtronic; Terry Peters, Robarts Research Institute; Alla Reznik, Lakehead University; Graham A. Wright, Sunnybrook Research Institute; Cari Whyne, Sunnybrook Health Sciences Centre</i></p>	Metropolitan Ballroom – Centre

13:45 – 14:45	Oral Presentations 11: Optical Imaging & Ultrasound Imaging	Oral Presentations 12: General 2
	Metropolitan Ballroom – Centre	Metropolitan Ballroom – East
	<i>Chairs: Amoon Jamzad & Sule Karagulleoglu</i>	<i>Chairs: Dafna Sussman & Carla Kulcsar</i>
	O11-01: Deep Learning-Enabled 3D Fluorescence Imaging for Surgical Guidance: Assessing Surgical Margins <i>Hikaru Kurosawa, Princess Margaret Cancer Centre</i>	O12-01: Evaluating the Association Between Primary Motor Cortex Metabolite Levels and Dexterity Following Spinal Surgery for Degenerative Cervical Myelopathy <i>Scott Wilson, Robarts Research Institute</i>
	O11-02: Three-Dimensional Ultrasound Synovial Blood Flow Volume Assessment in Thumb Osteoarthritis Patients <i>Megan Hutter, Western University</i>	O12-02: Accelerating Monte Carlo Light Propagation Models for Deep Learning-Enabled Fluorescence-Guided Surgery <i>Matthew Siracusa, Princess Margaret Cancer Centre</i>
	O11-03: In Vivo Hyperspectral Ultra-Broadband Sub-MHz Photoacoustic Imaging: Volumetric Optical Contrast to 4 cm Deep and Beyond <i>Ivan Kosik, Princess Margaret Cancer Centre</i>	O12-03: Role of Imaging Contrasts in the Volumetric Prediction of MT-NOE Attenuated Tumour Sub-Region <i>Céline Dubroy-McArdle, Toronto Metropolitan University</i>
O11-04: Deep Learning Architecture Optimization for 3D Optical Imaging in Early-Stage Oral Cancer Models <i>Rooaa Shanshal, Princess Margaret Cancer Centre & University Health Network</i>	O12-04: Light-Based Pressure Monitoring Guidance in Neurosurgery Retraction: Development and Validation of an Optical Sensing Algorithm <i>Lee Sikstrom, Robarts Research Institute & Western University</i>	
14:45 – 15:15	Pitches 7: Optical Imaging & Ultrasound Imaging	Pitches 8: General
	Metropolitan Ballroom – Centre	Metropolitan Ballroom – East
	<i>Chairs: Megan Hutter & Eno Hysi</i>	<i>Chairs: Razieh Enjilela & Siddarth Sadanand</i>
	P7-01: Standardizing B-Line Annotation for Reproducible Lung Ultrasound Metrics <i>Maha Kesibi, Queen's University</i>	P8-01: A Language-Audio Foundation Model for Characterization of Cancerous Tissue in Mass Spectrometry Images <i>Alon Gabriel, Queen's University</i>
	P7-02: Automated Liver Segmentation using Attention Models in Point-of-Care Ultrasound Images <i>Zachary Szentimrey, University of Guelph</i>	P8-02: Histology Hide-and-Seek: Visually Navigating Latent Space Clustering for Pathology Exploration <i>Phoenix Wilkie, University of Toronto</i>
	P7-03: Influence of Laser Coherence Length in Polarization Speckle-Based Tumour Detection <i>Daniel Louie, University Health Network</i>	P8-03: A Comparison of Uncertainty Techniques on Basal Cell Carcinoma Mass Spectrometry Data <i>Tyler Elliott, Queen's University</i>
	P7-04: Quantifying Tendon Excursion in the Shoulder using a 3D-Ultrasound Musculoskeletal System <i>Marie Le, Western University</i>	P8-04: 3D ABUS System with Breast Needle Biopsy Capability and Integrated MRI-guidance Lesion Localization <i>Amal Aziz, Western University</i>
	P7-05: Self-Supervised Learning for Retinal Disease Classification: Reducing Annotation Dependency with Transformation-Based Pretext Learning with Limited Labels <i>Pramit Dutta, University of Guelph</i>	P8-05: Large Language Models are One-Shot Radiology Report Summarizers <i>Mahmoud Idbi, Queen's University</i>
	P7-06: Polyvinyl Alcohol Cryogels (PVA-C): Fabrication Method for Homogeneous Multimodal Phantoms <i>Olivia Qi, Western University</i>	P8-06: Accelerated 4D Flow with Respiratory Compensation and Cardiac View Sharing in Pediatric Congenital Heart Disease <i>Fatemeh Rastegar Jooybari, University of Toronto</i>
	P7-07: Spine Ultrasound Segmentation Trained on Registered CT As Ground Truth	P8-07: Forecasting Movement Patterns in Stroke Patients Utilizing Time Series Foundation Models

	<i>Junhui Zong, Queen's University</i>	<i>Dharsan Ravindran, Queen's University</i>
	P7-08: Ultrasound Based Evaluation of Stress Urinary Incontinence Pessaries on Bladder Neck, Bladder Descent, and Retrovesical Angle <i>Helena Kunic, University of Guelph</i>	
	P7-09: Polarization Speckle Analysis of Volumetric Scattering from Controlled Turbid Phantoms and Mouse Skin Tissues <i>Carla Kulcsar, University of Toronto</i>	
15:15 – 16:15	Break & Poster Viewing (Pitches 7 & 8 plus posters below presenting) P7-10: Impact of Ambient Light on Spatial Frequency Domain Imaging for Surgical Guidance <i>Jack Wunder, Princess Margaret Cancer Centre</i> P7-11: Tri-Modal Mosquito Bite Needle Endoscopy (MBNE) for Breast Cancer Diagnostics <i>Alexandre (Sasha) Douplik, Toronto Metropolitan University</i>	Posters & Exhibit Hall
16:15 - 17:00	Keynote Session II <i>Chairs: Joeana Cambranis-Romero & April Khademi</i> The Abundant Promise of Ultrasound in Neurosurgery <i>Amir Manbachi, Johns Hopkins University</i>	Metropolitan Ballroom – Centre
17:00 - 17:30	Closing Remarks and Awards <i>Dafna Sussman and Ali Tavallaei, Toronto Metropolitan University</i>	Metropolitan Ballroom – Centre

Talk and Pitch Abstracts (in order of the talks)

Oral Presentations 1: Cancer 1

Abstracts

The role of flow and microbubble-induced shear stress in endothelial cell immunobiology

Elahe Memari¹, Davindra Singh², Ryan Alkins³ and Brandon Helfield^{1,2}

- 1- Department of Physics, Concordia University, Montreal, Quebec, Canada
- 2- Department of Biology, Concordia University, Montreal, Quebec, Canada
- 3- Division of Neurosurgery, Department of Surgery, Kingston Health Sciences Centre, Queen's University, Kingston, ON, Canada

Objective: Blood flow-induced shear stress influences endothelial signaling pathways associated with the expression of cell adhesion molecules (CAMs) and the secretion of cytokines. However, the role of shear stress in improving cellular immunotherapy is poorly understood. Given that ultrasound-mediated microbubbles generate localized and large-magnitude shear stress, it presents a promising strategy to address the limitations of cellular immunotherapy. Therefore, this study aims to explore the influence of both fluid flow and ultrasound-mediated shear stress on CAM expression, endothelial secretome and migration of CAR NK-92 cells.

Methods: To investigate the bioeffects of flow preconditioning, either umbilical vein (HUVEC) or cerebral microvascular endothelial cells (HBEC-5i) were cultivated either statically or under a shear flow of 9 dyne/cm² for 0-48 hours. At different time points, cell culture supernatant was collected, and the level of secreted factors was quantified using Luminex xMAP technology. Additionally, cells were examined for the surface expression of either ICAM-1 or MadCAM-1 using immunohistochemistry. In the second set of experiments, cell-seeded chamber slides were continuously perfused with Definity, and four non-overlapping regions were sonicated (1 MHz, 20-cycle burst, 1ms PRI, 1- 4 minutes, peak-negative pressure of 150 or 210 kPa). The surface expression of ICAM-1 and MadCAM-1 was examined at either 1 or 4 hours post-sonication. Additionally, HBEC-5i secretome after ultrasound treatment was analyzed via Luminex xMAP, and its influence on transmigration of CAR-NK-92 cells was examined using the transwell immunoassay.

Results: Our results revealed that flow preconditioning of endothelial cells modulates the surface expression of ICAM-1 on HUVEC and HBEC-5i in a time-dependent and reversible manner, with a peak increase at 4h (1.98±0.15) and 24h (1.56-fold, p<0.001), respectively. Additionally, exploring the influence of shear flow on differential secretion of 96 cytokines demonstrated a drastic increase up to 16.2-fold in the secretion of inflammatory cytokines from HBEC-5i, including IL-6, TNF- α , TNF- β , GRO- α , CXCL16, CCL28 and SDF-1. In contrast, HUVEC responded to shear flow differently, with a significant downregulation of factors such as CCL5, CXCL16, SDF-1, TNF- β and CCL28. In the second set of experiments, ICAM-1 expression peaked at 4 hours post-sonication (1.4-fold, p<0.01), while MadCAM-1 expression peaked at 1 hour after sonication (1.5-fold, p<0.01), under similar acoustic conditions. Ultrasound-stimulated microbubbles also enhanced the secretion of 20 cytokines from HBEC-5i at 4 hours post-sonication, most of which have immune-activating function. Finally, the transmigration assay revealed that ultrasound-mediated HBEC-5i secretome enhanced the migration of CAR NK-92 cells by 2.35-fold (p<0.001) compared to control.

Conclusion: Our findings highlight that ultrasound-stimulated microbubbles can influence local endothelial immunobiology by modulating the expression of cell adhesion molecules and altering endothelial secretome, thus promoting immune cell trafficking. Overall, this study shows the potential of ultrasound treatment in combination with microbubbles in overcoming tumor microenvironment and improving cellular immunotherapy.

Using computed tomography perfusion (CTP) to assess changes in the contrast distribution volume in pancreatic cancer patients: a potential biomarker for patient response to standard-of-care therapy

Bang JY^{1,2}, Gaede S^{1,2}, Lee TY^{1,3}

¹Department of Medical Biophysics, Western University

²Verspeeten Family Cancer Center, Victoria Hospital, London, ON

³Robarts Research Institute, London, ON

Introduction: Pancreatic cancer is currently the third leading cause of cancer death in Canada with a 5-year relative survival rate of 10%. Approximately 90% of all pancreatic cancer patients are diagnosed with pancreatic ductal adenocarcinoma (PDAC), or malignancies derived from the ductal cells lining the epithelium of the pancreatic duct. In addition to its tendency to spread rapidly to the lymphatics and other organs, PDAC is characterized by a dense, fibrotic tumor microenvironment composed of a thick network of fibroblasts and extracellular matrix components, which can greatly limit pancreatic tumor perfusion and restrict the delivery of systemic cancer drugs to the tumor site. In our previous analysis, we demonstrated that acute irradiation of the pancreatic tumor using stereotactic ablative body radiotherapy (SABR)—an emerging form of radiotherapy that can precisely deliver high doses of radiation in only 3-5 fractions with the guidance of an integrated imaging system—could induce a significant increase in tumor blood flow to potentially enhance the systemic delivery of anticancer drugs to the tumor site. In this new analysis, we specifically analyzed the contrast distribution volume using computed tomography perfusion (CTP) to demonstrate its potential as an effective biomarker for prospectively monitoring patient response to standard-of-care therapy over the course of their treatment regimen.

Methods: Adults aged 18 or older with histologically confirmed primary pancreatic cancer were prospectively recruited with informed consent, provided that they were medically fit for surgical resection. The recruited patients were divided into 2 study arms based on the degree of involvement of the critical vessels around the tumor volume: resectable pancreatic cancer (RPC) (n = 1) and borderline resectable pancreatic cancer patients (BRPC) (n = 5). All patients underwent neoadjuvant SABR with a prescription dose to the planning target volume (PTV) ranging between 27-30 Gy in 3 fractions. A dose boost of up to 45 Gy was also given to the metabolically active areas of the tumor site indicated by positron emission tomography (PET). For perfusion analysis, CTP images of the abdominal region were acquired using the GE HealthCare Revolution CT scanner (GE HealthCare, Waukesha, USA) with a z-axis coverage of 16 cm. Images were acquired from patients in both arms at multiple instances over the course of their treatment: a) at baseline; b) 6 hours after administering the first fraction of neoadjuvant SABR (post-1st-fx); and c) 3-4 weeks after completing SABR, prior to surgical resection. For the BRPC patients, CTP scans were also taken after completing neoadjuvant chemotherapy. From the CTP images acquired at each study instance, a prototype deconvolution-based CTP software (GE Healthcare) was used to calculate the total distribution volume (V_D), extravascular volume (V_e), and blood volume (BV). Mathematically, $V_D = V_e + BV$.

Results: For the RPC patient, only the BV showed a noticeable change at 6 hours post-1st-fx, with a 38% increase relative to baseline. At 3-4 weeks post-SABR, all 3 volumes were consistently higher than baseline (post-SABR change relative to baseline: $V_D = +41\%$; $V_e = +52\%$; $BV = +29\%$). Similarly, for 2 BRPC patients who were able to acquire a pre-chemo baseline scan, the V_D was significantly higher both at post-chemo and at 3-4 weeks post-SABR relative to baseline (sample patient V_D : baseline = 12.5 mL/100g; post-chemo = 43.6 mL/100g; post-SABR = 44.6 mL/100g). Both V_e and BV showed similar trends in these 2 BRPC patients as well. In comparing all 5 BRPC patients together, despite observing little to no change in the mean V_D between the post-chemo and post-SABR timepoints (mean V_D : post-chemo = 43.1 mL/100 g; post-SABR = 45.0 mL/100 g) the mean BV was 18% lower, while the mean V_e was 11% higher at 3-4 weeks post-SABR than post-chemo. At 6 hours post-1st-fx, however, no consistent trend could be established for volume changes in the BRPC arm.

Conclusion: While these observations have yet to be verified with a larger sample size, we demonstrate that the contrast distribution volume measured by CTP may be a prominent biomarker that could help monitor patient response to standard-of-care therapy, including chemotherapy and radiotherapy. Additionally, the consistent increase in V_D and V_e , which was observed in both the RPC patient and the BRPC patients over the course of their treatment regimen, may translate to improved biodistribution of systemic cancer drugs post-treatment. Notably, in terms of V_e , its increase could also serve as a surrogate measure of a possible reduction in the tumor cell density, which is characteristically high in PDAC due to the presence of a dense, fibrotic stroma.

Advancing Treatment of Skeletal Metastases: Radiation-Induced Photodynamic Therapy (RadioPDT) with Novel Nanoparticles

Azin Mirzajavadkhan^{1,2}, Leanna Abraham³, Margarete Akens^{3,4,5}, Cari Whyne^{1,2,5}, Deepak Dinakaran^{2,3,6}

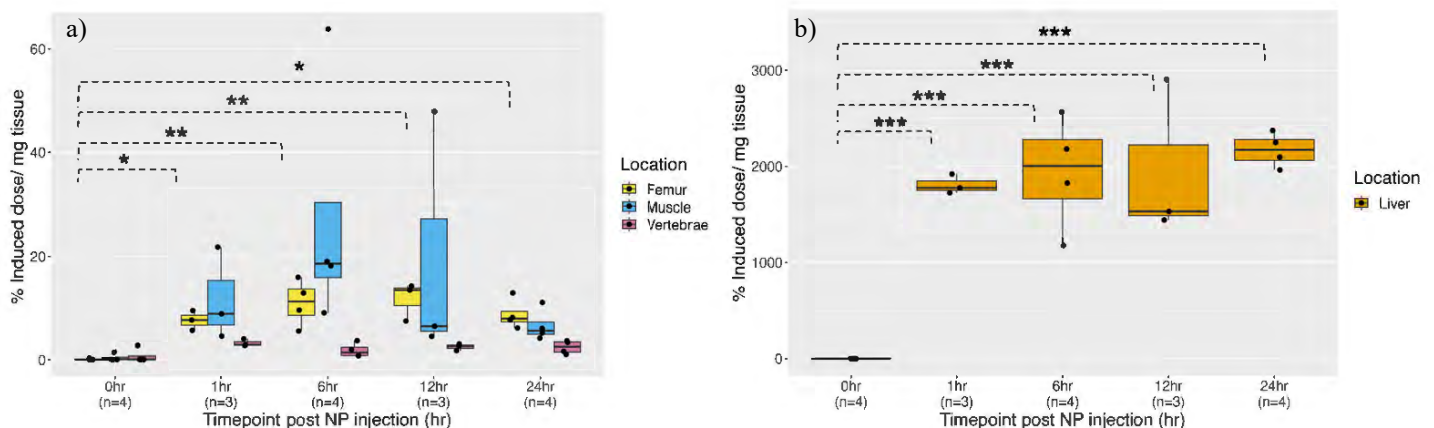
¹Institute of Biomedical Engineering, University of Toronto; ²Physical Sciences Platform and Holland Bone and Joint Program, Sunnybrook Research Institute; ³Department of Medical Biophysics, University of Toronto, Toronto; ⁴TECHNA Institute, University Health Network; ⁵Division of Orthopaedics, Department of Surgery, University of Toronto; ⁶Department of Radiation Oncology, University of Toronto

Introduction: Skeletal metastases impact the bone remodeling process, increasing the risk of pathological fractures. Local treatments for skeletal metastases include stereotactic body radiation therapy (SBRT) which delivers intense doses of radiation to targeted regions using image guidance, and photodynamic therapy (PDT, investigational stage) that uses a photosensitizer (PS) activated by light to destroy tumor cells by forming reactive oxygen species. PDT is challenged in treating deep-seated tumors by light delivery and its dosimetry. RadioPDT addresses this by using X-rays, with unlimited penetration and existing highly conformal treatment planning methods, to activate the PS via scintillating nanoparticles (NPs). These NPs further enable CT-based image-guided radiation therapy, combining treatment with diagnostic potential. This study aims to evaluate NP biodistribution in prostate cancer cells found within skeletal metastases and establish the optimal timing for RadioPDT treatment.

Methods: Eighteen six-week-old athymic male rats (Hsd: ^{RH-Foxn1}mu, Envigo, USA) were inoculated with luciferase-transfected ACE-1 canine prostate cancer cells via an intracardiac injection after a week of acclimation (day 0). Institutional approval was obtained, and the ARRIVE guidelines were followed [1]. On day 20 post inoculation, the rats underwent bioluminescence imaging (BLI) to observe the location and presence of metastases in the femora. On day 21, the animals were injected with 500mg/kg of a novel theranostic NP poly (ethylene glycol) methyl ether-*block*-poly(lactide-*co*-glycolide) (PEG-PLGA) nanospheres with Ce³⁺ doped lanthanum (III) fluoride (LaF₃:Ce³⁺) nanoscintillators and protoporphyrin IX photosensitizer co-encapsulated and administered via an intravenous injection [2]. The animals were then randomly assigned to sacrifice at 5 time-points post injection: 0hrs (n=4), 1hr (n=3), 6hrs (n=4), 12hrs (n=3), 24hrs (n=4). Following sacrifice, the femur, vertebrae, quadriceps muscle (control organ), and liver (clearance organ) were harvested and prepared for inductively coupled plasma mass spectrometry (ICP-MS) to measure the NP concentration found in each tissue.

Results: One-way ANOVA revealed significantly higher NP concentrations in the metastatic involved femur (p<0.01) and liver (p<0.001) across timepoints. Pairwise comparisons confirmed NP levels were significantly elevated compared to baseline, with peak concentrations at 12 hours in the femur (p<0.01, Figure a) and 24 hours in the liver (p<0.001, Figure b). Additionally, there was a positive moderate correlation between NP concentration found in the tumor within the femur and vertebrae with the average radiance obtained from BLI (R=0.56, p<0.001).

Conclusion: This study reveals that NP levels peak in the femur 12 hours post-injection, while liver accumulation suggests clearance via the mononuclear phagocyte system, consistent with polymeric NPs [2]. Identifying the timing at which the highest levels of NPs are found within the tumor will direct radioPDT treatment delivery to skeletal metastases in this preclinical model. Future work will evaluate the therapeutic effect of radioPDT on tumor ablation and bone quality in this preclinical model towards guiding future translational treatment strategies.



Biodistribution of PEG-PLGA NPs in the femur, muscle, vertebrae (Figure a), and liver (Figure b) across different timepoints. Tukey-Kramer pairwise comparisons test; *p < 0.05, **p < 0.01, ***p < 0.001.

Differences in Radiologist Search Patterns when Assessing mpMRI for Prostate Cancer

Ryan Au^{1,2}, Derek Cool^{3,4}, Harry Marshall⁵, Vibhuti Kalia^{4,6}, Shubreet Randhawa^{4,6}, Anat Kornecki^{4,6}, Carol Johnson², Glenn Bauman^{1,2,7}, Aaron Ward^{1,2,7}

¹Departments of Medical Biophysics, Western University, Canada, ²Verspeeten Family Cancer Centre, London Health Sciences Centre, Canada, ³Division of Interventional Radiology, Western University, Canada, ⁴Department of Medical Imaging, Western University, Canada, ⁵Department of Radiology, Vanderbilt University Medical Center, United States of America, ⁶Department of Medical Imaging, St Joseph's Health Care, Canada, and ⁷Department of Oncology, Western University, Canada.

Introduction: The Prostate Imaging – Reporting and Data System (PI-RADS) guidelines specify the use of multiparametric magnetic resonance imaging (mpMRI), including the use of the T2-weighted (T2w), apparent diffusion coefficient (ADC) map, and T1-weighted dynamic contrast-enhanced (DCE) MR images, for prostate cancer (PCa) diagnosis. However, radiologists with fewer years of experience may be less accurate at identifying PCa when performing a PI-RADS assessment.¹ Reviewing the search patterns of expert radiologists captured using eye tracking technology has shown to be an effective training tool for junior radiologists to develop proficiency at searching for abnormalities within planar x-ray images.^{2,3} No studies have investigated the search patterns in the PCa mpMRI domain. Therefore, as the first step of building a potential training tool involving radiologist search patterns, the objective of this study was to assess whether different radiologists have different search patterns when performing a PI-RADS assessment.

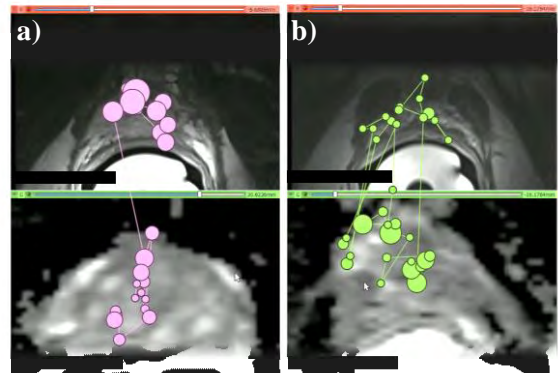
Methods: A Research Ethics Board-approved cohort of 40 patients with biopsy-proven PCa and had *in vivo* mpMRI acquired was used for this research. All mpMR images were loaded into the Image Quizzer 3DSlicer module where 4 board-certified radiologists with varying levels of experience were tasked to complete a PI-RADS assessment for all patients. During their assessment, eye tracking data was collected using the Gazepoint GP3HD system. Radiologists were then tasked to contour each of the lesions they identified during their PI-RADS assessment. The time spent on each mpMR image type, percentage of prostate covered with foveated vision, and duration on slices contoured vs. non-contoured during their PI-RADS assessment were calculated.

Results: Figure 1 shows the search pattern of the two most experienced radiologists in our study, with radiologist 1 (R1, 10 years experience) predominantly focusing along the centre of the prostate for relatively long periods of time, while radiologist 2 (R2, 8 years experience) scanned more of the prostate and focused for relatively shorter periods of time. R2 and radiologist 4 (R4, 1 year experience) spent significantly more time on the T2w and ADC compared to R1 and radiologist 3 (R3, 4 years experience) ($p < 0.001$). R4 spent the least amount of time on the DCE image ($p < 0.001$). R2 reviewed 57.6% of the prostate on ADC using foveated vision compared to $< 50.0\%$ by the other radiologists ($p < 0.006$), while R3 reviewed 51.6% of the prostate on DCE compared to $< 35.0\%$ by the other radiologists ($p < 0.001$). R4 spent significantly more time on mpMRI slices they did not contour compared to slices they contoured; this trend was not seen with the other radiologists.

Conclusions: Radiologists have significantly different search patterns when performing a PI-RADS assessment. Notably, the radiologist with the least number of years of experience spent more time on mpMRI slices they did not find PCa on, suggesting it may take more years of experience to develop confidence in ruling out image slices without cancer. Future work includes assessing the relationship between mpMRI search patterns with the underlying histology to identify potential search patterns that may lead to better accuracy at identifying PCa.

References:

1. Xu, L., *et al. Abdom. Radiol.* 2020.
2. Donovan, T., *et al. Proc. SPIE.* 2008.
3. Litchfield, D., *et al. J. Exp. Psychol. Appl.* 2010.



Duration Size Legend (0.2s→0.5s→0.8s): ●→●→●

Figure 1: a) Radiologist 1 and b) radiologist 2's search pattern on the T2w (top) and ADC (bottom) over a 10 second period. Circles represent focus locations, size of circles represents duration at focus location (the larger the circle, the longer the duration), and lines between circles represents search path.

Oral Presentations 2: MRI & Neuroimaging

Abstracts

Fetoplacental Blood-Mimicking Phantoms for Optimizing Susceptibility Weighted Imaging

Dylan Young^{1,2}, Alexander Dunn^{1,2}, Siddharth Sadanand^{1,2}, Michelle Sholzberg^{1,2,3}, Naimul Khan¹, Dafna Sussman^{1,2,4*}

¹Department of Electrical, Computer and Biomedical Engineering, Toronto Metropolitan University, Toronto, Canada; Institute for Biomedical Engineering, Science and Technology (iBEST) at Toronto Metropolitan University

²St. Michael's Hospital, Toronto, Canada & Keenan Research Centre for Biomedical Science, St. Michael's Hospital. ³Division of Hematology/Oncology, Departments of Medicine and Laboratory Medicine and Pathobiology, St. Michael's Hospital. ⁴Department of Obstetrics and Gynaecology, Faculty of Medicine, University of Toronto, Toronto, Ontario, Canada.

Introduction: Iron is essential for metabolic processes such as DNA synthesis, red blood cell production, and oxygen transport¹. During pregnancy, iron demands rise significantly to support maternal blood volume and fetoplacental development². Iron deficiency is the most common micro-nutritional deficiency globally, affecting up to 80% of pregnant women in low- and middle-income countries and 45% in high-income countries³⁻⁵. Ferritin, stored in the liver and placenta, buffers maternal and fetal iron levels during pregnancy⁶. Non-invasive MRI techniques, including Susceptibility Weighted Imaging (SWI), exploit iron's paramagnetic properties for sensitive quantification of iron metabolites such as ferritin⁷⁻⁹. This study aims to develop blood-mimicking phantoms to optimize an SWI protocol for quantifying iron metabolite concentrations in the liver and placenta in normal and anemic pregnancies. While this is not a motion phantom, sequence parameter optimization will aim to maintain expeditiousness of current SWI protocols while improving sensitivity and specificity to ferritin.

Methods: Blood-mimicking phantoms, designed to simulate normal and anemic iron ranges, will be imaged using carrageenan-based hydrogel wells (Fig. 1) to minimize susceptibility artifacts. These phantoms will contain calcium chloride and carbonate within normal range, along with anemic and high ranges of ferritin to allow testing of the SWI sequence's sensitivity, specificity, and robustness against confounds such as overlapping metabolites, paramagnetic compound accumulations and susceptibility artifacts. Imaging parameters will be refined to enhance ferritin sensitivity and address motion-related limitations in current methods.

Expected Outcomes: The optimized SWI protocol is expected to demonstrate:

1. Improved sensitivity and specificity for detecting ferritin and other iron metabolites.
2. Robust performance in the presence of metabolite confounds and paramagnetic accumulations.
3. Practical utility in quantifying iron levels in the maternal liver, fetal liver, and placenta under clinically relevant conditions.

Conclusions: An optimized SWI protocol offers a novel, non-invasive approach for iron quantification in pregnancy, addressing critical gaps in the understanding of conference of iron status from mother to baby which when deficient is associated with maternal, fetal and childhood morbidity and mortality. By leveraging blood-mimicking phantoms and advanced MRI techniques, this study aims to contribute to improved prenatal care and maternal-fetal health management through enhanced imaging capabilities.

References: [1] Ems, T et al., *Biochemistry*, Iron Absorption (2024). [2] Fisher, A et al., *Am J Clin Nutr* **106**, 1567S-1574S (2017). [3] Mégier, C et al., *Metabolites* **12**, 129 (2022). [4] Camaschella, C. *N Engl J Med* **372**, 1832–1843 (2015). [5] Auerbach, M et al., R. *J Matern Fetal Neonatal Med* **34**, 1002–1005 (2021). [6] Georgieff, M. K., *Am J Obstet Gynecol* **223**, 516–524 (2020). [7] Reeder, S. B. et al., *Radiology* **307**, e221856 (2023). [8] Halefoglu, A et al., *World J Radiol* **10**, 30–45 (2018). [9] Haacke, E et al., *AJNR Am J Neuroradiol* **30**, 19–30 (2009).

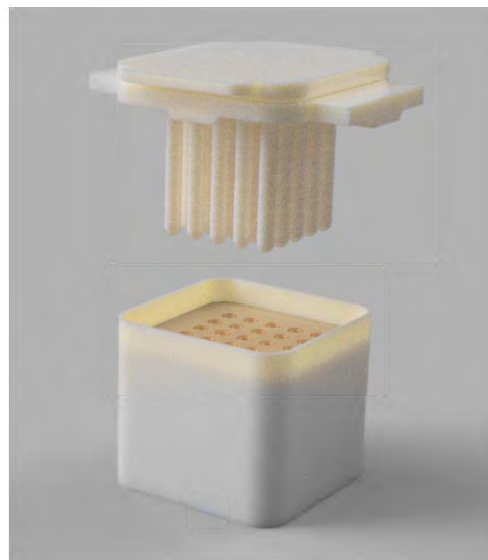


Figure 1. Mold used for carrageenan-based imaging wells to contain phantoms.

A pulse sequence for single breath hold saturation transfer imaging of the entire gravid abdomen

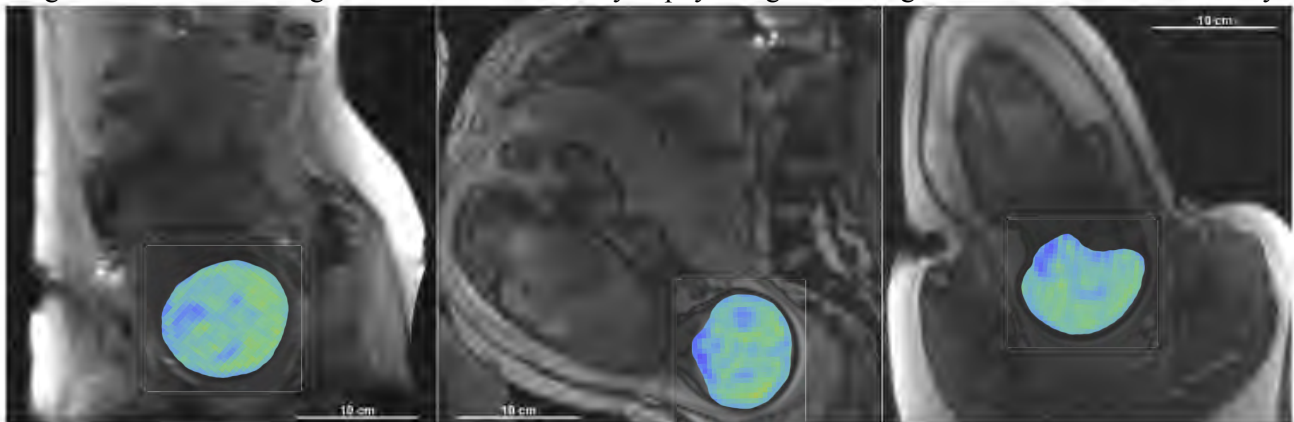
Sid Sadanand^{1,2}, Rob Stobbe³, Tim van Mieghem^{4,5}, Shiri Shinar^{4,5}, Pradeep Krishnan⁶, Elka Miller⁶, Greg Stanisz^{7,8}, Dafna Sussman^{1,2,4}

¹Departments of Biomedical Physics and of Biomedical Engineering, Toronto Metropolitan University, Toronto, ²Institute for Biomedical Engineering, Science and Technology (iBEST) at Toronto Metropolitan University and St. Michael's Hospital, Toronto, ³Departments of Radiology Biomedical Engineering, University of Alberta, Edmonton, ⁴Fetal Medicine Unit, Department of Obstetrics and Gynaecology, Mount Sinai Hospital, Toronto, ⁵Department of Obstetrics & Gynaecology, University of Toronto, Toronto, ⁶Neuroradiology, Department of Diagnostic Imaging, The Hospital for Sick Children, Toronto, ⁷Sunnybrook Research Institute, Toronto, ⁸Department of Medical Biophysics, University of Toronto, Toronto

INTRODUCTION: Saturation transfer (ST) imaging is an MRI method that allows amplification of metabolite signal, enabling more sensitive detection of tissue function than current clinically-translated sequences[1]. Metabolic imaging such as ST imaging could allow investigation of disease aetiology and earlier detection of pathologies[1]. Application to fetal imaging in particular could further facilitate understanding of maternal-fetal metabolic dynamics[2]. Magnetization transfer (MT), a form of ST sensitive to macromolecules defining tissue microstructure, could specifically be used to visualize fetal brain myelination[3]. Thus far, long sequence acquisition time has limited clinical translation of MT imaging in anatomy with unpredictable motion, such as with maternal peristalsis and fetal movement[2]. We present a clinically-feasible, whole-uterus MT-weighted (MTw) 3D pulse sequence that acquires a 350mm fields of view at 5mm isotropic resolution within a 14s maternal breath hold. The methods used to expedite imaging are generalizable to other metabolites, facilitating clinical translation of endogenous contrast metabolic MRI.

METHODS: Phantom and in vivo imaging were conducted on a Siemens Prisma fit 3T clinical scanner at the Hospital for Sick Children in Toronto. The sequence implemented is RF-spoiled SSFP UTE, followed by a yarnball trajectory[4] with 512 interleaves, TE = 120 μ s, TR = 3.3 ms, FA = 3.15°, tRO = 2 ms, matrix size = 70. A Fermi-apodized multiband[5] alternating phase[6] pulsed saturation was optimized via genetic algorithm[7] for MT signal with $t_{\text{pulse}} = 99.8$ ms, FA_{pulse} = 2000°, $n_{\text{pulses}} = 30$, DC = 99%, $\delta_{CS} = 12$ & 3.5 ppm. The total acquisition time for the 3-point measurement, including dummy repetitions to drive steady state magnetization, was 28 s, including the 14 s breath hold. MT phantoms were made at a range of MT-producing agar concentrations, with varying concentrations of glucose as an ST confound. Participants were recruited from the Ontario Fetal Centre at Mount Sinai Hospital in Toronto with mildly complicated pregnancies (eg. borderline ventriculomegaly), and imaged at 31-38 wks gestational age, in accordance with SickKids REB#62640.

RESULTS: Phantom imaging found an MTw signal of 6.8% per %w/w of agar with a limit of quantitation of 0.62%/w/w. In utero MTw contrast on structural imaging of a recruited mildly complicated pregnancy is shown in the figure below. These images demonstrate sensitivity to physiological MT signal and breath hold tolerability.



CONCLUSIONS: We developed, optimized, and tested an endogenous contrast MTw pulse sequence for single breath hold, whole-uterus gestational imaging. The developed sequence was evaluated for sensitivity and robustness to confounds in phantoms, then translated to mildly complicated pregnancies, showing contrast in human fetal physiology. This sequence facilitates metabolic and microstructural fetal imaging, offering a potential tool for studying fetal brain development. The methods used here to expedite imaging are generalisable to other analytes and contrasts.

REFERENCES: [1] Jones, KM et al., JMRI (2018) 47(1):11-27. [2] Welsh, RC et al., (2011) 22(3):119-131. [3] Vavasour, IM et al., Magn Reson Med (1998) 40(5):763-768. [4] Stobbe, RW et al., Magn Reson Med (2021) 85(4):1840-1854. [5] Lee, J-S et al., Sci Rep (2013) 3(1):1707. [6] Närviäinen, J et al., JMRI (2010) 207(2):242-250. [7] Yoshimaru, ES et al., JMRI (2016) 263:184-192. [8] Zaiß, M et al., NMR in Biomed (2015) 28(2):217-230.

Laterally Oscillating Trajectory for Undersampling Slices (LOTUS)

Mayuri Sothynathan^{1,2}, Paul I. Dubovan^{1,2}, Corey A. Baron^{1,2}

¹Department of Medical Biophysics, Western University, London, Ontario, Canada, ²Centre for Functional and Metabolic Mapping, Western University, London, Ontario, Canada

Introduction: Diffusion magnetic resonance imaging (dMRI) is significantly limited by long scan times, giving rise to patient discomfort and strain on clinical resources. “Blipped-CAIPI” echo-planar imaging (EPI) is a simultaneous multislice (SMS) approach that is used to accelerate dMRI via 3D k-space sampling.¹ While spiral sampling allows for signal-to-noise ratio (SNR) gains in the order of 40-80% over EPI,² its acceleration with SMS remains relatively unexplored. A “CAIPI-like” spiral trajectory that samples multiple planes of k-space was previously proposed^{3,4} (Fig. 1a). Additionally, preliminary investigations of the addition of sinusoidal oscillations to a spiral trajectory has shown potential for non-Cartesian SMS^{5,6}, but questions about the choice of oscillation period and noise amplification remain. This study proposes a similar 3D k-space trajectory — Laterally Oscillating Trajectory for Undersampling Slices (LOTUS) — where the Golden Angle is maximally distributes k_z oscillations through the k_{xy} plane (Fig. 1b). While pure random sampling is impractical due to hardware and physiological constraints, it is hypothesized that LOTUS will approximate random sampling to increase compressed sensing (CS) efficacy.⁷

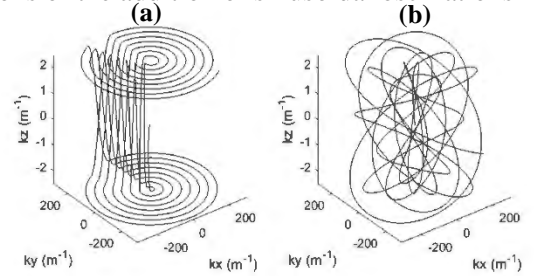


Figure 1: (a) CAIPI spiral (SMS=2) and (b) LOTUS

Methods: Simulations: Simulated data sampling of a numerical phantom was performed using spiral, CAIPI spiral, and LOTUS. A CS reconstruction was performed using MatMRI after Gaussian noise was added to the simulated data.^{8,9} CS solves $\hat{x} = \operatorname{argmin}_x \frac{1}{2} \|Ax - y\|_2^2 + \lambda \|\psi x\|_1$, where. The data consistency term $\frac{1}{2} \|Ax - y\|_2^2$ measures the difference between reconstructed and acquired data, while the regularization term $\lambda \|\psi x\|_1$ ensures sparsity; adjusting λ enables error minimization. Mean square error (MSE), structural similarity index (SSIM), and entropy were calculated for varying λ . Both 2 and 5 simultaneous slices were investigated, and the remaining parameters were: noise standard deviation=0.01, FOV=200x200 mm², in-plane resolution=1.5x1.5 mm², and in-plane undersampling rate (R)=2. G-factor maps illustrating noise amplification were determined for R=1, 2, and 3.¹⁰ **In vivo:** Two healthy volunteers’ brains were scanned on a Siemens 3T MRI using diffusion-weighted acquisitions with informed consent and institutional ethics board approval. CAIPI EPI, CAIPI Spiral, and LOTUS were acquired with: (a) SMS=4, R=2, and TR=7500ms; and (b) SMS=2, R=4, and TR=15000ms. TR was doubled for SMS=2 to keep interslice crosstalk comparable between the two cases. The remaining common parameters were: isotropic 1.7mm resolution, 60 slices, TE=62ms, 6 diffusion directions, and b=1000s/mm². Images were reconstructed in MATLAB using matMRI. Noise variance maps were computed with $\lambda = 0$.¹⁰

Results: In simulated results, error was comparable for all trajectories for SMS=2, but for SMS=5 LOTUS demonstrated better performance in all metrics. Noise amplification was comparable for SMS=2, but LOTUS had dramatically reduced noise amplification for SMS=5. Benefits were more evident with increased slice acceleration.

In-vivo results showed comparable CS reconstruction performance across trajectories, but noise variance advantages for LOTUS for SMS=4 (Fig. 2).

Discussion: Simulated and in-vivo results both indicate benefits of LOTUS with increased slice acceleration. Overall, much larger noise amplification is observed in the in-vivo EPI acquisitions because in-plane undersampling only occurs in one direction compared to the undersampling being distributed across x and y for spiral.² Notably, it is difficult to discern if improved CS performance is due to the reduction in noise amplification or due to LOTUS’ ability to mimic random sampling, since these two sampling features are strongly linked.

Conclusions: A novel k-space trajectory for dMRI, LOTUS, demonstrated benefits for increased slice acceleration and reduced noise amplification.

References: ¹Setsoy et al., MRM, 67(5):1210-1224 (2012), ²Lee et al., MRM, 85(4):1924-1937 (2021), ³Wu et al., ISMRM, 2024. doi:10.58530/2023/3614, ⁴Zahneisen et al., Neuroimage, 92:8-18 (2014), ⁵Herbst et al., MRM, 78(4):1476-1481 (2017), ⁶Chu et al., ISMRM, 21:3317 (2013), ⁷Lustig et al., MRM, 58(6):1182-1195 (2007), ⁸Varela-Mattatall et al., MRM, 90(2):615-623 (2023), ⁹Baron, Zenodo, 2021. doi: 10.5281/zenodo.4495476, ¹⁰Robson et al., MRM, 60(4):895-907 (2008)

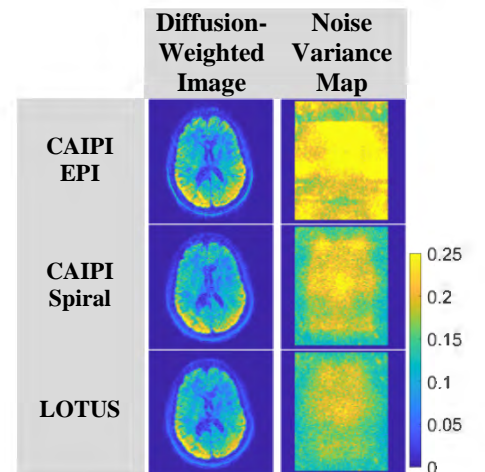


Figure 2: In-vivo diffusion-weighted image of a sample slice and corresponding noise variance map for SMS=4 and R=2

THE EFFECT OF MRI RF COIL SELECTION ON SPATIAL TRENDS IN T₁ RELAXATION

Sandra Alexander^{1,2}, Sid Sadanand^{1,2}, Dafna Sussman^{1,2,3}

¹Department of Electrical, Computer and Biomedical Engineering, Toronto Metropolitan University, Toronto, Canada, ²Institute for Biomedical Engineering, Science and Technology (iBEST), Toronto Metropolitan University and St. Michael's Hospital, Toronto, Canada, ³Department of Obstetrics and Gynecology, University of Toronto, Toronto, Canada

INTRODUCTION: Magnetic Resonance (MR) imaging phantoms play a crucial role in evaluating MR sequence performance and developing quantitative imaging protocols optimized for scan time and image accuracy. These phantoms, designed to accurately mimic tissue-specific T₁ relaxation times, are instrumental in reproducing MR T₁ image contrast, guiding pulse sequence design, and providing a standardized comparison across scanners and imaging centres [1]. Aqueous solutions of paramagnetic salts are commonly employed to simulate a range of T₁ relaxation times due to their homogeneity, stability, and ease of preparation and storage [2]. However, preliminary studies conducted at various imaging centres using aqueous paramagnetic phantoms of different concentrations have revealed a lack of fitted T₁ spatial homogeneity when imaged with a gold standard inversion recovery (IR) sequence through interleaved coronal slices from the top to the bottom of the phantoms. It is hypothesized that the T₁ relaxation of the phantoms may be influenced by the RF receive coils, which constitute the external environment of the phantom and affect signal uniformity throughout the sample [3]. This observation underscores the need for a comprehensive investigation into the impact of RF receive coil selection on quantitative T₁ studies.

Aim: We aim to investigate the potential correlation between T₁ spatial trends detected in aqueous phantoms and the specific RF receive coil arrangement employed during scanning.

METHODS: We prepared a series of 50 mL aqueous phantoms at room temperature, each containing one of five different T₁-modifying MnCl₂ paramagnetic salt concentrations. These phantoms were scanned using a 3T Siemens Prisma MRI scanner. An inversion recovery sequence was employed to acquire T₁-weighted images across 6 to 8 interleaved coronal slices. T₁ was fitted across TI = 500, 1000, 1500, 2000, and 3000 ms. To investigate the presence of significant spatial trends throughout the acquired slices, we utilized three distinct RF coil arrangements specifically chosen to assess the impact of coil placement on T₁ spatial distributions, as illustrated in Figure 1.

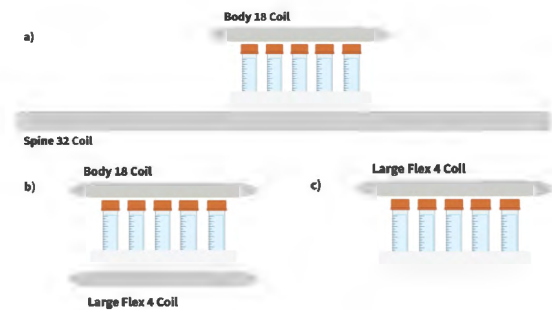


Fig. 1: Illustration of three receive-only coil arrangements: a) spine coil with the appropriate channels activated and body coil; b) body coil and flex coil; c) flex coil alone.

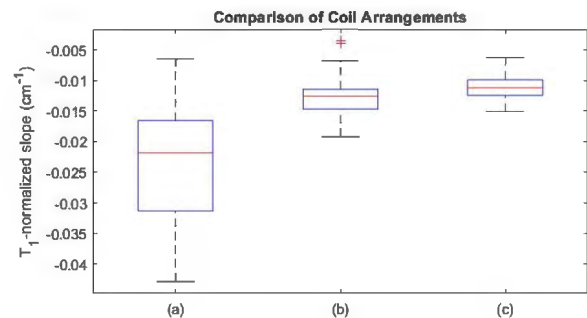


Fig. 2: Box plot comparing spread and variability of T₁ slope coil arrangements (a), (b), (c).

RESULTS: The mean slope characterizing the dependence of normalized T₁ on slice position of five aqueous paramagnetic phantoms of varying MnCl₂ concentrations was calculated by linear regression for the three coil arrangements tested. The mean slopes of the three coil arrangement were compared with an ANOVA test ($p > 0.1$). As illustrated in Figure 2, coil arrangements (b) and (c) improve T₁ variability throughout the sample.

CONCLUSIONS: Our findings indicate that RF receive coil arrangements utilizing smaller coils, such as the body and flex coils in arrangements (b) and (c), better preserve quantitative T₁ homogeneity and variability along small phantoms compared to arrangements employing larger coils like the spine coil (a). These results demonstrate that RF receive coil selection significantly influences T₁ relaxation measurement variability, and challenge the reliability and quantitative accuracy of literature and past relaxometric measurements.

REFERENCES: [1] J. K. Barral *et al.*, *Magn. Reson. Med.*, (2010) 64(4); 1057-1067. [2] K. Thangavel and E. Ü. Saritaş, *Turk. J. Electr. Eng. Comput. Sci.*, (2017) 25; 108–212. [3] W. E. Kwok, *RadioGraphics*, (2022) 42(3); 898–918.

Pitches 1: Cancer 1

Abstracts

Automatic Gleason Grading for Better Prognosis Prediction

Matthew McNeil^{1,2}, and Anne Martel^{1,2}

¹University of Toronto, ²Sunnybrook Research Institute

Introduction

The Leopard challenge (leopard.grand-challenge.org) was a recent challenge aiming to improve patient outcomes by generating AI models capable of better predicting patient outcomes. This allows patients to better understand their risk and if they require more aggressive therapies. Conversely, many pathologists are wary of machine learning (ML) methods in digital pathology, since many models rely on opaque implementations that show no indication of the internal workings that derive the outputs. To make our models more interpretable, we aim to create a model that uses features pathologists are already familiar with to make a recurrence prediction. In this case specifically: the Gleason grade was selected¹. This is an evaluation of the glands in the prostate tissue; more aggressive tumours have poorly differentiated or poorly formed glands.

Methods

To train our model we used the PANDAS dataset². Half of these biopsy images had individual glands labelled as different grades. This left us with over 5000 whole slide images, which we turned into over 30,000 patches. We trained a U-Net with an EfficientNet backbone to recreate those labels automatically. We then calculated the area of each label over the entire slide and normalized it by the number of patches analyzed. We then summed the normalized area of grade 4 and 5 tissue to get a risk score.

Results

This method was able to win the Leopard challenge, beating several methods with more complicated end-to-end architectures. The table below shows the top 3 teams from the challenge, with our method showing the best results. The test was divided into two sections: internal which were slides originating from the same location as the training data, and external which came from a separate medical center.

Team	Internal C-Index	External C-Index	Average
Martel Lab	0.723	0.711	0.717
Mevis ProSurvival	0.682	0.738	0.710
Paicon	0.705	0.695	0.700

Conclusion

Using deep learning to recreate pathologists' labels presents an exciting opportunity for improving care. It can create predictions that a physician could inspect and verify while also matching the predictive power of more complicated end-to-end methods.

References

1. Gleason, D.F.: Histologic grading and clinical staging of prostate carcinoma. *Urologic pathology. The prostate* (1977)
2. Bulten, W., Kartasalo, K., Chen, P.H.C., Ström, P., Pinckaers, H., Nagpal, K., Cai, Y., Steiner, D.F., Van Boven, H., Vink, R., et al.: Artificial intelligence for diagnosis and gleason grading of prostate cancer: the panda challenge. *Nature medicine* 28(1), 154–163 (2022)

LLM-Based Prostate Cancer Grading Through Reasoning Segmentation

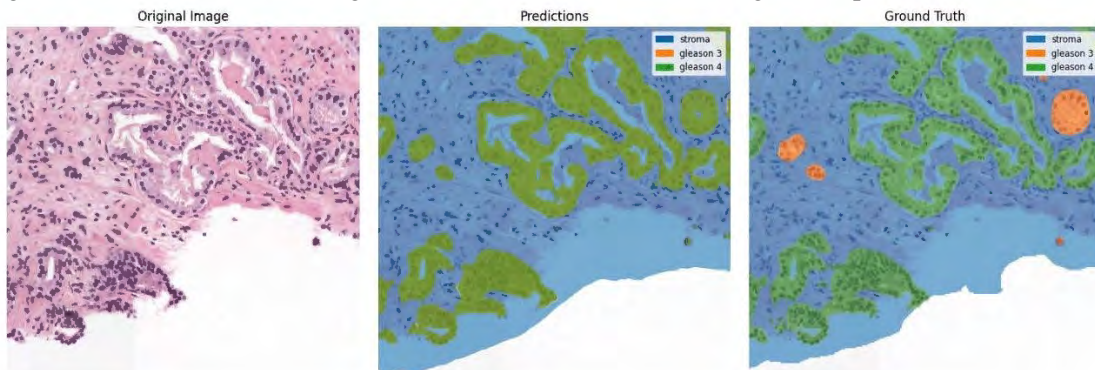
Emma Willis, Alon Gabriel, Tarek Elghareb, Parvin Mousavi, Purang Abolmaesumi
Queen's University, Kingston, Canada

INTRODUCTION: Prostate cancer (PCa) is the second most common cancer among Canadian men, accounting for 20% of all cases. Diagnosing PCa relies on pathologists visually grading histopathology slides from biopsies to assign an International Society of Urological Pathology (ISUP) grade, a key factor in treatment decisions. However, this process suffers from high inter-observer variability, leading to potential misdiagnoses.

Automating PCa detection and grading can improve consistency and efficiently prioritize high-risk cases for treatment. Large-language models (LLMs) can perform classification tasks with minimal fine-tuning, making them adaptable across domains, including healthcare, where they are increasingly explored as diagnostic tools. Vision backbones such as the Segment Anything Model (SAM) similarly provide significant image segmentation capabilities with minimal fine-tuning [1]. In [1], Lai et al. propose a segmentation task called “reasoning segmentation” and introduce the Language Instructed Segmentation Assistant (LISA) to address it. Their approach combines the linguistic reasoning of an LLM with the visual interpretation of a segmentation model to output segmentation masks based on input prompts, including unseen labels and descriptions.

METHODS: Using the Prostate Cancer Grade Assessment (PANDA) dataset [3], the LISA [1] and BiomedParse [2] reasoning segmentation models were evaluated for segmentation accuracy and ISUP classification accuracy. The models were fine-tuned on histopathology data with textual diagnostic criteria to learn the relationship between tissue features and ISUP labels. The dataset included 236 training patients and 60 validation patients. Textual prompts included: (1) “To grade prostate cancer severity, which parts of the image should be examined?” and (2) “What ISUP score would a pathologist assign this histopathology slide?” These prompts were paired with segmented output images and the expected ISUP scores.

RESULTS: Preliminary results using LISA with the natural image-based SAM backbone showed very low gIoU and cIoU scores on the validation dataset, indicating that SAM is not a sufficient vision backbone for segmenting specific histopathology structures. The BiomedParse model, pretrained on medical images, achieved a cumulative Dice coefficient of 91.91, CIoU of 0.85, and an overall ISUP grade prediction accuracy of 42%. This model demonstrated perfect precision for ISUP grades 0 and 2 but struggled with intermediate grades, highlighting the need for further data augmentation and advanced modeling techniques.



Histopathology patch (left), with BiomedParse segmentation (center) and radiologist segmentation (right).

CONCLUSIONS: These findings validate the hypothesis that language-based segmentation can bridge text and histopathology modalities for automated PCa grading. Future work will focus on utilizing larger datasets, refining class balance, and improving segmentation backbones to enhance accuracy for all ISUP grades.

REFERENCES:

- [1] X. Lai, Z. Tian, Y. Chen, Y. Li, Y. Yuan, S. Liu, and J. Jia, "LISA: Reasoning Segmentation Via Large Language Model," *arXiv*, 2023. [Online].
- [2] Zhao, T., Gu, Y., Yang, J. et al. A foundation model for joint segmentation, detection and recognition of biomedical objects across nine modalities. *Nat Methods* 22, 166–176 (2025).
- [3] G. Litjens, H. Pinckaers, K. Kartasalo, M. Eklund, P. Ruusuvaori, P. Ström, S. Dane, and W. Bulten, "Prostate CANcer GraDe Assessment (PANDA) Challenge," 2020. [Online].

Evaluating the synergistic effects of antiangiogenic therapy and stereotactic body radiation therapy in pancreatic cancer using multi-modal optical coherence tomography

Héctor A. Contreras-Sánchez¹, W. Jeffrey Zabel¹, Edward Taylor², and Alex Vitkin^{1,2}.

¹Department of Medical Biophysics, University of Toronto, Toronto, ON, Canada

²Department of Radiation Oncology, University of Toronto, Toronto, ON, Canada

Introduction: The anomalous regulation of angiogenesis is now recognized as an important hallmark of cancer, and thus the tumour vasculature and various cell-secreted factors involved in vessel growth are becoming relevant targets in cancer therapy. The use of antiangiogenic therapy (AT) in combination with standard-of-care treatment modalities such as radiation therapy is being investigated in both preclinical and clinical trials. Further, with the emergence of stereotactic body radiation therapy (SBRT), and the likely microvascular injuries caused by such high doses, SBRT might benefit from the temporary downregulation of angiogenic pathways, although comprehensive understanding of the microvascular effects of both therapies is needed to confirm the existence of potential synergistic effects [1,2]. Here, we propose a preclinical study using optical coherence tomography (OCT) to characterize tumour microvascular networks and to evaluate the individual and additive effects of antiangiogenic therapy and SBRT in pancreatic ductal adenocarcinoma in a dorsal skin window chamber mouse model, with the aim of elucidating the role of tumour vessels in cancer radiobiology and the therapeutic benefits of the concomitant use of angiogenic inhibitors and SBRT. **Methods:** Immunocompromised, tumor-bearing mice (NRG) inoculated with human-derived, Ds-Red labelled, pancreatic adenocarcinoma cells (Bx-PC3 cell line) were used for this study. Mice were assigned into four distinct groups (N=10 each): controls, AT-treated (bevacizumab and/or erlotinib), SBRT-treated (10, 20 and 30 Gy), and AT + SBRT treated groups. Snapshots of the tumour blood microcirculatory system and tumour cell viability were acquired over the period of seven weeks using multi-modal OCT (structural, speckle-variance and Doppler) and fluorescence microscopy respectively. Microvascular quantification metrics were further extracted from the longitudinal datasets and analyzed over time. **Results:** Tumour microvascular systems exhibited higher blood flow values than healthy mouse skin in early time points (+12% increase), which then decreased (-40% decrease) and fluctuated as tumours continued to grow. Tumour cell viability, measured with Ds-Red fluorescence images, seems affected by the changing blood flow. Initial preclinical results of SBRT-treated mice exhibited a degree of capillary density loss in a dose- and fraction- dependent manner compared to the control group. AT and combined AT + SBRT effects are currently being investigated.

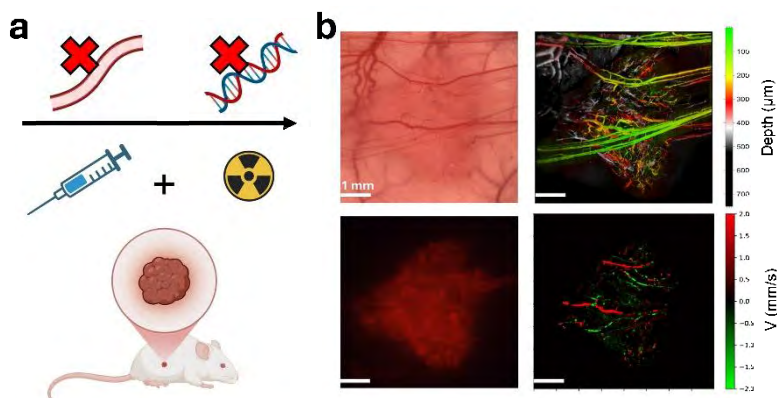


Figure 1. Summary of proposed AT+ SBRT preclinical study. **a)** Schematic illustration of the dual therapy strategy and their primary effects in the tumour mouse model. **b)** One representative dataset of tumour microvascular architecture, blood flow, brightfield image and Ds red fluorescence image.

[1] Lopes-Coelho, F. et al. *Int. J. Mol. Sci.* **22**, 3765 (2021).

[2] Sun, X. et al. *Chin. J. Cancer. Res.* **30**, 147-156 (2018).

Characterization of Osteosarcopenia Quantified With AI-Enabled Musculoskeletal Imaging Biomarkers in Patients Undergoing Spine SBRT

Yessica Castano^{1,2}, Saleh Tabatabaei^{1,3}, Tayler D. Ross^{1,4,5}, Geoff Klein^{1,6}, Stephen Chen^{1,4}, Cari M. Whyne^{1,3,4,5}, Arjun Sahgal⁶, Michael Hardisty^{1,3,5}

¹Sunnybrook Research Institute, ²School of Information Technology, York University, ³Institute of Biomedical Engineering, University of Toronto, ⁴Institute of Medical Science, University of Toronto, ⁵Department of Surgery, University of Toronto, ⁶Department of Medical Biophysics, University of Toronto, Toronto, ON, Canada, ⁷Department of Radiation Oncology, Odette Cancer Centre, Sunnybrook Health Sciences Centre, Toronto, ON, Canada

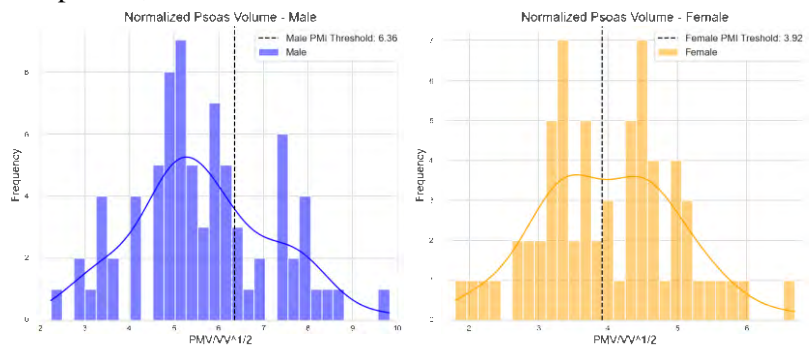
INTRODUCTION: Osteosarcopenia, the coexistence of osteoporosis (decreased bone mineral density - BMD) and sarcopenia (low muscle mass and strength), is increasingly recognized as a critical musculoskeletal (MSK) condition impacting patient outcomes. Its presence is associated with worse functionality, prolonged hospital stays, and increased mortality (1). In patients with cancer, sarcopenia frequently accompanies bone metastases (2), making it essential to characterize the number of sarcopenic patients. Stereotactic body radiotherapy (SBRT) is an evidence-based treatment for spinal metastases, recommended over conventional radiation in international guidelines and supported by randomized clinical trials. SBRT has demonstrated excellent pain relief and local tumor control, however, is associated with an elevated rate (14%) of vertebral compression fractures (VCF) (3). Given previous associations between metastatic cancer, sarcopenia and osteoporosis in the literature and the relationship between MSK health and the risk of fractures, we sought to assess MSK health in patients being treated for spinal metastases with SBRT.

OBJECTIVE: This study focuses on characterizing the prevalence of osteoporosis and sarcopenia in patients preparing to undergo SBRT, using AI-enabled musculoskeletal imaging biomarkers. This information may be utilized to enhance treatment planning and improve patient care.

METHODS: A prospectively maintained database of all patients with spinal metastases treated with spine SBRT at Sunnybrook Health Sciences Centre between January 1, 2008, and December 31, 2022, was utilized. We selected patients receiving SBRT treatment in the lumbar spine because treatment planning imaging allowed quantification and visualization of the lumbar bone density, psoas muscle density and size. The BMD of the lumbar vertebral bodies, as well as the volume and density of the psoas muscle, were automatically quantified using segmentations generated by a combination of neural networks, including ResNet, CNNs, and U-Net. For evaluating osteoporosis, vertebrae at the L1–L5 levels were analyzed. Large standard deviations in density (Hounsfield Units (HU) $STD > 75$) were used to classify metastatically involved vertebrae. Metastatically involved vertebrae were excluded from BMD analyses. A threshold of 135 HU was used to classify vertebral bodies as osteoporotic. The Psoas muscle segmentation was used to quantify sarcopenia. The superior and inferior boundaries of the psoas muscle were set at the midpoints of the L2/L3 and L4/L5 intervertebral discs, respectively. The psoas muscle volume (PMV) was normalized by the square root of the volume of the L3 vertebra ($VV^{1/2}$) and used to classify patients as having sarcopenia, based on the derived relationship: $PMI = c * PMV/VV^{1/2}$, where $c = 0.2074$, obtained from fitting linear regression. PMI thresholds proposed in the literature for both females and males were applied to define sarcopenic patients, as shown in the figure.

RESULTS: 143 patients, 78 Female and 65 Male (mean age=64 years [28-90 years]) were analyzed. 83 patients were classified as osteoporotic and 54 as non-osteoporotic, and 6 could not be determined because of metastatic involvement of every lumbar vertebral body. 87 patients had sarcopenia, 56 did not have sarcopenia. 56 patients had osteosarcopenia.

CONCLUSIONS: This study highlights the notable prevalence of osteosarcopenia (39%) among patients preparing for stereotactic body radiotherapy (SBRT) for spinal metastases. A substantial proportion of patients were found to have both osteoporosis and sarcopenia. The findings emphasize the need for integrated management strategies that address both bone and muscle health to enhance patient outcomes.



REFERENCES: 1. Fuggle, N. et al. Best Pract Res Clin Rheumatol, 31:218–242, 2017. 2. Massaad, E. et al. J Neurosurg Spine, 37:263–273, 2022. 3. Guninski, R.S. et al. Radiother Oncol, 109969, 2023.

Assessing diffuse optical spectroscopy and magnetic resonance imaging for quantification of multimodal gadolinium-incorporated porphyrinsomes for theranostic guidance of oral cancer in mice

Theo Husby¹, Jason Townson², Alessandra Ruaro², Diego Martinez^{1,3}, Kat Zaraska³, Juan Chen², Ian R.O. Connell^{1,3}, Gang Zheng^{1,2,4}, Brian C. Wilson^{1,2}, Robert A. Weersink^{1,2,4}

¹Department of Medical Biophysics, University of Toronto, Toronto, ON

²Princess Margaret Cancer Center, University Health Network, Toronto, ON

³Biomedical Engineering, University Health Network, Toronto, ON

⁴Institute of Biomedical Engineering, University of Toronto, Toronto, ON

Introduction: Simultaneous fluorescence and MRI contrast imaging enabled by gadolinium-incorporated porphyrinsome (GP) nanoparticles presents opportunities for novel oncological workflows. GPs provide T1 MRI contrast, long circulation half life (13.6h), and fluoresce on dissociation. In this proposed workflow, preoperative T1-weighted MRI enables margin assessment and assessment of agent uptake in oral cancers while intraoperative diffuse reflectance and quantitative fluorescence spectroscopy (DRS/QFS) measurements provide a means to quickly distinguish healthy and cancerous tissue in the surgical field and enable photodynamic therapy planning and monitoring. This application rests on two hypotheses: 1) that GPs provide equivalent or better tumor MRI contrast than Gadovist, the current contrast agent of choice for oral cancer imaging and 2) that diffuse reflectance and quantitative fluorescence spectroscopic (DRS/QFS) point measurements of porphyrinsome concentration (GPS or GJPS) enable delineation of residual tumor.

Methods: A pilot study was performed (n=4) to demonstrate feasibility of the multi-modal contrast imaging and to develop techniques and imaging methods. With these methods established, we present a follow up experiment that tested these hypotheses. Five mice bearing oral squamous cell carcinoma (MOC2) xenograft tumours in their tongues were injected with Gadovist. After a 48-hour delay to let the Gadovist clear, mice will be injected intravenously with 20 mg/kg of GPS. T1 maps were acquired with a 7T MRI pre and immediately post Gadovist injection, and at pre, 15 minutes, 24 hours, and 48 hours post GP injection. DRS/QFS measurements were recorded immediately after each MR acquisition, with one set of measurements taken on the tumour, and a second set on healthy mucosa adjacent the tumour. Delta T1 between healthy mucosa and tumour were compared between Gadovist and GPs to test hypothesis 1. GP concentration measured by DRS/QFS of tumour and healthy mucosa were compared to test hypothesis 2. Additionally, GP concentration measured by DRS/QFS and T1 maps were compared to ensure agreement. We will also be acquiring T1 maps with a 0.5T scanner for comparison against 7T.

Results: In the T1 maps, GPs provided a substantially different tumour contrast vs. Gadovist, showing accumulation around the periphery of the tumour and lasting at least 44 hours, whereas Gadovist showed less specific uptake and cleared completely within 48 hours. DRS/QFS was successful in measuring GP concentrations in vivo, distinguishing between intact and dissociated GPs. Strong DRS/QFS contrast was observed between tumour and healthy mucosa.

Conclusions: This study demonstrates the viability of GP nanoparticles as a contrast agent for multi-modal image-guided surgery in oral cancers.

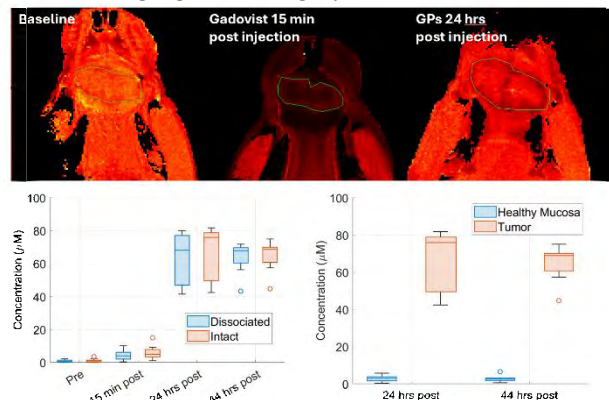


Figure 1: Top, T1 maps of the lower mandible and tongue of a mouse with a large MOC2 tumour pre injection, 15 min post Gadovist, and 24 h post GP. Bottom left, GP concentration measured with DRS. Bottom Right, GP concentration in tumour vs healthy mucosa measured with DRS/QFS

Designing an Endometrial Pathology Slide Classification User Interface for Efficient Diagnostics

Matthew Lam^{1,2}, Farhan Wasim^{1,2}, Michael Pereira^{1,2}, Mara Sobel^{3,4}, Dafna Sussman^{1,2,4}

1. Department of Electrical, Computer, and Biomedical Engineering, Toronto Metropolitan University (formerly Ryerson University), Faculty of Engineering and Architecture Sciences, Toronto, Ontario, Canada; 2. Institute for Biomedical Engineering, Science, and Technology (iBEST), Toronto Metropolitan University (formerly Ryerson University) and St. Michael's Hospital, Toronto, Ontario Canada; 3. Department of Obstetrics and Gynaecology, Mt. Sinai Hospital, Toronto, Ontario, Canada; 4. Department of Obstetrics and Gynecology, Faculty of Medicine, University of Toronto, Toronto, Ontario, Canada.

Introduction: Endometrial cancer, which starts in the lining of the uterus, is the fifteenth most common gynecological cancer worldwide. [1] Early and accurate diagnosis is essential for effective treatment and better patient outcomes. However, traditional diagnostic methods face challenges like delays in pathology results—often taking days—and a global shortage of gynecologic pathologists. [2] [3] These issues can increase patient anxiety and allow the cancer to progress, making treatment more difficult.

To overcome these challenges, advancements in artificial intelligence (AI) and digital pathology are opening new possibilities. Unfortunately, many AI models in pathology are too complex and difficult to integrate into everyday clinical use, limiting their accessibility for gynecologic pathologists. To bridge this gap, we are designing a web application tailored for the digital pathology of endometrial biopsy. This web application uses our previously-developed Endometrial Pathology tissue classification AI algorithm.[4] The application is designed to accept high-resolution whole slide images (WSI) and to output the tissue classification along with a heatmap to identify regions of interest in the WSI.

Methods: Users upload biopsy slide images, which the system verifies for proper format (SVS) and ensure they are captured at the required 20x magnification. If adjustments are needed, the image is automatically resampled to match the resolution used in model training, ensuring classification accuracy. The application uses advanced algorithms to isolate the tissue, removing background elements and artifacts for a cleaner analysis. Classification is then performed through a series of four specialized AI models developed by MFI Lab. These models, trained on 1,193 images across various categories, leverage a Multi-Instance Learning (MIL) approach, with the highest-performing model achieving an accuracy of approximately 93%.[4] These models categorize slides into one of the key endometrial tissue groups: Benign, Neoplasia, or Hyperplasia. Based on the initial classification result, the images are directed to a specialized model tailored to the respective category for tissue subclassification.

Results are displayed as an interactive heatmap using the OpenSeadragon toolkit, allowing users to zoom in and explore fine details. The classification output includes confidence levels for each prediction, and users can easily download these results for documentation and reporting.

Result: The web application integrates the four specialized AI models, enabling users to seamlessly upload images and access results directly through the platform. Hosting the application in a AWS cloud environment means users don't need to download any software or rely on local computational resources, making it easy to access the latest analytical features anytime.

Conclusion: The development of a user-friendly web application integrated with AI-driven digital pathology models can aid in the diagnostic process for endometrial cancer by simplifying access to advanced AI tools. The inclusion of heatmaps highlights critical areas for review, enhancing interpretability in AI predictions and facilitating trainee education. This tool has the potential to improve time efficiency and a better understanding of the pathophysiology of endometrial cancer.

Reference:

- [1] "Endometrial cancer statistics | World Cancer Research Fund International," WCRF International. Accessed: Feb. 16, 2024. [Online]. Available: <https://www.wcrf.org/cancer-trends/endometrial-cancer-statistics/>
- [2] "Waiting for Your Biopsy or Cytology Test Results." Accessed: Nov. 25, 2024. [Online]. Available: <https://www.cancer.org/cancer/diagnosis-staging/tests/biopsy-and-cytology-tests/waiting-for-your-biopsy-or-cytology-test-results.html>
- [3] A. J. Zimolzak et al., "Why Test Results Are Still Getting 'Lost' to Follow-up: a Qualitative Study of Implementation Gaps," J. Gen. Intern. Med., vol. 37, no. 1, pp. 137–144, Jan. 2022, doi: 10.1007/s11606-021-06772-y.
- [4] M. Lam, F. Wasim, D. Sherman, M. Sobel, and D. Sussman, "Classification of Endometrial Greyscale Pathology Slide," presented at the ObGyn Research, Jan. 2024.

Diagram Workflow Structure

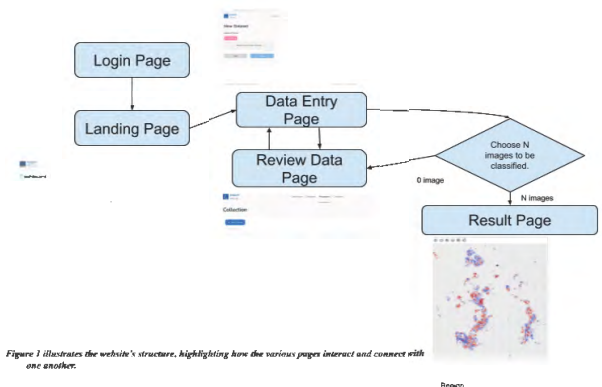


Figure 1 illustrates the website's structure, highlighting how the various pages interact and connect with one another.

Evaluating Osteosarcopenia Progression in a Preclinical Model of Prostate Cancer Bone Metastases with Imaging Biomarkers

¹ Leanna Abraham, ² Azin Mirzajavadkhan, ² Christine Huang, ^{2,3,4} Cari Whyne, ^{3,4} Michael Hardisty, ^{1,3,5} Margarete K. Akens

¹ Department of Medical Biophysics, ² The Institute of Biomedical Engineering (BME), ³ Department of Surgery, University of Toronto, ⁴ Sunnybrook Research Institute, ⁵ Princess Margaret Cancer Centre, University Health Network, Toronto, ON, Canada

Introduction: Growing evidence shows a significant link between sarcopenia and osteopenia in many diseases, including cancer. Common systemic treatments with docetaxel (DTX) and bisphosphonates [zoledronic acid (ZA)] in metastatic prostate cancer may have an impact on muscle and bone. The study aims to quantify early changes to the psoas muscle secondary to metastatic prostate cancer and its treatment.

Methods: Twenty-five athymic rats were randomized and received an intra-cardiac injection of luciferase-transfected ACE-1 prostate cancer cells ($1.5 \times 10^6/200 \mu\text{L}$) [n=15, control n=10]. Injected and control rats were randomized into DTX (5 mg/kg, i.v.) (n=12), ZA (Zometa; 60 $\mu\text{g/kg}$, s.c.) (n=7), or untreated (n=6) groups on d9 and sacrificed on d21. Grip tests to evaluate muscle strength were conducted on rats on days(d) -2, 12, and 19, and bioluminescence imaging (IVIS Spectrum) on d 13, and 21 monitored tumor formation. Gd-contrast in vivo μMR and μCT (NanoScan, Mediso) scans were performed on days after each grip strength test d-1, 13, and 20, post-tumor-cell injection in the same rat bed with rats positioned identically and maintained under the same anesthesia, allowing for automatic and manual co-registration. Psoas muscles were manually segmented from fused in-vivo MR/CT images to obtain muscle volume and attenuation and normalized to the L2 vertebral volume (Figure 1). The excised psoas muscle was stained with Oil Red O (ORO) to visualize lipid content (Figure 2), and the vertebrae were used for high resolution μCT ($\mu\text{CT}100$, Scanco, 34.4 μm isotropic voxels) imaging for stereological analysis.

Results: Bioluminescence imaging, histology, and ex-vivo μCT imaging confirmed bone metastases in 9 of the injected rats (Figure 3). Significant reductions in bone mineral density of DTX treated rat vertebrae were found. DTX treated rats also displayed significantly smaller increases in normalized psoas volume from d-1 to d20 post-cell-injection compared to ZA or untreated animals (two-factor ANOVA, $p < 0.05$). DTX treated rats had a significantly weaker grip strength 3 days post-treatment than untreated and ZA treated animals (two-factor ANOVA, $p < 0.05$). Within the DTX group, tumor cell injected animals, had a significantly greater negative change in psoas attenuation compared to healthy DTX treated rats, suggesting a higher degree of fatty infiltration (two-factor ANOVA, $p < 0.005$). Additionally, DTX treatment also showed significantly less negative changes in attenuation from d-1 compared to d20 than ZA treated animals. Quantification of psoas ORO histology show DTX treated rats have a significantly lower fat content in the muscle compared to ZA or untreated groups.

Conclusion: Psoas muscle attenuation and volume loss are measurable in this preclinical rat model of mixed bone metastases and show differences due to treatment and tumor presence, demonstrating sarcopenia. These imaging biomarkers can potentially be used to evaluate disease progression, leading to the earlier intervention of osteosarcopenia.

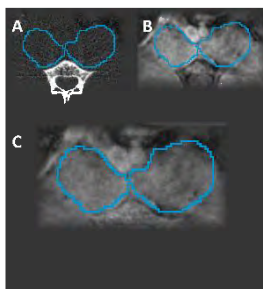


Figure 1: Rat CT(A), MR (B), and co-registered(C) axial slice with segmented psoas muscle in blue

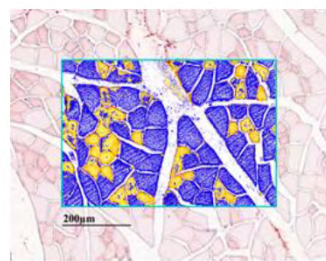


Figure 2: Oil Red O stain of psoas showing lipid content with positive pixel analysis in blue square

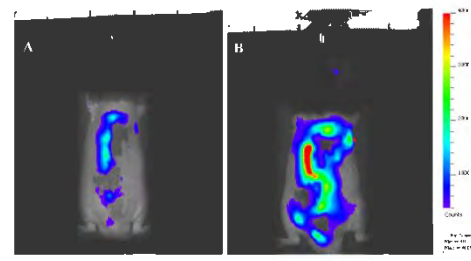


Figure 1. Bioluminescent image of tumor injected rat on d13 (A) and d21(B) post-cell injection.

Leveraging Transformers to Improve Dose Prediction in Complex Multi-lesion Lung SABR Plans

Edward Wang,^{1,2} Ryan Au,^{1,2} Daniel Markel,³ Houda Bahig,³ Pencilla Lang,⁴ Sarah A. Mattonen^{1,2,4}

¹ Department of Medical Biophysics, Western University, London, Ontario, Canada

² Baines Imaging Research Laboratory, London Regional Cancer Program, London, Ontario, Canada

³ Department of Radiation Oncology, Centre hospitalier de l'Université de Montréal, Montreal, Quebec, Canada

⁴ Department of Oncology, Western University, London, Ontario, Canada

Introduction: The lung is the second most common site of cancer metastasis.¹ Stereotactic ablative body radiotherapy (SABR) is a radiation technique that allows for high doses to be delivered accurately to tumors and has been shown to increase survival in patients with metastatic disease.² Over-irradiating healthy lung tissue can lead to radiation toxicity, while under-irradiating cancer increases the risk of recurrence. Determining whether a treatment will be both safe and effective is resource intensive and relies on a dosimetrist fully planning the prescription via specialized software. When a prescription does not meet dose constraints, another one must be chosen and re-planned, potentially leading to treatment delays. In extreme cases, a suitable prescription may not be possible, requiring the patient to undergo alternate treatment options. Significant work has been dedicated to using artificial intelligence to predict dose distributions,^{3,4} thereby allowing radiation oncologists to quickly estimate whether a given prescription is feasible. Existing models typically utilize convolutional neural networks that are not well suited to overlapping lesions. Transformers are a powerful alternate architecture that utilizes the attention mechanism to achieve strong results across many domains.⁵ In this work, we introduce a novel transformer framework for dose prediction (LDFormer) of multi-lesion plans and compare it to a state-of-the-art generative adversarial network (GAN)⁴ on both internal and external data.

Methods: A retrospective review of patients who received SABR treatment for two or more lung lesions between 2014 and 2023 was conducted at a single tertiary academic center in Canada. All prescriptions were converted to their equivalent doses in two Gray fractions. The data was split into training (70%), validation (15%) and testing (15%) sets. A two-stage transformer framework was created for dose prediction. In the first stage, tumour contours, organ contours and dose information is encoded into latent spaces. In the second stage, a transformer learns to predict dose latents from anatomical latents. LDFormer was compared to the GAN⁴ based on dose-volume-histogram metrics (DVH) and conformality metrics (CM) on the testing set as well as an external validation set from another Canadian centre. DVH metrics measure the radiation received by organs at risk. CM describe the shape of the dose distribution around the lesions. CM were calculated for all lesions, as well as only for overlapping lesions. T-test and Wilcoxon rank-sum test were used to test for significance.

Results: In total, 234 plans were collected from our institution, and 18 plans from the external institution. On both the testing and external dataset, LDFormer significantly outperformed the GAN on CM, with the greatest improvement on overlapping lesions. For the DVH metrics, LDFormer performed comparably to the GAN on the testing dataset across all metrics but was outperformed in lung metrics on the external dataset.

Table 1: The absolute differences in the DVH (upper table) and CM (lower table) between predicted and ground truth doses in the testing (blue rows) and external (orange rows) sets are reported as mean±SD. Lower values are better. Bold font indicates significantly better performance (p<0.05). Heterogeneity index (HI) is dimensionless. Ln=Lung, Es=Esophagus, Hr=Heart, Aw=Airways, Gv=Great Vessels, Cw=Chest Wall, Ov = Overlap.

Model	LnCV14 (cc)	LnV15 (%)	EsD5cc (Gy)	HrD15cc (Gy)	AwD5cc (Gy)	GVD10cc (Gy)	CWD5cc (Gy)
LDFormer	122±120	3.3±4.1	4.5±8.2	5.8±8.8	5.8±7.1	5.3±4.5	22±20
GAN	70±53	1.7±1.5	4.7±6.5	5.3±7.2	3.6±5.1	4.4±4.8	17±22
LDFormer	141±87	5.5±4.3	3.5±4.0	7.4±6.8	6.8±6.5	9.1±8.7	16±15
GAN	50±51	2.0±2.9	3.7±2.3	6.1±3.5	5.3±3.3	6.7±4.8	17±11
Model	HI	D1cm (Gy)	D2cm (Gy)	OvHI (Gy)	OvD1cm (Gy)	OvD2cm (Gy)	
LDFormer	0.44±0.40	32±28	22±19	0.67±0.49	44±32	39±25	
GAN	0.74±0.69	53±40	27±28	1.71±0.66	97±35	65±40	
LDFormer	0.40±5.24	26±22	20±18	0.20±0.16	18±18	28±23	
GAN	1.2±0.46	58±31	20±17	1.48±0.57	81±22	49±34	

Conclusions: In this work, we introduce a transformer framework for multi-lesion lung SABR dose prediction. LDFormer outperforms a state-of-the-art GAN in CM and is most beneficial for plans with overlapping lesions. Multi-lesion lung SABR is an effective but resource intensive treatment. Our work has the potential to reduce resource burden and increase the adoption of this technique.

References: (1) Jamil et al., *Statpearls*. 2023. (2) Palma et al., *Lancet*. 2019. (3) Kearney et al., *Nat Sci Rep*. 2020. (4) Wang et al., *IJROB*. 2024. (5) Vaswani et al., *Adv Neural Inf Process Syst*. 2017.

Precursor droplet extrusion for the production of size-controlled lipid-stabilized drug-loaded nanobubbles

P.D.M. Chang¹, N. Matsuura^{1,2,3}

¹Institute of Biomedical Engineering, ²Department of Materials Science & Engineering, ³Department of Medical Imaging, University of Toronto, Ontario, Canada

Introduction. Drug-loaded phospholipid-stabilized nanobubbles (NBs) have emerged as promising candidates in the past decade for ultrasound-mediated drug delivery to treat solid cancerous tumours.^{1,2} The acoustic response of bubble-based agents is heavily dependent on its size distribution and therefore, minimizing the range of sizes can improve control over its cavitation regimes to elicit specific bioeffects ranging from cell pore formation to blood vessel disruption.³ Conventional techniques to produce drug-loaded NBs rehydrate a dried lipid-drug film with an aqueous buffer before sonication, agitation, or microfluidic assembly in the presence of the desired gas core where the resulting bubbles must undergo size purification and elimination.^{1,4} Moreover, the resulting drug-loaded NBs retain relatively low drug loading due to its stabilizing lipid monolayer. The literature has demonstrated the ability to produce size-controlled, high-yield drug-loaded agents by extrusion through pores of specified sizes. The objective of this study is to therefore demonstrate how this technique can be adopted with a novel precursor droplet process to yield a suspension of acoustically active NBs with enhanced drug loading.

Methods. Droplet-to-bubble synthesis. Phospholipids DPPA, DPPC, and DPPE-mPEG5,000 were vortexed with the anticancer drug docetaxel (DTX) to form an oil-in-water emulsion. Extrusion was performed on a LIPEX[®] system (Evonik, Germany) with a circulating water bath (Lauda-Brinkmann, USA) at 80°C with the emulsion passed through polycarbonate membrane filters of decreasing pore sizes of 8-, 3-, 1-, and 0.6- μm eight times. The final droplet suspension was aliquoted to serum vials before subject to freeze drying. The resulting cake in the vial was sealed before subsequently removing any air and filling the vial with perfluorobutane gas using a pump. The cake was then hydrated with 0.7 mL of saline to produce a suspension of DTX-loaded NBs (DTX-NBs). A control bubble was synthesized with the identical excipients by mechanical agitation using a VialMix[™]. **Size characterization.** Particle size distributions were measured using the 10- μm aperture of the Multisizer[™] 4e (Beckman, USA). **Drug loading quantification.** DTX loading was assessed using an ultrahigh performance liquid chromatography system with tandem mass spectrometry. **Contrast-enhanced ultrasound (CEUS) assessment.** DTX-NBs were diluted to 10^5 to 10^8 #/mL in saline and imaged using a 2 wt% agarose phantom with the linear L8-4 transducer (Mechanical index = 0.07) and clinical iU22 ultrasound system (Philips, Netherlands).

Results. $95.0 \pm 0.6\%$ of DTX-loaded lipid-stabilized oil droplets were preserved and directly converted to DTX-NBs (Figure 1) with a d_{mode} of 265 ± 16 nm and total number concentration of $\sim 2 \times 10^{10}$ #/mL where $99.7 \pm 2.0\%$ of the bubbles were $< 1 \mu\text{m}$ ($n \geq 4$). DTX loading quantification revealed $214 \pm 23 \mu\text{g/mL}$ and $19 \pm 2 \mu\text{g/mL}$ of the DTX-NBs produced by extrusion and VialMix[™] respectively, demonstrating significantly enhanced DTX loading using the precursor droplet assembly technique ($n \geq 5$). DTX-NBs demonstrated decreasing contrast enhancement with decreasing bubble concentrations (Figure 2).

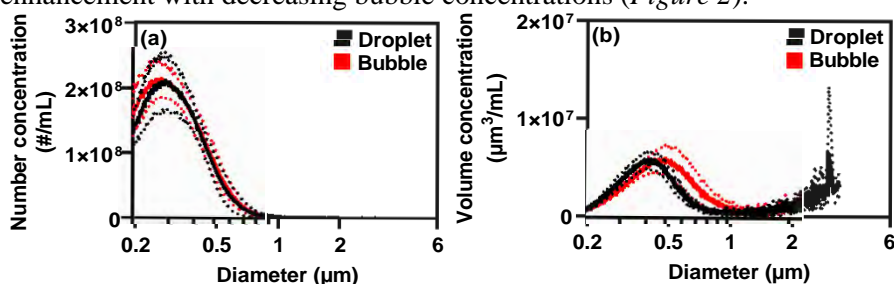


Figure 1. (a) Number and (b) volume distributions of DTX-loaded phospholipid-stabilized droplets and bubbles shown in black and red respectively. Solid and dotted lines represent the mean and SD respectively ($n \geq 4$)

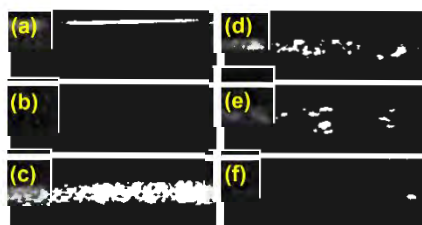


Figure 2. Ultrasound imaging of DTX-NBs flowing through an agarose phantom: (a) brightness mode (B-mode); (b) CEUS mode; DTX-NBs at (c) 10^8 #/mL; (d) 10^7 #/mL; (e) 10^6 #/mL; and (f) 10^5 #/mL ($n \geq 3$).

Significance & Future Work. The precursor droplet technique can be employed to extrude size-controlled lipid-stabilized DTX-loaded droplets that directly convert to a suspension of DTX-NBs that provide greater drug loading than conventional bubble assembly strategies using VialMix[™]. Future work will examine the acoustic behavior of DTX-NBs (i.e. pressure-dependent cavitation regimes) as well as their *in vivo* biodistribution on tumour-bearing mice models in comparison to a clinical DTX formulation (Taxotere[®]).

References. ¹Helfield et al., *Frontiers in Physics*, 2021; ²Batchelor et al., *Current Opinion in Colloid & Interface Science*, 2021; ³Roovers et al., *ACS Langmuir*, 2019; ⁴Upadhyay and Dalvi, *Ultrasound in Med. & Biol.*, 2018.

Photodynamic Therapy-Based Photochemical Immune Stimulation for the Treatment of Ovarian Cancer in a Xenograft Mouse Model

Breana Shehetila¹, Lauren Philp^{2,3}, Gang Zheng^{1,4,6}, Layla Pires⁵, Carla Calcada⁴, Brian C. Wilson^{4,6}

¹*Institute of Biomedical Engineering, University of Toronto, Toronto, ON*

²*Department of Obstetrics and Gynecology, University of Toronto, Toronto, ON*

³*Division of Gynecologic Oncology, University Health Network / Sinai Health System, Toronto ON*

⁴*Princess Margaret Cancer Center, University Health Network, Toronto, ON*

⁵*Department of Biomedical Engineering Texas A&M University, College Station, USA*

⁶*Department of Medical Biophysics, University of Toronto, Toronto, ON*

Introduction: Ovarian cancer is the most lethal gynecological malignancy, with 80% of diagnoses occurring at an advanced stage. Despite current chemotherapy and surgical cytoreduction, disease recurs in about 50% of patients, often as incurable chemo- and radio-resistant disease. This high recurrence rate, along with tumor heterogeneity, lack of diagnostic biomarkers, and a complex tumor microenvironment, highlights the urgent need for therapies that eradicate primary tumors and induce a specific anti-tumor immune response to prevent progression and metastases. This response should ideally occur through immunogenic cell death (ICD), activating the adaptive immune response.

Photodynamic therapy (PDT) is a potentially immunogenic anti-tumor treatment for ovarian cancer. Combining a photosensitizer (PS), light, and oxygen, PDT produces reactive oxygen species (ROS) that destroy cancer cells. Preferential PS accumulation in tumors and localized light delivery enhance effectiveness while minimizing damage to healthy tissue. However, PDT has limitations that hamper its effectiveness. Limited light penetration restricts tumor accessibility, reducing efficacy, especially in deeper tissues. Photosensitizers often accumulate non-specifically in off-target tissues, and unconfined illumination may damage adjacent tissues, particularly with diffuse light in metastatic disease. In ovarian cancer, intraperitoneal PDT is further constrained by the lack of compounds that are both effective photosensitizers and efficient tumor localizers.

Methods: This project aims to optimize PDT parameters and explore its potential for photochemical immune stimulation (PCIS) as a novel therapeutic strategy for ovarian carcinomatosis. We hypothesize that PCIS will eradicate primary ovarian tumors and induce a specific anti-tumor immune response, improving survival.

The research will begin with *in vitro* studies using murine parental and GFP/luciferase-expressing ID8 ovarian cancer cells to optimize PDT treatment parameters: photosensitizer dose, drug-light time interval and light dose. Evaluations will assess photosensitizer dark toxicity and determine cell death pathways, focusing on identifying markers indicative of ICD. Subsequently, optimized parameters will be applied to *in vivo* subcutaneous xenograft tumor models in immunocompetent albino C57BL mice. Tumor monitoring before and after treatment will be conducted using longitudinal fluorescence and bioluminescence imaging. Initially, the established photosensitizer chlorin e6 will be used, followed by extensions to multifunctional porphyrin-lipid nanoparticles (Porphysomes), both folate receptor-targeted and untargeted. The optimal parameters will be those achieving primary tumor eradication or maximum growth delay, disease-free survival, and overall survival, with minimal systemic toxicities. Results obtained with chlorin e6 and Porphysomes will be compared. Immune stimulation through PCIS will be evaluated by applying the optimized PDT parameters. Endpoints will include primary tumor eradication, disease-free and overall survival, tumor re-challenge, abscopal effect and immune transfer.

Results: We anticipate that optimizing PDT parameters will enhance efficacy against ovarian cancer cells *in vitro* and *in vivo*. Optimized PDT is projected to induce ICD markers including calreticulin exposure, ATP release and HMGB1 secretion *in vitro*, and lead to significant tumor regression or eradication *in vivo*, thereby prolonging disease-free and overall survival. We also expect a robust anti-tumor immune response, evidenced by resistance to tumor re-challenge and potential abscopal effects, indicating systemic immune activation.

Conclusion: Advanced imaging modalities are integral to this study, enabling precise treatment delivery and monitoring. Fluorescence imaging will track photosensitizer distribution within tumors, offering real-time visualization of PDT delivery. Ultrasound and bioluminescence imaging will non-invasively monitor tumor growth and regression, while PET imaging with ⁶⁴Cu-labelled Porphysomes will determine the pharmacokinetics to optimize the photosensitizer-light interval. Integrating these imaging techniques not only deepens our understanding of PDT's effectiveness but also underscores their pivotal role of imaging in advancing therapeutic strategies against ovarian cancer.

This work is supported by the Terry Fox Research Institute New Frontiers Program (#1137)

Automated Detection of Lymph Node Metastasis in Prostate Cancer Using Whole Slide Images

Fatemeh Zabihollahy^{1,2,3}, Kangdi Shi^{1,4}, Collins Wangulu³, Ioannis Prasses^{1,2}, Theoder van der Kwast^{1,2}, Neil Fleshner³, and George Yousef^{1,2,4}

¹Laboratory Medicine Program, University Health Network, Toronto, ON, Canada

²Department of Laboratory Medicine and Pathobiology, University of Toronto, Toronto, ON, Canada

³Divisions of Urology and Surgical Oncology, Department of Surgery, University Health Network, Toronto, ON, Canada

⁴Keenan Research Centre for Biomedical Science at the Li Ka Shing Knowledge Institute, St. Michael's Hospital, Unity Health Toronto, Toronto, ON, Canada

Introduction: Prostate cancer (PCa) is the most common cancer in men. Lymph node metastasis (LNM) is associated with a higher risk of PCa-related death, and poor prognosis, and requires modification of the treatment plan¹. Manual assessment of LNs on glass slides is a time-consuming task, which is prone to error and observer variability. Moreover, the limitation of the human eye in the identification of small metastatic deposits led to the missing rate of 8.8%-13%². The recent transition to digital pathology, combined with breakthroughs in deep learning (DL), has the potential to help pathologists accurately examine LNs through whole-slide images (WSIs). In this study, we present a novel DL-based algorithm for the automated detection of LNM of PCa using digital pathology images.

Methods: A dataset consists of 378 WSIs of pelvic LNM including 59 positive and 319 negative cases was leveraged in this REB approved study to train and evaluate the method. A senior GU pathologist with 30 years of experiences (T.K) reviewed the positive cases and highlighted LNM on digital slides. Incomplete and sparse manual annotation strategy was adopted to capture the concept and diversity of metastasis cells rather than time-consuming and expensive pixel-level annotation process.

A coarse to fine strategy was adopted to detect and segment metastatic cancer cells on WSI of lymph node tissues. A convolutional neural network was trained using training set (328 slides comprised 44 positive and 284 negative cases) to delineate lymph node tissue. The prediction map was used as a reference to compute the region of interest (ROI) for metastasis detection and discard the image background. Small patches were extracted from ROI, where both data augmentation and under-sampling techniques were used to balance the training samples. A vision transformer was trained using the transfer learning framework, to fine-tune the pre-trained Virchow foundation model³. A hard negative mining method was then applied to identify and remove false positives from the predictions. The performance of the proposed method was evaluated using the sensitivity and specificity metrics. Any non-zero overlap between manual annotation and AI prediction of LNM was considered as a criteria for sensitivity calculation at the slide level.

Results: The proposed method was tested using 50 WSI including 15 positive and 35 negative cases and achieved sensitivity and specificity of 100% and 98%, respectively. Figure 1 shows the results for two patients randomly selected from the tests set.

Conclusion and Discussion: The results of our study demonstrate that the automated detection of PCa LNM on WSI is feasible. A more rigorous evaluation of the proposed method using a larger test cohort from multi-center is needed, which is the direction of our future study.

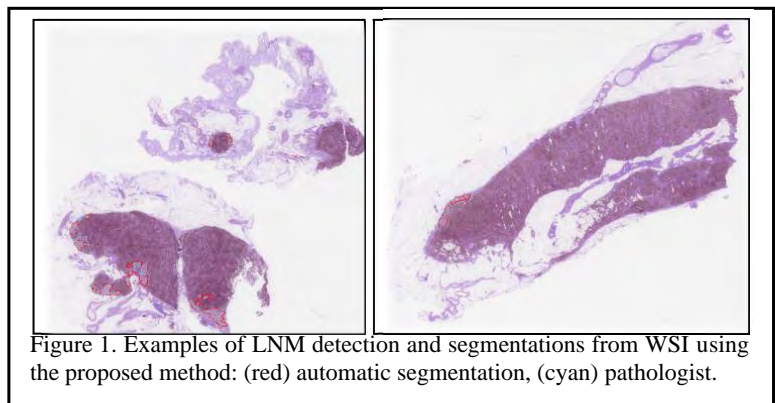


Figure 1. Examples of LNM detection and segmentations from WSI using the proposed method: (red) automatic segmentation, (cyan) pathologist.

REFERENCES

- [1] Perera M, et al. Oncologic outcomes of patients with lymph node invasion at prostatectomy and post-prostatectomy biochemical persistence. *Urol Oncol.* 2023;41(2):105.e19–105.e23.
- [2] Maxeiner A, et al. Lymphatic micrometastases predict biochemical recurrence in patients undergoing radical prostatectomy and pelvic lymph node dissection for prostate cancer. *Aktuelle Urol.* 2019;50(6):612–618.
- [3] Vorontsov, E., et al. A foundation model for clinical-grade computational pathology and rare cancers detection. *Nature Medicine.* 2024;30(10), 2924-2935.

Oral Epithelial Cell Quantification for Dysplasia Grading Using Histopathology Images

Yasaman Soleymani^{1,2}, Kangdi Shi^{2,3}, and Iona Leong^{†1}

¹Department of Pathology and Laboratory Medicine, Mount Sinai Hospital, Toronto, ON, Canada

²Laboratory Medicine Program, University Health Network, Toronto, ON, Canada

³Department of Laboratory Medicine and Pathobiology, University of Toronto, Toronto, ON, Canada

[†]These authors contributed equally.

Introduction: Oral squamous cell carcinoma (OSCC) is a malignant tumor of the oral mucosa. It is the most common type of oral cancer, and it accounts for a significant proportion of head and neck cancer cases¹. The prognosis for advanced-stage OSCC is poor, with a five-year survival rate of only 40%². However, early diagnosis can drastically improve the survival rate to 80–90%, underscoring the importance of early detection². Many OSCC are preceded by premalignant lesions which are highly associated with the presence of oral epithelial dysplasia (OED). OEDs are histopathologically graded as mild, moderate and severe. The risk of malignant transformation rises with the severity of the OED. The World Health Organization lists various cytological and architectural histological features used to grade OED⁴. However, grading of OED is prone to high inter- and intra-observer variability. The recent shift to digital pathology, along with advancements in deep learning (DL), holds promise for assisting pathologists in accurately examining epithelial tissue. In this study, we propose a DL-based method to quantify epithelial cells and predict cell-crowded regions, which is essential for grading OSCC.

Methods: The proposed algorithm consists of three main components: detecting and segmenting epithelial tissue, quantifying cells in the epithelial region, and predicting cell-crowded areas as a key feature for dysplasia grading. A dataset of 40 cases was used to develop and evaluate the model, which was divided into 29 training and 11 testing subsets. To train the AI-based model for epithelial segmentation, the UNI foundation model was implemented using a transfer learning framework that eliminates the need for extensive data annotation. Additionally, a StarDist-based model was fine-tuned to detect cells within the epithelial area. Image density was then calculated based on the predicted cells, resulting in a heatmap that represents the cell-crowded regions. The performance of the epithelial segmentation model was evaluated using the Dice similarity coefficient (DSC) metric. A senior pathologist reviewed the generated heatmap for each test case to assess the AI model's performance in labeling cell-crowded regions.

Results: Figure 1a shows one sample of the epithelial segmentation results obtained using our proposed method. Our method achieved an average DSC of 0.90 with standard deviation of 0.08 on the test cohort. Figure 1b and 1c illustrate the cell prediction using our proposed method for one test case and its corresponding heatmap, respectively. The qualitative assessment of the heatmap showed that the cell-crowded regions have been correctly highlighted by AI and that there is a high correlation between AI and pathologists in cell presence prediction for dysplasia cases.

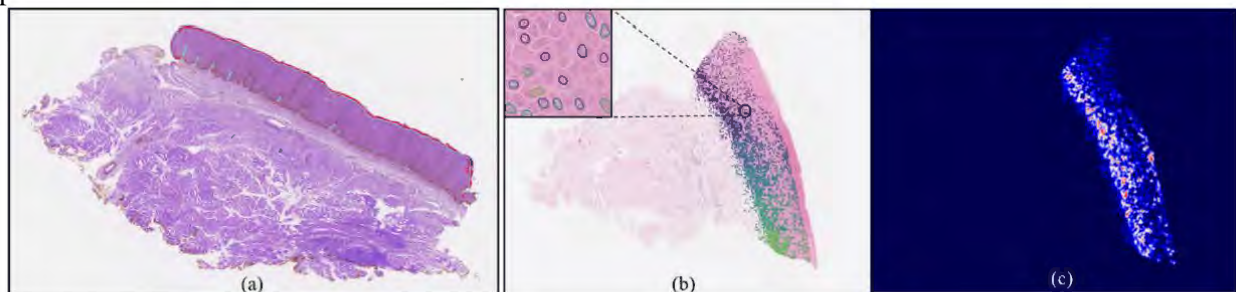


Figure 1. Examples of the result using our proposed method a) segmentation of epithelial tissue (cyan: AI and red: human expert), b) automated cell segmentation, and c) heatmap of cell-crowd regions where red to blue correspond regions with high to low cells.

Conclusion and Discussion: We developed an AI-based model for fully automated epithelial cell detection and quantification from histopathology images. Our experimental results demonstrate the developed method is accurate and fast. Nevertheless, our current approach does not account for all architectural histological features needed for dysplasia grading. Extracting these features is the direction of our future study. Moreover, the method needs to be tested using more number of images.

REFERENCES

- [1] Pai SI, Westra WH. Molecular pathology of head and neck cancer: implications for diagnosis, prognosis, and treatment. *Annu Rev Pathol.*2009;4:49–70.
- [2] European Cancer Patient Coalition. European Cancer Patient Coalition: Head & Neck Cancers [Internet]. [cited 2021 Jul 21]. Available from: <https://ecpc.org/news-events/head-neck-cancer-make-sense-campaign/>.
- [3] El-Naggar AK et al, WHO classification of head and neck tumours. 4th ed. Vol. 9. International Agency for Research on Cancer; 2017.
- [4] WHO Classification of Tumours Editorial Board. Head and neck tumours [Internet; beta version ahead of print]. 5th ed. Lyon, France: International Agency for Research on Cancer; 2023.

Pitches 2: MRI & Neuroimaging

Abstracts

Suppression of Lipid Contamination in Whole Brain Slice Magnetic Resonance Spectroscopic Imaging using Two-Dimensional Selective Excitation

Jason Rock^{1,2}, Simon Graham^{1,2}, Jamie Near^{1,2}

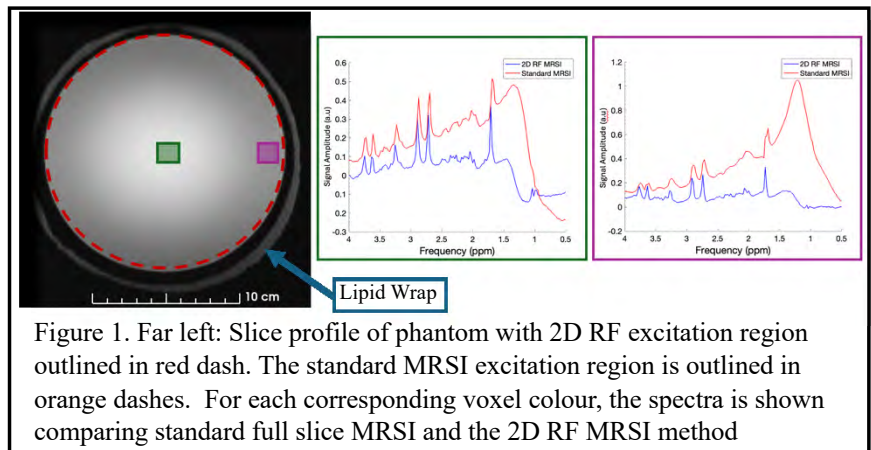
1 Medical Biophysics, University of Toronto; 2 Sunnybrook Research Institute

Introduction: Magnetic Resonance Spectroscopic Imaging (MRSI) is a versatile tool for investigating metabolism in brain tumors and neurodegenerative diseases, including Alzheimer's and Multiple Sclerosis (1,2). However, a significant challenge of performing MRSI on whole-brain slices is the issue of lipid contamination. Extracranial lipids, found in the skin and adipose tissue of the scalp, produce MRSI signals with substantially greater amplitudes compared to the brain's primary metabolites, due to their orders-of-magnitude higher concentrations. These extracranial lipid spectral signals tend to 'ring' into MRSI voxels within the brain, owing to the inherently low spatial resolution (typically on the order of centimetres) of MRSI. Consequently, the dominant lipid spectral signal obscures the weaker spectral signals originating from common brain metabolites, such as N-acetylaspartate (NAA), choline, creatine, and myo-inositol, making accurate quantification challenging. By using two-dimensional (2D) radiofrequency (RF) pulses, an arbitrary excitation region can be formed. By creating a brain shaped excitation region, we aim to effectively eliminate lipid contamination in MRSI by exclusively exciting the brain and excluding extracranial lipids. This improvement has the potential to enhance diagnostic accuracy and treatment monitoring as the mentioned brain metabolites are no longer obstructed by the large lipid peak from extracranial lipids.

Methods: An MR spectroscopic phantom (GE Braino) was used with lard pasted on the exterior to mimic extracranial lipids. A rapid slice-selective spin-echo MRSI sequence with a rosette k-space trajectory was modified by replacing the conventional slice selective excitation pulse with a 2D RF pulse and the associated trajectory gradients. The 2D RF pulses were designed using Pauly's small-tip-approximation work (3), with a spiral-in k-space trajectory (15 spirals, $k_{\max} = 1.15 \text{ cm}^{-1}$, 8 ms duration). A custom excitation region was prescribed in the x-y plane within the phantom.

Results: The MRSI data were processed using FID-A (4). Figure 1 shows the spectra in three locations within the phantom for the 2D RF MRSI sequence and the standard full slice MRSI sequence. The standard MRSI acquisition produces severe lipid contamination, resulting in a distorted baseline and spectral overlap with metabolites of interest. For voxels closer to the edge of the phantom, the lipid contamination increases. Using our 2D RF MRSI sequence, the lipid contamination within the same centre voxel is reduced by a factor of ~ 3.5 , and the lipid contamination within the edge voxel is reduced by a factor of ~ 20 .

Conclusion: Using a 2D selective excitation pulse for MRSI is feasible for exciting arbitrary regions of interest in the brain with significantly reduced lipid contamination. Further work will involve 1) translating the workflow for in-vivo experiments and; 2) using machine learning algorithms to design excitation profiles with minimal residual excitation (see abstract ID #113). Ultimately, this method is expected to help improve the clinical usage of MRSI by improved brain coverage with removed lipid contamination.



References: [1] Posse et al. J Magn Reson Imaging. [2] Graff-Radford et al. Neuropsychiatric Dis Treat 2013 [3] Pauly et al. Journal of Magnetic Resonance (1989) [4] Simpson et al. Magn Reson Med. 2017

Deep-Learning Based Detection of Placenta Previa from Fetal MRI: A Cascaded CNN Approach

Nika Momeni¹, Joshua Eisenstat¹, Matthias W. Wagner^{2,3,4}, Alejo Costanzo¹, Justin Lo¹, Logi Vidarsson³, Birgit Ertl-Wagner^{2,3,4}, and Dafna Sussman^{1,5,6}

¹Department of Electrical, Computer and Biomedical Engineering, Toronto Metropolitan University, Faculty of Engineering and Architectural Sciences, Toronto, Ontario, Canada

²Division of Neuroradiology, The Hospital for Sick Children, Toronto, ON M5G 1X8 Canada.

³Department of Diagnostic Imaging, The Hospital for Sick Children, Toronto, ON M5G 1X8 Canada.

⁴Department of Medical Imaging, Faculty of Medicine, University of Toronto, Toronto, Ontario, Canada.

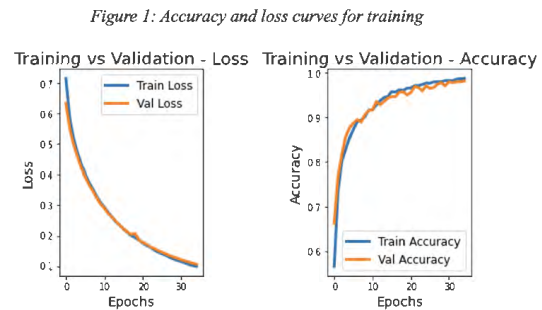
⁵Institute for Biomedical Engineering, Science and Technology (iBEST), Toronto Metropolitan University and St. Michael's Hospital, Toronto, Ontario, Canada

⁶Department of Obstetrics and Gynecology, Faculty of Medicine, University of Toronto, Toronto, Ontario, Canada.

Introduction: Placenta previa, a condition in which the placenta blocks the cervical os, affects approximately 0.5% of pregnancies in North America. Early diagnosis of this condition is essential to the fetal birth plan to minimize risk for the fetus and mother [1]. Following ultrasound, the use of Magnetic Resonance Imaging (MRI) provides better clarity for diagnosing several fetal-placental abnormalities making it the gold standard as a secondary imaging modality. Automatic assessment techniques for fetal MRI have been developed to compensate for a lack of radiological expertise in fetal MRI. As part of the full automation of the fetal MRI report, the placental position as well as detection of placenta previa are vital.

Methods: Our study resulted in the design of a robust cascaded convolutional neural network (CNN) that automatically selects an MRI slice which clearly shows the necessary structures for diagnosis of the condition: the cervical os and the placental position. These slices are then classified to detect the presence or absence of placenta previa. Using the VGG16 architecture, the model leverages transfer learning techniques to improve the model's accuracy and efficiency [2].

Results: The dataset used in this study consisted of 77 3D fetal MRIs where 37 of them contained images showing placenta previa, and 40 did not. Each slice was then categorized on whether or not they visually showed the cervical os for accurate diagnosis, which was validated by a physician. Upon a variety of testing including a transfer learning test, ablation study and cross-fold validation, the final cascaded model achieved a 94.84% accuracy and a loss of 0.1505, as seen in figure 1.



Conclusions: We present an automatic tool for the detection of placenta previa from either 2D or 3D fetal MRI datasets. The work presented compensates for an absence of radiological expertise in diagnosing and identifying fetal-placental conditions. Our model can be used independently or alongside any of our other machine-learning algorithms for fetal MRI processing, and brings us closer to fully automating the fetal MRI radiological report [3-6].

[1]: J. A. Cresswell, C. Ronsmans, C. Calvert, and V. Filippi, "Prevalence of placenta praevia by world region: a systematic review and meta-analysis," *Trop. Med. Int. Health*, vol. 18, no. 6, pp. 712–724, 2013, doi: <https://doi.org/10.1111/tmi.12100>. [2]: L. Schmarje, M. Santarossa, S.-M. Schroder, and R. Koch, "A Survey on Semi-, Self- and Unsupervised Learning for Image Classification," *IEEE Access*, vol. 9, pp. 82146–82168, 2021, doi: 10.1109/ACCESS.2021.3084358. [3] Lim A., Lo J., Wagner M.W., Ertl-Wagner B. & Sussman D. (2023). Motion Artifact Correction in Fetal MRI Based on Generative Adversarial Network Method. *International Society for Magnetic Resonance in Medicine, Toronto, Canada*. [4] Eisenstat J., Wagner M., Vidarsson L., Ertl-Wagner B. & Sussman D. (2023). Automatic Fetal Orientation Detection Algorithm in Fetal MRI. *International Society for Magnetic Resonance in Medicine, Toronto, Canada*. [5] Lim A., Lo J., Wagner M.W., Ertl-Wagner B. & Sussman D. (2023). Artifact detection algorithm using deep learning in fetal MRI. *Imaging Network Ontario, London, Canada*. [6] Costanzo A., Wagner S., Ertl-Wagner B. & Sussman D. (2023). Placental MRI Segmentation Using a Novel Convolutional Neural Network. *Imaging Network Ontario, London, Canada*.

Accounting for Fat Contamination in Amine/Amide Concentration Independent Detection (AACID) CEST MRI of the Human Spinal Cord

Victoria Little^{1,2}, Sarah Detombe³, Neil Duggal³, and Robert Bartha^{1,2}

¹Department of Medical Biophysics, Western University; ²Centre for Functional and Metabolic Mapping, Robarts Research Institute; ³Department of Clinical Neurological Sciences, London Health Sciences Centre

Introduction: Chemical exchange saturation transfer (CEST) is an MRI contrast mechanism capable of creating image contrast using low concentration exchangeable amine and amide protons.¹ A selective radiofrequency pulse is applied to the sample to saturate the target protons which then exchange with bulk water protons.¹ This transfer of energy results in a decreased bulk water signal, and the rate of proton exchange is pH dependent.¹ Amides and amines are functional groups found on endogenous proteins and peptides.¹ The ratio of the amide proton and the amine proton exchange-induced signal change, called amine/amide concentration independent detection (AACID) is inversely related to pH and produces image contrast sensitive to tissue pH.¹ Our group has recently applied this approach to create pH-weighted images in the brain and spinal cord.² Unfortunately, due to its small diameter, the spinal cord is susceptible to fat contamination from surrounding tissue. Exchangeable fat protons resonate at several different frequencies based on the structure of the lipids. Aliphatic fat protons resonate at -3.5 ppm,³ while olefinic fat resonates around 0.6 ppm.⁴ Previous AACID pH-weighted imaging in the spinal cord has not accounted for the 0.6 ppm olefinic proton pool. The objective of this study is to determine if inclusion of the olefinic proton pool in the fitting model impacts the AACID value of the tissue.

Methods: Three healthy participants (1 female, 2 males, mean age (\pm SD) 63 \pm 18 years) and four participants with cervical myelopathy (3 females, 1 male, mean age (\pm SD) 61 \pm 14 years) were scanned on a 3T Siemens MAGNETOM Prisma Fit MRI with a 64-channel head and neck coil. Spinal cord CEST scans incorporated 30 Gaussian RF pulses (0.5 μ T B₁ amplitude, 100 ms pulse length) for selective saturation followed by a 3D gradient echo readout (2.0 x 2.0 x 5.0 mm³, matrix size: 96 x 96 x 14 and TR/TE: 3.35/1.16 ms). To perform a B₁-inhomogeneity correction two additional CEST scans were acquired using RF saturation pulse B₁ amplitudes of 0.2 μ T and 0.8 μ T. A B₀ correction was also applied using the WASSR method (5 Gaussian pulses, 0.5 μ T amplitude, 100 ms pulse length).⁵ The Spinal Cord Toolbox⁶ was used to semi-automatically segment the spinal cord from C3 to C6. CEST spectra from each pixel (Fig. 1) in the cord were fitted in MATLAB using both a six-pool Lorentzian model² that included: water (0.0 ppm), macromolecular magnetization transfer (-2.0 ppm), amide (3.5 ppm), amine1 (2.75 ppm), amine2 (2.0 ppm), fat (-3.5 ppm); and a seven-pool model that also included olefinic protons (0.6 ppm). AACID values for each slice in the cord were compared for each model as well as amide and amine peak areas using a paired t-test ($p < 0.05$ considered significant).

Results: Results are presented as mean \pm SD. The average absolute difference for all participants between the six- and seven-pool models are illustrated in Fig. 2. Significant differences were observed for amide (0.153 \pm 0.070, $p < 0.01$) and amine2 (0.298 \pm 0.215, $p < 0.05$), whereas no differences were observed for AACID (0.021 \pm 0.019, $p = 0.87$) and amine1 (0.176 \pm 0.156, $p = 0.21$). The average chemical shift of the olefinic proton pool with respect to water was 0.066 ppm and average amplitude was -11.9%.

Conclusion: Preliminary results show no significant difference in AACID values when calculated after fitting the CEST spectrum with a seven-pool Lorentzian model incorporating olefinic fat protons compared to a six-pool Lorentzian fit model. Despite differences in amide and amine2 peak amplitudes the AACID value was unaffected as it is calculated using the final fitted spectrum, indicating it provides a robust metric to monitor tissue pH. Future work will include a larger number of participants and examine the results for each sub-group.

References: [1] McVicar, N et al. J. Cereb. Blood Flow Metab. 2014; [2] Cronin, A et al. NMR Biomed. 2024 [3] Malis, V et al. Magn. Reson. Med. Sci. 2023 [4] Ohno, N et al. Magn. Reson. Imaging. 2018 [5] Kim, M et al. Magn. Reson. Med. 2009 [6] De Leener, B et al. Neuroimage. 2017

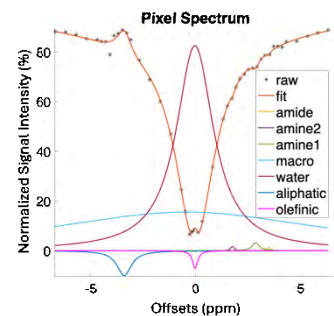


Figure 1. CEST spectrum of individual components of seven-pool Lorentzian model.

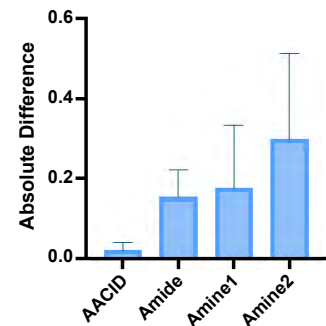


Figure 2. Absolute difference of AACID (unitless), amide (%), and amine (%) pools between models.

Modelling ^{13}C -bicarbonate signal changes due to lactate oxidation pathways in hyperpolarized MRI

Dylan Archer Dingwell^{1,2} and Charles H. Cunningham^{2,1}

¹Department of Medical Biophysics, University of Toronto; ²Physical Sciences, Sunnybrook Research Institute

INTRODUCTION: In hyperpolarized ^{13}C MRI, injected ^{13}C -pyruvate can be reversibly converted to ^{13}C -lactate in a reaction dependent on the balance of NAD (NAD⁺/NADH) coenzymes. Both pyruvate and lactate can also be transported into mitochondria, where irreversible pyruvate consumption fuels the tricarboxylic acid cycle, generating ^{13}C -bicarbonate as a byproduct. Recent *in vivo* evidence indicates that bicarbonate generation is linked to lactate oxidation (back-conversion to pyruvate) in the brain, as shown in Figure 1: radiofrequency saturation of ^{13}C -lactate,

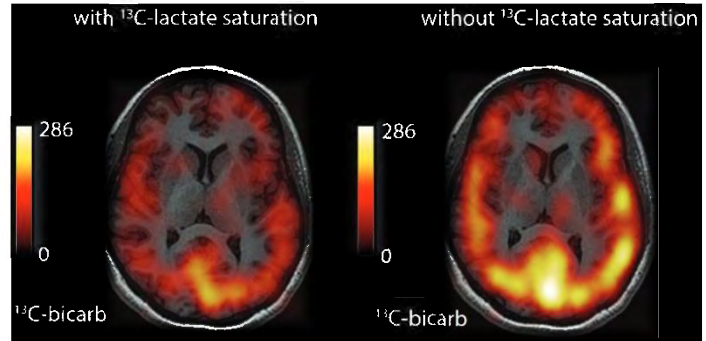


Figure 1 – ^{13}C -bicarbonate brain images (red-yellow).

which causes non-recoverable loss of lactate signal, also reduced regional ^{13}C -bicarbonate signal intensities.¹ This suggests that oxidation of ^{13}C -lactate back to ^{13}C -pyruvate precedes production of some ^{13}C -bicarbonate. The objective of this study was to test whether this change in bicarbonate signal was more likely explained by transport of pyruvate into mitochondria following interconversion with lactate in the cytosol, or by transport of lactate into mitochondria for oxidation (implying mitochondrial use of lactate as an energy source).

METHODS: A 10 micron cubic volume representing a single brain cell with a spherical mitochondrial compartment comprising 10% of the cellular volume was modelled using the biochemical simulator Smoldyn² with MR.³ Particles for ^{12}C and ^{13}C metabolites were initialized at a scale of 5000 particles per 1 mM, with initial concentrations of 1 mM ^{13}C -pyruvate, 0.1 mM ^{12}C -pyruvate, and 0.5 mM ^{12}C -pyruvate, with 0.3 mM NAD⁺ and 0.06 mM NADH. The NAD pool was subdivided differently for three conditions: uniform NAD (10% in mitochondria), astrocytic (25% in mitochondria at a 5:1 NAD⁺:NADH ratio), and neuronal (50% at a 5:1 ratio).

RESULTS: Modelling typical reactant concentrations and NAD distributions at cellular scale for neurons and astrocytes, as well as a uniform NAD distribution, enabled tracking of pathways followed by individual ^{13}C -labelled metabolites in simulation (Figure 2). Proportions of ^{13}C -bicarbonate produced from lactate transported into mitochondria and oxidized were 9%, 32%, and 55% for the uniform, astrocytic, and neuronal NAD distributions respectively. In all three cases, lactate oxidation occurred primarily in mitochondria, with relatively minimal (<10%) back-conversion of ^{13}C -pyruvate to lactate occurring in the cytosol.

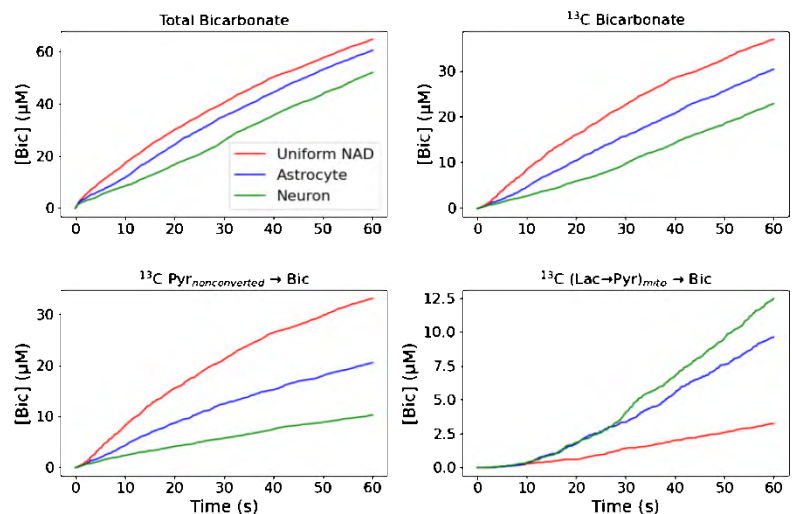


Figure 2 – Time courses of simulated bicarbonate concentrations.

CONCLUSIONS: The decrease in ^{13}C -bicarbonate MR signal observed *in vivo* shows that some bicarbonate production follows lactate oxidation, but not the pathways by which this occurs. This model indicates that lactate oxidation inside mitochondria is a more likely pathway than cytosolic back-conversion of lactate, and that the proportion of bicarbonate produced after mitochondrial lactate oxidation is higher with realistic partitioning of the NAD pool. These results are consistent with the mechanism of mitochondria using lactate as an energy source.

REFERENCES: 1. Uthayakumar, B. et al. *Magn. Reson. Med.* 91, 2162–2171 (2024). 2. Andrews, S.S. *Bioinformatics* 33 (2017). 3. Dingwell, D.A. & Cunningham, C.H. *Magn. Reson. Med.* 93, 369–383 (2025).

Comparison of Lipid Suppression Techniques for *in vivo* Whole Brain MR Spectroscopic Imaging

Kaito Hara-Lee¹, Jaime Near²

¹Queen's University, Kingston, ON, Canada; ²Sunnybrook Research Institute, Toronto, ON, Canada

Introduction: Magnetic Resonance Spectroscopic Imaging (MRSI) is a non-invasive technique for mapping metabolite concentrations in the human brain *in vivo*, enabling the study of neurochemical changes associated with diseases like Alzheimer's, Multiple Sclerosis, and ALS [1]. A significant challenge in MRSI is lipid signal contamination from extracranial fat, which interferes with accurate metabolite measurement. While acquisition-based methods reduce lipid interference, they often limit whole-brain coverage and increase scan times. Post-processing techniques offer a promising alternative by leveraging spectral or spatial decomposition based on prior knowledge of lipid signal characteristics. This work compares post-processing methods for lipid removal in whole-brain MRSI.

Methods: Three lipid suppression techniques were compared: L2-Regularization (L2) [2], Signal-Space Projection (SSP) [3], and Fast Lipid Reconstruction & Removal Processing (FLIP) [4]. L2 is a spectral prior algorithm that minimizes the loss between the reconstructed and original spectra while imposing a lipid-basis penalty. SSP is a spectral prior algorithm that uses a lipid signal matrix to remove the spatial pattern of lipid signals from the original image. FLIP is a spatial prior algorithm that reconstructs high-resolution lipid coefficients and removes them from the original image in the frequency domain (K-space). The methods were tested on a 3D spatial-spectral MRSI dataset from an *in vivo* scan of a healthy human brain, acquired with a 240x240 mm field of view, a 48x48 encoding matrix, Rosette K-space trajectories, and TR/TE of 1000/30 ms. Spatial segmentation masks defining lipid and metabolite regions in MRSI data were generated using MATLAB's Statistical Parametric Mapping package, enabling a priori specification of the spatial extent of brain and extracranial tissue, as needed for the post-processing algorithms.

Results: The average signal-to-noise ratio (SNR, peak signal/STDEV(noise)) for the brain metabolite creatine was 34 for the original images, 15 for SSP, and 4 for L2. For lipid signals, the average values were 29 for the original, 1.3 for SSP, and 0.84 for L2, calculated by integrating over the lipid peaks. L2 performed better in reducing lipid signals but significantly suppressed metabolite signals due to its larger average SNR loss. In contrast, SSP achieved a better overall balance, effectively removing lipid signals while preserving metabolite signals (Figure 1A). FLIP was implemented and demonstrated promising results in simulated data, effectively suppressing lipid contamination while preserving metabolite signals (Figure 1B).

Conclusion: Despite their efficient lipid suppression capabilities, a notable limitation of L2 and SSP is their reliance on spectral priors, which leads to the suppression of intracranial lipids, such as those in brain tumours. FLIP showed promise in simulations but has been ineffective in *in vivo* data. Its theoretical advantage lies in using purely spatial priors, which could preserve intracranial lipid signals, such as those associated with tumours. Future work will focus on successfully implementing FLIP for *in vivo* data and exploring the potential for combining it with other methods.

References: [1] Posse et al. J Magn Reson Imaging. 2024 [2] Bilgic et al. J Magn Reson Imaging. 2014 [3] Tsai et al. Magn Reson Med. 2019 [4] Adany et al. Magn Reson Med. 2021

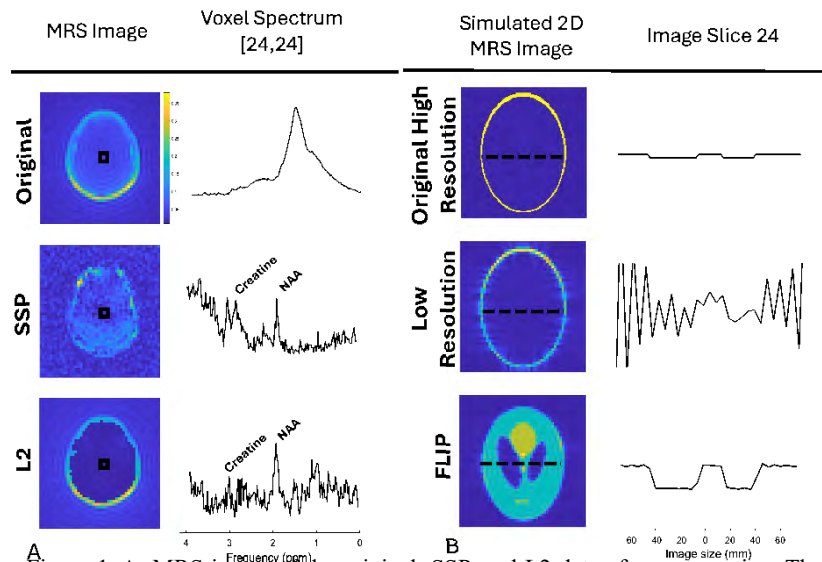


Figure 1. A: MRS image of the original, SSP, and L2 data after suppression. The middle voxel spectrum is shown in the second column between zero and four ppm B: Simulated 2D MRS image in high resolution, low resolution, and FLIP after suppression. The low resolution was obtained through K-space truncation. The metabolite image intensities across the middle of all the images are plotted, respectively.

Title: Microscopic fractional anisotropy of the hippocampus in dementia patients.

Authors: Ricardo Rios-Carrillo¹, Rubina Malik², Ali Khan¹, Elizabeth Finger², and Corey Baron¹

Affiliations: ¹Centre for Functional and Metabolic Mapping (CFMM), Robarts Research Institute, Western University, London, ON, Canada, ²Clinical neurological sciences, Western University, London, ON, Canada

Introduction Dementia is a predominant brain disease affecting the aging population, with the number of people living with dementia expected to increase[1]. Diffusion-Weighted MRI (dMRI)[2] has potential to aid in the diagnosis of dementia, as it can give insight into microstructural alterations. Although conventional dMRI techniques have been used to study dementia, they lack specificity to differentiate between pathological changes, especially in gray matter[3]. In this work, we show that a state-of-the-art dMRI metric, microscopic Fractional Anisotropy (μ FA)[4], is sensitive to microstructural changes that occur in several types of dementia. μ FA is related to the classical Fractional Anisotropy as an indicator of microstructure integrity, although it is better suited for gray matter (e.g. hippocampus) as it is not affected by microstructure dispersion[4].

Methods: We enrolled patients with Alzheimer's disease (AD, n=16), Fronto Temporal Dementia (FTD, n=13), Lewy Body Dementia (LBD, n=13) and a group of healthy subjects (n=8). Ages: 67.79 +/- 7.95. Sex: 21/29 females/males. Imaging was performed using a 3T Siemens Prisma. The protocol consisted of an anatomical T1 weighted image with 0.8 mm isotropic resolution and a dMRI protocol with a modified in-house EPI sequence tailored for μ FA acquisition[4]. Other parameters: TE/TR = 92/4900ms, 1.8mm isotropic resolution. We obtained μ FA maps with MatMRI[5] and registered the maps to the T1w brain image of each participant. We used Hippunfold[6] to automatically segment the hippocampus from the T1w images to generate ROIs for the subiculum, CA subfields, and the dentate gyrus. We excluded six subjects (2 AD, 1 LBD and 3 FTD) with failed segmentations from the study.

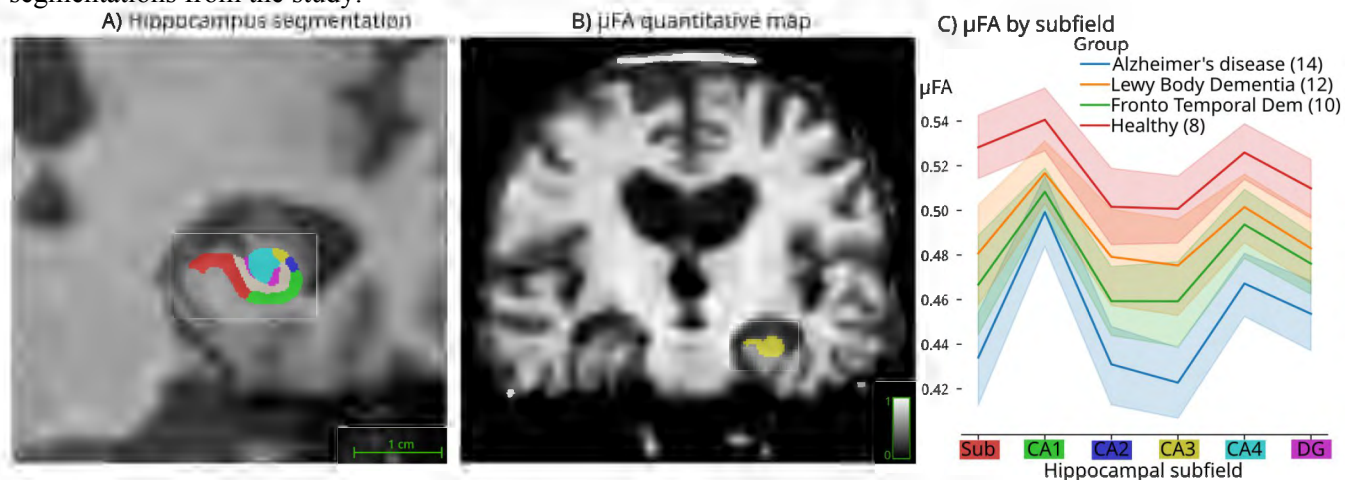


Figure: A) Segmentation of hippocampus of a dementia patient. B) Quantitative μ FA map. C) μ FA mean and confidence intervals (95%) values by subfield for the different groups in the study.

Results: Figure A shows an example of a segmented hippocampus on T1w image of an AD patient. Figure B shows its corresponding μ FA map, clearly showing the enlarged ventricles and atrophy in the hippocampus. The data of the hippocampal segmented subfields by each group is visualized in Figure C. Quantitative values have little overlap between groups, with the greatest difference being between the Alzheimer's patients and the control group. The volume changes observed here agree with the well-characterized cell loss of subiculum and CA1 in AD[3]. Interestingly, μ FA decreased in all subfields which suggests more broad loss of axons. These results align with the expectation of microstructural degeneration in dementia, especially for AD in the hippocampus.

Conclusion: μ FA in the hippocampus was observed to vary with different forms of dementia making it a potential marker of hippocampal degeneration that could complement standard imaging analysis.

References: 1 Breijyeh, Z. et al. *Molecules* 25, 5789 (2020). 2 Le Bihan, D. et al. *Radiology* 161, 401–407 (1986). 3 Karat, B. G. et al. *J. Neurosci.* 44, (2024). 4 Arezza, N. J. J. et al. *Magnetic Resonance Imaging* 80, 132–143 (2021). 5 Baron, C. A. et al. *zenodo.8276948* (2023). 6 DeKraker, J. et al. *eLife* 11, e77945 (2022).

Preliminary PET Imaging Reveals Reduced Synaptic Density in Autistic vs Non-Autistic Youth

Christin Schifani¹, M. Omair Husain^{1,2}, Erin W. Dickie^{1,2}, Giselle Mirfalah¹, Kim L. Desmond^{1,2}, Carme Uribe^{1,2}, Meng-Chuan Lai^{1,2}, Hsiang-Yuan Lin^{1,2}, Neil Vasdev^{1,2}, George Fousias^{1,2}, Vanessa Goncalves^{1,2}, Erica Vieira^{1,2}, Aristotle N. Voineskos^{1,2}, Isabelle Boileau^{1,2}, Stephanie H. Ameis^{1,2}

¹ Campbell Family Mental Health Research Institute, Centre for Addiction and Mental Health

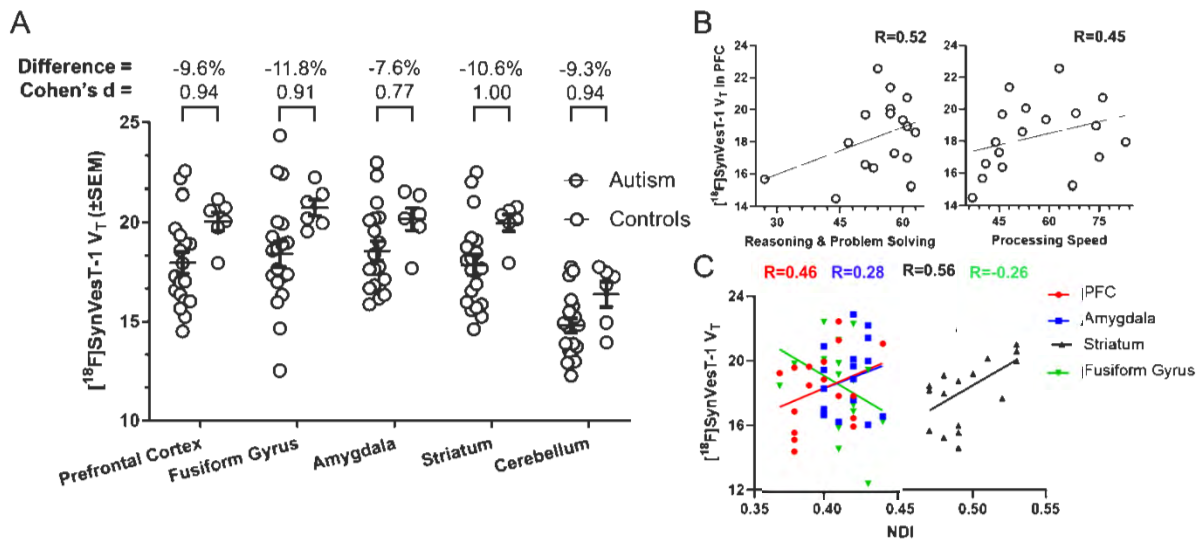
² Department of Psychiatry, University of Toronto

Introduction: Impairments in functioning and cognition are debilitating features of autism. Rising evidence implicates synaptopathology in autism. Initial studies using PET targeting the synaptic vesicle glycoprotein 2A (SV2A) indicate lower synaptic density in depression and schizophrenia that relates to cognition, and very recently a reduction has been reported in a small autistic sample (n=12) using a reference tissue model approach to estimate SV2A binding (Matuskey et al. 2024, *Molecular Psychiatry*). Herein, we present preliminary imaging of synaptic density in autistic youth/young adults using the SV2A PET radiopharmaceutical [¹⁸F]SynVesT-1 to correlate with cognition and more widely accessible MRI-derived markers (Neurite Orientation Dispersion and Density Imaging [NODDI]).

Methods: Autistic participants (16-35 yrs), IQ \geq 70 and age-/sex(assigned at birth)-matched controls were recruited from an existing NIMH-study sample (117 autism/43 control participant data available). Cognition was assessed with the MATRICS cognitive consensus battery (MCCB). Participants complete a 120-min [¹⁸F]SynVesT-1 PET scan with arterial blood sampling. Distribution volume (V_T) was estimated with the 1-tissue compartment model. Neurite density (NDI) & orientation dispersion (ODI) was derived from MRI-NODDI. V_T /NDI/ODI was extracted from prefrontal (PFC), cerebellar cortex (CC), fusiform gyrus (FG), striatum, amygdala (strong evidence for morphological alterations in autism shown); relationships with MCCB were examined in PFC.

Results: Twenty-one autistic participants (10M/7F) and 8 controls completed all procedures (incl. the 2h PET scan). Data of 18 autism and 6 controls have been processed (V_T of 5 participants pending; for 3 autism additional motion correction will be required). Preliminary analysis shows that the V_T of [¹⁸F]SynVesT-1 was lower across ROIs in autism vs controls (A; Cohen's d=0.8-1.00 (large effect sizes); PFC:-9.6 \pm 1.3%, amygdala:-7.6 \pm 1.0%, striatum:-10.6 \pm 1.4%, FG:-11.8 \pm 1.6%, CC:-9.3 \pm 1.0%). PFC V_T was positively related to cognitive performance across domains shown to be most impaired in autistic vs control participants (processing speed/reasoning-problem solving/general (B; r=0.35-0.52). The V_T and NDI were mainly positively related across ROIs (C; r=0.3-0.92).

Conclusions: Our initial findings replicate the reported reduced synaptic density in autism in a larger sample using arterial blood-derived input function (as opposed to reference tissue) and indicate that PFC synaptic density relates to cognition in autism as in other conditions. Initial associations between V_T and NDI support NDI's potential to provide a proxy measure of synaptic density potentially usable in settings/samples where PET is not feasible. Ongoing recruitment and characterization with an expanded sample will provide more definitive indication of whether SV2A binding is lower in autistic youth/emerging adults and about associations with neurocognition, social cognition and functioning, as well as NODDI indices.



Oral Presentations 3: Device, Systems, and Robotic Development

Abstracts

Generating and measuring flow for hemodynamic simulations of interventional vascular procedures

David Ng^{1,2}, Ian A. Cunningham^{1,2}, Leandro Cardarelli-Leite³, Maria Drangova^{1,2}, and David W. Holdsworth^{1,2}
¹Robarts Research Institute, ²Department of Medical Biophysics, ³Department of Medical Imaging, Schulich School of Medicine, Western University

Introduction: Image-guided vascular interventions involve precise manipulation and visualization of vascular flow during procedures such as embolization, angioplasty, stent placement, and clot removal. These interventions often involve significant variations in flow rates, making their simulation challenging. Characterizing flow changes can advance technologies, train residents, and support imaging research, with flow phantoms playing a key role. However, measuring arterial flow rates in flow phantoms is difficult, as existing commercial sensors target high flow rates (> 5 mL/s) or require specialized fluids. This study aimed to evaluate non-intrusive sensors capable of real-time measurement of microlitre to decilitre per second flow rates.

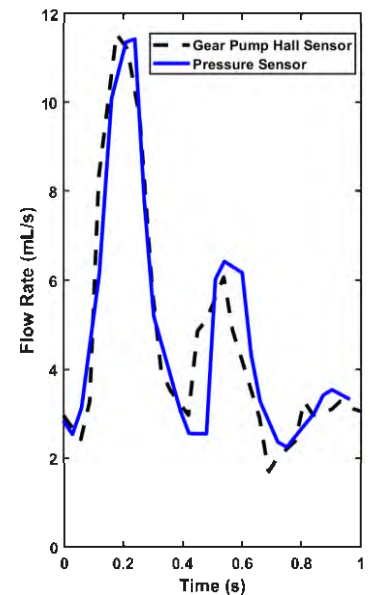
Interventional radiology also involves diverse anatomical regions with varying flow characteristics, where simulation with flow phantoms require pumps that accurately mimic these conditions. Piston and syringe pumps provide steady but intermittent flow due to pauses, while gear pumps allow continuous flow but may introduce pulsatility from discrete fluid transfer between gear teeth. This study also aims to quantify the ability of a gear pump to replicate arterial blood flow rates and waveforms, aiding in the simulation of image-guided therapies, the development of imaging techniques, and the training of residents with phantoms that include physiologic flow.

Methods: To characterize the performance of different flow meters, a piston pump circulated a water-glycerol mixture simulating human blood viscosity and provided constant flow rates from 0.01 to 5 mL/s to two flow-rate sensor designs. A gravimetric flow meter was created with a 100 g load cell and a container to measure mass over time, then determining flow rate from the slope. Secondly, a liquid pressure sensor measured pressures upstream of an outlet tube and was calibrated with flow rate data from the gravimetric flow meter at the tube outlet.

Using the developed flow meters, we evaluated a 0.2 mL/revolution gear pump driven using a brushless DC motor and controlled by an Arduino R4 microprocessor. The gear pump circulated the water-glycerol mixture at constant flow rates from 0.5 to 15 mL/s to measure the output flow stability using the gravimetric and pressure sensors. To determine the pump's frequency response, sinusoidal waves with a 15 mL/s peak-to-peak amplitude were generated at frequencies from 0.5 to 15 Hz, comparing peak flow rates measured by the Hall sensor built into the gear pump motor to programmed values. Lastly, the ability to generate physiological pulsatile flow was evaluated by creating a physiological waveform with a mean flow rate of 4.6 mL/s and measuring the flow rate with the gear pump's Hall sensor and a downstream pressure sensor.

Results: The gravimetric flow meter showed a normalized root mean square error of less than 1% at flow rates above 1.5 mL/s, increasing to 27% at 0.05 mL/s. The pressure sensor demonstrated a quadratic relationship between flow rate and pressure, with a coefficient of variation rising from less than 1% at 5 mL/s to 12% at 0.05 mL/s. The gear pump produced stable flow with a coefficient of variation $< 1\%$ from 15 to 3 mL/s, increasing to 4% at 0.05 mL/s. When generating a sinusoidal waveform with a nominal 15 mL/s peak-to-peak amplitude, the gear pump achieved 100% of the programmed peak flow rate below 1.25 Hz, dropping to 95% at 3 Hz. The figure illustrates example gear-pump generated and measured (pressure-based) physiological flow waveform, with a mean flow rate of 4.6 mL/s.

Conclusions: Both the gravimetric and pressure-based sensors accurately quantified flow rates typical in arterial systems without disrupting flow dynamics. The pressure sensor allows for continuous measurement, but its accuracy relies on maintaining calibration conditions. Using this flow meter in phantom research can provide insights into how image-guided therapies affect flow over time and allows correlation with other measurable parameters. The gear pump, operating with basic equipment, can produce steady, constant flow but may struggle replicating waveforms with frequency content over 3 Hz. Combining a gear pump with a pressure sensor offers a simple and compact method for continuous generation and measurement of physiological flow rates and pulsatile waveforms, making it a versatile tool for aiding in vitro tissue perfusion experiments, image-guided therapy training, and validating imaging algorithms.



One cycle of a physiological waveform generated by a gear pump with flow rate measured at the source (hall sensor) and downstream (pressure sensor)

Design and Testing of an MRI Phantom Faraday Cage Using Rapid Prototyping Techniques

Alexander Dunn^{1,2}, Sid Sadanand^{1,2}, Dafna Sussman^{1,2,3}

¹Departments of Biomedical Physics and of Biomedical Engineering, Toronto Metropolitan University, ²Institute for Biomedical Engineering, Science and Technology (iBEST) at Toronto Metropolitan University and St. Michael's Hospital, ³Department of Obstetrics and Gynecology, University of Toronto

INTRODUCTION:

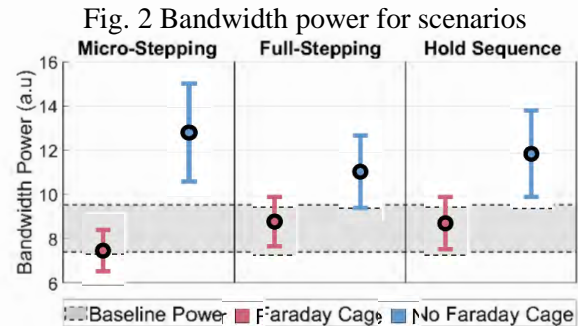
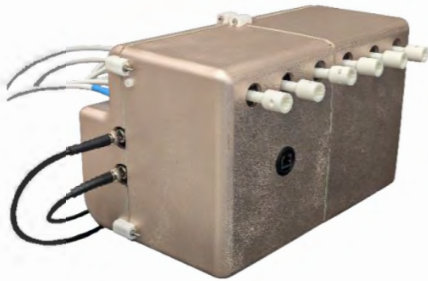
Electromagnetic interference (EMI) in magnetic resonance imaging (MRI) can degrade image quality and create artifacts [1]. Electronic devices, such as clinical equipment or experimental setups, must be designed to not emit radio frequencies that would be detected by the receiver coils. Motion phantom systems tend to produce EMI since they often require electronics and actuators within or near the bore. Faraday cages are often employed to limit the effect of EMI on MR images. Consisting of a conductive enclosure, Faraday cages allow the free redistribution of surface charges that result in EM wave reflection, containing emissions [2]. This study investigates the feasibility of using rapid prototyping techniques to create an effective Faraday cage for a 3T MRI system to shield six stepper motors and motor drivers used in a motion phantom actuator developed by our lab [3].

METHODS:

A 3D-printed shell was fabricated using ABS plastic in a Bambu X1E 3D printer. The design houses six 17E1K-05 2A stepper motors (OMC Corporation Limited, Nanjing, Jiangning, China) along with the stepper drivers on a PCB. The power cables and output drive shafts are routed through openings smaller than 23.5 mm, approximately 1/100 of the wavelength of a 3T system, to maintain shielding integrity. The exterior and adjoining surfaces of the Faraday cage pieces were coated twice with conductive paint (843AR, MG Chemicals, Burlington, Canada) to create a conductive layer of ~100 μm thickness. The enclosure components were joined with conductive gaskets to ensure minimal impedance to charge redistribution across the whole enclosure (Fig. 1) and the system was grounded to the room waveguide via braided copper cable sheaths.

Data was collected using a Philips Achieva 3T MRI scanner without radio frequency excitation to only record emitted noise over a bandwidth of 312 kHz. Four scenarios were measured: motors micro-stepping, motors full-stepping, motors in a hold sequence and without the motors present for a baseline measurement. 510 readouts were recorded for each scenario and repeated with and without the Faraday cage. To determine the data's EMI power measurement, each readout line of the raw k-space data was demodulated and Fourier transformed. These spectra were then averaged across all phase encoding lines and squared to construct a power spectrum, which was integrated to determine the total bandwidth power (Fig. 2).

RESULTS: Fig. 1 Faraday cage with coating



The Faraday cage was 3D printed in 4 sections and coated according to the manufacturer's instruction. The EMI powers for each scenario are shown in Figure 2. All tests with the Faraday cage fall within one standard deviation of the baseline measurement and the Faraday cage had a measured noise reduction 52.21%, 31.76% & 41.53% while micro-stepping, full-stepping and performing a hold sequence respectively. While these results demonstrate an EMI reduction, it is important to note this methodology is sensitive to baseline noise level variations, which complicates the comparison of EMI changes that are close to the baseline level. Future work will explore more robust methods to quantify EMI.

CONCLUSIONS:

The 3D-printed Faraday cage with a conductive coating was able to reduce EMI from our phantom actuator electronics near the MRI bore. These findings demonstrate the potential for accessible, rapid prototyping techniques in designing custom EMI mitigation solutions for MRI systems.

REFERENCES: [1] L. Erasmus et al., SA Journal of Radiology (2004) 8(2). [2] B. Lee et al., Magn. Reson. Med. (2018)79(3) pp.1745-1752. [3] D. Sussman et al., USPTO #: 63/326,265.2022/03/31.

Resection cavity tracking using a bench-top robot and electromagnetic tracking

¹Kian Hashtrudi-Zaad, ²Coleman Farvolden, ²Laura Connolly, ²Colton Barr, ²Gabor Fichtinger
1. University of Toronto, Toronto, Ontario, Canada 2. Queen’s University, Kingston, Ontario, Canada

INTRODUCTION: Breast-conserving surgery (BCS) is the preferred treatment for breast cancer as the objective is to remove the tumor while preserving healthy tissue. However, up to 40% of patients who undergo BCS require corrective surgery to remove residual cancer [1]. Cavity sweeping by various imaging modalities is emerging as a solution for identifying residual cancer. However, imaging the cavity is challenging due to the deformable nature of breast tissue and dynamic motion caused by respiration. We introduce a new approach to track cavity motion during surgery by using a low-cost bench-top robotic arm that follows the motion of a retractor embedded with an electromagnetic (EM) sensor.

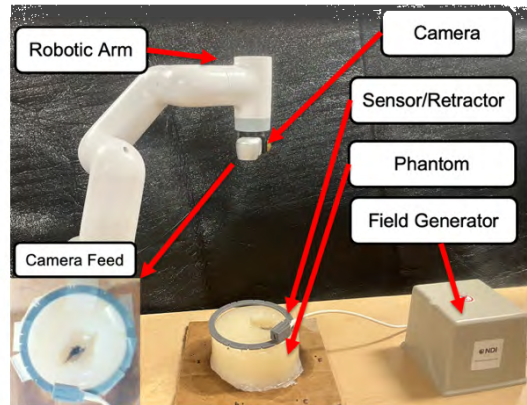


Figure 1: Diagram of the proposed robotic solution

METHODS: Our system includes a low-cost (~1000 CAD) robotic arm (MyCobot 280, Elephant Robotics) and an Ascension 3DG (Northern Digital) EM Tracker (Fig. 1). A previous study on the proposed robot and tracking system found no significant EM field distortion [2]. A 3D-printed camera mount fixes an RGB-D camera (Intel RealSense 415) as the robotic End-Effector (Fig. 1). The EM tracker, RGB and Depth data are streamed into Slicer through PLUS Toolkit (<https://plustoolkit.github.io/>) and OpenIGTLink (<https://openigtlink.org/>). Communication with the robot is facilitated via ROS2, and the motion planning is executed with the MoveIt2 package. We use SlicerIGT to register the robot coordinate system to the EM and camera coordinate systems. A 3D-printed retractor, which holds the cavity open, is embedded with an EM sensor that detects changes in position. When a change is detected, the new position of the retractor is published to MoveIt2 via SlicerROS2, where motion planning is executed to recentre the cavity in the frame [3]. We evaluated our approach by tracking 36 unique positions in the workspace and measuring latency from when Slicer publishes a command to movement initiation. We also assess tracking success through camera visibility of the cavity at each position. **RESULTS:** The system had a latency of 0.83 ± 0.13 seconds, indicating the robotic arm can adjust its position within a typical breathing cycle under anesthesia, 5 to 7.5 seconds. The cavity tracking was successful in 30 out of 36 test positions, with the remaining 6 positions being partially or totally occluded in the camera frame by the links of the robot. Despite occasional occlusions, the system effectively tracked the cavity's motion, suggesting its feasibility for dynamic surgical environments. **CONCLUSIONS:** The study demonstrates the feasibility of integrating electromagnetic tracking with a low-cost robotic arm for soft-tissue cavity tracking in an open-source framework. Challenges posed in clinical translation, such as sterilization and setup time, should be addressed in future work.

REFERENCES:

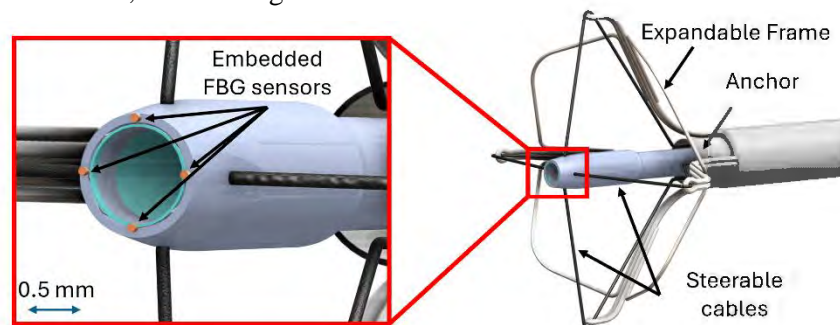
- [1] Schwarz, J., and Schmidt, H., “Technology for intraoperative margin assessment in breast cancer,” *Annals of Surgical Oncology*, 27(7), 2278–2287 (2020).
- [2] Connolly, L., Deguet, A., et al., “An Open-Source Platform for Cooperative Semi-Autonomous Robotic Surgery,” *IEEE International Conference on Autonomous Systems*, 1-5 (2021).
- [3] Connolly, L., Kumar, A. S., et al. “SlicerROS2: A Research and Development Module for Image-Guided Robotic Interventions,” *IEEE Transactions on Medical Robotics and Bionics*, 6(4), 1334–1344 (2024)

Accurate Catheter Tracking for Image-Guided Therapy Applications using Fiber-Bragg Grating

Mohammadmahdi Tahmasebi,^{1,2} Alykhan Sewani,³ Rene Gilliland-Rocque,^{1,2} Mohammad Khoobani,¹ Mohammadmahdi (Sina) Keshavarz,^{1,2} Graham Wright,^{2,3} Xijia Gu,¹ M. Ali Tavallaei^{1,2,3}

¹Faculty of Engineering and Architectural Science, Toronto Metropolitan University, ²Sunnybrook Health Sciences Centre, ³Magellan Biomedical Inc., Toronto, Canada

Introduction: Catheter-based interventions require precise control and navigation to reach specific anatomical targets. However, these procedures are often constrained by limited device tracking capabilities, as they primarily rely on 2D projection X-ray guidance. To address this limitation, expandable cable-driven parallel mechanisms (X-CADPAM), such as the CathPilot, have been developed to enable direct, localized control and tracking of the catheter tip relative to the target anatomy. In these mechanisms, tracking has traditionally relied on kinematic modeling and cable displacement measurements. However, these approaches are influenced by the catheter path profile and the frame's expansion size, both of which vary depending on the anatomy, limiting the average tracking accuracy to 0.56-0.88 mm. For applications requiring higher precision, such as imaging, drug delivery, or precise tool guidance (e.g., laser tissue ablation), this level of accuracy may be insufficient. To address this challenge, we propose integrating fiber Bragg grating (FBG) sensors within the catheter of X-CADPAMs to significantly enhance tracking accuracy. **Methods:** Four fiber Bragg grating (FBG) sensors were selected for this experiment. The sensors, with a sensing length of 3.4 mm and a fiber diameter of 125 μm , were inscribed using the phase mask technique and operated within a wavelength range of 1540–1558 nm. For improved precision, the FBGs were arranged in an orthogonal configuration at the catheter's distal tip, as depicted in the figure. The proximal ends of the fibers were connected to an interrogation monitor to capture real-time wavelength shifts induced by catheter tip movements from the based anchor point. To control the expansion size of the frame, a 3-D printed fixture with a diameter of 12.5 mm was used. To calibrate and validate the sensors, a 20 μm tip marker was affixed to the catheter tip and tracked using a high-resolution camera. The camera served as the primary tracking tool, enabling precise measurement of the catheter tip position by capturing wavelength shifts at 13 known positions across 10 independent tests. The camera and catheter body were securely mounted using a 3D-printed fixture, maintaining a fixed distance of 1 cm in front of the catheter tip, which was free to steer. A polynomial model correlated the recorded wavelength shifts with the corresponding tip positions. **Results:** Using a 3-degree polynomial model, two functions were obtained to relate FBG wavelength shifts and the catheter tip's X and Y positions relative to the catheter anchor. Using this model, the FBG sensors achieved an



Optical fiber configuration at the distal end of the catheter

average mean absolute error of $42.9061 \pm 1.2179 \mu\text{m}$ for the X-axis and $54.9958 \pm 25.1363 \mu\text{m}$ for the Y-axis. Different catheter path configurations supported the same results. **Conclusion:** Integrating FBG sensors into the CathPilot catheter significantly enhanced tip tracking accuracy, achieving an average catheter tip position estimation error of $69.74 \pm 25.13 \mu\text{m}$, which is significantly higher than any existing method for catheter tracking to the best of our knowledge. This high-accuracy tracking has various applications which range from image reconstruction for the identification of fine anatomical details, such as microchannels for crossing arterial occlusions, to precise tool guidance, such as laser ablation. References: Zhou et al. (2022): 5812-5823, Sewani et al. TMI.2023.3309781.

Oral Presentations 4: Deep Learning/Machine Learning Methodology 1

Abstracts

Foundation Models for Cancer Tissue Margin Assessment with Mass Spectrometry

Mohammad Farahmand¹, Amoon Jamzad¹, Fahimeh Fooladgar², Laura Connolly¹, Martin Kaufmann¹, Kevin Yi Mi Ren¹, John Rudan¹, Doug McKay¹, Gabor Fichtinger¹, Parvin Mousavi¹

¹Queen’s University, Kingston, Canada

²The University of British Columbia, Vancouver, BC, Canada.

INTRODUCTION: Rapid Evaporative Ionization Mass Spectrometry (REIMS) is a critical tool for intraoperative margin assessment during cancer surgeries, providing metabolic profiles for tissue analysis. Classifying the complex resulting spectra is only possible through machine learning models. The scarcity of labeled data in surgical contexts, however, limits the utility of such models. Foundation models, known for their ability to generalize from pretraining on large datasets, offer a promising solution to this challenge by leveraging learned representations that work well on downstream tasks even when finetuned with a small dataset. This potential is best exemplified when the foundation model was pretrained on a similar modality to that of the downstream task. While currently there are no foundation models tailored to REIMS data, this study evaluates three models from related modalities—DreaMS [1], CLIP [2], and CLAP [3]. These models were selected based on their adaptability and compatibility with REIMS data. The latter two were considered over alternative image / audio encoders due to the model’s inherent support for additional text prompts, which can be of considerable use in future studies.

METHODS: To assess the suitability of DreaMS, CLIP, and CLAP for REIMS data, we conducted a finetuning-only evaluation using a labeled dataset of 693 spectra (252 cancerous and 441 benign), collected in a Basal Cell Carcinoma (BCC) study. The dataset included samples collected during and after BCC resection surgeries. REIMS data were preprocessed to normalize intensity, calibrate masses, and select features in the 100–1000 m/z range. To expand the training data, we applied intensity-aware augmentation, simulating calibration errors and introducing controlled noise to dominant peaks. Each backbone was adapted to process REIMS spectra. For DreaMS, a tokenizer originally designed for tandem mass spectrometry was employed, despite its reliance on fragmentation patterns absent in REIMS data. CLIP was modified to handle REIMS spectra by converting the data into image-like representations, mimicking CLIP’s original text-image association framework. For CLAP, the spectral similarities between REIMS and audio Mel-spectrograms allowed us to directly map REIMS spectra onto CLAP’s input space. We stack a randomly initialized MLP head on each model for binary classification. We used weighted sampling to account for the imbalance in the data and trained the models using AdamW optimizer ($\eta = 10^{-4}$).

RESULTS: The performance of the foundation models after finetuning is summarized in the Table 1. As shown in the table, these models consistently outperform PCA-LDA, a common baseline for REIMS data in literature. Both CLIP and DreaMS outperform the baseline statistically significantly (one-tailed Wilcoxon signed-rank test, p -value < 0.05) in terms of both balanced accuracy and AUROC, but the difference between these two is not significant. Furthermore, while CLAP fails to perform as well as CLIP and DreaMS in terms of balanced accuracy, its AUROC is still significantly higher than the baseline, and the model’s inherent design for sequential data necessitates further examination of this model.

CONCLUSION: This study highlights the viability of foundation models like CLIP and DreaMS for REIMS data classification. The promising results from finetuning alone suggest that, based on the current literature on foundation models and precedents set by cases like SAM and MedSAM, with further pretraining on in-modality data, these foundation models can be expected to perform even better. Future work will focus on developing pretraining pipelines to better align these models with the intricacies of REIMS data, as well as the possibility of utilizing text prompts to provide additional context to the models for more precise classification.

REFERENCES: [1] Radford A, Kim JW, Hallacy C, Ramesh A, Goh G, Agarwal S, Sastry G, Askell A, Mishkin P, Clark J, Krueger G. Learning transferable visual models from natural language supervision. In International conference on machine learning 2021 Jul 1 (pp. 8748-8763). PMLR. [2] Elizalde B, Deshmukh S, Al Ismail M, Wang H. Clap learning audio concepts from natural language supervision. In ICASSP 2023-2023 IEEE International Conference on Acoustics, Speech and Signal Processing (ICASSP) 2023 Jun 4 (pp. 1-5). IEEE. [3] Bushuiev R, Bushuiev A, Samusevich R, Brungs C, Sivic J, Pluskal T. Emergence of molecular structures from repository-scale self-supervised learning on tandem mass spectra.

	Balanced Accuracy	Sensitivity	Specificity	Area Under ROC
PCA-LDA	69.7% \pm 2.3	66.0% \pm 3.3	73.5% \pm 1.7	73.9% \pm 1.3
DreaMS	74.0% \pm 1.9	71.4% \pm 7.6	76.5% \pm 6.3	83.1% \pm 1.4
CLIP	75.5% \pm 2.0	75.2% \pm 7.2	81.1% \pm 9.9	82.9% \pm 1.8
CLAP	71.9% \pm 1.6	65.8% \pm 5.0	78.0% \pm 5.3	78.1% \pm 2.3

Table 1. The performance of the foundation models and PCA-LDA baseline, finetuned on BCC data.

From Text to Insight: Classifying Microcalcifications in Radiology Reports with AI

Zardar Khan¹, Grey Kuling², Anisa Karim¹, Anne L. Martel^{1,2},

¹Physical Sciences, Sunnybrook Research Institute, ²Dept of Medical Biophysics, University of Toronto, Toronto, ON, Canada

Introduction: Radiology departments generate millions of unstructured free-text reports containing valuable clinical information including cancer history, imaging modalities, and examination types, presenting significant untapped potential for research cohort discovery in breast imaging. However, manually extracting and analyzing this information remains time-consuming and prone to human error. The Breast Imaging Reporting and Data System (BI-RADS), developed by the American College of Radiology, provides standardized reporting guidelines that add inherent structure to these reports [1]. In this study, we focus specifically on automating the extraction of microcalcification information – a crucial indicator for early breast cancer diagnosis and treatment planning. Inspired by recent advances in artificial intelligence, particularly in natural language processing, we explored automated approaches to extract this structured information from these reports.

Methods: We evaluated three approaches to classify microcalcification status in breast imaging reports. The first two employed supervised learning with encoder models and classification heads to label patient status as positive, negative, or not stated. The first approach [2] included segmenting reports according to BI-RADS structure to reduce input sequence length into BERT, a bi-directional encoder model that captures the context of words in all directions [2]. The second approach employed RadBERT, a model pre-trained on 4M radiology reports, processing reports with 512-token truncation. Our third approach explored zero-shot and few-shot capabilities of Large Language Models (LLMs) including Yi-34B, Mixtral 8x22B (MoE), Meditron-70B and Qwen-72B, all sourced from the HuggingFace repository [3]. These LLMs are known for their extensive pre-training on vast and diverse datasets. We evaluated LLM performance using unnormalized log likelihood scoring, while encoder models were assessed using classification accuracy.

Results: Performance varied across approaches, with encoder models achieving the highest accuracy. As shown in Figure 1, Yi-34B demonstrated strong baseline performance with 76% zero-shot accuracy, improving to 79% with few-shot learning. Other LLMs showed mixed results: Qwen-72B (46% to 60%), Mixtral 8X22B (50% to 72%), and Meditron-70B (72% zero-shot, declining to 34% few-shot, 61% with prompt-tuning). BERT models demonstrated superior performance, with Gatortron and RadBERT achieving 94% weighted accuracy, while the AWD-LSTM baseline reached 75%. Few-shot experiments were conducted for models showing promising initial performance and deployment feasibility.

Conclusions: Our study demonstrates that relying less on structured preprocessing and more on the latent capabilities of LLMs offers promising results for medical text classification. While BERT-based models achieved the highest accuracy at 94%, the strong performance of Yi-34B (79% accuracy) with minimal tuning suggests that it may be a more efficient path for medical NLP deployment. Notably, larger parameter counts did not necessarily equate to better performance, as evidenced by Yi-34B outperforming larger models. Transformer-based architectures consistently outperformed traditional LSTM approaches in this medical text classification task. Future research will focus on optimizing these models for broader medical applications while maintaining deployment efficiency.

Acknowledgements: A special acknowledgment to the Biomatrix Team, Sunnybrook Research Institute, and the Information Management Team, Sunnybrook HSC. **References:** [1] (www.acr.org/Clinical-Resources/Reporting-and-Data-Systems/Bi-Rads) [2] BI-RADS BERT and Using Section Segmentation to Understand Radiology Reports (2022), Kuling et al. [3] (<https://huggingface.co/models>).

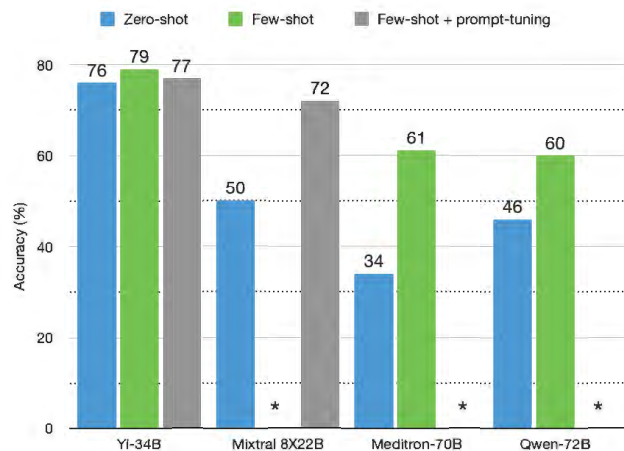


Figure 1 Performance comparison of LLMs (Yi-34B, Qwen-72B, Mixtral 8x22B [MoE], Meditron-70B) on microcalcification classification. Accuracy (%) shown for zero-shot, few-shot, and few-shot + prompt-tuning approaches. Asterisk (*) indicate experiments not conducted due to resource constraints or initial performance considerations.

Automatically segmenting curved catheters in prostate brachytherapy ultrasound images with a deep learning and feature extraction pipeline

Jessica de Kort^{1,2}, Nicole Kitner³, Tamas Ungi³, Martin Korzeniowski⁴, Timothy Olding⁴, Parvin Mousavi³, Gabor Fichtinger³, and Jessica R. Rodgers¹

¹ Department of Physics and Astronomy, University of Manitoba, Winnipeg, Manitoba

² Department of Physics, University of Winnipeg, Winnipeg, Manitoba

³ School of Computing, Queen's University, Kingston, Ontario

⁴ Department of Oncology, Queen's University, Kingston, Ontario

Introduction: Prostate cancer is the leading cancer in males, where one treatment option is high-dose-rate brachytherapy (HDR-BT). HDR-BT involves inserting multiple catheters (typically 16–18) into the prostate and surrounding tissues. A radioactive source is then passed through these catheters to target and destroy cancer cells. Transrectal ultrasound (TRUS) imaging is commonly used to guide catheter placement, however, due to shadowing artifacts, small catheter diameter, and natural bending of the catheters upon insertion, accurately locating catheters inside TRUS image slices can be challenging and time-intensive. To minimize risks associated with prolonged anesthesia, integrating intraoperative tools to improve procedure efficiency is essential. The study's objective was to extend a previous deep-learning and feature extraction pipeline to the identification of curved catheters in three-dimensional (3D) TRUS images.

Methods: The pipeline was uploaded into 3D Slicer software as a custom-made module. The module processed TRUS images using a 3D U-Net architecture, generating point-cloud predictions that provided segmentations at each point within the images. These point-cloud outputs were refined using a 3D Hough transform to identify curved catheter shafts, and curve-fitting was applied to create smooth, continuous catheter predictions. The pipeline was trained on 67 different patient datasets, while testing the pipeline used 21 patients. Each patient's data contained 3D TRUS images and ground truth catheter, manually identified by medical physicists which were compared to predictions from the pipeline (Fig. 1). The overlap between predictions and ground truths was assessed, and the Hausdorff distance (HD) was calculated for each catheter to measure the maximum distance between a ground truth point and its nearest predicted point.

Results: After refinement with curve fitting, predictions were produced in about 30 s/patient. The average Dice coefficient was 0.42 ± 0.17 ($n = 343$), indicating a moderate pixel-wise overlap between the predicted and ground truth catheters, suggesting the need for further refinement. The average position difference for the catheter shafts was 1.9 ± 0.1 mm, while the average tip difference was 3.0 ± 0.4 mm. The maximum tip difference for the curved catheters ($n = 343$) was 3.2 ± 1.5 mm (Fig. 2), requiring further refinement. Despite the need for improved tip identification, the catheters showed good overall agreement, with an average Hausdorff distance of 1.4 ± 0.6 mm.

Conclusions: Future studies will aim to improve catheter tip identification errors. The deep learning and feature extraction pipeline for automatically segmenting HDR-BT catheters can help shorten procedure times, thereby minimizing risks associated with prolonged anesthesia and improving the clinical workflow by reducing human uncertainties.

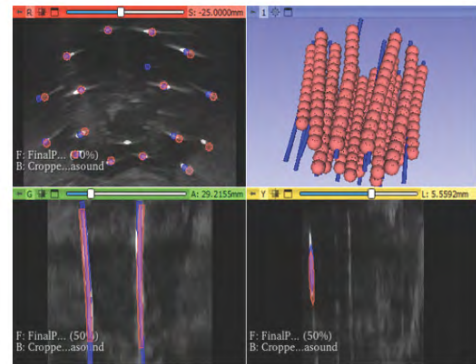


Fig. 1: Ground truth catheters (pink) and predicted catheters (blue) overlaid in 3D TRUS images with corresponding anatomical slices.

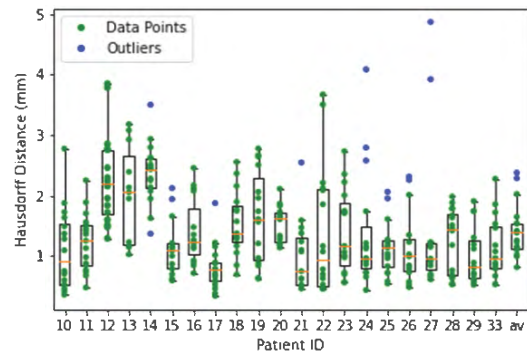


Fig. 2: Boxplot representing the average HD for each catheter for each test patient ($n = 21$), where 'av' is the overall average across all catheters in all patients, the orange line is the median value, and the box represents the interquartile range

Evaluating the use of automatic workflow recognition for central venous catheterization training

Catherine Austin, Rebecca Hisey, Denise Wong, Bining Long, Gabor Fichtinger

Laboratory for Percutaneous Surgery, School of Computing, Queen's University, Kingston, Canada

Introduction: Comprehensive feedback is crucial in medical education, yet time constraints often limit the feedback supervisors can provide, which leaves medical students lacking in the amount of feedback they receive. To address this, the video-based training system Central Line Tutor was designed to deliver real-time guidance for Central Venous Catheterization (CVC) without requiring expert oversight [1]. Central Line Tutor achieves this by identifying upcoming steps and procedural errors using workflow recognition. This study evaluates the effectiveness of this workflow recognition method against multiple expert reviewers in order to determine its viability in acting as an expert substitute.

Methods: Ten participants, consisting of five experts and five medical students, each performed CVC for ten trials using the Central Line Tutor system. The system used a webcam to record each participant's trials and collected the position data of tools such as the ultrasound probe and needle using an electromagnetic tracking system. Each recording was labeled by four independent human reviewers with the times at which each task occurred. A ground truth for the task labels was established by finding the average time at which the reviewers labelled each task. TeCNO, a multi-stage temporal convolutional network used for surgical workflow recognition, was adapted for our workflow recognition system [2]. The network was trained with the individual frames from each recording and their corresponding ground truth task labels using a leave-two-user-out cross-validation scheme for five total folds. To evaluate our workflow recognition's performance, the task labels predicted by the network were compared to those of the reviewers by comparing the number of frames assigned to each task by the network and the reviewers.

Results: The overall test accuracy of the network was 0.842. How well the network was able to predict each task is shown by the confusion matrix in Figure 1. The network performed best when identifying the cross-section ultrasound scan task.

Conclusions: When compared to an average assessment from multiple expert reviewers, the network was able to reliably identify the majority of tasks in the workflow. This shows that the Central Line Tutor workflow recognition system is a promising substitute for expert supervision. Tasks that used similar tools or movements to those of other tasks were more likely to mislabelled; this was especially true for the shortest tasks in the workflow. By experimenting with different data sampling techniques on a larger dataset when training the network, the accuracy of the poorest performing tasks could be improved in future work.

References: [1] Hisey R, Camire D, Erb J, Howes, Fichtinger G, Ungi T. System for central venous catheterization training using computer vision-based workflow feedback. *IEEE Transactions on Biomedical Eng.* 2021 Nov. 2

[2] T. Czempiel *et al.*, "Tecno: Surgical phase recognition with multi-stage temporal convolutional networks," *MICCAI 2020*, pp. 343–352, Mar. 2020. doi:10.1007/978-3-030-59716-0_33

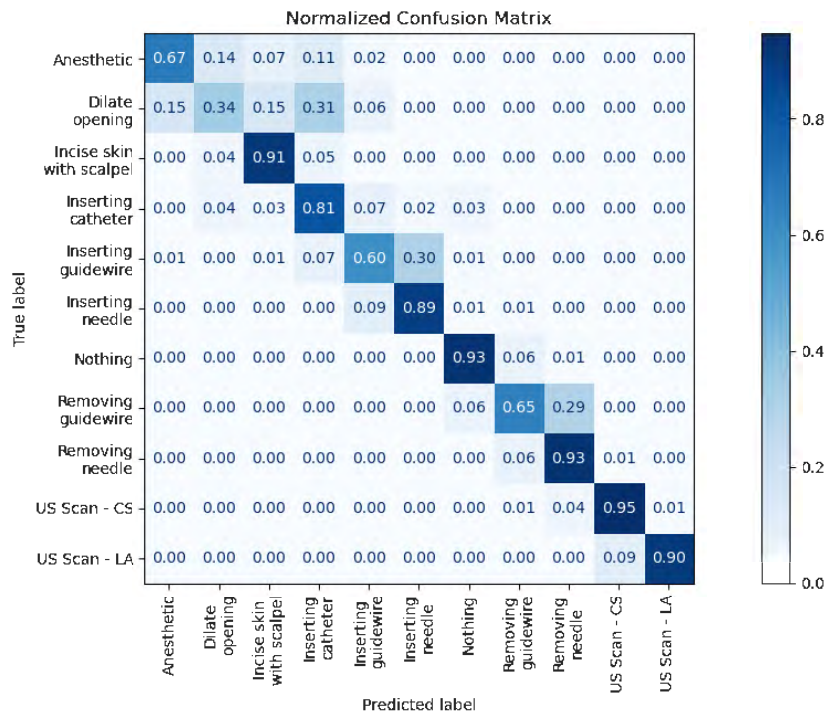


Figure 1. A normalized confusion matrix showing the network's ability to predict each task.

Pitches 3: Device, Systems, and Robotic Development

Abstracts

Design and Ergonomic Assessment of Steerable Catheter Handles for the CathPilot System

Sina Keshavarz^{*1,2}, A. Sewani^{1,2}, R. Gilliland-Rocke^{1,2}, A. Dueck², M. Ali Tavallaei^{1,2}

¹Toronto Metropolitan University, Toronto, Canada, ²Sunnybrook Health Sciences Centre, Toronto, Canada

Introduction Atherosclerosis, a leading cause of heart disease and stroke, often progresses to peripheral artery disease (PAD), affecting over 200 million people worldwide. Despite advancements in minimally invasive endovascular interventions like angioplasty, these procedures face up to a 20% failure rate due to challenges in maneuverability within patient-specific vascular structures. Our previous work on CathPilot, a novel steerable catheter, showed promise in addressing these issues [1]. This study aims to design and ergonomically evaluate various catheter handles for the CathPilot.

Methods Based on anthropometric data spanning from the 5th percentile female to the 95th percentile male, we developed three catheter handle prototypes (as shown in the Figure below):

Design A: Features perpendicular handle design where the handle is perpendicular to the catheter shaft.

Design B: Mimics conventional catheters with the catheter handle in parallel to the catheter shaft.

Design C: Mimics a pilot joystick with a 90-deg and perpendicular to the catheter shaft.

Each handle was 3D printed and integrated with a catheter (12 Fr, 70 cm in length). A joystick circuit (ElecGear EL1 ALPS) was embedded within the handle and connected to an Arduino UNO for user joystick manipulation to simulate the GUI of the CathPilot system and its corresponding tracking. A Python-based graphical user interface provided real-time feedback on catheter tip movements based on user input. Ergonomic assessments included a formative phase with 8 biomedical engineers to refine designs and a summative phase with 10 clinicians using the System Usability Scale (SUS), NASA Task Load Index (NASA-TLX), and hand anthropometry to evaluate comfort and ease of use during simulated navigation.

Results Design A demonstrated superior ergonomics with minimal stress on the hypothenar and palmar regions and reduced wrist deviation. SUS scores averaged 85 out of 100, indicating high user satisfaction. Participants reported enhanced directional control and comfort with prolonged use. The straight handle was deemed unintuitive, causing forearm fatigue and scoring an average SUS of 60. The pilot handle was found to be bulky with limited movement, receiving an average SUS of 55. User-reported feedback indicated that designs B and C induced higher perceived stress on the wrist and distal phalanx of the thumb compared to design A. Furthermore, Design A gained a significantly higher NASA-TLX score of 80.47, reflecting lower workload and higher comfort.

Conclusion Design A outperformed the other prototypes in ergonomic assessments and user satisfaction, suggesting its potential to improve maneuverability and outcomes in endovascular interventions. Future work will integrate this handle with a steerable catheter for further evaluations, assessing procedural success based on handle design and feasibility.

References

[1] James Zhou et al., "The CathPilot: A Novel Approach for Accurate Interventional Device Steering and Tracking", IEEE/ASME Transactions on Mechatronics, 2022

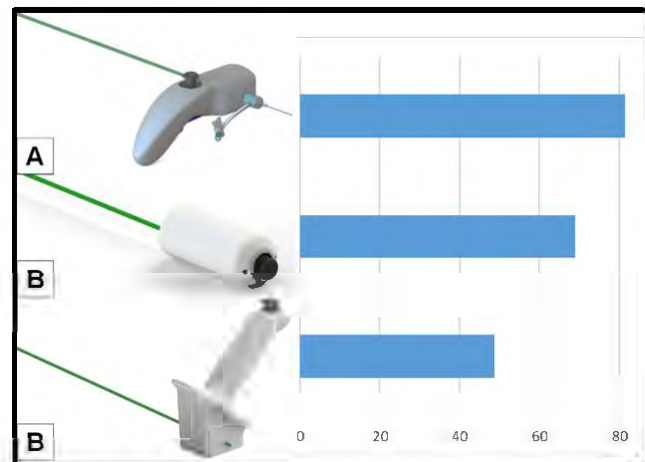


Figure. Catheter handles and corresponding SUS scores are shown **A.** Perpendicular to catheter handle design, **B.** Parallel to catheter handle design, **C.** Pilot joystick perpendicular to catheter.

Validation of 3D Ultrasound Musculoskeletal System

Clara Duquette-Evans^{a,b}, Megan Hutter^{a,b}, Randa Mudathir^{a,b}, Aaron Fenster^{a,b}, Emily Lalone^b

^aRobarts Research Institute, 100 Perth Drive, London, ON, Canada N6A 5K8; ^bWestern University, 1151 Richmond Street, London, ON, Canada N6A 3K7

Introduction: Musculoskeletal disorders (MSDs), damaging the muscles, bones, joints, and surrounding connective tissues, are the leading cause of disability worldwide.¹ Early diagnosis and consistent monitoring of MSDs are important in ensuring the best possible outcomes for patients,² making point-of-care imaging an invaluable tool. Ultrasound (US) imaging is accessible, safe, and effectively visualizes soft-tissue anatomy and bony contours.² 3-dimensional ultrasound (3D US) allows 3D visualization of anatomy, providing physicians with volumetric images and allowing them to “scroll” through areas of interest. It also permits clinicians to obtain volumetric measurements, such as synovial effusion or changes in blood flow, from patient scans. Our lab has developed a 3D US musculoskeletal imaging system, equipped with a mechatronic counterbalanced arm that supports a 3D US-based linear motorized scanner and allows tracking of the 3D US probe (Canon 14L5, frequency of 10MHz). This capability provides a method to fuse multiple acquired 3D US images into a larger view. The objectives of the following research are to evaluate both the accuracy of the mechatronic arm’s tracking and of the volumetric measurements in the fused 3D US images.

Methods: Experiments with agar-based phantoms containing varying inclusions were conducted. In the first, a phantom containing 5 embedded spherical inclusions was imaged from varying positions with the 3D US system. Coordinates for each of the inclusions visible in the tracked images were recorded, and the target registration error (TRE) was calculated (from 7-11 images, depending on the inclusion). In the following experiment, a phantom containing a semi-cylindrical inclusion was made, and 3D US images were acquired and fused. Manual segmentation of the inclusion was repeated 8 times by one observer, and the percent error between the segmented volume and true volume was determined.

Results: In the tracked images, the fiducials’ overall TREs and coordinate component TREs in the X, Y, and Z direction were calculated to be <2.02mm, demonstrating consistent tracking by the system. The volumetric measurements obtained from the manual segmentation of the semi-cylindrical inclusion also showed strong agreement to the true volume. The average error between the segmented volume and true volume, as determined by a water-displacement test, was 4.67%.

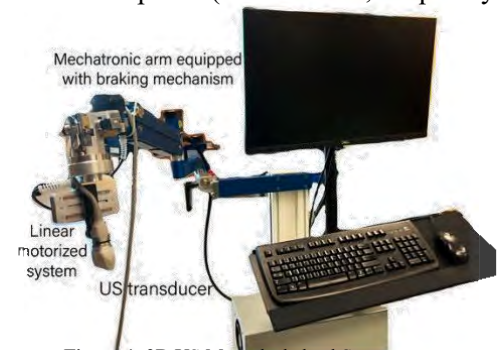


Figure 1. 3D US Musculoskeletal System

Table 1. TRE and its three coordinate components, for the 5 fiducials

5.5cm				
Fiducial	Coordinate Component TRE (mm)			Overall TRE (mm)
	X	Y	Z	
1	0.48	0.12	1.08	1.19
2	0.85	0.19	1.47	1.71
3	0.97	0.36	1.73	2.02
4	0.64	0.49	1.26	1.49
5	0.99	0.26	1.69	1.98
7.5cm				
Fiducial	Coordinate Component TRE (mm)			Overall TRE (mm)
	X	Y	Z	
1	0.40	0.19	1.15	1.23
2	1.28	0.26	1.14	1.73
3	0.83	0.25	0.99	1.32
4	1.03	0.26	1.03	1.48
5	1.37	0.31	1.18	1.84

Table 2. Manually segmented volumes and error (%)

	Manually Segmented Volume (cm ³)	Error (%)
1	6.23	5.5
2	6.31	4.2
3	6.34	3.8
4	6.20	5.9
5	6.38	3.2
6	6.24	5.3
7	6.24	5.3
8	6.27	4.9

Conclusions: The results of this work describe the tracking and fusion by the 3D US musculoskeletal system. The low TREs in the tracked images and feasibility of obtaining accurate and precise measurements from the fused images support the continued validation of the system. This work points to the system’s eventual clinical translation and indicates its potential as a tool to reliably image soft-tissue structures in MSDs.

References:

1. World Health Organization. (2022, July 14). *Musculoskeletal Health*. <https://www.who.int/news-room/fact-sheets/detail/musculoskeletal-conditions>
2. Chen, W., Zhang, Y., Wang, X., Liu, J. (2024). Comparative Analysis of Imaging Modalities for Diagnosing Musculoskeletal Disorders. *Journal of Innovations in Medical Research*, 3(1), 45-53. doi: 10.56397/JIMR/2024.03.06

Multi-material hand fracture model for spatial learning

Trinette Wright¹, Stephanie Williams¹, Jimmy Qiu¹, Blake Murphy^{2,4}, Stefan Hofer^{3,4}, Joseph Catapano^{2,4}

¹Techna, University Health Network, Toronto, Ontario; ²Unity Health Toronto, Toronto, Ontario;

³University Health Network, Toronto, Ontario; ⁴University of Toronto, Toronto, Ontario

Introduction: Surgical intervention for hand fractures can be challenging for new learners and residents due to limiting factors in a traditional surgical education program. These include spatial understanding and visualization for alignment and reduction of fractures, use of fluoroscopy, technical use of instruments, and access to cadavers or realistic models for skills practice and improving proficiency. In this work, we present a reproducible method for creating a multi-material hand fracture model for Bennett's and 5th metacarpal shaft fracture utilizing 3D printing, silicone casting, and electromagnetic (EM) tracking, enabling quantitative evaluation of fracture reductions in competency-based education.

Methods: CT images of a healthy hand were segmented to create a 3D reference mesh model of bones and skin. A Bennett's and 5th metacarpal shaft fractures were artificially added, with skin mesh updated to match displacements. Bone meshes were prepared for 3D printing and EM integration, including fracture bridging, through-holes for silicone adhesion, wire channels, fiducials, and a baseplate for mold alignment. A 2-part mold was designed, with added alignment and silicone pouring holes.

The bone and mold pieces were 3D printed using a Prusa i3 MK3S+. NDI Aurora 6 degree-of-freedom EM sensors were set and glued into wire channels before rigid registration was completed, enabling position and orientation measurements of the hand, thumb, and 5th metacarpal shaft. Flex Foam-iT was cast around fracture bridging points for realistic movement and compression. The hand with sensors was secured into the mold, followed by silicone skin casting (EcoFlex 00-30).

To evaluate 3D print reproducibility, four partial thumb and index sets were printed and scanned via CT. Segmented meshes were aligned and printing errors analyzed via Hausdorff distance in MeshLab. For feasibility of EM tracking, three hands with fiducials were fabricated, and point-based rigid registration was performed using paired points between NDI Aurora and model fiducials.

Results: The average mean Hausdorff distance values were 0.11mm and 0.12mm for the index and thumb post mesh alignment with reference CT, within 0.3mm printing tolerance of the Prusa i3 MK3S+. Average fiducial registration errors across the three hands were 0.55mm, 0.69mm, and 0.74mm for hand, thumb, and pinky respectively between model fiducials and the NDI Aurora system.

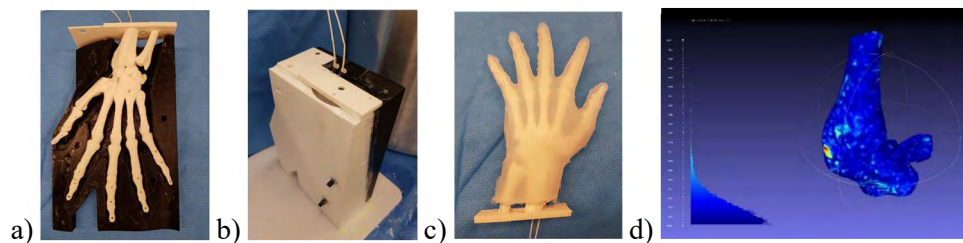


Figure 1. a) 3D printed hand seated in mold; b) silicone casting of 2-part mold with bone; 3) completed hand with silicone skin and sensors; d) Hausdorff distance between thumb-index meshes and reference

Conclusions: This work demonstrates a reproducible pipeline for creating a multi-material hand fracture model with rigid bone and soft tissue silicone. By incorporating EM sensors into the casting process, bony anatomy motion can be tracked and measured, enabling quantitative assessment of learner's clinical skill in a controlled and reproducible case scenario such as fracture reductions in support of competency-based education programs.

A Preclinical SPECT System Using Ultrahigh Energy Resolution CZT Detectors for Alpha and Beta Emitter Radiopharmaceutical Therapy Imaging

Dr. Can Yang^{1,2}, Dr. Ching Fong¹, Ansong Qin¹, Xiaopei Huang¹, Dr. Zhonghua Ouyang¹, Dr. Sengeeta Ray⁵, Dr. George Sgouros⁵, Dr Yong Du⁵, Dr. Lingjian Meng^{1,2,3,4}

¹MH3D Inc. Ann Arbor, MI, ²Department of Nuclear, Plasma, and Radiological Engineering, ³Department of Bioengineering, ⁴Beckman Institute for Advance Science and Technology, University of Illinois at Urbana-Champaign, Urbana, IL, USA, ⁵Radiology and Radiological Science at Johns Hopkins, School of Medicine, Baltimore, MD

Introduction

This study introduces a commercially developed single photon emission computed tomography (SPECT) system utilizing cadmium zinc telluride (CZT) detectors with ultrahigh energy resolution, designed specifically for preclinical imaging and precise quantification of alpha, beta emitter radiopharmaceuticals based on prior work [1]. This system aims to address the shortage of preclinical SPECT systems capable of identifying densely populated gamma- and X- rays while providing high sensitivity. The Alpha-SPECT MiniTM system delivers superior energy efficiency and field of view, meeting critical needs in radiopharmaceutical drug development. Additionally, it enables precise quantification of multiple energy peaks and demonstrates consistent reproducibility, making it well-suited for commercial applications.

Methods

The Alpha-SPECT MiniTM system consists of a main device gantry housing the CZT detectors, an animal bed system connected to imaging cells, an integrated cooling system, and a controller PC for data acquisition and image processing. A total of 3 experimental trials were conducted using ²²⁵Ac, ¹⁷⁷Lu, and ²²³Ra respectively. In experiment 1, 2 μCi of ²²⁵Ac was injected intravenously, and images were acquired at 4 hours and 24 hours post injection. In experiment 2, 300 μCi of ¹⁷⁷Lu was injected intravenously, and dynamic imaging was performed at 5 minutes post injection. In experiment 3, 1 μCi of ²²³Ra was injected intravenously, and images were taken 10 minutes, 40 minutes, 3h, and 24h post injection.

Results

In all three experiments, we successfully reconstructed 3D images that revealed identifiable organ structures, including the liver, kidneys, bladder, and spinal vertebrae. Notably, in Experiment 1, reconstructions were performed using five different energy peaks (80 keV, 100 keV, 117 keV, 218 keV, and 440 keV, Figure 1). Quantification was conducted in all three experiments.

Mouse Ac-225 2μCi Image 4h/24h post injection (1h imaging)

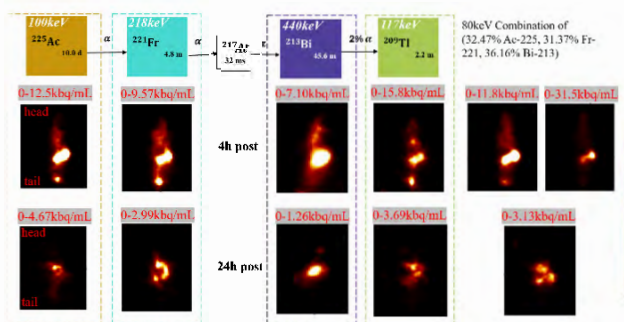


Figure 1 Ac-225 3-D Reconstruction and Activity Quantification

Conclusion

In this work, we present a preclinical SPECT system equipped with high-sensitivity CZT detectors, designed to enable precise imaging and quantification of alpha and beta emitter radiopharmaceuticals.

Reference

- [1] C. Yang *et al.*, “An Ultrahigh Energy Resolution SPECT System for Quantitative Preclinical Imaging of Targeted Alpha Therapy,” *J. Nucl. Med.*, vol. 64, no. supplement 1, pp. P1559–P1559, Jun. 2023

Design Optimizations of an Expandable Cable-Driven Parallel Mechanism for Minimally Invasive Cardiovascular Interventions (CathPilot)

Sina Keshavarz^{*1,2,3}, James Zhou³, Alykhan Sewani³, M. Ali Tavallaei^{1,2,3}

¹ Toronto Metropolitan University, Toronto, Canada, ² Sunnybrook Health Sciences Centre, Toronto, Canada, ³ Magellan Biomedical, Toronto, Canada,

Introduction Peripheral arterial endovascular revascularization procedures face technical failures of up to 20%. Effective navigation of narrow tortuous vessels and interaction with target anatomy is limited with existing tools. To address these challenges, our team has previously introduced CathPilot system [1, 2]. However, initial designs faced challenges, including high mechanical complexity of the handle and, therefore, high costs, robustness, and, most importantly, sterilization of all complex components within the handle. In this work, we present major and novel design revisions to address these limitations.

Methods The design of CathPilot was guided by key clinical and engineering inputs: sterility, modularity, minimal user input force, ergonomic operation, and cost efficiency. To address this, we propose splitting the system into two main components—a reusable handle portion and a disposable single-use catheter.

The reusable handle houses the complex cable manipulation and tracking mechanisms previously described in [1, 2]. To transfer the user input to the single-use catheter, various coupling mechanisms were explored to efficiently transfer torque with the constraint of maintaining the sterility of the reusable handle. Magnetic coupling was chosen as it allowed for contactless torque transfer and physical isolation for sterility. The interface is designed to be modular and allows for connecting to various catheters regardless of frame size and shape. In the current version, the single-use catheter portion includes the catheter and a self-expandable frame currently miniaturized to fit within a 7 Fr sheath. Brakes on each cable shaft were integrated into the single-use portion to allow for coupling/decoupling without disruption of cable tension and catheter alignment. Preliminary evaluations were performed to assess system functionality, coupling and decoupling, and workspace coverage.

Results Qualitative benchtop tests showed that the proposed magnetic coupling effectively transfers steering inputs to the single-use catheter, allowing for full workspace coverage. The users were able to repeatedly engage and disengage the modules with consistent performance. Sterility was addressed by covering the reusable handle within a plastic sterile cover and maintaining isolation during the operation of the system. Force evaluations confirmed that the max required input force was consistently below 13 N, which is within ergonomic ranges, reducing clinician fatigue and enhancing procedural efficiency. Additionally, the friction on the disposable side was halved to below 100 mN compared to previous designs.

Conclusion The proposed design modification addresses key challenges of sterility, cost, and modularity. This separation is accompanied by design optimizations to reduce friction and required input force, improving clinician control and patient outcomes. Future verification and validation studies will assess the device's accuracy, tracking, and feasibility.

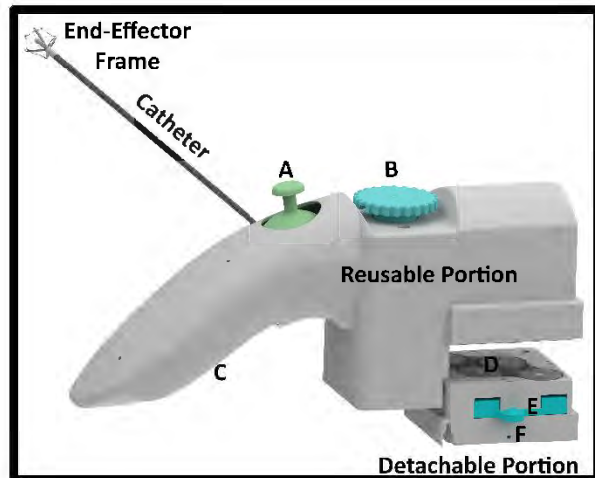


Figure. The revised design of the CathPilot system is shown. The reusable handle features the cable tensioning mechanisms, the circuitry for cable displacement measurements, and a thumb-stick for capturing user input (A), a tension adjustment knob (B), and batteries placed within the base of the handle (C). The detachable section connects via magnetic coupling, transferring user input through magnetic pulleys (D); removable brakes (E) must be disengaged before operation. An entry hole (F) allows introduction of guidewires/microcatheters.

[1] James Zhou et al. "The CathPilot: A Novel Approach for Accurate Interventional Device Steering and Tracking", IEEE/ASME TM, 2022

[2] James Zhou et al. "The CathPilot: Performance Validation and Preclinical Safety and Feasibility Assessment," TBME, 2023

[3] Sina Keshavarz et al. "A Self-Expandable Nitinol Frame for Cable-Driven Parallel Mechanisms~," JMBBM, 2024

Developing low-cost 3D-printed prosthetics with a functional wrist for patients along the Thai-Myanmar border

Emese Elkind¹, A. T. Tun², O. Radcliffe¹, L. Connolly¹, C. Davison¹, E. Purkey¹, P. Mousavi¹, G. Fichtinger¹, K. Thornton²

¹Queen's University, Kingston, Canada, ²Burma Children Medical Fund, Mae Sot, Tak, Thailand

INTRODUCTION: Inadequacies in the Burmese healthcare system, heightened by the 2021 military coup and related civil war in Myanmar and the COVID-19 pandemic, have contributed to an influx of refugees to Thailand to seek medical aid. An estimated 1.5 million Myanmar nationals entered Thailand since January 2023 [5]. Without immigration status, these refugees are unable to receive healthcare. Burma Children Medical Fund (BCMF) is a nonprofit based in Mae Sot, Tak, Thailand that focuses on funding underserved Burmese communities' medical treatment and providing support services, including accessible prosthetics for refugees who have experienced limb loss [1]. Prosthetics in lower-income countries are usually passive, meaning they lack mechanisms to restore critical limb functions such as gripping, rotation, or complex hand movements. Therefore, patients cannot fully perform their daily functions, impacting their abilities to work and affecting family caretakers. BCMF aims to make prosthetics that work best in low-resource settings using open-source designs, which only allow for fixed hand positions. The usage of prosthetic arms depends heavily on their functionality and comfort. Patients are more likely to consistently use prosthetics if it aids them in returning to normalcy. In this study, we present a design for an interchangeable and functional prosthetic wrist that enables critical hand motions such as rotation.

METHODS: BCMF currently provides custom-fitted, low-cost, 3D-printed prostheses that are found on Thingiverse, a public library of 3D designs. One such design is the Kwawu Arm 2.0 [2], which can be adjusted with OpenSCAD [4], a software for modifying 3D CAD models to fit the recipient's measurements. To maintain BCMF's workflow, the interchangeable wrist model was created using the 3D design software, Autodesk Fusion 360, and designs from open sourced Quick-Connect Wrist (QCW) designs found on Thingiverse [3]. The wrist was merged onto the Kwawu Arm, printed, assembled, and tested for durability and comfort both with and without patients. This is an iterative process where patient feedback ensures the prosthetics cater to the diverse needs of the recipients.

RESULTS: Since the launch of the prosthetics project in 2019, BCMF has provided 3D-printed prosthetics to almost 80 patients, one of whom is wearing the functional wrist (Fig.1). The interchangeable hand provides a solution to many patients' everyday activities, featuring 360-degree rotation by pressing a button in the QCW and twisting their gripper hand (Fig.2). Patients carry litres of water to test the durability of the arm and success is measured in patient satisfaction. This arm bridges the gap between open-sourced models and patient needs.

CONCLUSIONS: The BCMF prosthetics project provides a low-cost solution to healthcare challenges in the context of poly-crisis experienced in Myanmar, enhancing the resilience and adaptability of affected refugee communities. The collaboration between BCMF and Queen's University demonstrates the potential for future partnerships between educational institutions and NGOs to address health care access disparities. Future work includes continuing to fill the gap between open-sourced models and patient-specific needs to refine the 3D-printing workflow by continuing to create customizable, generalized designs. We also plan to test the interchangeable wrist with more patients and develop body-powered prosthetic designs to support more critical movements. This work advances low-resource medical device innovation by improving passive prosthetics.

REFERENCES: [1] *Burma Children Medical Fund - Mae Sot, Thailand*. BCMF | Burma Children Medical Fund - Mae Sot, Thailand - Operating to give people a future. (n.d.). <https://burmachildren.com/> [2] Buchanan, J. (2018, March 27). *Kwawu Arm 2.0 - Prosthetic - socket version*. Thingiverse. <https://www.thingiverse.com/thing:2841281> [3] NIOP. (2022, February 9). *NIOP Q-C VI quick-connect wrist*. Thingiverse. <http://www.thingiverse.com/thing:5238794> [4] *OpenSCAD*. The Programmers Solid 3D CAD Modeller. (n.d.). <https://openscad.org/> [5] UN. *Overview of Myanmar nationals in Thailand*. IOM UN migration. <https://thailand.iom.int/sites/g/files/tmzbd1371/files/documents/2024-10/overview-of-myanmar-nationals-in-thailand-october-24.pdf>



Fig. 1: BCMF patient using the QCW with the existing open-sourced 3D-printed prosthetic arm.



Fig. 2: Different hand attachments that are suitable for the arm with a 360 degrees rotation. Left to right: Utensil holder, bicycle attachment, gripper hand (neutral and 90 degrees rotation shown).

Validating and Iterating the TRU-VU Wrist Positioning Aid and Educational Training To Improve the Standardization of Wrist Radiography

Laura Vancer^{1,2}, Maxwell Campbell^{2,3}, Gregory Garvin⁴, Emily Lalone^{1,2}

¹ School of Biomedical Engineering, Western University, ² Roth McFarlane Hand and Upper Limb Centre, ³ School of Mechanical and Materials Engineering, Western University, ⁴ Schulich School of Medicine and Dentistry

Introduction: Radiography is the first imaging modality performed when investigating wrist trauma and carpal instability given its minimal health risks, diagnostic utility, and accessibility in remote regions (1,2,3). However, wrist radiograph sensitivity depends on correct anatomical positioning and rotation due to **the wrist's complicated bony anatomy**—small changes in rotation can create significant radiographic differences (4). Consequently, radiograph quality can be compromised in fast-paced clinical environments, leading to missed diagnoses that can progress to more serious carpal diseases such as osteoarthritis (4). Furthermore, due to the limitations and high cost of current aids, wrist positioning is often performed based on **a technologist's best judgement, which can lead to variability in radiograph quality**. These concerns are further exacerbated in remote communities where technologists may not receive adequate training or resources (3).

To address these limitations, my lab developed the TRU-VU Wrist Positioning Aid and educational training modules to consistently ensure correct wrist position and rotation. The tool provides references for common wrist projections while the educational modules deliver specialized wrist specific positioning training. We hypothesize that the **TRU-VU Wrist Positioning Aid will aid the 'novice' technologists to produce radiographs of similar diagnostic quality to the 'expert' technologists**.

Methods: In-vivo wrist positioning of a healthy cadaveric specimen was performed by a total of six participants, comprising three 'expert' and three 'novice' technologists. For this study, 'expert' technologists are defined as clinicians with more than five years of clinical experience, whereas 'novice' technologists are those with less than two years of experience. Following recruitment, participants completed three testing scenarios: pre-intervention, post-educational intervention, and post-tool intervention. In the pre-intervention phase, technologists positioned the cadaveric specimen for four standard wrist radiograph projections: [1] posteroanterior (PA), [2] 45° internal oblique, [3] 60° external oblique, and [4] lateral. The positioning procedure was then repeated after the introduction of the educational intervention. Lastly, the tool intervention phase involved technologists completing the positioning tasks once more with the assistance of the TRU-VU tool. Furthermore, participants completed a pre-intervention, post-educational intervention, and post-tool intervention questionnaire to measure impressions and gain feedback on the design of the TRU-VU tool and educational training. The resulting radiographs were anonymized and evaluated for diagnostic quality by a radiologist using a grading scale previously developed by our study team, based on the findings from Campbell et al (4). Intrarater reliability was determined through 2 separate analyses performed by the same blinded radiologist 10 days apart.

Results: Preliminary results suggest that the use of the TRU-VU Wrist Positioning Aid and educational modules do not result in a significant increase or decrease in the overall diagnostic value of a radiograph. The post-intervention surveys however, indicated an overall positive satisfaction and perceived use of both the tool and educational modules. In addition, the surveys revealed technologist feedback to provide direction for future design iterations.

Conclusions: The quantitative and qualitative results of the study provide insight on the efficacy of the TRU-VU tool and aid to inform the direction of future iterations. Once design iterations are complete, future studies must include a greater number of participants to find statistically significant effects of the device to increase the power of the study.

The TRU-VU tool is a frugal device that aims to standardize wrist radiography and consequently improve the consistency of accurate wrist injury diagnosis. Given the long-term consequences of misdiagnosed wrist injuries, proper diagnosis and subsequent treatment are paramount to patient mobility and overall well-being.

1. Ferreira Branco D, Bouvet C, Hamard M, Beaulieu JY, Poletti PA, Boudabbous S. Reliability of radio-ulnar and carpal alignment measurements in the wrist between radiographs and 3D imaging. *Eur J Radiol*. 2022 Sep 1;154:110417.
2. Copeland J. Wrist imaging [Internet]. U.S. National Library of Medicine; 2023 [cited 2024 Nov 14]. Available from: <https://www.ncbi.nlm.nih.gov/books/NBK554525/>
3. Pennock AT, Phillips CS, Matzon JL, et al. The Effects of Forearm Rotation on Three Wrist Measurements: Radial Inclination, Radial Height and Palmar Tilt. *Hand Surg*. 2005. doi:10.1142/S0218810405002528
4. Davidson M, Kieler A, Tonseth RP, Seland K, Harvie S, Hanneman K. The landscape of rural and remote radiology in Canada: Opportunities and challenges. *Canadian Association of Radiologists Journal*. 2023 Aug 28;75(2):304–12. doi:10.1177/08465371231197953
4. Campbell M, Schurmans G, Suh N, Garvin G, Lalone E. The Sensitivity of the Scapholunate Interval and Bony Landmarks to Wrist Rotation on Posteroanterior Radiographs. *Hand N Y N*. 2024 May 30;15589447241255705.

Bridging the Gap with Customizable Above-Elbow Prosthetic Designs to Balance Open-Source Models and Patient-Specific Needs

Emese Elkind¹, A. T. Tun², N. Learned¹, C. Mccauley¹, L. Windover¹, A. Gammage¹, K. Wisener¹, M. Wolkoff¹, C. Davison¹, E. Purkey¹, G. Fichtinger¹, K. Thornton²

¹Queen's University, Kingston, Canada, ²Burma Children Medical Fund, Mae Sot, Tak, Thailand

INTRODUCTION: Myanmar's healthcare system, strained further by the 2021 military coup and civil war, has led millions of refugees to Thailand seeking medical aid [1]. Burma Children Medical Fund (BCMF), based in Mae Sot, Tak, Thailand funds these Burmese communities', who are unable to receive medical treatment by providing support services, including prosthetics for refugees [2]. BCMF makes prosthetics for low-resource settings using open-source designs. The usage of prosthetic arms depends heavily on their functionality and comfort, as patients are more likely to use prosthetics if it restores normalcy. The staff at BCMF have limited Computer Aided Design (CAD) experience so Queen's Biomedical Innovation Team (QBiT) at Queen's University has started a prosthetic project to support them. The student-led biomedical engineering design team modifies open-sourced designs to tailor them to patient needs. Specifically, we aim to add an above-elbow prosthetic to the existing below-elbow prosthetics currently used by BCMF to produce an affordable and functional prosthetic.

METHODS: BCMF currently adapts Thingiverse designs, such as the below elbow Kwawu Arm 2.0 [3], which can be adjusted with OpenSCAD [4], a software for modifying models to fit the recipient. QBiT has modified the Kwawu arm and designed a shoulder piece and harness system to extend the below elbow prosthetic to fit above elbow amputees (fig.1). A polyester strap forms a harness and is secured with snap buttons so the patient can control the prosthetic by adjusting their shoulder to move the elbow joint and to operate the hand attachment (fig.2). The arm is undergoing an iterative testing process for durability and comfort with constant communication between the BCMF and QBiT. Patient feedback ensures the prosthetics cater to the needs of each recipient. QBiT has developed a comprehensive manual, complete with detailed images, outlining the steps for setting up the harness to fit the patient's measurements.

RESULTS: Since 2019, BCMF has provided 76 3D-printed prosthetics. The new above elbow design eliminates electronic components, reducing complexity and cost while improving durability for Burmese climates and living conditions during the war, making it more accessible for a wider range of users. The prosthetic incorporates interchangeable end-effectors to adapt to the patients' daily activities. The control wires connecting the harness to the dynamic prosthetic are routed internally, minimizing the risk of snagging. The final design will restore partial range of motion to the patient through the use of the prosthetic.

CONCLUSIONS: The BCMF prosthetics project provides a low-cost solution to healthcare challenges in the context of the poly-crisis experienced in Myanmar, enhancing the resilience and adaptability of affected refugee communities. This collaboration demonstrates the potential for future partnerships between educational institutions and NGOs to address health care access disparities and empowers BCMF to expand their reach and improve access to low-cost, body-powered prosthetic solutions for a growing number of patients in need. Future work includes continuing to fill the gap between open-sourced models and patient-specific needs to refine the 3D-printing workflow by creating customizable, generalized designs.

REFERENCES: [1] UN. *Overview of Myanmar nationals in Thailand*. IOM UN migration. <https://thailand.iom.int/resources/overview-myanmar-nationals-thailand-april-2024> [2] *Burma Children Medical Fund - Mae Sot, Thailand*. BCMF | Burma Children Medical Fund - Mae Sot, Thailand - Operating to give people a future. (n.d.). <https://burmachildren.com/> [3] Buchanan, J. (2018, March 27). *Kwawu Arm 2.0 - Prosthetic - socket version*. Thingiverse. <https://www.thingiverse.com/thing:2841281> [4] *OpenSCAD*. The Programmers Solid 3D CAD Modeller. (n.d.). <https://openscad.org/>



Fig. 1: Assembly CAD of the arm prosthetic.



Fig 2: Dorsal view of A.R.M. harness.

Miniaturized Gamma-Imaging Probe for Lung Cancer Detection

Alysha Prem¹, M. Ali Tavallaei^{1,2}

¹Toronto Metropolitan University, Toronto, Canada

²Sunnybrook Health Sciences Centre, Toronto, Canada

Introduction: Lung tumor resection is typically achieved with a bronchoscopy in which an Endobronchial Ultrasound (EBUS) can identify masses and extract them using Needle Aspiration (NA), but EBUS-NA has a false negative rate of about 15% [1]. Positron Emission Tomography (PET) uses radiotracers, such as Technetium-99m (Tc-99m), to image tumors. Using the principle that radiotracers emit gamma rays as radioactive decay occurs and certain radiotracers have an affinity for tumors, real-time detection and biopsy of tumors is proposed using a miniaturized gamma probe catheter. With a maximum diameter of 2 mm, the gamma probe can be guided through the bronchus and bronchioles in a minimally invasive manner.

Methods: While achieving the target maximum diameter of 2 mm, the proposed device aims to produce 1-dimensional signal acquisitions proportional to the radiation intensity detected at a specific point. A thallium-doped cesium iodide (CsI:Tl) scintillating crystal and silicon photomultiplier (SiPM) sensor will detect radioactivity and produce an electrical output relative to the source's distance. CsI:Tl crystals are one of the brightest scintillators, emitting 52 photons/keV and with a peak emission wavelength at 550 nm, making them compatible with SiPM readout. SiPM sensors are compact, being only a few millimeters in size, and can produce an electrical pulse for each photon detected on the sensor's array in a matter of milliseconds. Mathematical modeling was performed, assuming that a rectangular gamma detector consisting of a CsI:Tl crystal detected radiation emitted from a Tc-99m point source at a distance of 1 cm with a source intensity of 370 Bq (10 mCi) assumed. The dominant decay energy of Tc-99m is 140.5 keV, at a yield of 98% [2].

Results: Based on preliminary calculations, for a range between 10%-100% scintillation efficiency of the CsI:Tl crystal, 731-7306 photons will be generated per 140.5 keV gamma ray. Given the detector's yield, this should result in ~0.211-2.11 million photons/second produced by the scintillator, implying the theoretical counted photon should be sufficient despite the size constraints for integration within a 6 Fr catheter. Further, incorporating device tracking (e.g., electromagnetic or optical tracking) would also allow for stitching of acquisitions to provide 3-dimensional gamma images of the target area for biopsy.

Conclusions: The next step in this research is to develop the system prototype and perform verification testing using various SiPMs paired with the CsI:Tl scintillating crystal, aiming for peak readout. This proposed device may potentially bridge the gap between the imaging and tumor resection processes of lung cancer treatment using real-time gamma-ray detection.

References: [1] S. Kim et al., "Are there differences among operators in false-negative rates of endosonography with needle aspiration for mediastinal nodal staging of non-small cell lung cancer?," *BMC Pulmonary Medicine*, vol. 19, no. 1, Jan. 2019, doi: <https://doi.org/10.1186/s12890-018-0774-6>. [2] A. Duatti, "Review on 99mTc radiopharmaceuticals with emphasis on new advancements," *Nuclear Medicine and Biology*, vol. 92, May 2020, doi: <https://doi.org/10.1016/j.nucmedbio.2020.05.005>.

Pitches 4: Deep Learning/Machine Learning Methodology 1

Abstracts

Comparative analysis of deep learning approaches for urethral segmentation in high-dose-rate prostate brachytherapy using transrectal ultrasound images

Nicole Valencia^{1,2}, Timothy Olding³, Martin Korzeniowski³, Jessica R. Rodgers¹

¹Department of Physics and Astronomy, University of Manitoba, Winnipeg, Manitoba, Canada

²Department of Physics, University of Winnipeg, Winnipeg, Manitoba, Canada

³Department of Oncology, Queen's University, Kingston, Ontario, Canada

Introduction: High-dose-rate (HDR) brachytherapy is a form of specialized radiation therapy for the treatment of prostate cancer, the leading cancer type amongst Canadians assigned male at birth [1]. The treatment process involves the insertion of interstitial catheters directly into the prostate, guided by transrectal ultrasound (TRUS) images (Fig. 1) [2]. After meticulous dose planning, radioactive isotopes are directed through the catheters and placed within or near cancerous tissue to deliver high doses of radiation to targeted cancer cells while sparing normal tissue [2]. The success of treatment is dependent on accurate manual segmentation by trained clinicians of anatomical structures and clinical tools, including the clinical tumour volume (CTV), implanted catheters, and organs at risk (OARs), such as the urethra [2]. Despite improved imaging technologies, manual segmentation of structures in TRUS images remain a challenge due to subjectivity, variability, and time constraints, which can negatively impact clinical workflow and patient safety [2]. This study aims to contribute to a comprehensive automated pipeline for brachytherapy treatment planning by providing a comparative analysis of parameterized deep learning neural networks for urethra segmentation using TRUS images and examining the effects of dataset size and augmentation on model training, performance, and robustness.

Methods: The dataset consists of 99 TRUS images taken from individual patients receiving HDR prostate brachytherapy treatment. The dataset was processed into 2D and 3D image formats, normalized, then divided patient-wise into training, validation, and test subsets of 67, 11, and 21 patients, respectively. Variability and data diversity was introduced through image augmentation of the 2D and 3D formats to increase the training dataset size by 10%, 50%, and 100%. Training using a U-Net convolutional neural network architecture was then performed, with different iterations on the same training set offering comparisons of adjusted hyperparameters such as different learning rates (e.g., $1e-5$ to $1e-3$), epochs (ranging from 10 to 50), and loss functions (e.g., cross-entropy and dice loss). Predicted segmentations were then compared against clinician-defined ground truth masks (Fig. 1) to assess performance and segmentation accuracy.

Results: Initial results showed poor pixel-wise agreement with ground truths, with an average Dice Similarity Coefficient (DSC) of 0.21 ± 0.11 for low-epoch training after hyperparameter optimization on 3D data, without any dataset size increase through augmentations. However, proof-of-concept findings indicate that expanding the training dataset using image augmentation techniques offers promising improvement of urethra prediction performance. Based on ongoing work, better agreement with ground truth masks is also expected for 2D imaging data with augmentation due to increased training dataset size. Acquisition of additional patient images is also underway.

Conclusion: The approach of this work demonstrates the potential of auto-segmentation tools in daily clinical prostate brachytherapy treatment workflows. Further refinement of the pixel-wise agreement between predictions and ground truths are necessary through further comparative analyses; however, the integration of these tools can help streamline OAR delineation, reduce clinician workload, and enhance dose accuracy to ultimately improve prostate cancer patient outcomes.

References: [1] Prostate Cancer Statistics. Canadian Cancer Society. 2023. <https://cancer.ca/en/cancer-information/cancer-types/prostate/statistics>. [2] Hampole P, et al. Med Phys 2023;51(4):2665–2677.

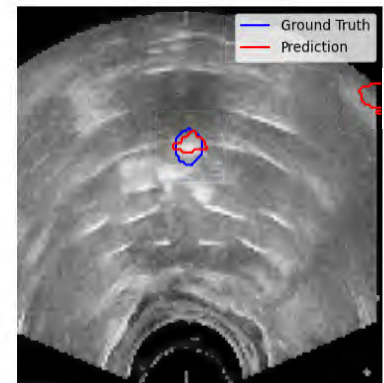


Figure 1: Example of algorithm prediction (red) compared to clinician ground truth (blue).

Predicting Inspiratory Chest CT Image Viability Using Deep Learning

S. Rezvanjou¹, D. Genkin¹, S.E. Collins^{2,4}, W.C. Tan³, J.C. Hogg³, J. Bourbeau², M.K. Stickland³, and M. Kirby¹
¹Toronto Metropolitan University, Toronto, Canada. ²McGill University, Montreal, Canada. ³University of British Columbia, Vancouver, Canada. ⁴University of Alberta, Alberta, Canada.

Introduction: Chest CT images are used to evaluate structural changes in patients with chronic obstructive pulmonary disease (COPD), such as airway disease and emphysema, and are acquired by coaching participants to full inspiration. However, evidence has shown that there is significant variability in inspiratory effort during this process¹, potentially skewing diagnosis of conditions which depend on accurate lung density measurements²⁻⁴. Comparing the CT-derived total lung volume (TLV) to the plethysmography-measured total lung capacity (TLC) could be used to confirm sufficient inspiratory effort immediately following image acquisition. However, these measurements are often not available, leading to uncertainty

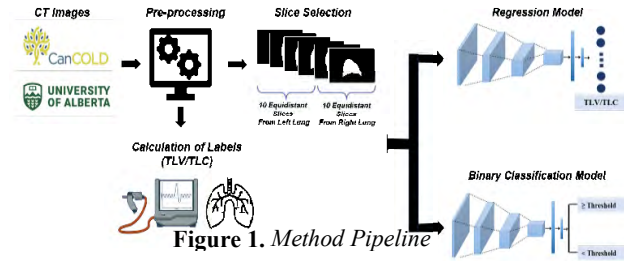


Figure 1. Method Pipeline

in inspiratory effort. The objectives this study were to introduce TLV/TLC as a novel metric for assessing inspiratory effort, and, for the first time, apply a CNN-based deep-learning model to predict the TLV/TLC ratio from chest CT images with validation using an independent external dataset.

Methods: 1,293 CT scans from the Canadian Cohort for Obstructive Lung Disease (CanCOLLD)⁵ were

divided for training/validation and internal testing using a 968:325 split. An independent cohort of 57 chest CT scans of COPD patients⁶ was used to externally test the model. CT scans were processed to include lung tissue through automatic segmentation using TotalSegmentator⁷, windowed to the range [-1000 HU, 0 HU], and normalized⁸. Finally, 20 equidistant sagittal lung slices (25%-75% of the lung) were selected and resized to (128, 128, 20) as the final model input. The TLV/TLC ratio was computed by counting all voxels belonging to the lung tissue segmentation (converted to litres) to determine TLV and dividing by plethysmography-measured TLC. A ratio closer to 1 indicates sufficient inspiratory effort during image acquisition. A 3D VGG-like CNN consisting of 4 convolutional, 2 dense, 4 batch normalization, 4 max-pooling layers, the ReLU activation function, and an L2 kernel regularizer, was implemented. A regression model was used to calculate TLV/TLC values, whereas a classification-based model was used to predict low (TLV/TLC<0.80), and acceptable (TLV/TLC≥0.80) categories (Figure 1). Models were trained by 5-fold cross validation. Regression and classification models' performance were evaluated using the mean square error (MSE), mean absolute error (MAE), and accuracy (ACC), area under the receiver operating characteristic curve (AUC), and F1 score, respectively. **Results:** For internal tests, the regression model had an MSE of 0.010± 0.000, while the classification task achieved an AUC of 0.81±0.04. Externally, the MSE improved to 0.005± 0.000 and the AUC increased to 0.93±0.07. **Conclusion:** This study established TLV/TLC as a novel metric for assessing inspiratory effort and image quality during chest CT acquisitions and, for the first time, developed an automated CNN system for assessing the TLV/TLC ratio. The high accuracy and robustness, demonstrated by low MSE and high AUC scores across test datasets, validate its generalizability. The importance of this threshold will be assessed in future work to demonstrate its role in improving emphysema progression prediction.

Table 1. Performance of Models with Threshold of TLV/TLC = 0.80 on Internal (CanCOLLD) and External Test Sets (The University of Alberta).

	Regression		Binary Classification		
	MSE	MAE	Acc	AUC	F1
Internal	0.010±0.000	0.073±0.001	0.75 ± 0.05	0.81 ± 0.04	0.75 ± 0.05
External	0.005±0.000	0.053±0.002	0.86 ± 0.09	0.93±0.07	0.86 ± 0.09

Mean Square Error (MSE), Mean Absolute Error (MAE), and Area Under the Receiver Operating Characteristic Curve (AUC)

Reference: ¹J.B. Moser, et al. *Clinical Radiology*, 2017; ²Camargo JJ, et al. *Pediatr Transplant*. 2009; ³Yamashiro T, et al. *Acad Radiol*. 2010; ⁴Mets, O. M., et al. *Lung*, 2012; ⁵Jean Bourbeau, et al, *COPD: Journal of Chronic Obstructive Pulmonary Disease*, 2014; ⁶Collins, S, et al. *University of Alberta*. 2018. ⁷Wasserthal J, et al. *Radiol Artif Intell*, 2023; ⁸Au, R, et al. *Phys. Med. Biol*. 2021.

Involvement-Aware Foundation Models for Prostate Cancer Detection in Ultrasound

Mohamed Harmanani^{1,3}, Amoon Jamzad^{1,3}, Minh Nguyen Nhat To^{2,3}, Paul F. R. Wilson^{1,3}, Zhuoxin Guo¹, Fahimeh Fooladgar^{2,3}, Samira Sojoudi², Mahdi Gilany^{1,3}, Silvia Chang², Peter Black², Michael Leveridge¹, Robert Siemens¹, Purang Abolmaesumi², Parvin Mousavi^{1,3}

¹Queen’s University ²University of British Columbia ³Vector Institute

Introduction: Prostate cancer (PCa) detection from ultrasound (US) using deep learning (DL) models has shown potential for enhancing real-time guidance during biopsies. However, prostate US images lack pixel-level cancer annotations, and are instead labeled through coarse histopathology annotations of the entire core, introducing weak labels. Current approaches [1, 2] to PCa detection fail to address this issue due to their focus on local features and lack of context awareness, with foundation models [3, 4] offering a promising alternative to these methods by analyzing entire images to capture global context. However, despite this improvement, foundation models still encounter challenges stemming from weak labels, leading to imprecise localization of cancer in the image. We propose to address this limitation by designing a specialized loss function that incorporates cancer involvement, defined by the proportion of cancer tissue reported by pathology, into the training objective. By providing the model with a more complex form of supervision, our proposed method improves the robustness of foundation models for PCa detection.

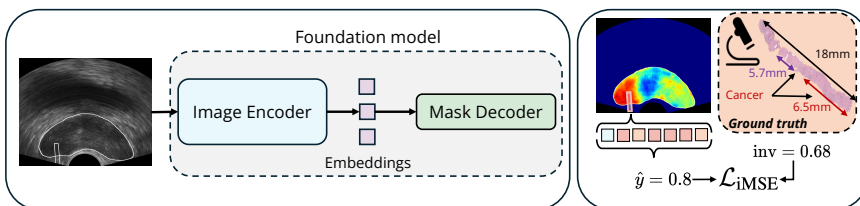


Figure 1: High-level overview of our training method

However, despite this improvement, foundation models still encounter challenges stemming from weak labels, leading to imprecise localization of cancer in the image. We propose to address this limitation by designing a specialized loss function that incorporates cancer involvement, defined by the proportion of cancer tissue reported by pathology, into the training objective. By providing the model with a more complex form of supervision, our proposed method improves the robustness of foundation models for PCa detection.

Methods: We use 2631 biopsy cores collected from 311 patients who underwent prostate biopsy in 2 centers under the guidance of trans-rectal ultrasound (TRUS). Our proposed method uses MedSAM [4], a foundation model for medical images, to segment cancer in the US image using involvement as a ground truth. We design the involvement-aware mean-squared error (iMSE) loss function to minimize the distance between the average intensity of the model’s predictions within the region of interest and the reported cancer involvement of the core. iMSE aims to mitigate the impact of coarse labeling by allowing the model to learn some information regarding the spread of cancer in the core. The model’s final prediction is computed by averaging the activations of the segmentation output within the labeled region, and iMSE is computed using: $\mathcal{L}_{iMSE}(\hat{Y}, inv) = (1/R) \sum_i \sum_j (\hat{Y}[i, j] \cdot \mathbb{1}_{\hat{Y}[i, j] \in R} - inv)^2$.

Results: Our results are shown in Table 1. We compare our method against iLR [1], a strong baseline method that minimizes the difference between true and predicted involvement to combat label noise, and 2 foundation models, SAM [3] and MedSAM [4]. Our proposed method leads to superior cancer detection, outperforming all baselines, with an AUROC of 75.2 (+1.3%), a balanced accuracy of 69.3 (+0.4%), and better sensitivities across all thresholds (+1.7%, +3.9%).

Method	AUROC	Bal. Acc.	Sen.@40Spe	Sen.@60Spe
iLR [1]	67.0	63.7	83.1	67.0
SAM [3]	71.2	68.4	80.6	68.4
MedSAM [4]	73.9	68.9	81.9	71.7
MedSAM +iMSE	75.2	69.3	85.7	75.6

Table 1: Comparing the performance of our method against prior work and baselines for PCa detection

Conclusion: Our findings underscore the promise of involvement-aware loss functions in advancing foundation models for weakly labeled ultrasound data. Future work can further enhance robustness by training models to learn variations of prostate cancer tissue over time.

References

- [1] M. N. N. To *et al.*, “Coarse label refinement for improving prostate cancer detection in ultrasound imaging,” *International Journal of Computer Assisted Radiology and Surgery*, 2022.
- [2] P. F. Wilson *et al.*, “Toward confident prostate cancer detection using ultrasound: a multi-center study,” *International Journal of Computer Assisted Radiology and Surgery*, 2024.
- [3] A. Kirillov *et al.*, “Segment anything,” in *Proceedings of the IEEE/CVF International Conference on Computer Vision*, 2023.
- [4] J. Ma *et al.*, “Segment anything in medical images,” *Nature Communications*, 2024.

Automated CNN-based Segmentation of Carotid Atherosclerotic Plaque and Morphological Characterization of Carotid B-mode Ultrasound Images

Nahid Babazadeh Khameneh^{1,2}, Robert A. Brown³, Ioannis Psaromiligkos⁴, Stella S. Daskalopoulou^{1,2}

¹Department of Medicine, McGill University, Montreal, QC, Canada; ²Vascular Health Unit, Department of Medicine, Research Institute of McGill University Health Centre, Montreal, QC; ³ShadowLab Research, Toronto, ON, Canada; ⁴Department of Electrical and Computer Engineering, McGill University, Montreal, QC, Canada

Introduction: Carotid atherosclerosis is a major cause of cerebrovascular events including ischemic strokes leading to high morbidity and mortality worldwide. In clinical practice, quantification of atherosclerotic plaque morphology parameters, such as thickness (T), total plaque area (TPA), and total plaque volume (TPV) are important and require plaque border delineation. B-mode ultrasound serves as a safe, widely available, and cost-effective imaging tool for decision-making towards medical management or surgical intervention of carotid atherosclerosis. However, inter-operator variability in the interpretation of ultrasound images may lead to misdiagnosis. Recently, fully automatic deep learning-based segmentation methods have been proposed to increase accuracy, reproducibility, and time efficiency [1, 2]. We hypothesize that in comparison to the semi-automatic approaches [3], a deep learning-based approach will improve accuracy, reproducibility, and time efficiency of plaque detection and quantification of plaque parameters. Compared to previous studies [1, 2, 3], the innovation of this work is to develop a fast and automatic deep convolutional neural network (CNN)-based segmentation on both longitudinal and corresponding transverse B-mode ultrasound images to detect the atherosclerotic plaque, and consequently compute three plaque parameters including T , TPA , and TPV to get a more detailed characterization of the plaque. **Methods:** First, to detect the atherosclerotic plaque from B-mode ultrasound images, a CNN-based semantic segmentation model with U-Net architecture was trained to produce the plaque mask. For transfer learning, we used the ResNet34 model, pre-trained on the ImageNet dataset. For training, the cross-entropy loss function and the Adam optimizer with a learning rate of 0.0001 were applied. The CNN-based segmentation model was developed using Tensorflow 2.1.0 in Python 3.6.13 and trained on an NVIDIA GeForce GTX 1060 graphics card. Second, based on the plaque mask, the plaque parameters T , TPA , and TPV were quantified using automatic image processing methods such as the principal component analysis (PCA), [4]. **Results:** Ethics approval for this study was granted by the McGill University Health Centre's Research Ethics Board (2021-7661). Patients ($n=141$) with severe carotid atherosclerotic plaques underwent US examination prior to carotid endarterectomy. A set of (467) ultrasound images including longitudinal (326) and transverse (141) images were anonymized and masked. Manual annotations of the plaque border as ground truths were performed by an expert radiologist. Patients were assigned to training (80%), validation (10%), and unseen testing (10%) groups. Translations, rotations, and moderate scaling were used to augment the training images. The Intersection Over Union between manual and algorithm-based segmentation was 0.80 ± 0.18 (mean \pm standard deviation) on 46 unseen US images. The mean absolute error of (ΔT), (ΔTPA), and (ΔTPV) were 0.22 mm, 0.73 mm², and 0.89 mm³. The total time (detection/quantifications) was <1 second per image. Fig. 2 shows qualitative results of the developed CNN-based (red) versus manual (green) plaque segmentations. **Conclusions:** The developed fully automatic system for 1) detection and segmentation of carotid atherosclerotic plaques, and 2) quantification of T , TPA , and TPV achieved accurate results in a time efficient manner (less than 1 second per image). This is essential in clinical routine workflows to characterize atherosclerotic plaque morphology immediately after B-mode ultrasound image acquisition. This work will serve as a non-invasive computer-aided diagnostic tool that will improve clinical diagnosis of patients with atherosclerotic plaques, leading to 1) accurate risk stratification, 2) optimal selection of patients for medical and surgical interventions, and 3) improved monitoring of treatment efficacy for anti-atherosclerotic medications. Importantly, based on ultrasound (safe, inexpensive, and most widely clinically used carotid imaging method), our work will inform guidelines and empower clinicians to better predict and prevent strokes by delivering individualized care. **References:** [1] Y. C. Li, et al., "Automatic Detection of Atherosclerotic Plaque and Calcification from Intravascular Ultrasound Images by Using Deep Convolutional Neural Networks," *IEEE Trans. Ultrason. Ferroelectr. Freq. Control*, vol. 68, no. 5, pp. 1762–1772, 2021. [2] R. Zhou, et al., "Deep Learning-Based Measurement of Total Plaque Area in B-Mode Ultrasound Images," *IEEE J. Biomed. Health Inform.*, vol. 25, no. 8, pp. 2967–2977, 2021. [3] A. A. Khan, et al., "Semi-automatic Quantification of carotid Plaque Volume with Three-dimensional Ultrasound Imaging," *J. of Vasc. Surg.*, vol. 65, no. 5, pp. 1407-1417, 2017. [4] J. Salvi, et al., "A Review of Recent Range Image Registration Methods with Accuracy Evaluation," *Image Vis. Comput.*, vol. 25, no. 5, pp. 578–596, 2007.

Automatic prostate segmentation in micro-ultrasound imaging using the Segment Anything Model

O. Radcliffe¹, I. Lawford-Wickham¹, P. Wilson¹, P. Abolmaesumi², and P. Mousavi¹

¹Queen’s University, Kingston, Canada, ²The University of British Columbia, Vancouver, Canada

INTRODUCTION: Prostate cancer is the second most common cancer among Canadian men. Accurate prostate segmentation in images is critical for treatment planning and diagnosis. However, manual segmentation is time-consuming and subjective, highlighting the need for more efficient and reliable techniques. Micro-ultrasound (μ US) imaging is increasingly used for prostate imaging due to its higher resolution than conventional ultrasound and comparable performance to Magnetic Resonance Imaging. The first deep learning (DL) model for μ US prostate segmentation, MicroSegNet [1], achieved promising results on μ US data. However, μ US data is scarce, making it challenging to train DL models that perform well in diverse clinical settings. Due to their extensive pre-training on large amounts of data, foundation models [2] have the potential to generalize to a wider array of tasks and domains. As a result, they have made significant improvements in robustness for segmentation across various medical imaging domains [3]. This study aims to investigate the potential of existing foundation models like Segment Anything Model (SAM) [2] for the task of automatic prostate segmentation in μ US data to improve performance and clinical workflows.

METHODS: We use a publicly available dataset [1] of μ US-guided prostate biopsies from 75 patients with corresponding prostate annotations. The data contains rotational ‘sweep’ scans of the prostate, performed from left to right, conducted using the ExactVu side-firing transrectal μ US probe. This resulted in 28-44 2D images per sweep. The data was split by patient with 44 used in training, 11 for validation and 20 for testing.

Drawing inspiration from manual segmentation and the advantage of knowing the frame index or the ability to view the images before and after, we explored several prompting strategies to enhance model performance. The architecture we used, shown in Figure 1, includes the SAM backbone along with our novel prompting methods. Our training strategy involved fine-tuning SAM using two sets of prompts: the index of the current frame, encoded as a decimal between 0 and 1, and the image mask of the previous frame. We believe these prompts help the model learn typical prostate shape and size across consecutive μ US images by providing additional spatial context to the model. We also experimented with different prompting strategies, such as using no prompting, using one set of prompts, and using both.

RESULTS: To evaluate our model’s performance, we used two common metrics, mean Dice coefficient and mean Hausdorff 95% distance, modified to penalize cases where predictions or ground truth segmentations are empty. Our model demonstrated improved performance in segmentation accuracy compared to state-of-the-art models. We found that the prompting strategies worked best in tandem. The mean Dice coefficient increased from 93.1 with the MicroSegNet model to 94.0, and the mean Hausdorff distance was reduced from 2.01 mm with the MicroSegNet model to 1.76 mm with our model.

CONCLUSION: We demonstrate the effectiveness of leveraging SAM for automatic prostate segmentation in μ US images by incorporating positional information through prompting. This highlights the potential of foundation models for seamless integration into a segmentation tool for targeted biopsy planning. Future work should validate these findings on a large, multi-center dataset of prostate μ US images to evaluate generalizability and potential for clinical deployment.

REFERENCES:

- [1] Jiang, H., et al., “MicroSegNet: A deep learning approach for prostate segmentation on micro-ultrasound images,” *Computerized Medical Imaging and Graphics*, 2024.
- [2] Kirillov, A., et al., “Segment anything,” *Proceedings of the IEEE/CVF International Conference on Computer Vision*, 2023.
- [3] Ma, J., et al. “Segment anything in medical images.” *Nature Communications*, 2024.

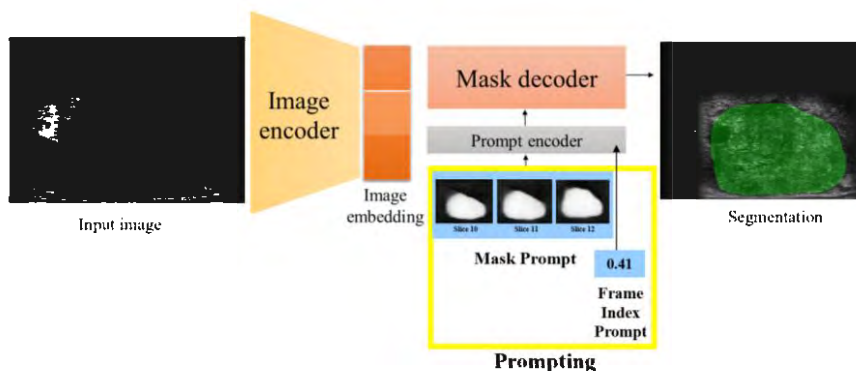


Figure 1: Proposed architecture using the Segment Anything Model (SAM) as a backbone with additional prompting (highlighted in yellow) for frame index and previous masks.

Advancing Kidney Ablation Analysis in 3D CT Images: A Deep Learning Segmentation Framework

Maryam Rastegarpour^{*1,3}, Derek W. Cool², and Aaron Fenster^{1,2,3}

¹Robarts Research Institute, Western University, London, ON, Canada

²Department of Medical Imaging, Western University, London, ON, Canada

³Department of Medical Biophysics, Western University, London, ON, Canada

Introduction

Renal tumor ablation is increasingly used as a targeted therapy, relying on precisely identifying the tumor and evaluating ablation coverage of the tumor in CT images [1]. Accurate segmentation of kidney ablation zones (KAZs) is critical for assessing treatment effectiveness and ensuring the preservation of kidney function [2]. However, manual segmentation is time-consuming and subject to interobserver variability [3]. AI-based methods offer the potential to overcome these limitations, improving consistency and efficiency [4]. We are the first to address the AI-based KAZ segmentation by leveraging deep learning with a promising segmentation performance.

Methods

We proposed a ResU-net-based framework integrating residual connections, attention mechanisms, and multi-scale feature fusion to segment the KAZs into five steps as shown in Fig.1. First, we preprocessed the dataset in two stages: initially, the 3D CT images were cropped to capture approximate regions of interest encompassing the kidney boundary, followed by radial slicing of the 3D KAZ around an estimated central axis of the KAZ. Then, we fed these 2D radial image slices to the modified 2D ResUNet++ model (i.e., adding a Squeeze-and-Excitation block at every block in the decoding arm) to train, validate, and test using random 5-fold cross-validation with a 60/20/20 split ratio from 46/15/15 patients for training/validation/testing. The KAZ margin inside the kidney was identified by manually selecting two points on the common border of the kidney and the KAZ. The 2D segmented boundaries were used to generate 3D reconstructed surfaces inside the kidney, which were needed for clinical evaluation. Metrics such as DSC and signed Hausdorff distance (sHD) were used to evaluate the performance of 2D segmentation.

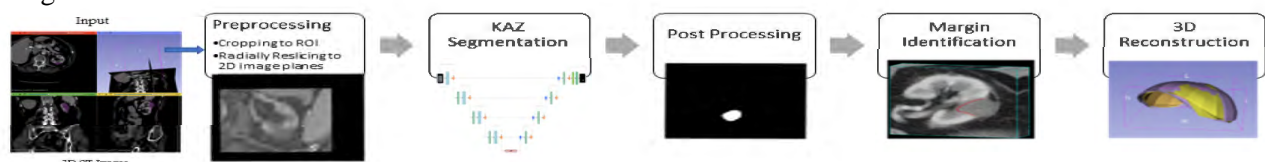


Figure 1. The proposed workflow

Results

We used a local dataset including 3D CT images of 76 patients from the London Health Sciences Centre (London, Canada). The KAZ was manually delineated by two trained experts supervised by an interventional radiologist (D.C.) to serve as ground truth. The proposed framework achieved an $82\pm 1\%$ DSC, indicating a high overlap between predictions and annotations. The sHD was 0.02 ± 2.4 mm, reflecting precise boundary detection. Compared to manual segmentation, the proposed approach reduced processing time from an average of 30 minutes to under one second per patient. Fig. 2 shows five samples of the segmentation result.

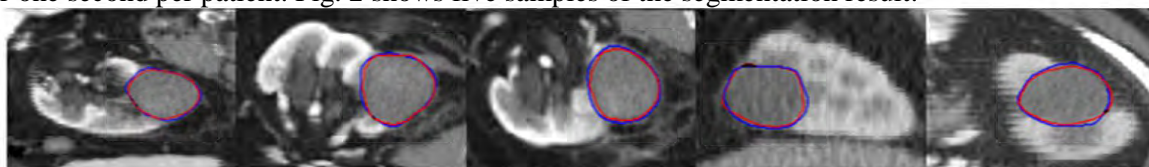


Figure 2 The original image and the segmentation result of the proposed model. Ground truth in blue, prediction in red.

Conclusions

This study demonstrates that deep learning can effectively segment KAZs, making it a valuable tool for clinical practice. Incorporating Explainable AI into the framework with a layer-wise explainable architecture opens the doors for future research to enhance model transparency, uncertainty, interpretability, and trust in AI predictions.

References

- [1] K. F. Chu and D. E. Dupuy, "Thermal ablation of tumors: biological mechanisms and advances in therapy," *Nature Reviews Cancer*, vol. 14, no. 3, pp. 199-208, 2014.
- [2] D. A. Gervais et. al., "Radiofrequency ablation of renal cell carcinoma: part 2, Lessons learned with ablation of 100 tumors," *American Journal of Roentgenology*, vol. 185, no. 1, pp. 72-80, 2005.
- [3] L. Joskowicz, et. al. "Inter-observer variability of manual contour delineation of structures in CT," *European Radiology*, vol. 29, pp. 1391-1399, 2019.
- [4] R. A. Campbell, et. al. "Kidney cancer diagnostics using AI and radiomics," in *Artificial Intelligence in Urology*: Elsevier, 2025, pp. 79-101.

Performing Prostate Segmentation Using SAM-Med2D Across Multiple Ultrasound Modalities

Vivian Nguyen¹, Amoon Jamzad¹, Paul Wilson¹, Mahdi Gilany¹,

Purang Abolmaesumi², Michael Leveridge¹, Robert Siemens¹, Parvin Mousavi¹

¹Queen’s University, Kingston, ON, Canada, ²University of British Columbia, BC, Canada

INTRODUCTION: Prostate cancer (PCa) is the second most prevalent cancer in men [1]. Early detection begins with a PSA blood test and a digital rectal exam, followed by a transrectal ultrasound-guided biopsy for confirmation. However, biopsies often result in false negatives due to the lack of distinct visual appearances. Recent interest has focused on integrating artificial intelligence and ultrasound (US) imaging to enhance diagnostics. Segmentation is a preliminary step in many medical imaging pipelines, but the process is laborious and time-intensive when performed manually. To address

these challenges, foundation models (FMs) pre-trained on large-scale medical datasets can automate segmentation and address issues in US images such as acoustic shadows and unclear boundaries. While prior studies focused on B-mode US, other informative modalities for tissue characterization, like raw radiofrequency (RF) signals, remain underexplored. This work assesses the segmentation performance of the SAM-Med2D [2] FM on three US modalities: B-mode, RF, and RFB, which maps B-mode signals to the RF Cartesian coordinates.

METHODS: The study used a dataset of 964 prostate US images from 94 patients, collected during biopsy procedures using an end-firing probe. Raw RF images were acquired from a conventional frequency US machine at a medium resolution. Envelope detection and log compression were applied to create the RFB images. B-mode images were generated by spatially interpolating the pixel intensities to map the RF Cartesian coordinates to the Polar coordinate system. The SAM-Med2D model was finetuned on the US modalities separately, with and without adapter layers, using a 70/10/20 train/validation/test split at the patient level. The Dice Similarity Coefficient (DSC) metric was used for quantitative evaluation and predicted model masks were qualitatively compared with the ground truth masks annotated by non-experts. Additionally, the predictions were assessed across five anatomical prostate regions (base lateral, base medial, mid-lateral, mid-medial, and apex lateral/medial). **RESULTS:** Zero-shot performance was poor in all cases, highlighting a distribution shift between the pre-training data and our fan-beam-shaped images dataset. Finetuning improved segmentation performance across all modalities. Baseline configurations finetuned without adapter layers achieved the highest metrics for the RFB modality (Mean DSC: 87.6%). Incorporating adapter layers improved performance across all modalities, with smaller gains observed for RF configurations. Notably, the RFB modality still obtained the highest results (Mean DSC: 90.2%), as shown in Table 1. A qualitative assessment of a shadowed image showed that the predicted model mask was more accurately located than the manual annotation created by less experienced annotators. The results demonstrated consistent performance across anatomical locations, highlighting the model’s robustness. **CONCLUSION:** SAM-Med2D can reduce the burden of manual segmentation for prostate US images. Future work will include multi-institutional data to improve generalizability and explore the integration of text-based prompts to enrich contextual understanding, such as PSA levels and prostate size.

REFERENCES: [1] P. Rawla, “Epidemiology of prostate cancer,” *World Journal of Oncology*, vol. 10, no. 2, 2019. [2] J. Cheng, et al., “Sam-med2d,” *arXiv preprint arXiv:2308.16184*, 2023.

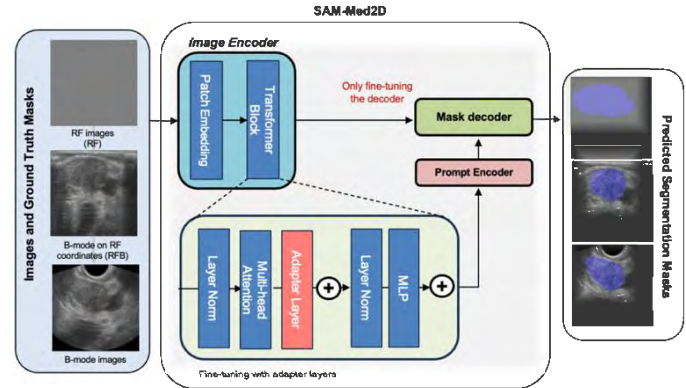


Figure 1. Overview of the pipeline consisting of the SAM-Med2D model, input images, and output masks.

Modality	Mean DSC (%)
B-mode	89.7
RFB	90.2
RF	86.6

Table 1. Performance metrics of the model configurations when finetuning with adapter layers.

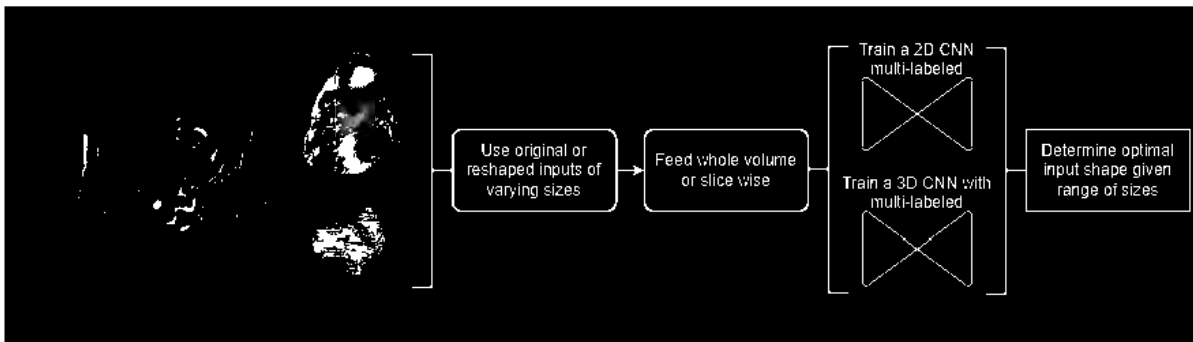
Evaluating the use cases of 3D and 2D segmentation in fetal MRIs

Alejo Costanzo^{1,2}, Adam Lim^{1,2}, Logi Vidarsson^{3,4}, Birgit Ertl-Wagner^{3,4,5}, Dafna Sussman^{1,2,6}

¹Department of Electrical, Computer and Biomedical Engineering, Toronto Metropolitan University, Faculty of Engineering and Architectural Sciences, Toronto, Ontario, Canada; ²Institute for Biomedical Engineering, Science and Technology (iBEST), Toronto Metropolitan University and St. Michael's Hospital, Toronto, Ontario, Canada; ³Department of Diagnostic Imaging, The Hospital for Sick Children, Toronto, ON, Canada, ⁴Department of Medical Imaging, Faculty of Medicine, University of Toronto, Toronto, ON, Canada; ⁵Division of Neuroradiology, The Hospital for Sick Children, Toronto, ON, Canada; ⁶Department of Obstetrics and Gynecology, Faculty of Medicine, University of Toronto, Toronto, Ontario, Canada

Introduction: Magnetic resonance imaging (MRI) is an imaging modality that provides high tissue contrast and resolution of anatomical regions [1]. Fetal MRI is commonly used to delineate soft tissues and diagnose diseases where ultrasound falters [1]. Currently, the wait times for fetal MRIs in Canada are growing, and the need to clinically evaluate MRIs automatically at a low cost is essential [2]. Automatic segmentation algorithms of Fetal Body (FB), placental, and Amniotic Fluid (AF) allow clinicians to access volumetric biomarkers to extract fetal weight, amniotic fluid volume, and placental weight/volume. Specifically, deep learning has succeeded in segmenting anatomical regions in various biomedical imaging applications [3], [4], [5]. When deciding whether to use whole 3D MRIs as inputs versus sequentially feeding 2D slices to a model, our research proposes a comparative study using Amniotic Fluid, Placental, and Fetal Body as labels.

Methods: Fifty-eight 3D Steady State Free Precessions on 1.5T or 3T scanners with and without SENSE MRIs were collected from the Hospital of Sick Children, with their gestational ages ranging from 20 to 37 weeks. Maternal-fetal radiologists created and validated the placental, AF and FB segmentation labels on the 3D MRIs. A novel convolutional neural network will be trained in 2D and 3D to compare optimal model performance and architecture efficacy. Additionally, a comparison between input tests from different resolutions (512x512x32, 384x384x64, 256x256x64, 512x512x12, etc.) will be conducted between models to inform clinicians which input modality is most appropriate for a given segmentation label. An analysis of upsampling and downsampling to reshape input images to the fixed model shape will be performed to assess any impact on the DICE similarity score.



Results: A 3D convolutional neural network trained on the cohort with adjusted histogram from (1% – 99% of pixels), normalized pixel values, and resized input shape to (384x384x64) produced a DICE similarity score of 95.06% for the fetal body, 95.50% for amniotic fluid, and 88.27% for the placenta. 2D segmentation results will be provided and compared with the 3D segmentation model.

Conclusion: This work is meant to inform researchers and practitioners on deciding the generalizability of a model concerning the vast variety of image input sizes and its impact on model performance.

References: [1] S. N. Saleem, “Fetal MRI: An approach to practice: A review,” *J. Adv. Res.*, vol. 5, no. 5, pp. 507–523, Sep. 2014, doi: 10.1016/j.jare.2013.06.001. [2] P. Jabehear Maralani *et al.*, “Canadian Association of Radiologists Recommendations for the Safe Use of MRI During Pregnancy,” *Can. Assoc. Radiol. J.*, vol. 73, no. 1, pp. 56–67, Feb. 2022, doi: 10.1177/08465371211015657. [3] A. Costanzo, B. Ertl-Wagner, and D. Sussman, “AFNet Algorithm for Automatic Amniotic Fluid Segmentation from Fetal MRI,” *Bioengineering*, vol. 10, no. 7, p. 783, Jun. 2023, doi: 10.3390/bioengineering10070783. [4] J. Lo *et al.*, “Cross Attention Squeeze Excitation Network (CASE-Net) for Whole Body Fetal MRI Segmentation,” *Sensors*, vol. 21, no. 13, p. 4490, Jun. 2021, doi: 10.3390/s21134490. [5] C. P. S. Kulseng, V. Hillestad, A. Eskild, and K.-I. Gjesdal, “Automatic placental and fetal volume estimation by a convolutional neural network,” *Placenta*, vol. 134, pp. 23–29, Mar. 2023, doi: 10.1016/j.placenta.2023.02.009.

Risk stratification of early-stage non-small cell lung cancer using PET-based radiomics

Christine A. Santiago¹, Viswam Nair², Sarah A. Mattonen¹

¹Department of Medical Biophysics, Western University, London, Ontario

²Clinical Research Division, Fred Hutchinson Cancer Center, Seattle, Washington

Introduction: Lung cancer is the most common cause of cancer death worldwide with non-small cell lung cancer (NSCLC) accounting for 85% of all lung cancer patients [1]. Surgery with a curative intent is the standard of care treatment for early-stage NSCLC (stage I-IIIa). However, it is estimated that 30-55% of lung cancer patients will have a recurrence within 5 years after treatment [2]. To prevent recurrence, adjuvant therapy, can be given after surgery such as chemotherapy, radiation therapy, and immunotherapy. However, there is the risk of severe side effects or toxicity [3]. Currently, the decision to give a patient adjuvant therapy depends on several factors such as the stage of the cancer, the patient's age, symptoms, and medical history. To determine the stage and extent of the disease, medical images are taken prior to treatment including computed tomography (CT) and ¹⁸F-fluoro-2-deoxy-D-glucose (¹⁸F-FDG) positron emission tomography (PET) [4]. PET-based radiomics and machine learning can extract information not visible to the human eye and potentially aid in risk stratification. The aim of this ongoing study is to train, test and externally validate a PET-based radiomic model to predict time to recurrence.

Methods: Our dataset included 300 patients with early-stage NSCLC from the Verspeeten Family Cancer Centre who have undergone surgical resection. ¹⁸F-FDG-PET scans were performed prior to surgery. The regions-of-interest (ROIs) we analyzed were the tumour and a peri-tumoural region, a 1cm expansion of the tumour. These ROIs were contoured using a semi-automatic segmentation tool in MIM Software. Radiomic features were extracted using PyRadiomics 3.1.0. Features include shape-based (n = 14), first-order statistic features (n = 18), gray level co-occurrence matrix (n = 22), neighbouring gray-tone difference matrix (n = 5), gray level run length matrix (n = 16), gray level size zone matrix (n = 16), and gray level dependence matrix (n = 14). The feature extraction was performed on the original image with a bin width of 0.2 SUV. The clinical features (n = 4) included were age, sex, overall stage, and primary surgery. This resulted in a total of 109 features for analysis. The dataset was split into independent training (70%, n = 195) and testing sets (30%, n = 105). We built a random survival forest to predict time to recurrence with 100 estimators, minimum sample split of 25, minimum sample leaf of 20, and a maximum depth of 5. Concordance was used to measure the model performance in the training and testing cohorts.

Results: The number of patients that had a recurrence was 103 (n = 67 in the training set and n = 36 in the testing set). The top performing feature was overall stage, followed by gray level dependence matrix features from the peri-tumoural ROI and gray level co-occurrence matrix features from the tumour ROI. The training set achieved a concordance of 0.768 and the testing set achieved a concordance of 0.612.

Conclusion: These preliminary results demonstrate a PET-based radiomics model can identify patients with low- and high-risks of recurrence. Ongoing work in this study involves comparing the performance to clinical features alone and increasing the size of the dataset. Future work includes implementing both diagnostic CT and PET images, analyzing additional regions of interest and comparing the performance of our machine learning model to a deep learning model.

References: [1] Chen R, et al. *J Hematol Oncol*. 2020;13(1). doi:10.1186/s13045-020-00881-7
[2] Garinet S, et al. *Cancers (Basel)*. 2022;14(6). doi:10.3390/cancers14061400
[3] Cronin C, et al. *Lung Cancer Manag*. 2023;12(1). doi:10.2217/lmt-2022-0014
[4] Purandare NC, Rangarajan V. *Indian J. Radiol. Imaging*. 2015;25(2):109-120. doi:10.4103/0971-3026.155831

Automatic Classification of Levator Ani Muscle Avulsion in 3D Transperineal Ultrasound Images

Mihir Gokal^{a,b}, Golafsoun Ameri^c, Shufei Zhang^c, Helena Kunic^d, Serdar Aydin^e, Ahmed Eltahawi^c
and Elvis C. S. Chen^{a,b,f,g}

^aSchool of Biomedical Engineering, Western University, ^bRobarts Research Institute, Western University, ^cCosm Medical Corp., Toronto, ^dSchool of Engineering, University of Guelph, ^eDepartment of Obstetrics and Gynecology, Koç University, ^fDepartment of Medical Biophysics, Western University, ^gDepartment of Electrical and Computer Engineering, Western University

Introduction: Levator ani muscle (LAM) avulsion is a common traumatic injury of the pelvic floor muscle occurring during vaginal childbirth and is linked to the development of pelvic organ prolapse (POP). POP is a pelvic floor disorder that affects up to 40 % of women during their lifetime. Pelvic floor ultrasound imaging is used to diagnose LAM avulsion, but it requires trained experts and is time-consuming, leading to weeks-long delays in receiving diagnostic results and treatment. The purpose of this study is to demonstrate the feasibility of a deep learning system to automatically classify the degree of LAM avulsion from 3D transperineal ultrasound images (TPUS).

Methods: 3D TPUS images of the pelvic floor from 150 patients with and without POP-related LAM avulsion were collected. Out of these, 113 patients were included in the study. Over 650 key slices were extracted from the ultrasound volumes and cropped to a region of interest. A two-stage cascading ensemble architecture was developed, combining three convolutional neural networks (MobileNetV3-Small, EfficientNet-B0, and RegNetY-800MF) with a final decision layer. The system performs hierarchical classification: first distinguishing between normal and avulsion cases, then determining unilateral versus bilateral involvement, and finally classifying the degree of avulsion.

Results: In 5-fold cross-validation, the ensemble model demonstrated strong performance in both binary classification tasks. For avulsion detection, it achieved 86.43% accuracy, 87.70% sensitivity, 84.94% specificity, and an AUC of 0.94, consistently outperforming individual base classifiers (which achieved AUCs of 0.71-0.75). For bilateral/unilateral classification, the model achieved 80.45% accuracy, 82.32% sensitivity, 78.38% specificity, and an AUC of 0.87. When evaluated on a test set for final patient-level classification across five classes (normal, complete bilateral avulsion, complete unilateral avulsion, partial bilateral avulsion, and partial unilateral avulsion), the system achieved 46.15% accuracy.

Conclusion: This study demonstrates the feasibility of a deep learning classification system to automatically classify the degree of LAM avulsion from 3D TPUS images. While the system showed promising performance in binary classification tasks, its sequential decision-making design means that a single slice misclassification in the first classification stage can impact the final patient-level accuracy. Additionally, the limited dataset size can hinder the model's ability to generalize effectively to unseen cases. Despite these limitations, the developed system shows the potential to expedite LAM avulsion diagnosis, overcoming the time constraints of manual diagnosis. This approach can broaden screening access, benefiting areas with limited healthcare resources, by reducing expert reliance and enabling timely treatment. Future work with larger and more diverse datasets could help address current limitations and further improve classification accuracy.

Oral Presentations 5: General 1

Abstracts

A Sensorless Freehand 3D Ultrasound Solution with a Novel Coupling Pad

Libin Liang^{1,2} Ling Dai², Aaron Fenster¹

¹Robarts Research Institute, Western University, London, ON, N6A 5B7, Canada

²Department of Biomedical Engineering, Xi'an Jiaotong University, Xi'an, Shaanxi, 710049, China

Introduction. Freehand 3D ultrasound (US) is a valuable imaging technique that makes 3D US applications more accessible in clinical practice. However, current methods often depend on external sensors, which add cost and complexity, or on deep learning approaches, which are prone to cumulative drift. To overcome these challenges, we propose a sensorless solution to simplify and enhance 3D US reconstruction.

Methods. Our approach introduces a novel coupling pad with three N-shaped lines that seamlessly integrates into standard 2D US scanning, enabling 3D spatial information acquisition without external tracking devices, as illustrated in Fig. 1a. Additionally, we developed a coarse-to-fine optimization method for estimating the positions of sequential 2D US images. The optimization starts with a coarse estimation of poses based on the points introduced by the N-shaped lines and is refined using a distance-topology discrepancy reduction strategy. The proposed method was evaluated using a sponge phantom under different scanning modes: linear, oscillating, and back-and-forth, as shown in Fig. 1b. For each scanning mode, five scans were conducted, and the length indicated in Fig. 1b was measured based on 3D US to estimate the reconstruction error.

Results. Currently, our method has been evaluated only on a wireless linear probe. Phantom experiments demonstrated good accuracy, achieving errors of less than 1 mm across different scanning modes, as shown in Fig. 1c. Future work includes testing the method with multiple probes and applying it to clinical image acquisition, particularly focusing on 3D centroid evaluation.

Conclusions. This study presents an innovative and efficient solution for sensorless freehand 3D US reconstruction, enabling reliable and accurate 3D US reconstructions without the need for external sensors.

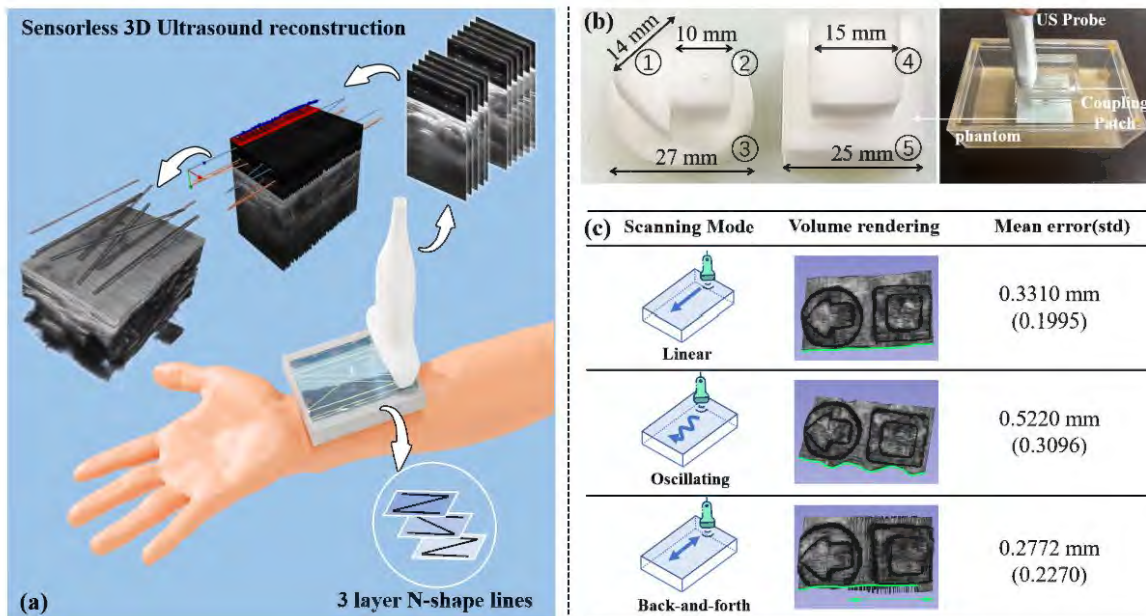


Fig.1 (a) Overview of the proposed sensorless 3D US reconstruction method. (b) Phantom experiment setup. (c) Reconstruction results under different scanning modes.

A motion assessment and image quality enhancement technique using retrospective frame averaging with low-dose volumetric 4D-CT for radiation therapy simulation

Yau T^{1,2}, Mehrez H³, Gaede S^{1,2}.

¹Department of Medical Biophysics, Western University, ²London Health Sciences Centre, ³Canon Medical Systems Canada Limited

Introduction: External beam radiation therapy is a common modality used in the treatment of lung cancers. However, patient breathing is known to introduce significant motion in the tumour that must be accounted for during treatment delivery to avoid damaging the surrounding normal tissue. Currently, four-dimensional computed tomography (4D-CT) is the gold standard for motion assessment in radiotherapy. However, due to machine constraints, conventional CT scanners are limited to an axial field-of-view (aFOV) less than 4mm. To enable the 4D reconstruction, conventional 4D-CT relies on oversampling each couch position and binning each reconstructed 4mm slice into a corresponding respiratory phase. The full dynamic volume is then retrospectively reconstructed under the assumption of periodic patient breathing. As a result, the reconstructed 4D dataset is limited to a single averaged respiratory cycle that may not fully capture the variability of patient breathing while being prone to significant motion artifacts in the presence of irregular breathing. Comparatively, the wider aFOV of newer volumetric 4D-CT (v4D-CT) of up to 160mm can allow for true dynamic imaging of tumour motion over multiple respiratory cycles that can more accurately capture irregular patient breathing while being free from motion artifacts. However, extended scan durations with the wider aFOV can significantly increase patient imaging dose. A low-dose protocol may allow for comparable imaging doses while still enabling effective motion assessment, with the large number of reconstructed volumes allowing for retrospective frame averaging to decrease noise from photon starvation. Our objective was to analyze the feasibility of a low-dose v4D-CT method for motion assessment with retrospective image quality enhancement using a frame-averaging technique.

Methods: An image quality phantom, the Catphan504, and the QUASAR Respiratory Motion Phantom were both imaged on a 320-slice Aquilion ONE PRISM CT scanner for 1 minute using a 160mm axial-field-of-view, 0.275s rotation time, and a tube current of 10mA and 100mA to simulate a low and standard dose acquisition and reconstructed using deep learning techniques. An in-house acrylic shell was created to wrap around the Catphan504 to simulate a thoracic anatomy following the shape described in the IEC Standard 61675-1. Modules for CT noise and low-contrast resolution were analyzed using an in-house MATLAB script following manufacturer specifications. Low-contrast resolution was assessed using the Rose SNR metric. The 10mA scans were subsequently frame averaged over the 60s acquisition and all metrics reassessed as functions of frames averaged. The QUASAR phantom was imaged with Delrin spheres embedded within a cedar insert while simulating a real patient breathing trace with 3cm peak-to-peak amplitude. The Delrin spheres were contoured at each phase and the centroid compared to the ground truth to verify low-dose motion assessment. Statistical testing was performed using two-tailed paired t-tests and the coefficient of determination, r^2 .

Results: CT noise was found to decrease non-linearly with a single-term power function ($r^2 > 0.99$, $p < 0.001$), with under 5 frames required to achieve CT noise in the 10mA scan superior to the 100mA scan. Rose SNR improved beyond the baseline high dose scan in 8 out of 9 inserts with frame averaging. Extracted motion profile from the 10mA QUASAR scan was found to be highly correlated to the ground truth motion ($r^2 > 0.99$, $p < 0.001$).

Conclusions: Motion assessment is feasible using low-dose v4D-CT, with significant quality enhancements observed with retrospective frame averaging. Mitigating motion artifacts while maintaining a low imaging dose will allow for better motion characterization for radiation therapy treatment planning, leading to improved clinical outcomes for patients with mobile tumours.

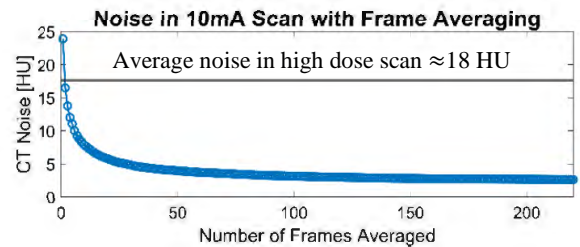


Figure 1: Noise reduction in 10mA scan observed with frame averaging

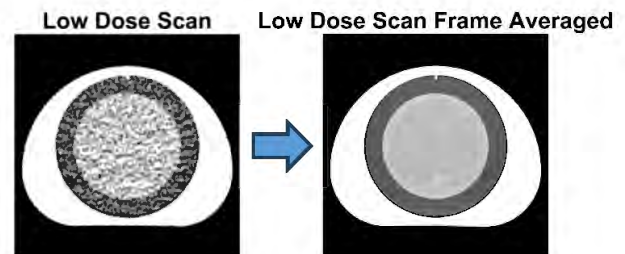


Figure 2: The noise corrupted image (left) has significant contrast improvements after frame averaging (right)

A Dual-Camera Simulation of Markerless, Optical Head Pose Tracking Using Deep Learning for Motion Correction in Magnetic Resonance Imaging

Marina Silic^{1,2}, Simon J. Graham^{1,2}

¹ Department of Medical Biophysics, University of Toronto, Toronto, ON

² Sunnybrook Research Institute, Toronto, ON

Introduction: Optical tracking (OT) methods for rigid body head pose estimation (HPE) boast high spatiotemporal resolution, making them attractive for head motion correction applications in magnetic resonance imaging (MRI). However, most OT methods require lengthy calibration routines and often rely on fiducial markers which can introduce errors if the marker becomes loose or falls out of view of the camera[1]. “Markerless” OT solutions using deep learning are a promising alternative and have achieved sub-millimetre pose estimation in robotic applications[2]; this accuracy is required for motion correction in MRI but has not yet been demonstrated. Therefore, to create a deep learning OT system, two MR-compatible cameras will be positioned in-bore above the head coil to view the markerless face. The present work demonstrates proof-of-concept of the proposed system by developing a synthetic dataset of head motion in MRI, training three neural networks, and comparing their performance towards selecting a suitable model for real-world dataset training.

Methods: A simulated dataset was generated to match the expected real-world dataset. The simulated environment was created in Blender 3D modelling software and featured a head coil model and two virtual cameras with camera parameters set to match the real cameras (e.g. focal length, f-stop, etc.) (Fig. 1). Twenty head models were used from the Headspace dataset[3] and were selected to balance sex, ethnicity, and age as well as possible. The model head pose was modified in six degrees of freedom (DOF) using six noisy sinusoids. The frequency of each DOF was randomized between [0.5, 2] mm/s or °/s and the absolute pose amplitude was 1.5 mm or °, as is typical for head motion in MRI[4]. For 2000 poses per head, images were rendered from two virtual cameras. Three neural network architectures were trained on this data. The three networks, selected for their high performance in image tasks, were a simple LeNet style convolutional neural network (CNN), an “off-the-shelf” ResNet18 model, and a twin neural network. Two sets of images are passed into these networks, whereby the first set of images are the two camera views from an initial time point and the second set of images are the same camera views at some subsequent time point. The desired 6DOF output of each model was the difference in pose between the two time points, as is desirable for motion correction methods in MRI. The hyperparameters used were an Adam optimizer, a learning rate of 1e-4, a weight decay of 1e-5, a mean-squared error (MSE) loss function, 100 epochs, a batch size of 32, and a train/validation/test data split of

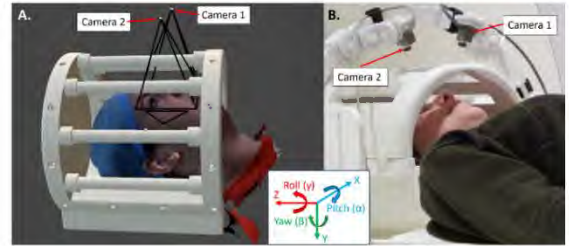


Figure 1. (A) Simulated environment, (B) Real environment

70%/20%/10%.

Results: Scatter plot results for the three models, across the 6DOF, are shown in Figure 2. The horizontal axis is the real pose difference, and the

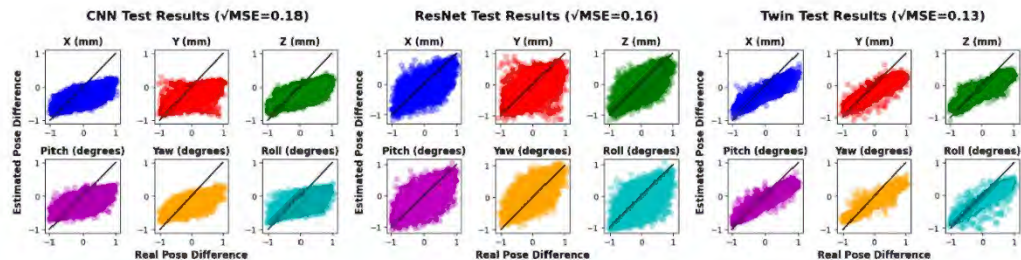


Figure 2. Test results for three neural networks

vertical axis is the model-estimate pose difference. The average \sqrt{MSE} loss is listed for each model. The twin network had the best performance on the test set and satisfied the goal of sub-millimetre and sub-degree accuracy.

Conclusion: The test results of three neural networks, trained on synthetic head motion data, demonstrate promising 6DOF head pose estimates. Although synthetic data does not capture some features found in real-world data (e.g. blinking, skin deformation, etc.) which may confound model performance on patients, by using these results as a “pre-training” step towards fine-tuned training on a real-world dataset, these features can be learned. This suggests that future development of this markerless system could lead to high quality motion correction in MRI, thereby reducing reimaging costs and improving patient outcomes.

References: [1] M. Zaitsev *et al.*, *JMRI*, 2015. [2] C. Yu *et al.*, *2019 IEEE/RSJ IROS*, 2019. [3] H. Dai *et al.*, *Int J Comput Vis*, 2020. [4] E. Seto *et al.*, *NeuroImage*, 2001.

Image Database Creation for Improved Imaging of Mitral Valve Surgery Training Phantoms

Emma Zhang^{a,b,d}, Ariana Rushlow^{b,c,e}, Patrick K. Carnahan^{b,c}, Wenyao Xia^b, John Moore^b, Gian L. Bisleri^f, Terry M. Peters^{a,b,c,d}, and Elvis C. S. Chen^{a,b,c,d,e}

^aSchulich School of Medicine & Dentistry, ^bRobarts Research Institute, ^cSchool of Biomedical Engineering,

^dDepartment of Medical Biophysics, ^eDepartment of Electrical and Computer Engineering ^fWestern University, London, Ontario, Canada ^fSt. Michael's Hospital ^fUniversity of Toronto, Toronto, Ontario, Canada

Introduction: Mitral Valve Repair Surgery (MVRS) corrects Mitral Valve (MV) pathology to ensure proper blood flow in the heart¹. Traditionally performed as open-heart surgery, MV repair has increasingly adopted minimally invasive approaches². While effective, these methods demand advanced skills and extended training, as surgeons rely solely on endoscopic views³. Competency-Based Medical Education (CBME) seeks to enhance trainee education through innovative tools like Mitral Valve Phantoms (MVPs) for Minimally Invasive MV Repair Surgery (MIMVRS) training⁴. However, MVPs lack the realistic appearance of the human MV, prompting use of Generative Adversarial Networks (GANs) to create lifelike replicas. GAN models require extensive datasets to prevent overfitting and loss of image fidelity⁵. Additionally, when generated images are connected to create a real-time video inference, a discrepancy between frames is present causing a flickering effect, indicating little to no temporal consistency. To address this, an open-source dataset for MIMVRS training was developed. Compared to an existing MV dataset⁶, our dataset contains 10,356 surgical video images, 6,625 MVP images, and 1,600 GAN-generated images. The dataset will support CBME advancements and improve MV training models.

Methods: The surgical videos were collected from MIMVRS performed by a Cardiac Surgeon (co-author GB). We manually reviewed 570 surgical videos with an average video length of 8 minutes and selected videos that contained a clear, unobstructed view of the patient MV. Next, every 60th frame from the selected sequences was extracted as an individual image. These images were then further scrutinized to filter out blurry frames or those that had an obstructed view of the mitral valve. An assortment of images containing the MV with various surgical instruments were obtained to train the algorithm to recognize the

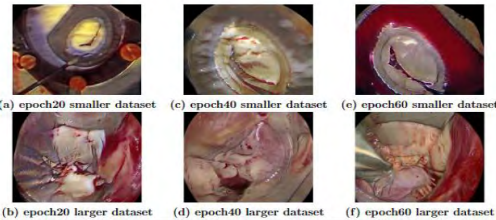


Figure 1. Generated image output for epoch 20, 40, 60 for CycleGAN comparison between Smaller Larger

MV in the presence of instruments. The MVP used for data collection was provided by Archetype Biomedical Inc. (Canada), where both healthy and prolapsed MV models were used in video recording. MVPs were first placed under the endoscope at an angle and depth similar to those in the surgical videos. Overall, 10 videos with an average of 20 minutes per video were collected using the MVP.

Results: Results from the use of CycleGAN to provide realism to the MVP model demonstrate that this approach can accurately mimic the appearance of a real MV when viewed on a static frame-by-frame basis. Moreover, by using the

Frechet Inception Distance (FID) metric⁷, we demonstrate that when a larger dataset is used to train CycleGAN, the closer the appearance between generated and real image, indicated by a lower FID score.

Epoch	Smaller_ep20	Smaller_ep40	Smaller_ep60	Larger_ep20	Larger_ep40	Larger_ep60
FID	26.975953	18.934947	22.764655	20.525597	16.942608	18.195643

Conclusion: We present a comprehensive open-source dataset that contains human MV images, MVP images, and generated “fake” realistic human MV images from the CycleGAN model. Improved realism was achieved by increased dataset size. This dataset will accelerate development of more sophisticated models to enhance the realism of the otherwise texture-free images from the MVP. In conclusion, the proposed dataset provides a basis for further development of other medical applications for MVs.

References: 1. Salik, I., Lee, L. S., and Widrich, J., StatPearls Publishing (2023). 2. St. John, A., Caturegli, I., Kubicki, N. S., and Kavic, S. M., Journal of the Society of Laparoscopic & Robotic Surgeons. (2020). 3. Unawane, A., Kamyab, A., Patel, M., Flynn, J. C., and Mittal, V. K., The American Journal of Surgery. (2013). 4. Owens, B., CMAJ. (2018). 5. Song, J., Li, P., Fang, Q., Xia, H., and Guo, R., Sustainability 14(21), 14304 (2022). 6. AdaptOR2022. (2022, April 15). 7. Heusel, M., Ramsauer, H., Unterthiner, T., Nessler, B., & Hochreiter, S., Guide Proceedings (2017, December 4).

Oral Presentations 6: Image Guided Intervention and Surgery 1 Abstracts

A feasibility study on enhanced navigation in breast-conserving surgery through haptic feedback

Laura Connolly¹, Tamas Ungi¹, Adnan Munawar², Anton Deguet², Chris Yeung¹, Russell H. Taylor², Parvin Mousavi¹, Gabor Fichtinger¹, Keyvan Hashtrudi-Zaad¹

1. Queen's University, Kingston, Ontario 2. Johns Hopkins University, Baltimore, Maryland

INTRODUCTION: It is difficult to distinguish cancer and healthy tissue during breast-conserving surgery (BCS) as tumors boundaries are often non-linear and non-palpable. As a result, many BCS procedures are unsuccessful and require revision surgery to ensure complete tumor removal. Forbidden region virtual fixtures (VF) are promising navigation tools that can prevent the surgeon from entering undesired areas, such as tumor boundaries, to avoid tumor breach. VF guidance can be deployed with cooperative or teleoperated robotic interfaces to communicate positional information through haptic feedback [1]. In this work, we present a surgical navigation system for BCS that has been enhanced with cooperative robotics and VF guidance.

METHODS: The NaviKnife system was developed at Queen's University to address the challenges in BCS with ultrasound (US) guidance and electromagnetic (EM) navigation [2]. This system relies on preoperative US to identify the shape and extent of the tumor and EM sensors that are on the surgeon's resection tool and fixed to a needle embedded in the tumor. During preoperative US, the operator annotates the tumor and a small safety margin to generate a 3D model. The position of the tool relative to this tumor model can then be visualized in a navigation interface. We extend this system by introducing a small haptic device called a Touch (3D Systems, USA) to cooperatively guide the surgeon's resection tool and impose haptic feedback around the tumor boundary (Fig. 1). We rely on the EM coordinate system to impose this boundary therefore no further registration is required. We have also shown in previous work that the Touch does not interfere with the EM tracking field [3]. To evaluate this system, we asked four users who were familiar with surgical navigation to perform resections on gel wax breast phantoms. Simulated tumors were made from gel wax and blue ultraviolet (UV) powder. Each user was asked to perform 6 tumor resections in total, 3 with VF guidance and 3 without. The first two trials were used to familiarize the user with the task and the third was used for evaluation. After the experiment, each user completed a NASA task load index survey to better understand how they felt about the enhanced navigation experience. We assessed the resection performance by looking at the tumor resections under UV light and evaluating the survey results. The percentage of total volume removed (healthy and tumor) and resection time was also calculated.

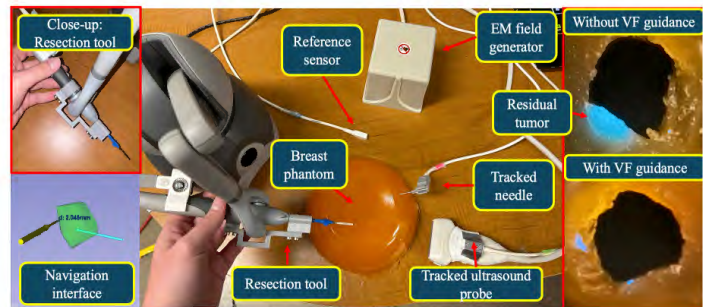


Figure 1: *Top left* – Close up of modified Touch end-effector. *Bottom left* – Navigation interface where green shape represents the tumor delineated from ultrasound, yellow is the resection tool, and blue is the tracked needle. *Middle* – Overview of navigation system. *Top right, bottom right* – Example phantom results from sample user with and without VF guidance.

RESULTS: Each user left either the same or less residual tumor tissue behind when VF guidance was applied. Generally, users also felt that the task was less frustrating, required less mental demand, and they felt more confident in their performance when haptic feedback was enabled. Interestingly, we found that users removed more combined tissue, 16.64% versus 14.4% of the total volume, when the haptic feedback was enabled and spent more time on the resection, 15.5 versus 11.6 minutes. We presume that the increased resection time and volume removal can be mitigated with more training.

CONCLUSIONS: We demonstrate that while haptic feedback reduces positive margins and alleviates mental load; at the same time, it may increase resection time and margin width. The insights gained from this feasibility study will inform the necessary design adjustments, training protocols, and operational parameters for future iterations of VF guidance in BCS. Future work will include an extensive user study to further validate these results and fine-tune our guidance system.

REFERENCES: [1] Abbott, J.J., et al. "Haptic virtual fixtures for robot-assisted manipulation." *Robotics Research: Results of the 12th International Symposium ISRR*. Berlin, Heidelberg: Springer, 2007. [2] Gauvin, G., et al. "Real-time electromagnetic navigation for breast-conserving surgery using NaviKnife technology: A matched case-control study." *The breast journal* 26.3 (2020): 399-405. [3] Connolly, L., et al., "An Open-Source Platform for Cooperative, Semi-Autonomous Robotic Surgery," *IEEE International Conference on Autonomous Systems (ICAS)*, 2021, pp. 1-5.

Physical replication and validation of mathematical mitral valve models

Patrick Carnahan^{a,b}, Charles C. X. Yuan^a, John Moore^a, Gianluigi Bisleri^c, Terry M. Peters^{a,b}, and Elvis C. S. Chen^{a,b,d}

^a.Imaging, Robarts Research Institute, London, CA, ^c.Cardiac Surgery Department, St. Michael's Hospital, University of Toronto, Toronto, CA

^b.School of Biomedical Engineering, ^d.Electrical and Computer Engineering, Western University, London, CA

INTRODUCTION: Mitral valve (MV) disease affects 2% of the Canadian population and 10% of those over the age of 75, with approximately 20% of this group requiring surgical intervention.¹ Evidence indicates the volume of MV repair cases that a surgeon performs is a determinant not only of successful mitral repair rates, but also freedom from reoperation and patient survival.² Heart simulator technologies have been developed which rely on patient-specific data to create valve replicas for surgical training and planning³. While dynamic patient-specific valve replicas have proven useful in surgical planning for specific cases, their ability to mimic actual valve geometry is limited by the spatial and temporal resolution of the images on which they are based. Alternatively, mathematical models of the mitral valve have been developed for computational applications, however, these models have not been replicated as dynamic, physical valve models and validated in a heart simulator system. We propose a new parametric representation of the mitral valve based on a combination of valve models from prior literature, combining both accurate leaflet shape, and annular geometry. Additionally, we utilize existing heart-simulator technology to validate our parametric MV model, replicated as a dynamic silicone physical valve.

METHODS: To create a valve that captures both leaflet and annulus geometry, we adapted existing mathematical mitral valve models from Shen *et al.* and Park *et al.*^{4,5} The work of Shen *et al.*⁴ describes a parametric model of

the mitral leaflets based on a set of piece-wise elliptic cylinder equations, with a flat, elongated annulus. We adapt their equations to utilize a piece-wise elliptic paraboloid geometry for the leaflets. We then use the hyperbolic paraboloid model of the annulus from Park *et al.*⁵ to modify the annulus from a flat structure to the anatomically correct 3-dimensional saddle shape with the resulting geometry shown in Figure 1. We have incorporated tunable coefficients into our model that allow for the individual control of the anterior, P1, P2, and P3 leaflet lengths and widths. We also introduce annular geometry coefficients to control anterior-posterior (AP) diameter, commissure-commissure diameter, annular

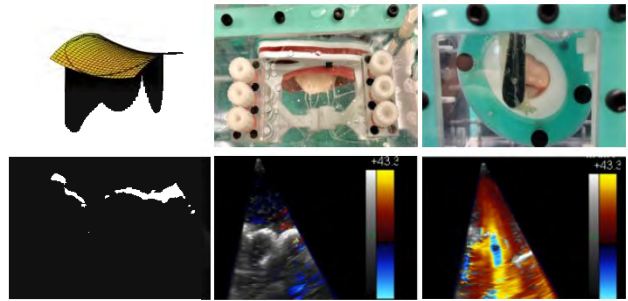


Figure 1: Generated valve geometry (top-left). Silicone valve replica in pulse duplicator (top-middle and top-right). TEE image of healthy valve (bottom-left), with Doppler images (bottom-middle). Doppler image of P2 prolapse valve showing regurgitant jet (bottom-right).

height, anterior annular curvature, and valve closure. These are standard quantitative measures used clinically which can be determined via diagnostic transesophageal echocardiography (TEE). We selected coefficients for two valves, one based on an average healthy valve, and another based on an average P2 prolapse valve. The valve models are 3D printed as a mold, then manufactured into a physical MV replica in silicone (Archetype Biomedical Inc.), and integrated into a pulse-duplicator system⁵. We use TEE to capture b-mode and colour Doppler ultrasound to evaluate valve geometry and function as would be done in a diagnostic setting clinically.

RESULTS: The replicated healthy dynamic valve model under healthy chordae tension shows no regurgitation in the pulse duplicator system. The valve shows expected systolic and diastolic behavior, with a visually realistic appearance as determined by an expert cardiac imaging clinician. The P2 prolapse valve replica exhibits significant regurgitation under colour Doppler imaging, which is consistent with expectations for a pathological valve. Both manufactured valves were quantified via 3D TEE to verify the geometry matches the dimensions defined by the computational model.

CONCLUSIONS: To our knowledge, we are the first to demonstrate a physical replica of *a priori* mathematical MV geometric models with full parametric control of clinically relevant valve dimensions. We demonstrate that physical valve replicas simulated in a pulse-duplicator show expected healthy and pathological valve behaviour. Future work will include further development of additional pathological valve models with evaluation against our healthy baseline valve to produce a library of valves for suitable for surgical training applications.

REFERENCES: 1. Asgar, A. W., *Canadian Journal of Cardiology* 33(9), 1197–1200 (2017). 2. Chikwe, J., *JACC* 69(19), 2397–2406 (2017). 3. Ginty, O. K., *Innovations (Phila)* 13, 11–22 (jan 2018). 4. Shen, X., *PLOS ONE* 12, e0183362 (aug 2017). 5. Park, J., *Semin. Thorac. Cardiovasc. Surg* 31(3), 399–411 (2019).

Non-invasive Ablation of Intra-abdominal Fetal Rabbit Umbilicus Using Magnetic Resonance Guided High Intensity Focused Ultrasound Therapy

Ava Danialy^{1,2}, Nikan Fakhari^{3,4}, Karolina Piorkowska², Tao Wang⁵, Jerome Baranger^{3,6}, Sydney Nowak², Olivier Villemain^{3,4,7}, Tim Van Mieghem⁸, Adam C. Waspe^{2,9}, James M. Drake^{1,2}

¹Institute of Biomedical Engineering, University of Toronto, Toronto, Ontario, Canada, ²Neurosciences and Mental Health, Hospital for Sick Children, Toronto, Ontario, Canada, ³Division of Cardiology, Department of Pediatrics, Hospital for Sick Children, Toronto, Ontario, Canada, ⁴Department of Medical Biophysics, University of Toronto, Toronto, Ontario, Canada, ⁵Pathology and Molecular Medicine, Queen's University, Kingston, Ontario, Canada, ⁶Physics for Medicine Paris, Inserm, ESPCI PSL Paris, CNRS, Paris, France, ⁷Bordeaux University Hospital (CHU), Department of Pediatric and Adult Congenital Cardiology; Institut Hospital-Universitaire Liryc, Fondation Bordeaux Université; Pessac, France, ⁸Maternal and Fetal Medicine, Mount Sinai Hospital, Toronto, Ontario, Canada, ⁹Department of Medical Imaging, University of Toronto Toronto, Ontario, Canada

Introduction: Twin reversed arterial perfusion (TRAP) sequence is a rare twin pregnancy anomaly characterized by inadequate cardiac development in a non-viable fetus, resulting in excessive cardiac strain on the healthy twin and a high risk of pregnancy loss if untreated. Current treatment involves invasive radiofrequency ablation, which carries significant risks, including pump twin mortality within the first month and increased likelihood of preterm labor. Magnetic resonance-guided high-intensity focused ultrasound (MRgHIFU) offers a non-invasive alternative to thermally ablate the umbilicus. This approach leverages magnetic resonance imaging (MRI) for precise spatial guidance and real-time thermal monitoring during treatment.

Methods: The objective of this study was to demonstrate that magnetic resonance (MR) guided HIFU can effectively ablate the umbilical cord in fetal rabbits and cause termination while preserving viability for untreated fetuses. Pregnant New Zealand white rabbits (gestational age: days 25-27, n=6 rabbits) were chosen for this study. Ultrafast ultrasound imaging (Vantage 256, Verasonics Inc) was performed to confirm variations in placental blood flow and cardiac output. MRI (d-stream 3T Achieva, Philips) evaluated the size and positioning of the fetuses and monitored the treatment. HIFU (Sonalleve, Profound Medical) ablated the intra-abdominal umbilical vessels in 18 fetuses with the power of 120Wac-130Wac for 16-20s, with 3-8 treatment cells each, depending on their positioning and location. MRI thermometry assessed thermal ablation in the target tissue. Post-treatment ultrafast ultrasound evaluated the placental perfusion and viability of targeted fetuses. Necropsy confirmed HIFU lesions.

Results: MR Thermometry confirmed maximum temperature of $72^{\circ}\text{C} \pm 8^{\circ}\text{C}$ across all cells, suggesting successful ablation (Figure 1). Ultrafast ultrasound imaging (UUI) confirmed termination or pre-mortem cardiac activity of 11 treated fetuses. UUI verified a decrease of $95 \pm 7.4\%$ of cardiac output in treated fetuses (n=6), compared with $11 \pm 4.6\%$ decrease in the control fetuses (n=3), $p < 0.05$. Doppler analysis showed a decrease of $83 \pm 10.0\%$ in placental perfusion of the target fetuses (n=10), opposed to $16 \pm 5.5\%$ decrease in control fetuses (n=5), $p < 0.01$. Necropsy confirmed termination of 83% of the target fetuses whilst verifying the viability of one adjacent untreated size-matched control fetus in all the experiments. No ablation marks were found on non-treated fetuses. Thermal necrosis was visible on the treated livers in 100% of the treated fetuses.

Conclusion: MR-guided HIFU therapy can effectively ablate the intra-abdominal umbilical vessels, causing termination in rabbit fetuses without harming non-targeted fetuses, as a model for a treatment procedure for twin-reversed arterial perfusion (TRAP) sequence.

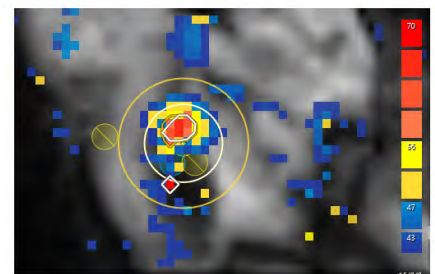


Figure 1 Coronal MRI images with thermometry overlay at 20 seconds, prior to cooling. The color scale indicates pixel temperatures: blue for $< 47^{\circ}\text{C}$, yellow for $47\text{--}56^{\circ}\text{C}$, red for $> 56^{\circ}\text{C}$. Ablated regions are segmented with a white overlay based on thermal dose calculations.

Radio-Ultrasound-Guided System for Real-Time Intraoperative Localization: A Phantom Study

Sydney Wilson^{1,2}, Hristo N. Nikolov², Amal Aziz^{1,2}, Aaron Fenster^{1,2,3}, David W. Holdsworth^{1,2,3}

¹School of Biomedical Engineering, ²Robarts Research Institute, ³Dept. of Medical Biophysics, Schulich School of Medicine and Dentistry, Western University

Introduction: Breast-conserving surgery is traditionally guided by either hand-held gamma probes or ultrasound imaging, but up to 25% of patients require a revision surgery due to limitations when using each modality alone. Hybrid imaging systems provide more accurate lesion assessment but are seldom used intraoperatively due to challenges in combining the modalities without image degradation. To address this need, we propose a novel radio-ultrasound-guided system that simultaneously acquires and co-registers high-resolution molecular data from a focused gamma probe [1] with ultrasound imaging. The objective was to design and evaluate the spatial resolution, sensitivity, and feasibility of a radio-ultrasound-guided system for real-time localization in a phantom study.

Methods: The hybrid, radio-ultrasound-guided system was realized by creating a two-part, 3D-printed receptacle; both an ultrasound transducer and the focused gamma probe securely attach to the conformal holder such that the gamma probe's focal region is aligned within the ultrasound imaging plane (Figure 1a). The two receptacles are connected through a sliding mechanism that repositions the gamma focal region at depths up to 3 cm in the ultrasound image. Real-time data was collected from each modality, packaged in PLUS Server, and broadcast using OpenIGTLink into a custom 3D Slicer module. The module displays a hybrid image consisting of a semi-transparent overlay of the reported radioactivity within a co-registered region of interest (Figure 1b).

The system was evaluated using an agar-based breast mimicking phantom with a low-activity, Co-57 radioactive inclusion (sealed source), 2 cm deep in the phantom. The first set of experiments utilized a precision stage to move the hybrid system in fixed increments to assess the spatial resolution and sensitivity. Second, one participant freehand imaged the phantom (n=3), confirming that lesions could be localized in real-time using the hybrid image.

Results: When testing the hybrid system, it was found that the focused gamma probe provided a lateral resolution of 5.3 mm, an axial resolution of 10.2 mm, and a sensitivity of 3.2 cps/kBq. As expected, the simultaneously acquired ultrasound images had a resolution and sensitivity consistent with the given imaging protocol. Further, this study confirmed that the radio-ultrasound-guided system is capable of real-time localization. Using only the hybrid display in Slicer, the device was successfully guided by hand back to the location of the inclusion.

Conclusions: The radio-ultrasound-guided system effectively combines complimentary molecular and anatomical imaging for precise, real-time localization of radiolabeled lesions. In addition to high-resolution ultrasound images, the radio-ultrasound-guided system provides simultaneous, spot detection of radiolabeled lesions with a resolution that is almost 10 times better than existing gamma probes, all while maintaining high sensitivity [2]. Overall, the radio-ultrasound-guided system has potential to improve intraoperative localization and enable clinicians to more accurately identify cancerous lesions from benign tissue in real-time in the operating room.

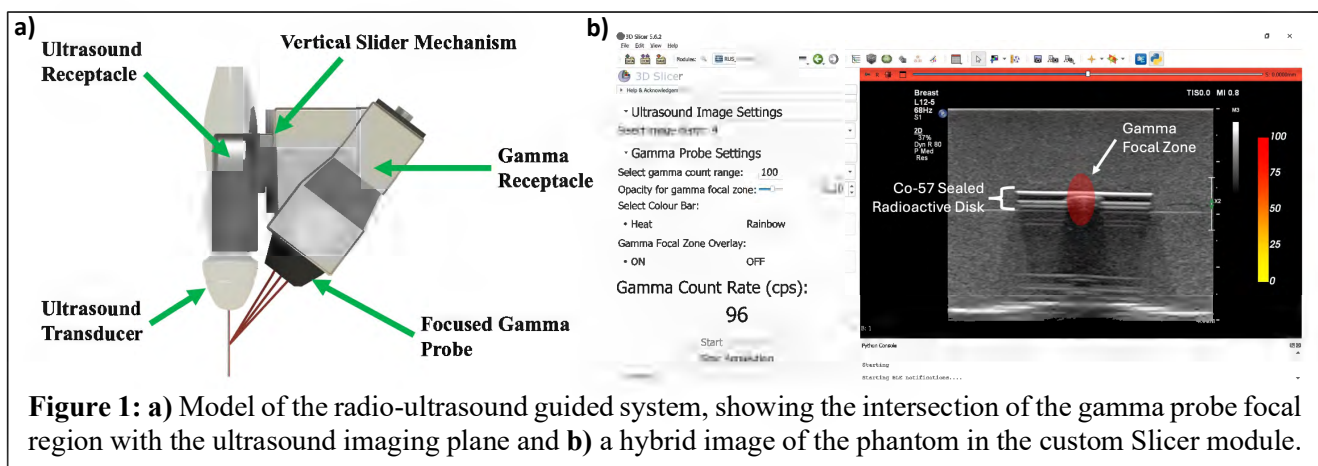


Figure 1: a) Model of the radio-ultrasound guided system, showing the intersection of the gamma probe focal region with the ultrasound imaging plane and b) a hybrid image of the phantom in the custom Slicer module.

References: 1. Wilson, S. *et al.*, "Performance assessment of a Focused Gamma Probe using Monte Carlo simulations," in *SPIE 12463*, 2023. 2. Radnia, A. *et al.*, "Development and characterization of an all-in-one gamma probe with auto-peak detection for sentinel lymph node biopsy based on NEMA NU3-2004 standard," *Ann Nucl Med*, 2021.

Oral Presentations 7: Deep Learning/Machine Learning Methodology 2

Abstracts

Micro-CT Anatomical Measurement of the Human Cadaveric Subaxial Cervical Vertebrae: Machine Learning Prediction of the Lamina Length

Joseph U. Umoh¹, James Faul², Michele Battie², and David W. Holdsworth^{1,3}

¹Preclinical Imaging Research Centre, Robarts Research Institute, ²Depts. of Anatomy and Cell Biology, ³Depts. of Medical Biophysics and Surgery, Western University, London, ON, Canada

Introduction: The lamina bone of the cervical spine is an anatomical structure that protects the posterior end of the neck spinal canal. This structure is clinically important in many operations including laminoplasty (where the lamina bone is widened to relieve pressure and pain on the spinal cord), laminectomy (where the laminar bone is removed), and laminar screw fixation for posterior fusion of the cervical spine. The lamina is situated, laterally, between the Bifid-spinous Process (BP) and the Articular Process (AP). The superior and inferior spinal canal connect the left and right lamina bone at the lamina-pedicle joint. The shape of the spinal canal is crescentic, wider at the lamina-pedicle junction. Critically relevant in operations like laminar screw fixation are the dimensions of the lamina since the dimensions determine the size of the screw that can be used.¹ In this study, we use micro-computed tomography (micro-CT) images of human cadavers and measure the relevant parameters of the subaxial cervical (C2-C7) vertebrae (fig. 1). A machine learning algorithm is then used to predict the lamina length. Our first objective is to measure and describe the relevant parameters of the cervical vertebrae that could potentially be used to predict the lamina length. These include lamina length (LL) and width (LW), Bifid-spinous Process Length (BPL) and width (BPW), Articular Process Length (APL) and width (APW), and the Superior Spinal-canal Crescentic-Length (SSCL). The second objective is to explore using multiple regression machine learning of SSCL, APL and BPL to predict LL (fig. 2).

Methods: Twelve human cadaveric cervical spines were imaged on a micro-CT scanner (GE Locus Ultra), with an x-ray tube voltage of 80 kV, a tube current of 55 mA, and a 3D-reconstructed image-volume voxel of 154 μm . All measurements of the anatomic parameters (fig. 2) were done on *MicroView*. The machine learning multiple linear regression was modeled as $LL = \beta_1 HSSCL + \beta_2 APL + \beta_3 BPL$ (without intercept), where *HSSCL* is half *SSCL*. The 48 datapoints used were split into 80% training, 10% validation, and 10% test set.

Results: Preliminary results showed the estimated multiple regression coefficients (fig. 3) as $\beta_1 = 1.20$, $\beta_2 = -0.14$, $\beta_3 = 0.12$; $R^2 = 0.5$, mean absolute error $mae = 1.9$. But with *HSSCL* alone $R^2 = 0.9$ ($P < 0.0001$). The mean left and right LL was largest at C2 (16.1 ± 2.0 mm, std) and smallest at C3 (12.0 ± 1.3 mm). Analysis of Variance (ANOVA) showed that the mean left and right LL at C2 to C7 was not significantly different from one another ($F=0.7$; $P=0.62$; $R^2=0.1637$). Similarly, maximum mean SSCL of 27.6 ± 2.8 mm was at C2 and a minimum of 24.5 ± 1.3 mm at C3.

Conclusions: This study has measured and described some anatomical parameters of the human cadaveric subaxial cervical (C2-C7) vertebrae. Multiple linear regression machine learning model was used to provide a formula that can be used to predict lamina length. This study shows that the superior spinal-canal crescentic length is the significant contributor to the lamina length prediction, and this structure can easily be measured. More data will continue to be analyzed and used to validate the regression model.

References:

1 Cho W, Le JT, Shimer AL, Werner BC, Glaser JA, Shen FH. The Feasibility of Translaminar Screws in the Subaxial Cervical Spine: Computed Tomography and Cadaveric Validation. *Clin Orthop Surg.* 2022;14(1):105-11.

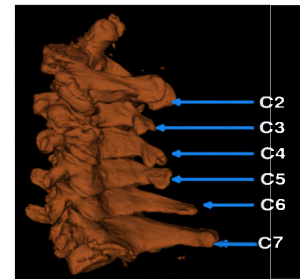


Fig. 1: Micro-CT sagittal view of the isosurface image-rendered human cadaveric cervical spine showing the subaxial cervical vertebrae C2-C7.

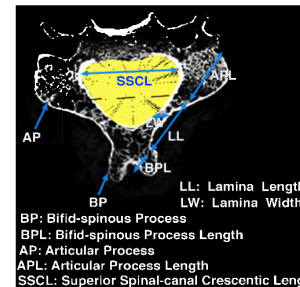


Fig. 2: Micro-CT anatomical axial view of the human cervical vertebra C3 showing the measured structures and spinal canal in yellow.

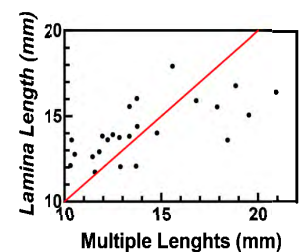


Fig. 3: Plot of the multiple linear regression of the lamina length against other variable lengths showing the predicted lamina length line in red.

Automated Diaphragm Segmentation using Deep Learning from Chest CT Images

M. Verdawala¹, D. Genkin¹, A. A. Donovan², S.E. Collins², W.C. Tan³, J. Bourbeau², M.K. Stickland⁴, B. Smith², and M. Kirby¹

¹Toronto Metropolitan University, Toronto, Canada; ²McGill University, Montreal, Canada; ³University of British Columbia, Vancouver, Canada; ⁴University of Alberta, Alberta, Canada.

Introduction: The diaphragm is the primary muscle for respiration. Previous studies show that CT-based left diaphragm morphology measurements are associated with lung function, exercise capacity, and respiratory health status in chronic obstructive pulmonary disease (COPD) patients [1]. However, these measurements are typically performed manually which is time consuming. To our knowledge, there exists no approaches to accurately and automatically segment the diaphragm volume. The objective of this study was to develop a deep learning model to automatically segment the left diaphragm dome from chest CT images. We hypothesize that the left diaphragm can be segmented using deep learning with high accuracy, and that morphological measurements extracted from the diaphragm segmentations will be significantly associated with lung function and exercise capacity in COPD.

Methods: Manual left diaphragm, defined as the portion of the diaphragm directly underneath the left lung, ground-truth segmentations were performed on 271 randomly selected CanCOLD participants by trained raters unaware of other participant information [2]. The right hemidiaphragm was not segmented due to the lack of contrast with its surrounding abdominal organs, especially the liver. A total of 150 CT images were used for training/internal testing using a 66:33% split matched for sex and COPD status. An external cohort of 33 CT images of COPD patients was used to externally test the model [3]. Preprocessing included down sampling to 256x256x256 dimensions. Known to extract high quality feature maps through multidimensional convolutions to learn spatial hierarchies at different scales, a 3D U-Net model was trained with a Dice-Sørensen coefficient (DSC) loss function with a 90:10% train/validation split until validation performance plateaued with ten-fold cross-validation to prevent overfitting. To denoise the output probability maps, post-processing was used, including: thresholding (≥ 0.5), resampling (1mm³), morphological image processing operations and thresholding ($-190 < HU \leq 150$). Performance of the deep learning model was evaluated with the DSC. This process was then applied to the entire CanCOLD cohort (n=1347); muscle composition biomarkers were extracted which included muscle volume (cm³) (DMV) and dome height (mm) (DH), which was defined as the maximum z-axis height of the 3D rotated diaphragm volume aligned with the global coordinate axes. Differences between the diaphragm measurements of no-COPD/COPD participants and associations with Forced Expiratory Volume in 1s (FEV₁), Maximum Oxygen Consumption (VO₂) and gas trapping quantified by Residual Volume/Total Lung Capacity (RV/TLC) were determined using an Analysis of Covariance test and linear regression models, adjusted for center ID, age, sex, height, BMI, race, smoking status and pack years.

Results: Demographics and lung function for the training, internal testing and external testing set is provided in Table 1. The model obtained a DSC of 0.93±0.03, 0.92±0.02, and 0.90±0.05 on the training, internal testing, and external testing datasets, respectively. For the entire CanCOLD cohort, automated segmentations were performed in 1347 participants (no-COPD (N=707): age=65.9±9.6yrs, 323(45.7%) females, FEV₁=100.6±16.6%pred; COPD (N=640): age=67.3±10.1yrs, 242(37.8%) females, FEV₁=82.5±18.9%pred). COPD participants had larger DMV (53.6±17.6cm³ vs. 49.6±16.9cm³; p<0.001) but comparable DH (45.92±13.40 mm vs 46.37±11.12 mm; p=0.524) compared to no-COPD participants, as visualized in Figure 1. Both DMV and DH were independently associated with FEV₁ (DMV: $\beta_{\text{stand}}=0.213$, p<0.001; DH: $\beta_{\text{stand}}=0.102$, p<0.001) and VO₂ (DMV: $\beta_{\text{stand}}=0.225$, p<0.001; DH: $\beta_{\text{stand}}=0.053$, p<0.05) but not with RV/TLC.

Conclusion: An automated and accurate 3D CT left diaphragm dome extraction pipeline was developed, to our knowledge, for the first time. As previously shown in the literature with manual segmentation, fully-automated CT-derived diaphragm measurements were significantly and independently associated with lung function and exercise capacity.

References: [1]Donovan et al., ATS, 2021. [2]Bourbeau et al., COPD Journal, 2012. [3]Collins et al., CHEST, 2024.

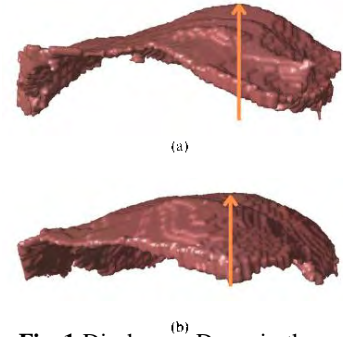


Fig. 1 Diaphragm Dome in those without (a) and with COPD (b)

Table 1. Demographics and Lung Function

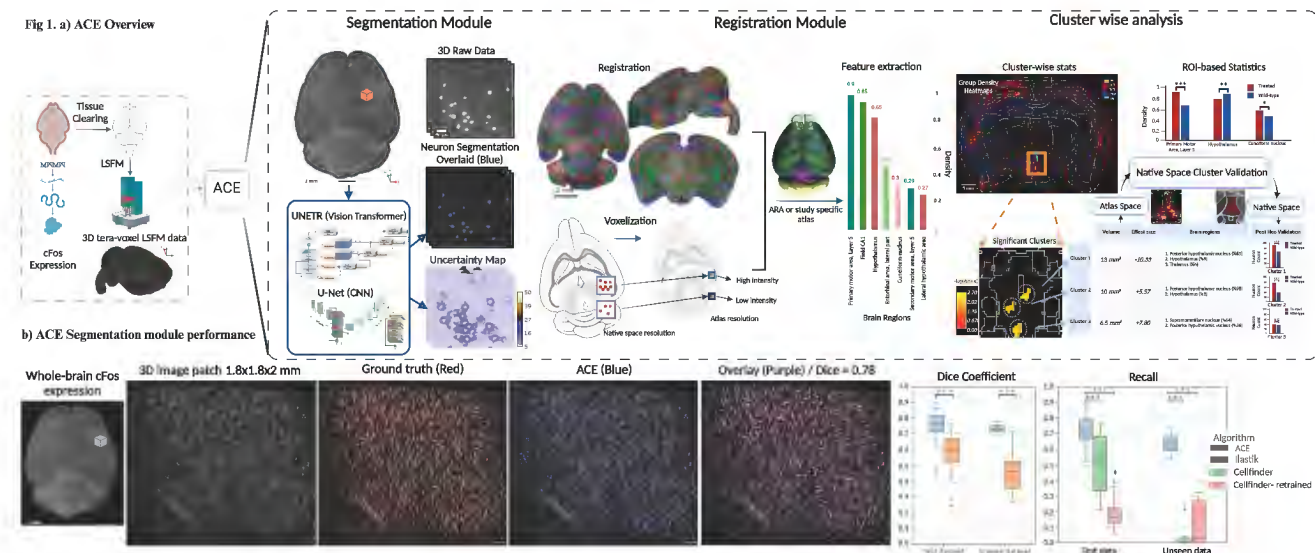
	Training (n=100)	Internal Testing (n=50)	External Testing (n=33)
Age, yrs	66.9±9.6	63.4±9.5	68.6±7.2
Female Sex (%)	50(50.0)	25(50.0)	17(51.5)
FEV ₁ , %pred	87.7±25.2	91.2±17.2	60.5±16.7

A deep learning pipeline for 3D brain-wide mapping of local neuronal ensembles in tera-voxel light sheet microscopy

A. Attarpour^{1,2}, J. Osmann, A. Rinaldi, T. Qi, N. Lal, S. Patel, M. Rozak, F. Yu, N. Cho, J. Squair, J. McLaurin, M. Raffiee, K. Deisseroth, G. Courtine, L. Ye, B. Stefanovic^{1,2}, M. Goubran^{1,2}

¹University of Toronto and ²Sunnybrook Research Institute, Toronto, Ontario, Canada.

Introduction. Mapping activity of specific neuronal populations is critical to understanding brain network dynamics underlying cognition and neurodegenerative processes¹. Light sheet fluorescence microscopy (LSFM) and tissue clearing have enabled high-fidelity imaging in intact tissue, producing large, high-resolution 3D datasets. However, analyzing these data with current computational pipelines is confounded given their reliance 1) on 2D or conventional algorithms that require laborious parameter tuning; and 2) on registration to brain atlases and aggregation of morphological features within brain regions that obscures the diversity within regions. We developed an end-to-end pipeline (ACE: AI-based Cartography of Ensembles; Fig. 1a). ACE incorporates cutting-edge convolutional neural networks- and vision transformer-based deep learning (DL) segmentation models² and threshold-free cluster enhancement (TFCE) cluster-wise permutation algorithms (Fig. 1a) to enable an unbiased and generalizable mapping of 3D neuronal local activity in whole-brain LSFM data.



Methods. ACE segmentation models were trained on optically cleared brains from 18 healthy transgenic mice (TRAP2-Ai9) expressing the c-Fos protein (~45,600 3D patches for training). Monte-Carlo dropout³ technique was deployed to estimate model uncertainty (via computing variance across models) and enhance robustness (via averaging predictions generated from 50 different models). We evaluated ACE against the state-of-the-art cell-detection and segmentation algorithms, Cellfinder⁴ and Ilastik⁵, using out-of-distribution unseen datasets (with different image characteristics, and signal-to-noise and contrast-to-noise ratios w.r.t training data). We then applied ACE to chart local and laminar neuronal ensembles across the whole brain during locomotion. **Results.** ACE demonstrated consistently superior segmentation performance (on all evaluation metrics) compared to Ilastik (an average improvement in Dice of 0.27, $p < 0.0001$, Fig. 1b) and detection performance compared to Cellfinder (an average improvement in F1 score of 0.45, $p < 0.0001$, Fig. 1b). ACE cluster-wise analysis shed light on several sub-regional and laminar neuronal ensembles activated during movement, including clusters confined to the secondary motor area layer 2/3, lateral hypothalamic regions (an ROI recently shown to play a crucial role in the recovery after lateral hemisection spinal cord injuries in rodents), and those spanning different layers of the primary motor cortex. **Conclusion.** ACE enables generalizable segmentation of neuronal somas in tera-voxel LSFM data and facilitates the discovery of differentially activated localized ensembles. ACE empowers researchers to uncover neural activity patterns independent of pre-defined atlas regions.

References. ¹Renier, N. *et al. Cell*, 2016. ²Hatamizadeh, A. *et al. ArXiv*, 2021. ³Kendall, A. & Gal, Y. *Adv. in Neural Info. Proc. Sys.*, 2017. ⁴Tyson, A. L. *et al. PLOS Comput. Biol.*, 2021. ⁵Berg, S. *et al. Nat. Methods*, 2019.

Evaluating Deep Learning Models to Classify Early-Stage Esophageal Cancer: A Preliminary Study

Marcus Milantoni¹, Rahul Nayak^{2,3}, Richard Malthaner^{2,3}, Mehdi Qiabi^{2,3}, & Sarah Mattonen^{1,3}

¹Dept. of Medical Biophysics, ²Div. of Thoracic Surgery, ³Dept. of Oncology, Western University

Introduction: In Canada, the incidence of esophageal adenocarcinoma (EA) is rising, driven largely by increasing rates of obesity and gastroesophageal reflux disease¹. Early detection and treatment can significantly improve survival, with the 5-year survival rate rising to 43% for patients undergoing curative surgery². Endoscopic resection (ER) provides a minimally invasive treatment for managing early-stage EA, however, it is limited to superficial cancers (T1N0)³. Currently, assessment of EA utilizes combined 18-FDG positron emission tomography and computed tomography (18-FDG PET/CT) to detect metastasis, followed by invasive endoscopic ultrasound (EUS) to determine the tumor (T) and nodal (N) stage⁴. This dual 18-FDG PET/CT and EUS approach uses increased resources, requires a skilled operator, and has limited accuracy (67%) in differentiating superficial lesions suitable for ER⁵. A more efficient approach is needed to determine T and N stages directly from PET/CT scans alone. Convolutional neural networks (CNNs) offer a promising alternative by extracting and analyzing complex features from medical imaging, offering the potential to characterize tumors without the need for EUS. This preliminary study aims to assess a CNN model using three different configurations to classify T and N staging.

Methods: This retrospective study included 163 patients with EA and no distant metastatic involvement, all of whom underwent esophagectomy and no induction treatment at the Verspeeten Family Cancer Centre. Prior to surgery, all patients received an 18-FDG PET/CT scan, and post-resection histopathology was used to determine the T and N stage. The dataset was split into 80% training (n=130), 10% validation (n=16), and 10% testing (n=17) stratified by T and N stage. Esophageal and stomach volumes were segmented on the CT scans using TotalSegmentator, an open-source AI tool. The CT and segmentations were down sampled to the PET voxel size, cropped to 208x208x128 voxels and used as input for a custom CNN model⁶ with the model's architecture shown in Figure 1. Three model configurations were tested: Model A, which classified T1N0 versus all other stages; Model B, a multitask model that predicted both T (T1 vs T2+) and N (N0 vs N+) stages simultaneously; and Model C, which used two separate models for T and N predictions. Models were trained for 650 epochs, with early stopping applied as necessary. Loss, accuracy, and area under the receiver operating characteristic curve (AUC) were evaluated for each model epoch on the training and validation datasets. The model with the lowest validation loss was selected for further analysis on the testing dataset.

Results: Table 1 summarizes the performance metrics of all models. While Models B and C demonstrated a lack of convergence and underperformed compared to Model A, all models exhibited the potential to classify early-stage EA effectively. The findings suggest that further optimization and a larger dataset could improve accuracy.

Conclusion: A CNN model (Model A) demonstrates promising potential for classifying early-stage EA based on PET/CT scans alone, with high accuracy in distinguishing superficial lesions suitable for ER. Although the multitask and separate-task models (Models B and C) showed lower performance, they still hold potential for future refinement on a larger dataset, with improvements made to the segmentation algorithm. These findings suggest that CNN-based analysis of PET/CT scans could streamline the staging process and reduce the need for invasive procedures like EUS.

References: (1) Sung H, et al. 10.3322/CAAC.21660 (2) ACS, Cancer Facts & Figures 2024 (3) Ilson DH, 10.1053/J.GASTRO.2017.09.048 (4) Rice TW, 10.5090/kjtcs.2015.48.3. 157 (5) Krill T, 10.21037/JTD.2019.06.50 (6) Wasserthal J, 10.1148/ryai.230024.

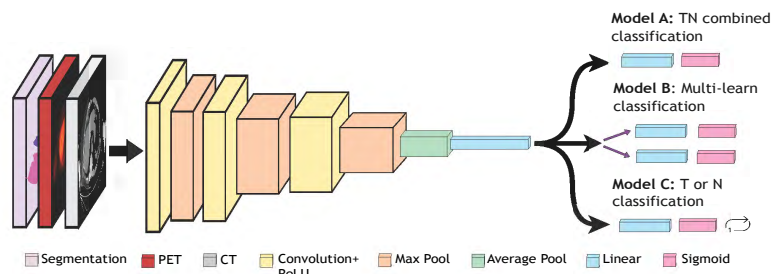


Figure 1. The convolutional neural network architecture.

Table 1. The performance metrics for models A, B and C.

Model	Epoch	AUC		Accuracy (%)		
		Validation	Testing	Validation	Testing	
Model A	519	0.64	0.61	81	94	
Model B	T	90	0.68	0.41	56	56
	N	90	0.71	0.71	56	56
Model C	T	210	0.68	0.46	56	76
	N	339	0.73	0.41	56	71

Oral Presentations 8: Image Guided Intervention and Surgery 2 Abstracts

Feasibility of three-dimensional ultrasound for cervical cancer treatment planning

Tiana Trumpour^{1,2}, Jamiel Nasser³, Lucas Mendez⁴, Douglas Hoover^{1,4,5}, Kathleen Surry^{1,4,5}, Aaron Fenster^{1,2,5}

¹ Department of Medical Biophysics, Western University, Canada ² Robarts Research Institute, Western University, Canada ³ Department of Medical Biophysics, University of Toronto, Canada ⁴ Verspeeten Family Cancer Center, Canada ⁵ Department of Oncology, Western University, Canada

Introduction: High dose-rate brachytherapy is considered a necessary part of the cervical cancer treatment paradigm. This treatment technique involves placing a highly radioactive source within the patient using specialized applicators. While conventional ultrasound (US) assists in guiding applicator insertion, computed tomography (CT) and magnetic resonance (MR) imaging are traditionally employed afterward for precise applicator localization and radiation dose planning. Although MR imaging shows superior soft tissue contrast for anatomical identification and CT effectively visualizes the applicator placement, these methods require patient relocation from the brachytherapy operating room and may be unavailable in limited-resource healthcare settings. To address these challenges, our group previously developed a three-dimensional (3D) US system capable of acquiring volumetric images of the female pelvis at the time of applicator insertion [1]. In this study, we propose the use of 3D US imaging as an alternative modality for the planning of cervical brachytherapy treatment.

Methods: This feasibility study evaluated 3D US-guided treatment with an intracavitary brachytherapy applicator through both a phantom study and clinical feasibility analysis. In each case, the test subject (currently N=2 phantoms, N=1 patients) was imaged using the 3D US system, MRI, and CT, followed by delineation of the target volume and nearby organs-at-risk (OARs) by two observers. The brachytherapy applicator was then digitized in the treatment planning software, and 3D US-based radiotherapy plans were created. For comparison, conventional MR/CT-based plans were developed for the same subjects following the clinical protocols at our institution. The effectiveness and clinical utility of the 3D US approach were then assessed by comparing these plans and ensuring the required treatment objectives were met.

Results: Volume comparisons showed that contours derived from CT images were consistently larger than those from 3D US, highlighting the need for cross-modality adjustments. Preliminary findings demonstrate that 3D US plans meet the majority of clinical requirements for dose delivery to the target volume and OARs, including the rectum and bladder. Dose-volume histograms and dose distribution overlays confirmed satisfactory target coverage. However, total source dwell times in the 3D US plans were higher than in typical CT-based cervical brachytherapy plans, suggesting that alterations in the thickness of the slices in each modality may be necessary.

Conclusions: This work demonstrates the feasibility of using 3D US as a viable approach to cervical brachytherapy treatment planning. Future work will focus on implementing 3D US-based radiotherapy planning for a wider range of brachytherapy applicators with ongoing phantom and patient studies. This approach has the potential to improve the accessibility of cervical brachytherapy, particularly in under-resourced healthcare environments.

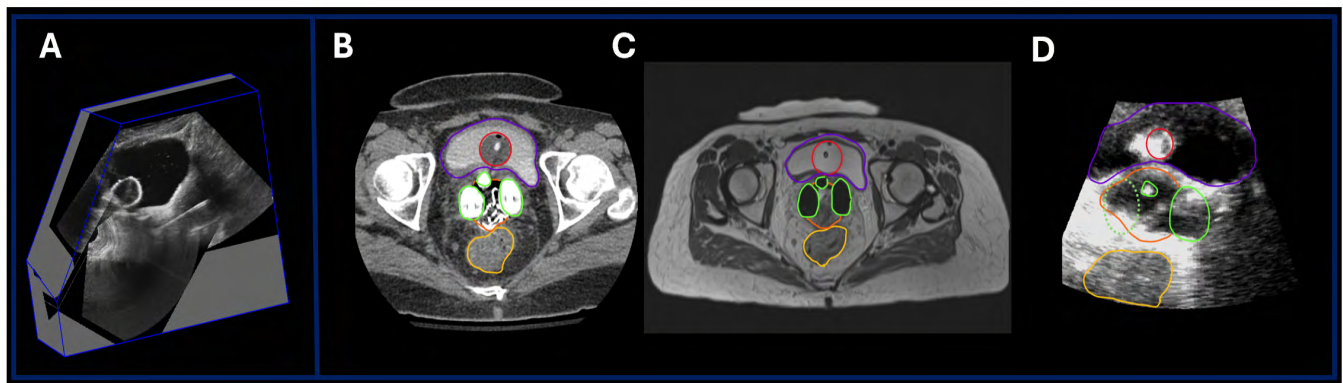


Figure 1: A) Fused 3D US image of a patient; B-D) Axial views of a CT, MRI, and 3D US image of a patient with overlays of the Foley catheter balloon (red), brachytherapy applicator (green), bladder (purple), cervix (orange), and rectum (yellow). These images were used for comparative radiotherapy treatment planning purposes.

References:[1] Trumpour T. et al. Three-dimensional trans-rectal and trans-abdominal ultrasound image fusion for the guidance of gynecologic brachytherapy procedures: a proof of concept study. *Scientific Reports* 14,18459 (2024)

First Demonstration of Functional Connectivity Mapping Using a 1.5T MR-Linac in Glioblastoma

Eaman Almasri,^{1,2} Liam S. P. Lawrence,^{1,2} James Stewart,³ Mark Ruschin,³ Aimee Theriault,³ Jay Detsky,³ Sten Myrehaug,³ Chia-Lin Tseng,³ Hany Soliman,³ Arjun Sahgal,³ Angus Z. Lau^{1,2}.

1. Medical Biophysics, University of Toronto. 2. Physical Sciences, Sunnybrook Research Institute. 3. Department of Radiation Oncology, Sunnybrook Health Sciences Centre.

Introduction: Glioblastoma (GBM) is a high-grade primary brain tumor typically treated with chemoradiation. Retrospective studies have shown an association between radiation doses to the default mode network (DMN), a set of brain regions associated with cognitive processing, and an elevated risk of cognitive toxicity, suggesting that irradiating the DMN should be avoided.¹ Furthermore, emerging evidence suggests that GBMs change in shape and size during radiotherapy,² but it is not clear how these structural alterations affect the brain's functional organization. MRI-linear accelerator systems (MR-Linacs) enable investigation of these changes through frequent MR imaging during radiotherapy. This study evaluates the feasibility of monitoring weekly changes in resting-state functional MRI (rs-fMRI) in GBM patients receiving MR-Linac-guided radiation treatment.

Methods: Twenty-five GBM patients were treated with concurrent chemoradiation using a 1.5T Elekta Unity MR-Linac. Patients received 15 or 30 MRI scans; dose schedules were 40Gy/15fx (N=1), 54Gy/30fx (N=8), and 60Gy/30fx (N=16). Imaging included daily structural T1w MRI and weekly rs-fMRI (duration = 6 min, TR/TE = 2.6/0.04s, voxel size = 3×3×5mm³). CONN, a functional connectivity toolbox, was used for rs-fMRI analysis. Individual DMN maps were obtained from a posterior cingulate cortex (PCC) seed. Resting-state functional connectivity (RSFC) matrices from 30 ROIs, selected for their involvement in key resting-state networks, were used to test if individual weekly scans could identify a single patient.³ Average within- and across-patient similarity matrix was then calculated by correlating the upper triangle part of each session's RSFC matrix against all others for all patients. Session similarities within and across patients were compared using a paired t-test.

Results: Single-patient images show that the DMN could be visualized at each treatment session. The connection between the PCC and medial prefrontal cortex (MPFC) varied across patients. In some cases, it increased (**Fig. 1A**), while in others, it decreased (**Fig. 1B**). The within-patient RSFC matrix similarity between repeated sessions (median correlation = 0.64 ± 0.02) was significantly higher (p-value <.001) than across-patient (median correlation = 0.42 ± 0.01) (**Fig. 1C**), similar to findings in healthy subjects.³

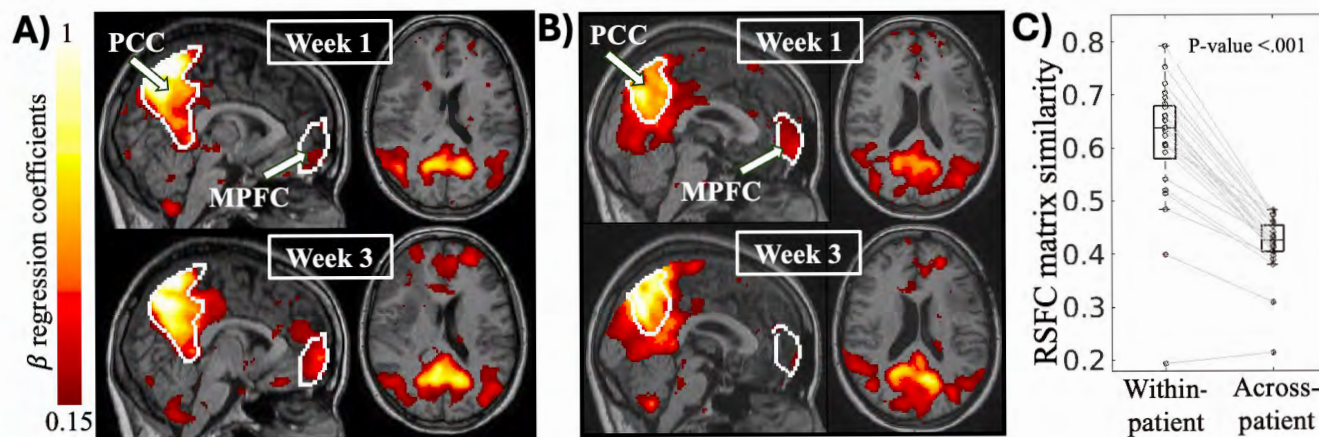


Figure 1: Weekly rs-fMRI on MR-Linac reveals PCC-MPFC connectivity changes during treatment. **A)** A 45-year-old female GBM patient (54 Gy/30 fractions) with increased connectivity. **B)** A 37-year-old female GBM patient (60 Gy/30 fractions) with decreased connectivity. **C)** RSFC matrix similarity within and across patients.

Conclusions: Our study is the first demonstration of rs-fMRI on an MR-Linac, illustrating its potential for personalized radiotherapy by detecting individual connectivity patterns. The observed PCC-MPFC connectivity changes may indicate functional alterations within the DMN during radiotherapy. Future studies will investigate co-varying factors such as patient age, tumor location, grade, and dynamics to better understand these changes. A limitation of this study is the proximity of tumors to functional networks, which will need to be accounted for through precise tumor contouring. Monitoring functional changes in rs-fMRI on MR-Linacs during GBM radiotherapy could guide treatment adaptation to eventually reduce cognitive toxicity.

References: 1. Rhodes et al, *JMIRS* 2019. 2. Stewart et al, *IJROBP* 2021. 3. Gordon et al, *Neuron* 2017.

Improving success rate of navigated breast-conserving surgery by needle stabilization

Chris Yeung¹, Tamas Ungi¹, Amoon Jamzad¹, Martin Kaufmann¹, Doris Jabs¹, Cecil Jay Engel¹, John F. Rudan¹, Parvin Mousavi¹, Gabor Fichtinger¹
¹Queen's University, Kingston, Canada

INTRODUCTION: Breast-conserving surgery (BCS) is a common treatment option for breast cancer, especially when detected at earlier stages. In BCS, balancing complete tumor excision and cosmetic outcome is a challenge. Minimizing the removal of healthy tissue improves cosmesis but also increases the chance of positive margins, where tumor is left behind. This challenge is further amplified by other factors, including the deformability of breast tissue, the lack of visibility within the breast, and the non-palpable nature of many breast tumors. The NaviKnife is a real-time electromagnetic (EM) navigation system designed to address these challenges [1]. The system visualizes the position of the surgical cautery relative to a 3-dimensional model of the tumor contoured using tracked ultrasound. The position of the tumor is determined in real-time by tracking the localization needle inserted into the tumor. Although this system showed promising results, the positive margin rate did not significantly improve, partially due to a small sample size but also due to needle slippage during the procedure rendering the navigation inaccurate [2]. The original design also required two carts, a footprint that is too large for some operating rooms (OR) and needing a longer setup time. Additionally, a radiologist must be present in the operating room to contour the tumor, increasing overall operation time and creating scheduling challenges. This study aims to address these limitations by designing a new hardware system with an updated clinical workflow.

METHODS: The new system consists of a single cart holding the ultrasound system (Teleded MicrUs), the EM field generator and sensors (NDI 3D Guidance), and the computer running the updated navigation software in 3D Slicer (Fig. 1). This allows the tumor to be contoured preoperatively, after which the whole system can be moved into the OR with minimal additional setup. In the OR, the localization needle is secured in the tumor by applying surgical glue between the needle and the guidewire and by bending the guidewire above the needle. This prevents slippage of the guidewire independent of the needle to which the EM sensor is attached. The new system was used to treat 31 patients with a single, ultrasound visible, non-palpable, biopsy-proven invasive breast cancer. Resection margins were determined by the radiology department following standard of care.

RESULTS: Positive margins were reported in 4 of the 31 patients who underwent BCS using the updated NaviKnife system, corresponding to a 12.9% positive margin rate. The system's footprint and setup time in the OR was reduced by approximately 40% and 60%, respectively.

CONCLUSIONS: With the improved system, the positive margin rate for BCS was reduced by over 40% compared to our previous work (22.5%) [1]. This is also lower than the positive margin rate reported in the literature of around 20% [3]. Since the EM sensor is attached to the needle and not to the wire or tumor, any movement of the needle independent of the wire could have falsely changed the position of the tumor in the navigation; this is prevented in this study by stabilizing the needle. The system updates also increased its efficiency and ease of use as confirmed by the clinicians, increasing the likelihood of its more widespread adoption. Overall, these findings further highlight the potential of using the NaviKnife for BCS.

REFERENCES:

- [1] G. Gauvin *et al.*, "Real-time electromagnetic navigation for breast-conserving surgery using NaviKnife technology: A matched case-control study," *Breast J.*, vol. 26, no. 3, pp. 399–405, 2020.
- [2] C. Yan *et al.*, "Study into the displacement of tumor localization needle during navigated breast cancer surgery," in *Proc.SPIE*, 2017, vol. 10135, p. 1013528.
- [3] S. G. Brouwer de Koning, M.-J. T. F. D. Vrancken Peeters, K. Józwiak, P. A. Bhairosing, and T. J. M. Ruers, "Tumor Resection Margin Definitions in Breast-Conserving Surgery: Systematic Review and Meta-analysis of the Current Literature," *Clin. Breast Cancer*, vol. 18, no. 4, pp. e595–e600, 2018.

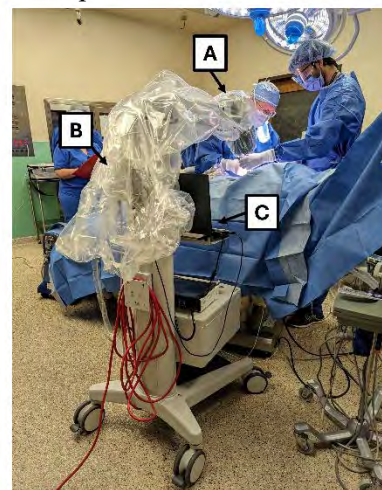


Fig. 1. New navigation system design. (A) EM field generator; (B) ultrasound system (hidden behind drape); (C) computer running navigation software.

Assessment of a mini stereotactic guidance system for percutaneous focal liver tumour ablation

Joeana Cambranis^{a,b}, Terry M. Peters^{a,b,c,d}, and Elvis C. S. Chen^{a,b,c,d,e}

^aSchool of Biomedical Engineering, ^bSchulich School of Medicine & Dentistry, ^cRobarts Research Institute, ^dDepartment of Medical Biophysics, ^eDepartment of Electrical and Computer Engineering, Western University, London, Ontario, Canada

Introduction: Percutaneous liver tumour ablation is the preferred treatment option for patients ineligible for surgery.¹ While Ultrasound (US)-guided manual insertion can achieve tumour access, it often requires multiple needle repositioning, increasing the risk of patient harm.² Surgical Navigation Systems (SNS) assist by providing additional information and mechanical support. The use of aiming devices may improve targeting accuracy, however, some designs could present limitations, such as reducing entry angles or restricting the range of movement of healthcare providers due to their large size.³ Our team developed a US-based-SNS that combines a magnetically tracked mini stereotactic, patient-attached, needle guider with virtual reality (VR) to facilitate needle positioning. Our system shows, in a computer monitor, the virtual path and ablation zone, in real-time, before needle insertion (shown in Fig. 1). Here, we present the preliminary results of comparing the traditional US guidance against our Mini-SNS, in a user trial.

Methods: Fifteen (15) non-experts performed two (2) needle insertions: 1) the traditional approach; 2) the Mini-SNS; in a random order. A custom Polyvinyl Alcohol Cryogel (PVA-c) phantom was used for the trial. The phantom replicated the left lobe of a liver with three embedded tumours and was US and CT compatible. The user's goal was to deliver the tip, of a tracked needle as close as possible to the centre of the designated tumour on each approach. Preparation time, insertion time, total procedural time, needle repositions, and final needle tip (tracked and virtual) poses were recorded.

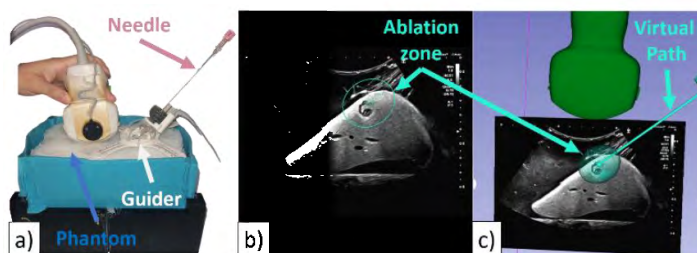


Figure 1. a) Mini-SNS components: Phantom, US and Needle Guider. b) Mini-SNS screen: virtual path and ablation zone superimposed on the US. c) Mini-SNS screen: 3D models.

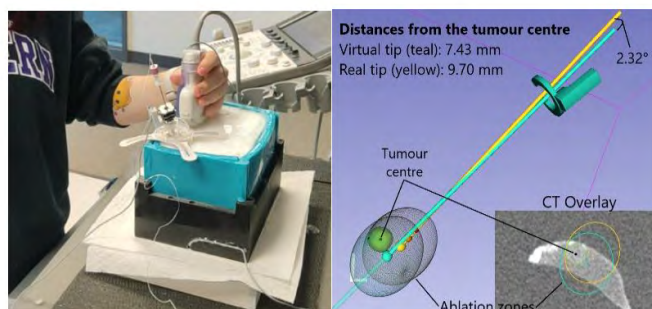


Figure 2. User VR results using the Mini-SNS approach

Results: The Mini-SNS results show a reduction in total procedural time compared to the traditional approach, most significantly in the insertion time (5 min Vs 1.4 min). The Mini-SNS mean accuracy, (Needle tip to tumour centre Euclidean distance) was 7.6 mm for the virtual tip and 9.9 mm for the tracked tip, against 18 mm for the traditional method. The average number of repositions with the Mini-SNS was 2 times compared to an average of 8 times with the traditional approach. The average angular error between the virtual path and the tracked needle was 5.30°.

Conclusion: These initial findings suggest that the Mini-SNS enhances efficiency in surgical navigation, with reduced insertion time and repositioning, supporting its potential to minimize patient harm. The non-expert cohort enabled the exploration of the Mini-SNS “out-of-plane” insertion (when was the first approach used), as participants were unfamiliar with the “in-plane” traditional technique. A limitation encountered was hand-eye disparity when using the Mini-SNS, which could be mitigated through training or augmented reality (AR) (e.g., Head-Mounted Display (HMD)) enhancing depth perception. The angular error results demonstrate needle bending during insertion, which could be attributed to the stiffness of the phantom (~ 55kPa, elastography). Future work includes testing the Mini-SNS with a real ablation needle, involving interventional radiologists (IR) and IR residents in follow-up studies, and enhancing visualization potentially using an Head Mounted Display and AR.

References: [1] Xia, Y., et al., “Long-term effects of repeat hepatectomy vs percutaneous radiofrequency ablation among patients with recurrent hepatocellular carcinoma: A randomized clinical trial,” *JAMA Oncology* (2020). [2] Engstrand, J., et al., “Stereotactic CT-guided percutaneous microwave ablation of liver tumors with the use of high-frequency jet ventilation: An accuracy and procedural safety study,” *American Journal of Roentgenology* 208 (2017). [3] Hungr, N., et al., “Design and validation of a CT- and MRI-guided robot for percutaneous needle procedures,” *IEEE Transactions on Robotics* (2016).

Pitches 5: Deep Learning/Machine Learning Methodology 2

Abstracts

Evaluating and Comparing the Surgical Tool Detection Performance of YOLO Object Detection Models in Simulated Central Venous Catheterization

Aden Wong¹, Rebecca Hisey¹, Gabor Fichtinger¹

¹School of Computing, Queen’s University, Kingston, ON, Canada.

Introduction: Ultralytics has recently introduced a new suite of YOLO (You Only Look Once) models, significantly advancing real-time object detection frameworks [1]. YOLO models are deep learning-based convolutional neural networks (CNNs) designed for fast and efficient object detection, capable of identifying and localizing multiple objects within an image or video frame in a single pass. Assessing the performance of these models in detecting surgical tools within simulated surgical videos is a critical step toward improving automated surgical workflows. Accurate and reliable detection of surgical tools is pivotal for developing assistive technologies, such as proctor-less surgical training systems and error prediction systems, which aim to enhance care, minimize errors, and improve patient outcomes. This study focuses on evaluating the enhancements in surgical tool detection offered by a premier YOLO object detection model.

METHODS: A total of 100 videos, equally divided between experts and novices performing simulated central venous catheterization, were analyzed using the YOLO models. Ten participants (five novices and five experts) each contributed 10 videos. Each video included the following tools, labeled with bounding boxes: anesthetic, catheter, dilator, guidewire, guidewire casing, scalpel, syringe, and ultrasound. Ultralytics’ four latest real-time object detection models: YOLOv8, YOLOv9, YOLOv10, and YOLO11 were selected for comparison and evaluation. Model performance was assessed using metrics such as precision, recall, mAP50, mAP50-95, and loss functions, derived from confusion matrices and training/validation data.

RESULTS: Our comparative analysis of the object detection models performing surgical tool detection in videos of simulated central venous catheterization did not reveal notable performance trends across various metrics. Although YOLO11 showed slight improvements in the mAP50 metric, this difference was not statistically significant ($p > 0.05$). Similarly, all other evaluated metrics showed little to no improvement. Training and validation loss functions were similar across all YOLO versions, with no substantial variations observed.

CONCLUSIONS: This analysis shows that YOLO11 did not achieve a statistically significant improvement in performance compared to earlier versions of the model. Additionally, the consistent performance in models across all evaluated metrics such as mAP50, and mAP50-95 underscores the limited advancements between versions for surgical tool detection. In conclusion, while newer YOLO models continue to demonstrate improved performance on benchmark datasets, their gains on simulated surgical video data remain relatively minor. This discrepancy raises an important question: why do these models excel in benchmark environments yet struggle to achieve similar progress in clinical and surgical contexts?

Understanding this gap could uncover limitations in how these models generalize to specialized applications like surgical tool detection. Future work could focus on optimizing YOLO11 to address these challenges, enhance its metrics specifically in clinical and surgical settings, and explore its performance across more diverse datasets and surgical problems.

REFERENCES: [1] Ultralytics, “Ultralytics YOLO11,” *Ultralytics.com*, 2024. <https://docs.ultralytics.com/models/yolo11/>

Table 1. Comparison of mAP50 and mAP50-95 Metrics

Model	mAP50 (B)	mAP50-95 (B)
YOLOv8	0.854	0.6552
YOLOv9	0.872	0.6355
YOLOv10	0.840	0.6069
YOLO11	0.880	0.6036

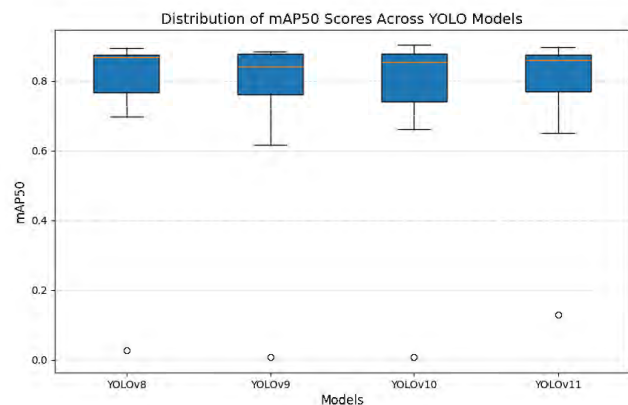


Fig 1. Distribution of mAP50 Scores Across YOLO Models

Machine Learning-Based Prediction of Vertebral Fracture Risk in SBRT Patients Using Quantitative Imaging Data

Dawit Gulta^{1,2}, Geoff Klein^{1,6}, Stephen Chen², Cari M. Whyne^{1,3-5}, Michael Hardisty^{1,3,5}

¹Sunnybrook Research Institute, ²School of Information Technology, York University, Toronto, Canada, ³Institute of Biomedical Engineering, University of Toronto, Toronto, Canada, ⁴Institute of Medical Science, University of Toronto, Toronto, Canada, ⁵Department of Surgery, University of Toronto, Toronto, Canada, ⁶Department of Medical Biophysics, University of Toronto, Toronto, Canada,

INTRODUCTION: Stereotactic Body Radiotherapy (SBRT) is effective for treating tumors in the bony spine, locally controlling tumours and decreasing pain, however there is a significant risk of vertebral compression fractures (VCFs) (14%) following Stereotactic Body Radiotherapy (SBRT) [1]. The spinal instability neoplastic score (SINS) is used clinically to assess the need for mechanical stabilization of patients with metastases in the spine. This investigation seeks to improve fracture risk assessments by using quantitative analysis of treatment planning imaging combined with machine learning algorithms. [2].

OBJECTIVES: To assess vertebral fracture risk using quantitative computed tomography (CT) based biomarkers, and combine these with clinical features in prediction models, and to compare the predictive performance of these models with Spinal Instability Neoplastic Scoring (SINS).

METHODS: We analyzed 300 spinal metastasis patients treated with SBRT (T4-L5), with an average follow-up of 17.3 months and 18.33% fracture rate. The new VCF was defined by the time interval between SBRT treatment and fracture occurrence. SINS scores extracted from the clinical dataset were used to stratify spinal instability and set thresholds for the quantitative biomarkers. Predictive features included clinical outcomes (age, sex, previous VCF), SBRT parameters, ECOG status, chemotherapy, and quantitative imaging biomarkers (volume, Hounsfield Units, collapse percentages, angle, blastic and lytic metrics). Data preprocessing involved StandardScaler for numeric features, OneHotEncoder for categorical features, and SMOTE (0.6) to address class imbalance. Six machine learning models were evaluated using stratified 80/20 split and 5-fold cross-validation, with balanced accuracy as the primary metric to predict new VCF occurrence.

RESULTS: ML models show similar performance with overlapping metrics and non-significant statistical differences. XGBoost achieved improved performance in all metrics over baseline manual SINS assessment by radiation oncologist (Table 1). Random Forest showed highest overall accuracy (0.800) and specificity (0.939) but lower sensitivity (0.182), while Neural Network achieved strong accuracy (0.767) with moderate specificity (0.898). Compared to SINS (accuracy: 0.613, sensitivity: 0.364, specificity: 0.669). Cross-validation (CV) confirmed model stability with accuracies from 59.3% to 76.7%, Random Forest showing lowest variance (std: 0.023). Sensitivity remained challenging across models (0.091-0.455). Analysis revealed that patient sex, ECOG status, age, and vertebral alignment were consistently important across the models.

Metric	XGBoost	Random Forest	Neural Network	AdaBoost	SVM	Logistic Regression	Manual SINS
Accuracy	0.750	0.800	0.767	0.750	0.650	0.517	0.613
Precision	0.357	0.400	0.286	0.167	0.188	0.154	0.198
Sensitivity	0.455	0.182	0.182	0.091	0.273	0.364	0.364
Specificity	0.816	0.939	0.898	0.898	0.735	0.551	0.669
F1-Score	0.400	0.250	0.222	0.118	0.222	0.216	0.256
Kappa	0.245	0.153	0.093	-0.014	0.006	-0.056	0.025
Balanced Accuracy	0.636	0.561	0.540	0.495	0.504	0.458	0.517
CV Mean Accuracy	0.687	0.757	0.763	0.753	0.643	0.593	N/A
CV Mean Accuracy	0.053	0.023	0.041	0.048	0.058	0.057	N/A

CONCLUSIONS: ML models demonstrated meaningful improvements over traditional SINS assessment, with XGBoost showing consistent improvement with highest balanced performance (23% higher balanced accuracy). These improvements suggest enhanced clinical decision-making potential. Future work will explore these approaches on larger datasets and in prospective studies to validate clinical utility.

REFERENCES: [1] Faruqi S, et al. Vertebral compression fracture after spine SBRT. 2018. [2] Whyne C, et al. Quantitative characterization of metastatic spine disease. 2007.

Predicting the Phase of Cataract Surgery with Deep Learning

Joshua Bierbrier¹, Rebecca Hisey¹, Bining Long¹, Adrienne Duimering¹, Christine Law¹, Gabor Fichtinger¹, Matthew Holden²

¹Queen's University, Kingston, Ontario, Canada, ²Carleton University, Ottawa, Ontario, Canada

Introduction. Cataract surgery, a widely performed procedure, involves replacing the native lens with an artificial one. Grading resident surgeons in this skill is challenging and labour-intensive. Automated approaches to assess surgical skills have been explored¹. Our overarching aim is to provide phase-specific skill assessments during cataract surgery. The first step, towards this aim, is to recognize the phases of cataract surgery. Deep learning approaches are used in several fields of surgical phase recognition². Therefore, our goal is to classify the phases of cataract surgery using deep learning. We trained a hierarchical Long Short-Term Memory (LSTM) model that uses features extracted from the ResNet50 Convolutional Neural Network (CNN) to classify the phase for each frame of a surgical video.

Methods. Thirty recordings of cataract surgeries performed at Kingston Health Sciences Centres were obtained from surgical microscopes. Fifteen surgeries were performed by resident ophthalmologists and fifteen from staff ophthalmologists. The ground truth data was created by an expert manually labelling each video frame as belonging to one of twelve surgical phases. The model was trained in two steps. The pre-trained CNN ResNet50 architecture was first trained to predict the phase for each frame of the surgical videos. After discarding the output layer of the ResNet50 model, the final layer was used as the input feature vector for a temporal model. A hierarchical LSTM model provided the final prediction, one of twelve classes, for each frame of each video. Class balancing with replacement was performed given the unequal number of frames in each phase. The dataset was divided into six folds, with a split of 20 training, 5 validation, and 5 test videos. The outcomes of interest included accuracy (the percent of correctly predicted frames), F-score (a measure of precision and recall), and Jaccard Index. Results were averaged across test videos.

Results. The model achieved an accuracy of 0.83 ± 0.06 , an F-score of 0.73 ± 0.10 , and a Jaccard Index of 0.62 ± 0.10 (Fig. 1). Fig. 2A demonstrates the model's predictions for a single video. The model performed best on the Phacoemulsification and Capsulorhexis phases with F-scores of 0.95 ± 0.05 and 0.89 ± 0.09 , respectively (Fig. 2B). Performance was poorest on Inserted Lens Positioning (F-score: 0.49 ± 0.41) and Hydration (F-score: 0.50 ± 0.28).

Conclusion. Phase recognition in cataract surgery is a challenging task due to factors like tool similarity across phases, differing surgeon technique and experience level, and ocular movements. The model performed well overall. It performed best on Phacoemulsification, the lengthiest and most technically challenging surgical phase in which the native lens is emulsified and resorbed. There are two instruments with large movement vectors in this phase, which makes it easier to differentiate from other phases. Capsulorhexis, which the model also performed well on, is similarly distinct. The model struggled with shorter phases with instruments that resemble those used in other phases, such as Hydration and Lens Positioning. Interestingly, there are instances where the model detects "Nothing" during other surgical phases when no instruments are in the field of view. Future work involves training the model on a larger dataset, comparing different architectures, and evaluating the performance against inter-rater variability. Eventually, the model can be used in surgical training by providing feedback and objective performance scores.

References. 1 Levin, M. *et al. J Surg Educ* 76, 1629–1639 (2019)

2 Demir, K. C. *et al. IEEE J Biomedical and Health Informatics* 27, 5405–5417 (2023)

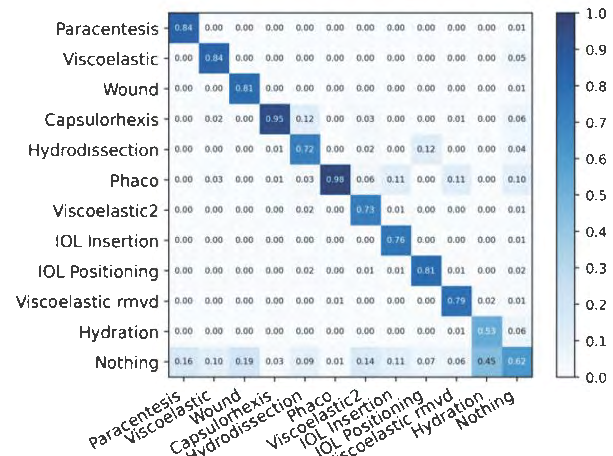


Fig. 1. Normalized confusion matrix.

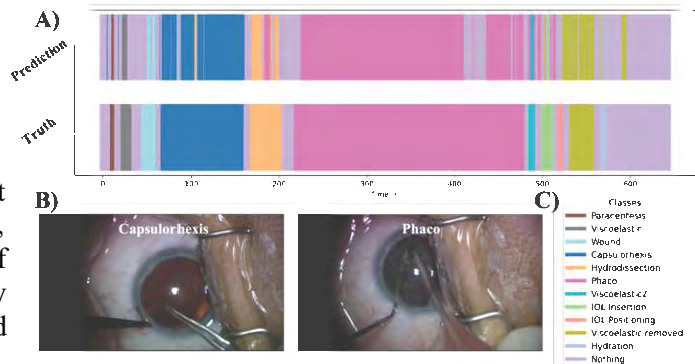


Fig. 2. A) Predictions and truth for one video B) Select phases C) Legend

Automated MRI-Based Segmentation of Multiple Fetal Brain Structures

Yasmin Modarai¹, Justin Lo^{1,2}, Matthias W. Wagner^{3,7}, Elka Miller^{3,4,6}, Logi Vidarsson⁶, Birgit Ertl-Wagner^{3,4,6}, Dafna Sussman^{1,2,5}

¹Department of Electrical, Computer and Biomedical Engineering, Faculty of Engineering and Architectural Sciences, Toronto Metropolitan University, Toronto, ON M5B 2K3, Canada,

²Institute for Biomedical Engineering, Science and Technology (iBEST), Toronto Metropolitan University and St. Michael's Hospital, Toronto, ON M5B 1T8, Canada, ³Division of Neuroradiology, The Hospital for Sick Children, Toronto, ON M5G 1X8 Canada, ⁴Department of Diagnostic and Interventional Radiology, The Hospital for Sick Children, University of Toronto, Toronto, ON M5T 1W7, Canada,

⁵Department of Obstetrics and Gynecology, Faculty of Medicine, University of Toronto, Toronto, ON M5G 1X8, Canada, ⁶Department of Diagnostic Imaging, The Hospital for Sick Children, Toronto, ON,

Canada, ⁷Institute of Diagnostic and Interventional Neuroradiology, University Hospital Augsburg, Germany

Introduction: Fetal brain MRIs allow physicians to assess and detect brain abnormalities complementary to ultrasonography [1]. Automatic segmentation of key brain structures has the potential to provide quantitative measurements, enhancing the diagnosis and detection of neurodevelopmental abnormalities [1]. Segmentation of the skull, cerebrum and external cerebral spinal fluid (CSF) can provide clinically valuable biometrics, improving diagnostic accuracy [2,3]. However, manual segmentation is time-consuming, prone to error and dependent on the radiologist's expertise and experience. This research aims to address these limitations by developing an automatic segmentation algorithm capable of segmenting the skull, cerebrum and external CSF from fetal MR images.

Methods: The dataset consists of 33 whole-body fetal MR images acquired using a 3-dimensional (3D) SSFP sequence with SENSE along 2 dimensions. The ground truth labels for the skull, cerebrum and external cerebral spinal fluid (CSF) were manually segmented using Amira Software (Thermo Fisher Scientific, MA, USA) and validated by an expert fetal radiologist. The 3D images were then sliced into 2D images in the axial plane. The 2D dataset was then split into a training, validation and test set with a ratio of 80:10:10, respectively. Convolutional Neural Networks along with vision transformers were used in developing the architecture.

Results: We will present the performance of the model, which was evaluated using the DICE similarity coefficient per class. The loss function employed is the DICE loss, which excludes the background class to prevent the model from disproportionately predicting the background.

Conclusions: An automatic fetal brain segmentation algorithm can benefit radiologists in detecting and diagnosing perinatal brain abnormalities by providing quantitative measurements accurately and reproducibly. Future work is focused on generalizing the model to include other common fetal MRI sequences and then testing its accuracy in a clinical validation study.

[1] O. A. Glenn, "MR imaging of the fetal brain," *Pediatric Radiology*, vol. 40, no. 1, pp. 68–81, Nov. 2009, doi: <https://doi.org/10.1007/s00247-009-1459-3>. [2] T. Ciceri, L. Squarcina, A. Giubergia, A. Bertoldo, P. Brambilla, and D. Peruzzo, "Review on deep learning fetal brain segmentation from Magnetic Resonance images," *Artificial Intelligence in Medicine*, vol. 143, p. 102608, Sep. 2023, doi: <https://doi.org/10.1016/j.artmed.2023.102608>. [3] J. Wang et al., "Semi-automatic segmentation of the fetal brain from magnetic resonance imaging," *Frontiers in Neuroscience*, vol. 16, Nov. 2022, doi: <https://doi.org/10.3389/fnins.2022.1027084>.

Leveraging Surgical Workflow Recognition for Skill Assessment in Simulated Cataract Surgery

Bining Long¹, Rebecca Hisey¹, Joshua Bierbrier¹, Christine Law¹, Gabor Fichtinger¹, Matthew Holden²

¹Queen's University, Kingston, Ontario, Canada ²Carleton University, Ottawa, Ontario, Canada

Introduction. Cataracts are a major cause of blindness affecting millions of individuals worldwide. Cataract surgery, which involves replacing the eye's cloudy lens with an artificial one to restore vision, is a precise procedure requiring skilled training. Automated surgical workflow recognition analyzes recorded surgical videos using deep learning to classify the major procedural steps. This approach has the potential to improve surgical training and evaluation by providing objective metrics that could facilitate task-specific skill assessment. Accurate workflow recognition relies on capturing spatial features and modeling temporal progression. While temporal convolutional networks (TCNs) have shown promise in video-based action recognition [1], their application to microscope video data, particularly in cataract surgery, remains underexplored. In this work, we deploy TCNs to recognize surgical workflow and demonstrate the potential of using the measured task durations derived from the recognized workflow as a measure for assessing surgical skill in cataract surgery.

Methods. A dataset of 25 monocular microscope videos of cataract surgeries on a Philips studio artificial eye was collected from Kingston Health Sciences Centre. The dataset includes videos of surgeries performed by one ophthalmologist and four residents, each completing five trials of four surgical steps: corneal entry, paracentesis and viscoelastic insertion, and two capsulorrhexis sub-steps: commencement of the flap and follow-through (Capsulorrhexis-A) and formation and circular completion (Capsulorrhexis-B). Videos range from 126 to 340 seconds (average 180 seconds) at 4 frames per second. Ground truths for surgical tasks were annotated by an ophthalmologist through video review. We employed a CNN-TCN approach for surgical workflow recognition. We extracted spatial features using a ResNet18 pretrained on ImageNet and fine-tuned for frame-wise tasks, and modeled long-term temporal dependencies using a TCN with dilated convolutions. Model performance was evaluated through five-fold leave-one-user-out cross-validation, with one participant for testing, one for validation, and the remaining three for training. We measured the model's performance using accuracy, defined as the proportion of video frames with correctly predicted tasks relative to the total frames. From the tasks recognized by the model, we calculated the time spent by the ophthalmologist and residents on each task for skill assessment. This was determined as the average number of predicted frames across their five videos, divided by the frame rate.

Results. The CNN-TCN model achieved a workflow recognition accuracy of 72.35%. Figure 1 presents whisker plots comparing predicted task duration variations between the ophthalmologist and residents, with ground truth durations as a reference. We observe that differences in predicted task durations generally align with ground truth patterns: residents consistently take less time than the ophthalmologist for corneal entry but more time for both capsulorrhexis sub-steps, as well as during periods of inactivity.

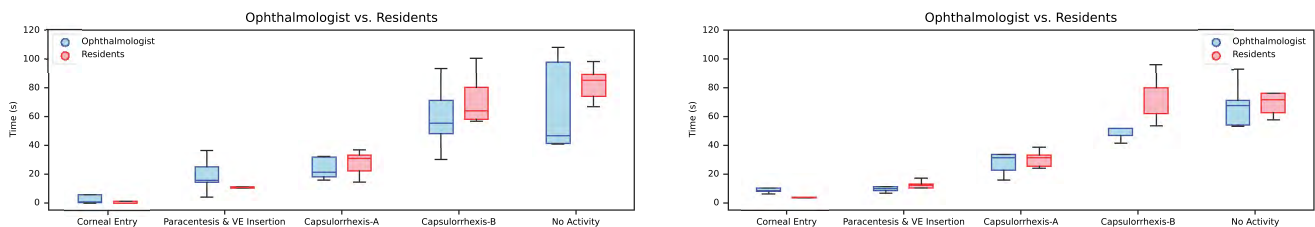


Figure 1: Whisker plots of the predicted (left) and ground truth (right) task durations for each surgical task.

Conclusions. In this work, we present a CNN-TCN approach for video-based surgical workflow recognition in simulated cataract surgery, and extend its application to calculate task durations for surgical skill assessment. While the model's task recognition performance leaves room for improvement, it was able to distinguish differences in task durations between the ophthalmologist and residents. Despite challenges posed by the small dataset size and the imbalance in surgeon expertise, with only one ophthalmologist included, this work demonstrates the potential of leveraging recognized workflow to provide objective, task-specific measures for surgical skill assessment.

References

- [1] T. Czempel, M. Paschali, M. Keicher, W. Simson, H. Feussner, S. T. Kim, and N. Navab, "Tecno: Surgical phase recognition with multi-stage temporal convolutional networks," in *International Conference on Medical Image Computing and Computer Assisted Intervention*, pp. 343–352, Springer, 2020.

Leveraging Convolutional Embeddings for AFib Detection in the Intensive Care Unit Setting

Nooshin Maghsoodi¹, David Maslove², Stephanie Sibley², Sarah Nassar³, Sophia Mannina⁴, Shamel Addas⁴,
Purang Abolmaesumi⁵, Parvin Mousavi¹

¹School of Computing, Queens University ²Department of Critical Care Medicine, Queens University ³Department of Electrical and Computer Engineering, Queens University ⁴Smith School of Business, Queens University ⁵Department of Electrical and Computer Engineering, University of British Columbia

Introduction. Atrial fibrillation (AFib), the most common cardiac arrhythmia encountered in intensive care units (ICUs), presents a significant health burden due to its associated risks of stroke, thromboembolic events, and mortality. The ICU setting poses unique challenges due to the critical nature of patient conditions and the corresponding need for immediate and accurate diagnostic information. Unlike non-ICU settings, the ICU presents a high-velocity, high-variability, yet more limited labeled data environment, complicating robust AFib detection models' development. Most existing literature on AFib detection using advanced computational methods focuses on non-ICU settings, taking advantage of larger, cleaner datasets, and does not address the nuances of critical care. Our study seeks to overcome these challenges and enhance AFib detection in ICU settings. Our work utilizes public, non-ICU ECG datasets to train Convolutional Neural Networks (CNN), which serve as feature extractors adept at identifying subtle and discriminative ECG signal patterns. These CNN-derived features, along with R-R interval analysis, provide a comprehensive feature set that feeds into a secondary more generalizable classifier. This dual-stage approach harnesses the strengths of deep learning and signal processing, informing our strategy to address the challenge of AFib detection in critical care.

Methods. Our study utilizes the data collected from bedside monitors in the 33-bed mixed-use ICU at Kingston Health Sciences Centre (KHSC). We extracted 613 10-second ECG segments from patients in the dataset, which was annotated by intensivists to rigorously validate the accuracy of the labels. This data was used as the test set to evaluate our method in the ICU setting. To detect AFib, our study employed a two-stage approach. Initially, bottleneck features were extracted from the penultimate layer of a CNN trained on the publicly available non-ICU Chapman dataset [1]. This layer was specifically chosen for its ability to capture the most discriminative, generalizable features ideal for classification tasks while avoiding the over-specialization of the final output layer. These features were then concatenated with a vector of derived R-R interval features, thereby integrating both morphological and temporal aspects of the ECG signals to form a comprehensive set of descriptors. This enriched feature set was input into the CatBoost classifier [2], a machine-learning method known for its effectiveness in managing high-dimensional feature spaces. We show that CatBoost's strengths in preventing overfitting through automatic feature selection, combined with its ability to capture non-linear relationships between features, can lead to superior performance.

Results. In our ICU dataset, 100 segments were identified as AFib and 513 as normal rhythm (prevalence 16%). Figure 1 presents an AFib rhythm sample from our dataset, which has been classified by our model as AFib. We compared our model against the CNN model and two foundation models: UniTS [3], designed for general multichannel time-series classification, and ECG-FM [4], a foundation model pre-trained specifically on ECG data. Our proposed model demonstrated improvements over these baselines, indicating that it can significantly enhance recall compared to foundation models and precision compared to the CNN model.

Conclusions. In this paper, we combine CNN-extracted features and R-R interval features using a robust classifier, CatBoost, surpassing the final layer of CNNs for classification and foundational models. By leveraging the strengths of deep learning architectures and gradient-boosting techniques, this methodology aims to enhance the performance of AFib detection in critical care settings.

References.

- [1] Zheng, Jianwei, et al. A 12-lead electrocardiogram database for arrhythmia research covering more than 10,000 patients. *Scientific data* 7.1 (2020): 48.
- [2] Prokhorenkova, Liudmila, et al. "CatBoost: unbiased boosting with categorical features. *Advances in neural information processing systems* 31 (2018).
- [3] Gao, Shanghua, et al. UniTS: A unified multi-task time series model. *The Thirty-eighth Annual Conference on Neural Information Processing Systems*. 2024.
- [4] McKeen, Kaden, et al. Ecg-fm: An open electrocardiogram foundation model. *arXiv preprint arXiv:2408.05178* (2024).



Figure 1. A sample of AFib rhythm correctly classified

Table 1. Comparison of the proposed model with baselines

Method	Recall	Precision	F1-score	AUROC
CNN	0.82	0.79	0.85	0.94
UniTS [3]	0.79	0.80	0.80	0.91
ECG-FM [4]	0.75	0.92	0.83	0.90
Our Model	0.87	0.86	0.87	0.96

Self-Supervised Parallel Transmit RF Pulse Design for 2D Spatially Selective Excitation

Yuliang Xiao¹, Jason Rock¹, Jamie Near¹, Mark Chiew¹, and Simon J. Graham¹; ¹Department of Medical Biophysics, University of Toronto, Toronto, ON, Canada

Introduction. Selective excitation is a powerful technique in MRI that enhances imaging flexibility and quality by focusing on a specific region-of-interest (ROI), which requires high-quality radiofrequency (RF) pulses. Traditional RF pulse designs, such as the small-tip-approximation (STA) algorithm, effectively concentrate on the ROI but often leave residual signals outside the target, resulting in Gibbs ringing artifacts. Recently, Jang et al. developed a framework to optimize RF pulses¹, providing an alternative that eliminates reliance on a labeled dataset. However, this method employs a simple network architecture designed for single channel transmit, limiting its ability to capture intricate details inherent in the datasets.

Significance: Using the increasing degrees of freedom provided by pTx, we introduce a self-supervised approach uses a new network and penalty strategies for pTx to ensure accurate ROI excitation in complex regions.

Methods. Our self-supervised learning framework employs an encoder-decoder architecture (Figure 1): the encoder, utilizing a convolutional neural network (CNN), captures global spatial features of input ROIs to generate RF pulses, while the decoder applies these pulses with gradients to simulate transverse magnetization for the comparison with input ROIs. We generated sufficient binary masks, each containing a closed shape (e.g., ellipse). Furthermore, 4-channel pTx simulations were conducted to obtain the B1+ maps and the gradient waveforms were designed based on a spiral-in trajectory. The overall training was optimized with the combination of several losses like mean-square error (MSE) and novel energy penalties. Additionally, we validated the framework on a single-channel transmit 3T MRI system using a phantom with a water-based central square, testing at 90° flip angles.

Results. The proposed framework successfully generated 2D spatially selective RF pulses for both pTx and single channel to target the ROI. In simulation and phantom plots (Figure 2 & 3), our framework reduced excitation outside the target area, minimizing ringing artifacts with MSE of 0.01, indicating close alignment between the simulated and target ROIs.

Conclusion. We introduced a self-supervised 2D selective excitation framework for pTx, validated by simulation and phantom experiments. The framework achieves precise ROI targeting, and reduced artifacts, with future potential for clinical MRI applications.

References

1. Jang A, et al. Physics-guided self-supervised learning: Demonstration for generalized RF pulse design. MRM. 2024

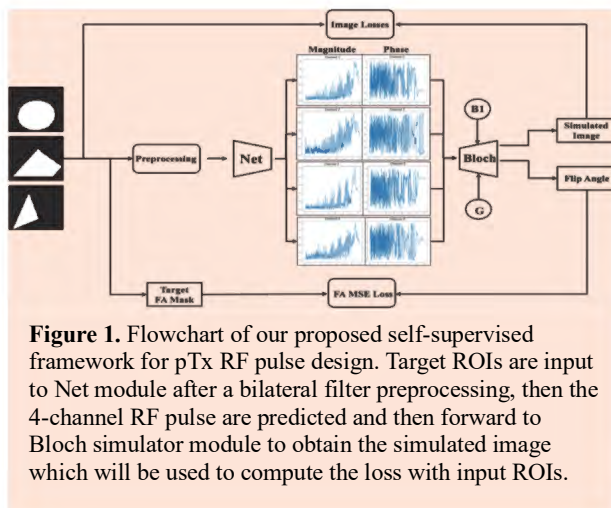


Figure 1. Flowchart of our proposed self-supervised framework for pTx RF pulse design. Target ROIs are input to Net module after a bilateral filter preprocessing, then the 4-channel RF pulse are predicted and then forward to Bloch simulator module to obtain the simulated image which will be used to compute the loss with input ROIs.

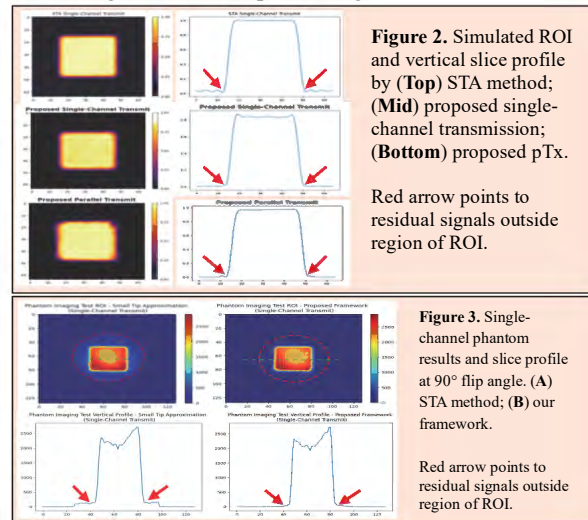


Figure 2. Simulated ROI and vertical slice profile by (Top) STA method; (Mid) proposed single-channel transmission; (Bottom) proposed pTx.

Red arrow points to residual signals outside region of ROI.

Figure 3. Single-channel phantom results and slice profile at 90° flip angle. (A) STA method; (B) our framework.

Red arrow points to residual signals outside region of ROI.

Ultrasound probe segmentation for RGB-D object tracking in central line insertion

Réna Hajar^a, Rebecca Hisey^a, Elizabeth Klosa^a, Catherine Austin^a, Gabor Fichtinger^a

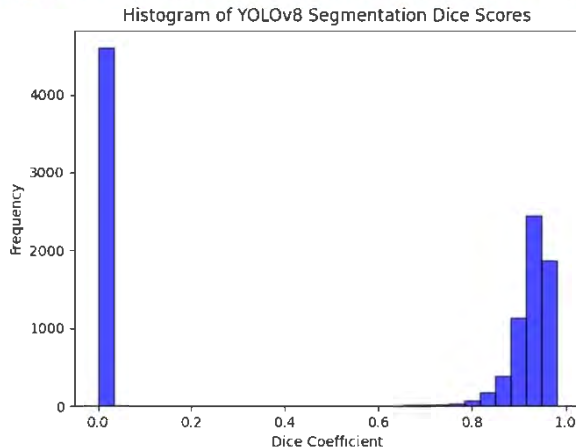
^aLaboratory for Percutaneous Surgery, School of Computing, Queen's University, Kingston, Canada

INTRODUCTION: Providing 3D guidance during medical training has been shown to enhance learning outcomes, as was demonstrated in our prior work¹. However, existing methods rely on electromagnetic or optical tracking systems, which are bulky and interfere with the natural handling of instruments during training. To overcome this, we propose a method for delivering 3D guidance without the need for additional sensors by leveraging the segmentation of medical instruments in RGB-D video streams. RGB-D cameras enable the localization of objects in 3D space by capturing both depth and color information. However, to use this capability for guidance, we need to accurately identify which pixels correspond to each instrument. This paper evaluates the first step of this pipeline: evaluating the performance of YOLOv8 in segmenting the ultrasound probe.

METHODS: Four participants were recorded performing a simulated central line insertion procedure on a phantom. Two participants were medical students, and two were experienced clinicians. With each participant performing an average of 5 trials, a total of 20 RGB-D videos were included in our dataset. Bounding boxes were created for each ultrasound probe image for each video, and these were used as a prompt for the Segment Anything model (SAM)² to create segmentations. The segmentations were finally manually refined in 3D Slicer ([slicer.org](https://www.slicer.org)). The ultrasound probe segmentations were then used to train a YOLOv8³ model to segment the ultrasound probe. A 4-fold, leave-one-user-out cross validation method was used to train the model. Each fold used three different participants' trials as training sets, one participant as a test set, and one of each training participant's trials as validation for fine-tuning. The

model was evaluated using the average dice scores among the 4 folds.

Figure 1: Dice score distributions among test set predictions



RESULTS: The following results were obtained by training and testing the segmentation model. The model received an average dice score of 0.56. Histograms made of the dice score distributions of testing images are shown in Figure 1. Where the model was found to falter most were situations in which the probe was obstructed by the participant's hand, or other tools in the frame. In these cases, the probe was not recognized. In clear images of the ultrasound probe, predicted segmentations were in line with the ground truth with high confidence.

CONCLUSION: The model's performance on images with a clear view of the ultrasound probe shows potential for future implementation of YOLOv8 to build an RGB-D dataset. The fault in the generated predictions isn't the segmentations themselves, but the identification of the ultrasound's presence entirely. The failure to recognize the ultrasound probe where occlusion is present motivates the need for more training data to improve the generalizability of the model. Future investigations may include self-supervised learning to account for the initial lack of data in training this model.

REFERENCES: [1] Tamas Ungi, Holden M, Zevin B, Gabor Fichtinger. Interventional procedures training. Elsevier eBooks. 2019 Oct 25; 909–29. [2] Meta AI, "Segment Anything Model," *segment-anything.com* (2023), <https://segment-anything.com/> [3] Ultralytics, "Ultralytics YOLO8," *Ultralytics.com*, (2023), <https://docs.ultralytics.com/models/yolov8/>

Pitches 6: Image Guided Intervention and Surgery

Abstracts

Validation of an electroanatomic map conversion tool for registration to radiation treatment planning images

Authors: Sarah Konermann, MSc¹, Ian J. Gerard, M.D., PhD², Martin L. Bernier, M.D.³, Tarek Hijal, M.D.², Gabriela Stroian, PhD¹, Neil Kopek, M.D.², Joanne Alfieri, M.D.², Lynn El-Hamed, BEng⁴, Piotr Pater, PhD¹

1. Medical Physics Unit, Gerald Bronfman Department of Oncology, McGill University, Montreal, Quebec, Canada
2. Division of Radiation Oncology, Gerald Bronfman Department of Oncology, McGill University, Montreal, Quebec, Canada
3. Division of Cardiology, Department of Medicine, McGill University, Montreal, Quebec, Canada
4. Biosense-Webster, Johnson & Johnson, Markham, Ontario, Canada

Introduction/Background: Cardiac radioablation – a novel treatment that targets areas of the heart with external radiation – is a promising therapeutic modality for refractory ventricular tachycardia. The radiation target is determined using electroanatomic maps, and then delineated on CT images. However, there is no native way to overlay electroanatomic maps on CT images in a radiation treatment planning system, making accurate targeting a challenge. We have developed a tool, Edico, which converts electroanatomic maps into image slices that can be imported into a radiation treatment planning system and registered to CT images¹. Edico creates maps of voltage points that fall within a certain distance, or fill threshold, of points where data was actually acquired in the mapping procedure.

Objectives/Methods: We hypothesize that Edico can convert electroanatomic maps from the CARTO3 mapping system (Biosense-Webster, Yokne'am Illit, Israel) accurately and without obscuring minute details. We designed three electroanatomic maps in the shape of 4 cm by 6 cm by 10 cm rectangular prisms: One with voltages of 1 mV at all points, on all of its sides, with true mapped points falling in each corner of the prism and a 10 mm fill threshold; one with ten voltage bands alternating between 0.5 mV, 1 mV, and 1.5 mV with a 1500 mm fill threshold; and one with a voltage gradient defined along all four of its long sides, from 0 to 2 mV with a 1500 mm fill threshold. All of these electroanatomic maps were processed using Edico and imported into the treatment planning system (Eclipse, Varian Medical Systems, Palo Alto, California), and relevant details of the maps were measured to ensure they matched the original data.

Results: All processed maps are shown in Figure 1. The first test case displays mapped regions within 10 mm of the true mapped points, as measured in the treatment planning system. The second test case shows ten clear bands of alternating voltages, as expected, with no issues at transitions. The third test case displays a gradient along its long sides, as expected.

This shows that Edico can be used to accurately represent electroanatomic maps in a treatment planning system along with other treatment planning images.

Conclusions: We have shown that Edico can be used to reliably create treatment planning system-compatible electroanatomic maps using three test cases that were processed using this software. In the future we hope to show that the use of Edico results in greater targeting accuracy, leading to improved patient outcomes and greater tissue sparing for organs surrounding the heart.

References:

1. Konermann SL, Gerard IJ, Bernier ML, et al. The conversion of electroanatomic maps for compatibility with treatment planning systems in cardiac radioablation target volume definition. *Med Phys*. Published online November 29, 2024. doi:10.1002/mp.17531

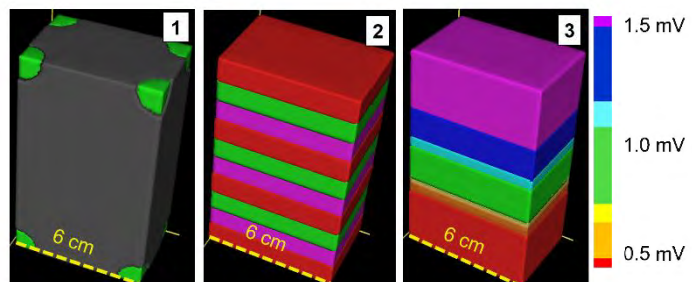


Figure 1: Test cases 1-3 after processing with Edico.

THROMBECTOMY ASSIST: LIVE THROMBUS DETECTION

Lola Assad¹, Alfred M. Franz², Jan Komposch², Timo Baumgärtner², Johannes Rosskopf³, Michael Braun³, Bernd Schmitz³

1. Queen's University, 2. Ulm University of Applied Sciences, 3. Neuroradiology Section, District Hospital Guenzburg

INTRODUCTION

Thrombectomy Assist^{1,2} focuses on the detection of vascular occlusions (thrombi) during the treatment of ischemic strokes using thrombectomy. This is accomplished by live detection of thrombi in digitally subtracted angiographies (DSA). This model is one of the first of its kind to couple an angiography machine with an artificially intelligent assistant for the noninvasive detection of thrombi using purely computational methods live during radiology-guided procedures. Thrombectomy Assist provides nearly hands-free assistance for neuroradiologists, allowing for accurate and timely detection of thrombi.

OBJECTIVES AND METHODS

Thrombectomy Assist aims to provide live thrombus detection in thrombectomies and other DSA-assisted procedures. A Siemens ARTIS Angiography machine is used for the collection and live transfer of DSA sequences. The AI model consists of (1) a convolutional neural network for the extraction of key features from the DSA sequences, (2) a recurrent neural network for pattern recognition from the extracted features, and finally (3) a deep learning classifier for the probabilistic classification of the DSA sequence as either thrombus free or non-thrombus free. The model was trained using 5-fold cross-validation then retrained on the whole of the available dataset. The objective of this study is to test the system on new DSA sequences that also contain smaller thrombi of M3 and M4 segments of the internal carotid artery.

RESULTS

Thrombectomy Assist was found to be effective in accurately classifying DSA sequences as thrombus-free or non-thrombus-free when the DSA sequences involved cases of M1 and M2 thrombus. The new small dataset from 25 patients and a total of 46 DSA sequences denote a recall of 85%, an accuracy of 91%, and a precision of 100%. The thrombi with the highest accuracy scores were M1 and M2, and those with the lowest were M3 and M4. This new dataset provides insight into where to target the expansion of the training dataset for the improvement of the model and will aid in Thrombectomy Assist's ability to generalize across various classes of thrombi.

CONCLUSION

These findings are important for future work in computer-assisted interventional radiology as they set the foundation for other models designed for live use in radiological procedures. Current work on Thrombectomy Assist is focused on the improvement of M3 to M4 thrombus detection, and the development of an assistant model for an entirely hands-free, automatic start and stop of the model without a technician's intervention. More cases are being collected where M3 to M4 thrombi are present to improve the classification of these thrombi, as they are far less prevalent than M1 and M2 thrombi.

REFERENCES

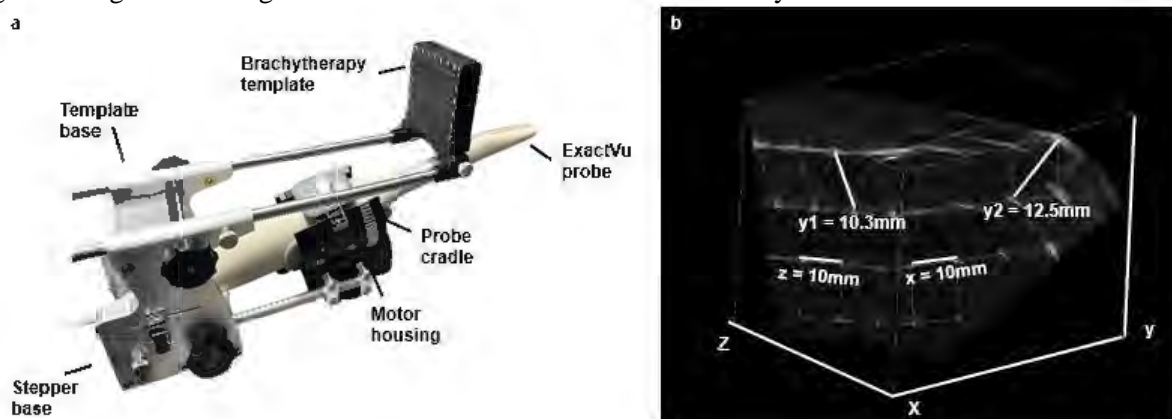
- Mittmann, Benjamin J et al. "Deep learning-based classification of DSA image sequences of patients with acute ischemic stroke." Int J Comput Assist Radiol Surg 17,9 (2022): 1633-1641.*
- Baumgärtner, Timo et al. "Towards Clinical Translation of Deep Learning-based Classification of DSA Image Sequences for Stroke Treatment." In: Bildverarbeitung für die Medizin 2023. Informatik aktuell. Springer Vieweg, Wiesbaden.*

Title: Development of a Novel System for Micro-Ultrasound-Guided Focal Low-Dose-Rate Prostate Brachytherapy. David Contella^{1,2}, ¹Kevin Barker^{1,2}, Aaron Fenster^{1,2}, Douglas Hoover^{2,3}, Lucas Mendez^{2,3}
¹Robarts Research Institute, London, Ontario, Canada. ²Western University, London, Ontario, Canada. ³London Health Sciences Centre, London, Ontario, Canada.

Background: Radiation therapy is a common method to treat prostate cancer, typically involving irradiation of the whole prostate gland. However, recent evidence has suggested that providing an additional dose of radiation confined to the most aggressive tumour, or a focal boost, is beneficial in preventing cancer recurrence.¹ Low-dose-rate brachytherapy (LDR-BT) is a technique that allows for precise control of radiation dose by implanting small pieces of radioactive material, known as seeds, inside the prostate. These seeds only irradiate the immediate region of surrounding tissue making it useful for delivering a focal boost.² To visualize the prostate gland and malignancies for focal LDR-BT, two imaging steps are required. Transrectal ultrasound (TRUS) is used intraoperatively to guide radioactive seed placement in the prostate; however, standard TRUS systems are incapable of visualizing intraprostatic tumours.² Thus, additional imaging with multiparametric magnetic resonance imaging (mp-MRI) is required to locate these malignancies and ultimately deliver a focal boost.³ While this method is effective in locating tumours, mp-MRI imaging increases the treatment's cost and complexity.³ Recent innovations in micro-ultrasound technology such as the ExactVu micro-ultrasound system, can be used to visualize intraprostatic tumours in real-time, and has been used as a substitute for mp-MRI in targeted prostate biopsy. This highlights an unmet need for a micro-ultrasound-guided focal LDR-BT treatment.

Objectives / Methods: Given the potential advantages associated with incorporating micro-ultrasound for focal LDR-BT, we developed a mechatronic stepper device that mimics clinical TRUS systems while accommodating the unique features of the ExactVu ultrasound probe. Additionally, we developed software for three-dimensional (3D) micro-ultrasound image reconstruction. Geometric validation of the system was performed by imaging a grid phantom suspending four layers of wires each creating a 10x10 grid and comparing the measured distance on the reconstruction to the actual spacing between wires. To ensure the device is feasible for clinical use, we aim to perform additional phantom tests, ensuring that volume measurements are accurate and the system easily interfaces with the clinically used treatment planning software VariSeed. Additionally, we plan to conduct mock LDR-BT treatments with prostate-mimicking phantoms by implanting non-radioactive brachytherapy seeds and imaging them with a computed tomography scan, which is the gold standard for imaging implanted seeds. Dose calculations would then determine if the system can accurately guide needles and achieve safe clinical outcomes.

Results: We have designed and built a mechatronic device, as seen in Figure 1(a), which houses the ExactVu micro-ultrasound probe and is capable of reconstructing 3D volumes using fan geometry. Geometric validation was performed on the image displayed in Figure 1(b) and confirmed that 3D reconstructions are accurate with the largest average error being .23mm off from the actual distance in the y1 direction.



Conclusion: The development of this system marks a step towards improving the accessibility of focal radiation therapy for prostate cancer by providing clinicians with a low-cost method to visualize prostate cancer intraoperatively. Given its capabilities, micro-ultrasound paired with our device could be the standalone imaging modality for focal LDR-BT and would be easily implementable for high-dose-rate focal brachytherapy.

References:

1. Kerkmeijer LGW, Groen VH, Pos FJ, et al. *JCO*. 2021;39(7):787-796.
2. King MT, Nasser NJ, Mathur N, et al. *Brachytherapy*. 2016;15(3):266-273.
3. Lorusso V, Kabre B, Pignot G, et al. *Clinical Genitourinary Cancer*. 2022;20(4):e339-e345.

3D Calyx Segmentation for the Volumetric Detection of Hydronephrosis

Marina Music¹, Rebecca Hisey¹, Gabriella d'Albenzio¹, Zhuoxin Guo¹, Catherine Austin¹, Gabor Fichtinger¹

¹School of Computing, Queen's University, Kingston, Canada

Introduction: Hydronephrosis (HN) is a condition affecting the kidney that occurs when an obstruction, often in the form of a kidney stone or tumor, leads to urine build up that dilates the renal pelvis and/or calyces. The timely diagnosis and treatment of HN is vital due to its potential to cause severe kidney damage and even kidney failure. Currently, HN is diagnosed by a radiologist using grading scales such as the Anterior–Posterior (AP) Diameter of Renal Pelvis (APDRP) and SFU, but the grading varies widely between radiologists, with APDRP only reaching consensus in 64% of physicians [1]. This work aims to develop a robust methodology for the 3D segmentation of renal calyces from computed tomography (CT) scans, enabling the precise quantification of calyx to kidney volume ratio as an objective metric for the detection and assessment of HN.

Methods: The KiTS23 dataset is a publicly available dataset containing the abdominal CT scans of the kidneys of 589 patients with renal cancer, some of which also present with HN, along with segmentations of their kidneys. A trained radiologist reviewed the first 126 cases of the KiTS23 dataset (due to time constraints) and provided HN labels, leading to the exclusion of cases 5 and 40 due to congenital anomalies. The CT scans were pre-processed to adjust contrast by setting the window level to 40 and the window width to 350. Kidney segmentations were pre-processed by applying morphological filling operations to fill any discontinuities within the segmentation contours, ensuring complete delineation of the kidney boundaries. The kidney segmentations were subsequently used to isolate the voxel intensities corresponding to the calyceal regions for further analysis. A median smoothing filter was applied to reduce noise, followed by application of the Otsu method for optimal thresholding of the calyces within the region of interest. Segmentations were used to quantify calyx and kidney volumes, and the ratio of the calyx to kidney volume was calculated for the left, right, and combined kidneys of each patient. Three Random Forest models were trained on either the left, right, or combined ratios with a 70-30 train-test split and a random state of 42. The class weight parameter was set to balanced and the Synthetic Minority Oversampling Technique (SMOTE) was applied to address the class imbalance in the data. Receiver Operating Characteristic (ROC) curves were plotted for the output of each model (Fig.1), and AUC score and balanced accuracy were computed to further assess the models.

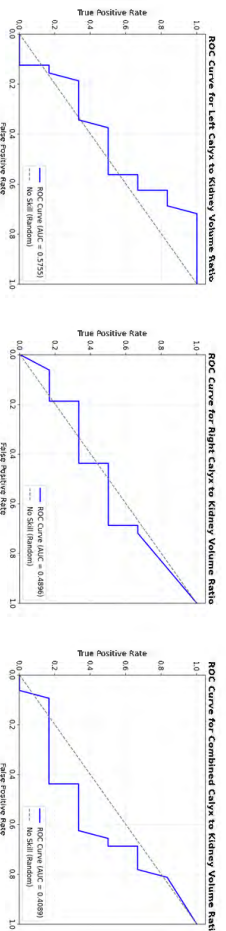


Fig.1: ROC curves for three Random Forest models trained on the left, right, and combined calyx:kidney volume ratios to predict HN **Results:** The radiologist detected a 15.32% prevalence of HN among the 124 cases. The AUC scores were 0.5755, 0.4896, and 0.4089, and the balanced accuracy was 0.4844, 0.4792, and 0.3646 for the left, right, and combined ratios, respectively.

Conclusions: Segmenting the calyces presents significant challenges due to their irregular shape, frequent absence of well-defined boundaries, and low contrast between calyces and surrounding renal structures. Given the complexity of this segmentation problem and the challenges posed by a highly imbalanced dataset, the modest AUC and balanced accuracy scores for our Random Forest models indicate the need for a more robust and expressive framework for calyx segmentation as well as more sophisticated strategies to address class imbalance. Future steps involve using the generated segmentations as ground truth labels to train a foundation model to automatically segment and quantify calyx volume from CT scans. Automated HN detection using the objective metric of calyx to kidney volume would allow for the earlier detection of HN and tracking disease progression over time.

References: [1] Omen, A. Front Pediatr. 2020.

Predicting patient-specific instantaneous spatial temperature maps for MR-guided laser interstitial thermal therapy for epilepsy using a physics-informed neural network

Saba Sadatamin^{1,2,3}, Steven Robbins³, Elise Donszelmann-Lund², Yin Hau Wallace Lee², Richard Tyc³, George M. Ibrahim^{1,2}, Lueder A. Kahrs¹, Adam C. Waspe^{1,2}, James M. Drake^{1,2}

¹University of Toronto, Canada, ²The Hospital for Sick Children, Canada, ³Monteris Medical, Canada.

Introduction: MR-guided laser interstitial thermal therapy (MRgLITT) is a minimally invasive technology to ablate seizure foci with the aid of MR thermometry (MRT). However, the heat distribution from the laser fibre is unpredictable due to natural heat sinks in the brain, creating a challenge for treatment planning. This study aims to improve preoperative MRgLITT planning for epilepsy. To achieve this, we developed a physics-informed neural network (PINN) by integrating a U-Net model with the bioheat transfer equation (BHTE) and segmented MRI planning images. This PINN is designed to increase the prediction accuracy of patient-specific temperature maps, addressing the limitations of purely data-driven approaches.

Methods: We utilized a dataset of MRI planning images and corresponding MR temperature maps collected during 184 cases of MRgLITT for medial temporal lobe epilepsy. The PINN model combined segmented MRIs with a simulated heatmap generated from the BHTE. We evaluated the performance of our model by comparing the treatment area and measuring the pixel-wise temperature accuracy using several metrics, such as root mean square (RMS) error, Hausdorff distance, and structural similarity (SSIM) index.

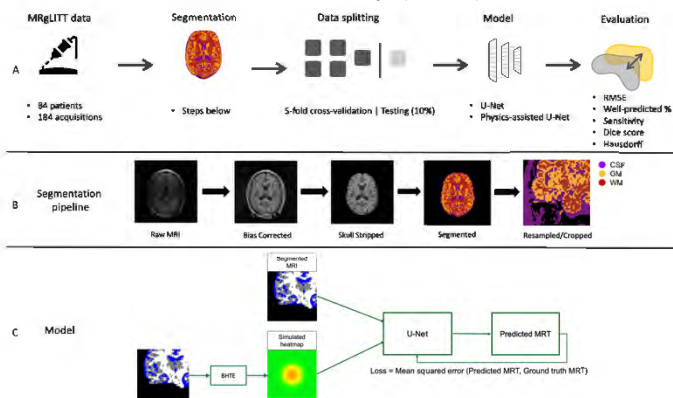


Figure 1 - Overview of our physics-assisted U-Net, A: Complete procedure of our study, B: Brain segmentation pipeline with 4 major steps included, bias field correction, skull stripping, segmentation, and resampling with cropping by the center of the laser tip. C: PA-U-Net, U-Net has the 2-channel input of a concatenated simulated heatmap with the segmented MRI, where blue represents CSF, gray and white corresponds to GM and WM, with the BHTE to produce a simulated heatmap.

Results: The PINN achieved a lower Hausdorff distance (2.55 ± 1.80) compared to a baseline U-Net model (2.44 ± 1.47), indicating better spatial alignment with ground truth contours. RMSE is 2 ± 0.8 °C in PINN, which is within an acceptable threshold of error. Also, the SSIM of a PINN aligns with the real temperature maps, accurately capturing the natural variability of the real temperature maps.

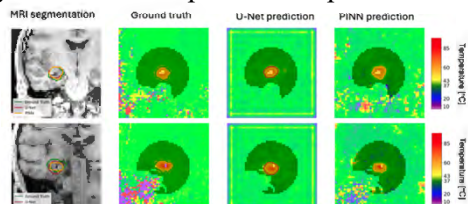


Figure 2 - Comparative results for three samples of the test set: anatomical MRI with ground truth, U-Net and PINN predictions' contours besides the ground truth, U-Net and PINN MRT images aligned with the valid temperature masking and their isotherm contour.

Conclusion: Our evaluation indicates that a PINN increases the accuracy of predicting MRgLITT thermal maps by embedding principles from the BHTE into a U-Net. The PINN showed better spatial alignment, enabling more accurate capture of temperature variations. Overall, this PINN-based treatment prediction model presents a promising novel approach to inform more precise presurgical MRgLITT planning.

Assessing the Impact of a Magnetic Field Generator on Fluoroscopic Image Quality

Mateen Mirzaei^{1,2}, Lisa M. Garland^{1,2}, Terry M. Peters^{1,2,3}, Ian A. Cunningham^{1,2} and Elvis C.S. Chen^{1,2,3}

¹Department of Medical Biophysics, Western University, London ON, ²Imaging Laboratories, Robarts Research Institute, London ON, ³School of Biomedical Engineering, Western University, London ON

Introduction: Many spinal operations are performed using fluoroscopic guidance due to its excellent visualization of osseous structures and surgical instrumentation in real-time (Pradhan et al., 2008), however operational efficacy is conditional on accurate needle placement. Image-guided surgical navigation systems allow for intraoperative and continuous localization of surgical tools with respect to patient anatomy, leading to significantly improved needle placement accuracy (Wilson et al., 2024). Specifically, magnetic navigational systems require a field generator (FG) whose placement must be near the patient and may partially obstruct the x-ray beam, causing image artifacts and degrading image quality. Furthermore, the placement of a FG near ferromagnetic surgical equipment has been known to affect needle tracking accuracy. Previous work has shown no clinically significant impact of a C-arm on tracking accuracy (Xing et al., 2024), and has successfully removed the image artifacts produced by a radiolucent FG (Xia et al., 2023); however, the x-ray photon scatter interactions from the FG may reduce image contrast, add noise and decrease spatial resolution. These scatter interactions can be assessed in terms of the scatter-to-primary ratio (SPR) and its effect on image quality can be described using the generalized modulation transfer function (MTF) and the generalized detective quantum efficiency (DQE). This project aims to assess the effect of the FG on image quality to ensure minimal deterioration by measuring the SPR, MTF and DQE.

Methods: To perform the SPR measurements, a slanted-edge technique was used as described by Garland and Cunningham (submitted to Medical Physics, 2024), who's work builds upon a previously developed edge spread technique (Cooper *et al.*, 2000). SPR measurements of a 20cm water phantom, used to mimic the x-ray scattering properties of an average-sized patient, were taken with and without a radiolucent FG prototype (Northern Digital Inc., Canada) in the x-ray beam of a Canon Alphenix C-arm at air gaps of 40cm, 45cm and 50cm. MTF and DQE measurements of the imaging system were taken with and without the FG, using the commercially available DQEPro (DQE Instruments Inc., Canada). All of the aforementioned images were taken at 80 kV and 5.0 mAs, and included the surgical table and detector anti-scatter grid. SPR measurements of the FG and phantom were also taken without the surgical table.

Results/Discussion: Using the above parameters, there is an 8% average increase in SPR at the three air gaps. The results also exhibit an SPR of 0.08 when the FG was introduced into the x-ray beam without the phantom or surgical table, decreasing with larger air gaps. In comparison, the SPR of the phantom without the surgical table was measured to be 0.42 at the smallest air gap. Given that the SPR of the phantom was on average 5 times larger than the SPR of the FG, the degradation of image quality caused by the scatter interactions within the FG would likely be minimal compared to the effect caused by scatter interactions within the patient. Furthermore, including the FG in the imaging system demonstrates no remarkable difference in generalized MTF, and an 8% average decrease in generalized DQE.

Conclusion: This work demonstrates the minimal effects on radiograph image quality with the introduction of a radiolucent FG directly into the x-ray beam of a C-arm imaging system. Further validation of this conclusion is necessary by obtaining the SPR, MTF, and DQE under a larger variety of clinical conditions, such as a varying kV. These results point towards promising outcomes in terms of maintaining image quality when integrating the FG into the C-arm operating suite, moving towards the seamless integration of magnetic tracking systems for fluoroscopy-guided interventions.

Designing a 6-Axis Testbed for Accessible Image-Guided Robotics Research

Coleman Farvolden¹, Kian Hashtrudi-Zaad¹, Laura Connolly¹, Colton Barr¹, Gabor Fichtinger¹

1. Queen's University, Kingston, Canada

INTRODUCTION: Cancer recurrence after surgery is often attributed to residual tumor tissue missed during the initial operation. This is particularly relevant in procedures like breast-conserving surgery (BCS), where preserving healthy tissue is paramount [1]. We hypothesize that intraoperative robotic imaging has the potential to improve BCS procedures by enabling precise inspection of the surgical cavity to identify and localize residual cancer. This paper presents an accessible and low-cost testbed for prototyping robotic cavity scanning with an optical imaging probe.

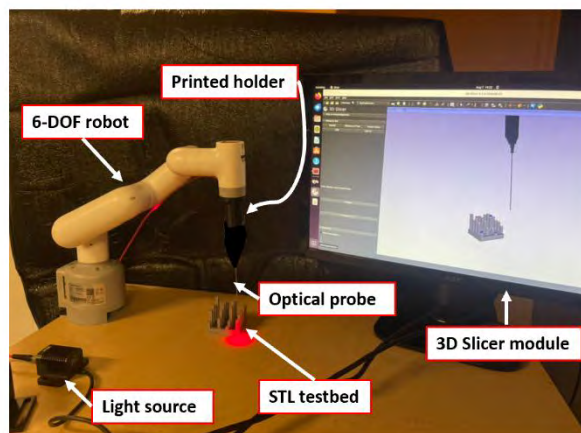


Figure 1: Benchtop robotic imaging system

METHODS: We developed a reusable, open-source testbed for controlling an inexpensive 6-axis robotic arm (MyCobot280, Elephant Robotics) with Robot Operating System (ROS, ros.org) and 3D Slicer (slicer.org). This testbed relies on communication between 3D Slicer and ROS using SlicerROS2 [2]. The motion planning is executed using the ROS control framework and MoveIt2. A custom 3D-printed end-effector was made to mount an optical probe. The end-effector screws into the arm and secures the probe with a friction fit. To evaluate the system's positional accuracy, we conducted experiments using a 3D printed phantom with 4 registration points and 16 target points. The robot was registered to the phantom using point-to-point registration. Following point-to-point registration, the robot was iteratively sent to 16 target points in 3 separate trials. End-effector X, Y positional error was calculated by subtracting encoder-derived positions from the desired positions (Z-axis distance remained fixed). From this experiment we were able to capture the combined impact of registration and path planning error on the overall positional accuracy of the testbed.

RESULTS: The system achieved an average positional accuracy of 3.6 ± 1.4 mm. Although this error is high for clinical translation, it is sufficient for benchtop prototyping and can likely be reduced by modifying the control strategy. Potential improvements include improving robot calibration and enhancing encoder resolution. Additionally, refining the control and path planning software could further enhance accuracy by optimizing trajectory generation and minimizing deviations from the intended path. By enabling accurate robot positioning within an imaging coordinate system, this study establishes a benchtop foundation for developing image-guided robotic applications for surgery.

CONCLUSIONS: This open-source testbed integrating 3D Slicer, ROS, and a low-cost robotic arm provides an accessible platform for developing and evaluating image-guided scanning systems. Future work will focus on refining the system's accuracy with visual servoing and working towards clinical translation for surgical cavity imaging during breast-conserving surgery.

REFERENCES: [1] Hargreaves et al. (2014). Intra-operative guidance: Methods for achieving negative margins in breast conserving surgery. *Journal of Surgical Oncology*, 110(1), 21-25. [2] Connolly, L., et al. (2024). SlicerROS2: A Research and Development Module for Image-Guided Robotic Interventions. *IEEE Transactions on Medical Robotics and Bionics*, 6(4), 1334-1344.

Evaluating Sensitivity Differences of Healthy Spinal Cord and Intramedullary Spinal Cord F98 Glioma in Response to Focused Ultrasound and Microbubbles

Mahsa Mokhlesabadi^{a,b}*, Danielle M Charron^b, Cynthia Hawkins^c, Meaghan A O'Reilly^{a,b}

a Department of Medical Biophysics, Faculty of Medicine, University of Toronto, Toronto, ON Canada

b Physical Sciences Platform, Sunnybrook Research Institute, Sunnybrook Health Sciences Centre, 2075 Bayview Avenue, Toronto, ON M4N 3M5 Canada

c Department of Pediatric Laboratory Medicine, The Hospital for Sick Children, 555 University Avenue, Toronto, ON, M5G 1X8, Canada

Introduction: Mediating damage to tumor vasculature through focused ultrasound (FUS) and microbubbles has been shown to elicit many beneficial anti-tumor effects. However, while tumor tissue in non-CNS organs is generally more sensitive to vascular effects than surrounding healthy tissue, the response of CNS tissues remains poorly understood in this context. Therefore, the primary objective of this study was to investigate the differing responses of spinal cord glioma tumors and adjacent healthy spinal cord tissue to treatment with FUS and microbubbles.

Methods: A total of 26 F344 Fischer rats were inoculated with f98 glioma tumors. Seven to 10 days following the tumor inoculation surgery, the tumor and the adjacent healthy tissue were targeted with FUS (580 kHz, 10 ms bursts, 1 Hz pulse repetition frequency, 40 s) after a bolus injection of house-made microbubbles ($1.00 \pm 0.85 \mu\text{m}$; 2.4×10^7 microbubbles/100 g) in four experimental groups of sham ultrasound and ultrasound pressures of 0.4 MPa, 0.8 MPa, and 1.2 MPa. Tissue samples were harvested 24 h post-treatment and processed for histology.

Results: Healthy tissue exhibited a progressive increase in damage with rising pressure, characterized by red blood cell extravasation, formation of hemorrhagic pools, and spinal cord tissue disintegration. Conversely, tumor samples exhibited histopathological features regardless of pressure, with no treatment-induced damage observed in the tumors. The collective findings indicate the reduced sensitivity of F98 glioma tumors to treatment with FUS and microbubbles compared to healthy tissue, which may result from the lower vascularity of F98 tumors, and the occurrence of vascular co-option as these tumors' mode of vascularization.

Conclusions: The findings of this study necessitate additional targeting strategies to deliver FUS to CNS tissues. Additionally, it is a critical safety consideration for FUS applications with milder exposures as the ultrasound exposures required to obtain a bioeffect in a tumor might be sufficient to induce damage in the healthy tissue.

The impact of propagation pathways on targeting accuracy in transspinal ultrasound focusing

David Martin^{1,2}, Meaghan O'Reilly^{1,2}, ¹ Physical Sciences Platform, Sunnybrook Research Institute, Toronto, Canada; ² Department of Medical Biophysics, University of Toronto, Toronto, Canada,

Background. Ultrasound-mediated drug delivery to the spinal cord has great potential to improve treatment of CNS pathologies, but the spinal column remains a challenging target. The irregular geometry and variable density of vertebrae can distort the transvertebral field and shift the focal maximum. Transspinal focusing is further complicated by unoccluded transmission pathways in the paralaminar spaces, which can cause additional aberration. In a recent benchtop validation study of transspinal focusing, unoccluded pathways were estimated to have increased targeting error by several millimeters in the most extreme cases [1]. Here, we explore *in silico* the possibility of mitigating off-target effects by optimizing transducer placement on a target-by-target basis.

Methods. Transspinal focusing was simulated for a spine-specific ultrasound array first proposed by Xu and O'Reilly in 2020. This design consists of 256 transducer elements arranged on a cylindrical surface in four 64-element panels: two panels targeting transvertebral transmission pathways and two panels targeting paravertebral pathways. In the initial design, the panels were positioned to intersect with the average maximum transmission pathways in the thoracic spine [2]. Here, three configurations of the spine-specific aperture were considered. In the first configuration, we simulated only the transvertebral panels in a fixed position, as a direct comparison to the previous benchtop study where only transvertebral components of the array had been fabricated. In the second configuration, we added the direct panels, also in a fixed position. In the third configuration, each panel was rotated independently about the aperture's radius of curvature, aligning it with the optimal transmission pathway for a given target. 80 targets were simulated in a specimen of *ex vivo* human thoracic spine. The simulation domain was populated with 3D meshes of stacked vertebrae, paired with CT-derived masks of acoustic properties. Simulations utilized a steady-state ray acoustics model previously developed by Xu and O'Reilly [3]. For each target, phase and inverse amplitude corrections were generated via an inverse simulation, where sound was propagated from the target location, through the spinal column to the array surface. Forward focusing simulations were then performed using the same ray acoustics model (with different mesh discretization) and focal pressure was recorded at 0.5 mm increments in an 11 mm × 11 mm × 11 mm volume centered on the target location. Targeting error r_{90} was calculated as the three-dimensional focal shift in the centroid of the 90% contour volume.

Results. When focusing with transvertebral panels only, mean r_{90} was 2.1 ± 1.5 mm and r_{90} exceeded 3 mm in 15 cases. Including the direct panels reduced mean r_{90} to 1.6 ± 1.5 mm, and r_{90} exceeded 3 mm in 9 cases. Finally, including all four panels and optimizing panel position on a target-by-target basis further reduced mean r_{90} to 1.1 ± 0.8 mm, and r_{90} exceeded 3 mm in only one target.

Conclusion. The results of this study emphasize the importance of targeting appropriate propagation pathways when focusing ultrasound to the spinal canal. Including the direct array components reduces targeting error when focusing along the average maximum transmission pathways, but a considerable number of outliers remain. Optimizing transmission pathways on a target-by-target basis further reduces average targeting error, while also vastly reducing the number of outlier targets. This suggests that, in transspinal focusing applications, adjustable apertures or large, fully populated arrays are needed to ensure consistent targeting accuracy.

References

- [1] D. Martin, R. Xu, M. Dressler, and M. A. O'Reilly, "Ex vivo validation of non-invasive phase correction for transspine focused ultrasound: model performance and target feasibility," *Phys Med Biol*, vol. 69, no. 23, p. 235001, Nov. 2024, doi: 10.1088/1361-6560/ad8fed.
- [2] R. Xu and M. A. O'Reilly, "A Spine-Specific Phased Array for Transvertebral Ultrasound Therapy: Design and Simulation," *IEEE Trans Biomed Eng*, vol. 67, no. 1, pp. 256–267, Jan. 2020, doi: 10.1109/TBME.2019.2912146.
- [3] R. Xu and M. A. O'Reilly, "Simulating transvertebral ultrasound propagation with a multi-layered ray acoustics model," *Phys Med Biol*, vol. 63, no. 14, p. 145017, 2018, doi: 10.1088/1361-6560/aacf75.

Oral Presentations 9: Cancer 2

Abstracts

Regional Predictors of Progression after Stereotactic Radiosurgery for Brain Metastases

Robert Policelli¹, David DeVries², Joanna Laba^{2,3}, Andrew Leung⁴, Terence Tang², Ali Albweady⁵, Ghada Alqaidey⁶, Hatim Fakir³, Aaron Ward^{1,3}

Department of ¹Medical Biophysics, Western University, London, Ontario; ²Department of Radiation Oncology, Verspeeten Family Cancer Centre, London Health Sciences Centre, London, Ontario; Departments of ³Oncology, ⁴Medical Imaging, Western University, London, Ontario; ⁵Department of Radiology, College of Medicine, Qassim University, Saudi Arabia; ⁶Radiodiagnostic and Medical Imaging Department, King Fahad Armed Forces Hospital, Jeddah, Saudi Arabia.

Introduction: Stereotactic radiosurgery (SRS) is an effective and non-invasive treatment option for brain metastases (BMs) that precisely targets BMs with ablative radiation. SRS to treat BMs in not perfect (local control rates between 70-95%)^{1,2}, as local disease progression can occur when not all cancer is eliminated, which requires retreatment.³ Studies have attempted to predict post-SRS progression based on the number of BMs and dose delivered, but no studies have investigated how these variables relate to local progression in the region directly around BMs.^{4,5} Therefore, we hypothesize that the presence of neighbouring BMs and dose distributions of SRS plans are correlated with local progression after SRS.

Methods: Our dataset consisted of 64 patients (117 BMs) treated using linear accelerator (linac)-based SRS at the Verspeeten Family Cancer Centre. We collected dose maps and contrast enhanced T1w-MRI scans for each patient. Progression or non-progression (including pseudo-progression) was determined for each lesion by a radiation oncologist and radiologist who used follow up scans (up to 2 years) and available pathology data. For patients with multiple BMs (33 patients with 86 BMs) the shortest distance between the edge of the index BM planning tumour volume (PTV) and the nearest neighbouring BM PTV were calculated. Over the entire dataset, biologically effective dose (BED) was also calculated at each voxel on the pre-treatment scan using the linear quadratic formula ($\alpha/\beta = 10$). BED values from voxels within the PTV and successive 1 mm-thick concentric shells (up to 10 mm) around each PTV were collected. The distance to adjacent BMs along with the median, 10th percentile, and 90th percentile of BED at varying distances from the index BM were correlated with progression and non-progression using the Mann-Whitney U test.

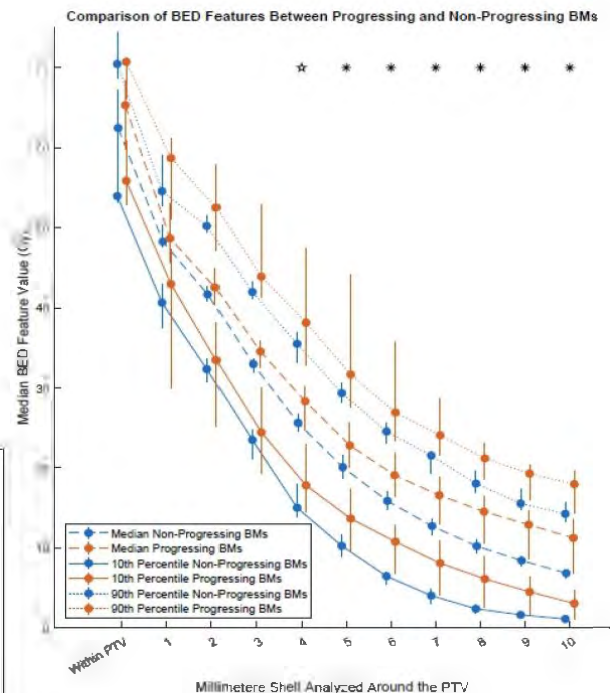
Results: A shorter distance between the index BM and the nearest adjacent BM was found to be a significant predictor of progression ($p = 0.03$, median distance for progressing BMs versus non-progressing BMs = 3.0 cm vs 5.1 cm). BED at distances of 5-10 mm from the PTV was also found to be a significant predictor of BM progression for all three features (Figure 1). A higher dose in this 5-10 mm range was associated with BM progression.

Conclusion: These findings in the region around BMs indicate that having a closer adjacent BM was correlated with progression in our data set. We speculate that higher observed BED at distances 5-10 mm around progressing versus non-progressing BMs is due to the proximity of an adjacent BM and its associated radiation dose. Once validated on a multi-centre data set, distance to the nearest BM could be incorporated into a nomogram to predict SRS outcome and could act as a factor for clinicians to consider when determining the best treatment options for BM patients.

References:

- 1.Redmond K et al. *Int J Rad Onc Biol Phys*. 2021.
- 2.Nieder C et al. *Rad Onc*. 2014.
- 3.Cummins D et al. *Wrlld Neurosrg*. 2022.
- 4.Hirata M et al. *Radiat Oncol*. 2022.
- 5.Wang H et al. *Med Phys*. 2021.

Figure 1: The comparison of BED feature values between progressing and non-progressing BMs. * = all features were a significant predictor of progression ($p < 0.05$) in the given concentric shell around the PTV. ★ = indicates the 90th percentile was a significant predictor of progression ($p < 0.05$) in that concentric shell. The lines indicate the 95% confidence interval.



Development of cisplatin prodrug-loaded microbubbles for ultrasound-aided targeted cancer therapy

Sean McGrath¹, Emma Durocher², Suresh Gadde² and Naomi Matsuura^{1,3,4}

¹Institute of Biomedical Engineering, University of Toronto, ²Division of Cellular and Molecular Medicine, University of Ottawa, ³Department of Material Science and Engineering, University of Toronto, ⁴Department of Medical Imaging, University of Toronto

Introduction: Cisplatin is a standard chemotherapeutic for various cancers but is often limited by systemic toxicity [1][2]. Cisplatin prodrugs, featuring cisplatin molecules bound to hydrocarbon ligands, offer reduced toxicity and controlled drug release [3]. Incorporating these prodrugs into drug carriers for tumor-specific delivery can further minimize toxicity and enhance local drug uptake [4]. This project focuses on developing cisplatin prodrug-loaded microbubbles (MBs) that cavitate upon high-pressure ultrasound exposure, enabling targeted drug release. Using two prodrugs, CisPt(octyl)₂ and CisPt(octadecyl)₂, we have synthesized loaded MBs, evaluated their echogenicity, stability, prodrug loading, and assessed cytotoxicity.

Methods: Two cisplatin prodrugs, CisPt(octyl)₂ (8-carbon chain) and CisPt(octadecyl)₂ (18-carbon chain), were synthesized [3]. Prodrug-loaded and unloaded MBs were prepared using a lipid shell with a perfluorobutane core. Echogenicity of MBs was evaluated under flow at 37 °C using contrast-enhanced ultrasound (Toshiba IU22, L8-4 probe, MI = 0.05). MB size distribution and stability were analyzed with a Coulter Counter (20 μm aperture, ~3×10⁶ MBs/mL, Multisizer 4e, Beckman Coulter). Prodrug loading was quantified by centrifugation (80 RCF, 3 minutes) and platinum (Pt) content measurement via inductively coupled plasma mass spectrometry (ICP-MS). Cellular uptake and cytotoxicity were assessed using AE17-OVA mouse mesothelioma cells. Cytotoxicity of the prodrugs and prodrug-loaded MBs was measured with an MTT assay, using cisplatin as a control. Statistical comparisons between treatment groups were performed using one-way ANOVA at each concentration, with significance set at p < 0.05.

Results: MBs loaded with cisplatin prodrugs exhibited echogenicity and size distributions comparable to controls. Prodrug-treated cells had higher intracellular Pt levels than cisplatin, with CisPt(octadecyl)₂ achieving the highest uptake (Figure 1A). Despite this, CisPt(octadecyl)₂ showed no increased cytotoxicity (Figure 1B). In contrast, CisPt(octyl)₂ MBs incorporated significantly more Pt (37% ± 2%) than CisPt(octadecyl)₂ MBs (12% ± 2%) (Figure 1C), suggesting lower shell integration efficiency for CisPt(octadecyl)₂. At lower doses, both prodrugs matched cisplatin's cytotoxicity, but at higher concentrations, CisPt(octyl)₂-loaded MBs demonstrated superior efficacy (p < 0.05) (Figure 1D). CisPt(octadecyl)₂ may preferentially localize to cell membranes, reducing cytoplasmic access [3].

Conclusion: Microbubbles (MBs) loaded with CisPt(octyl)₂ and CisPt(octadecyl)₂ were successfully synthesized and demonstrated echogenicity and stability at 37 °C, supporting their potential for targeted cisplatin prodrug release and reduced administered doses. Future work will focus on preclinical testing.

References: [1] Q Yao et al., *Theranostics*. 2022;12(5):2115-32. [2] R.Y. Tsang et al., *Drug Saf*. 2009;32(12):1109-22. [3] Y. Zheng et al., *J Am Chem Soc*. 2014;136:8790-98. [4] HK Chen et al., *Cancers*. 2018;10(9):31

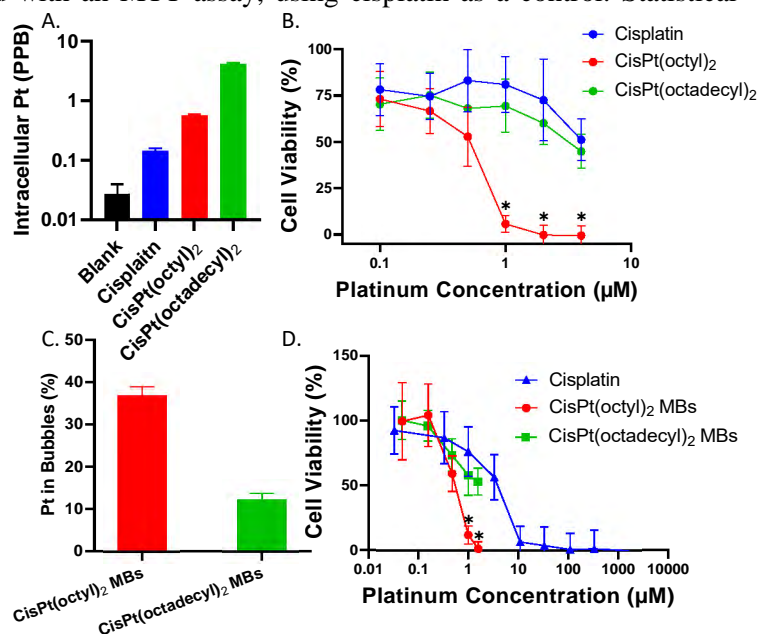


Figure 1: A) Concentration of Pt found intracellularly after treatment (p < 0.05); B) Cell viability after treatment; C) Percentage of prodrugs loaded successfully into MBs; D) Cell viability after exposure to pre-cavitated prodrug-loaded MBs (* p < 0.05).

Adaptive Resource-Efficient Federated Learning for Prostate MRI Using PCA and Early Stopping

Negin Piran Nanekaran¹, Eranga Ukwatta¹

¹School of Engineering, University of Guelph, Guelph, Ontario, Canada

Introduction: Developing robust machine learning models for medical imaging requires large and diverse datasets. Federated Learning (FL) facilitates collaborative model training while preserving data privacy, making it essential for such applications. However, variations in imaging protocols, devices, and patient cohorts across institutions create heterogeneous data, posing challenges to FL’s efficiency and effectiveness.

Methods: We propose an adaptive FL framework (Figure 1) with three key components: 1. **Data Preprocessing with Federated Incremental PCA (FIPCA):** Each center computes local statistics, aggregated to form a global covariance matrix without sharing raw data. This reduces dimensionality and aligns data distributions across centers to address heterogeneity. 2. **Client-side Training:** A custom loss function balances false negatives and positives. Early stopping and dynamic learning rates prevent overfitting and reduce computations. 3. **Server-side Coordination:** Training halts when client validation losses plateau, optimizing resource use.

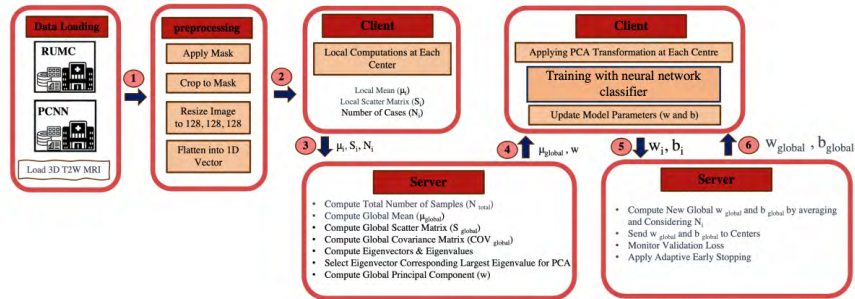


Figure 1: Proposed adaptive FL framework with Steps 5 and 6 repeating until convergence.

Results: The proposed method significantly reduced the number of global training rounds from 200 to 38, leading to a 98% reduction in energy consumption compared to the standard FedAvg algorithm. The incorporation of FIPCA improved generalizability, while adaptive early stopping optimized computational efficiency. The area under the curve (AUC), a measure of classification performance, increased from 0.68 to 0.73 on the test center’s data, demonstrating superior performance over standard FL. Moreover, sensitivity and specificity improved, reaching 0.784 and 0.786, respectively, compared to 0.526 and 0.784 for standard FL. Importantly, the proposed method achieved performance comparable to the centralized model, with an AUC of 0.733 vs. 0.749 for the centralized model, demonstrating its effectiveness in handling data heterogeneity while preserving privacy. The method also outperformed individual-center models, which struggled with generalization across institutions.

Conclusions: The proposed adaptive FL framework improves training efficiency, reduces computational overhead, and enhances robustness to non-identically distributed data. Its energy and time savings make it ideal for resource-constrained healthcare environments. Further validation on diverse medical imaging tasks is suggested.

References: [1] Saha, Anindo, et al. "Artificial intelligence and radiologists in prostate cancer detection on MRI (PI-CAI): an international, paired, non-inferiority, confirmatory study." *The Lancet Oncology* (2024). [2] McMahan, Brendan, et al. "Communication-efficient learning of deep networks from decentralized data." *Artificial intelligence and statistics*. PMLR, 2017.

A Mechatronic Needle Guidance System for Prostate-Specific Positron Emission Tomography and 3D Transrectal Ultrasound-Guided Trans-perineal Prostate Biopsy

S. Karagulleoglu-Kunduraci^{*a,b}, J. Bax^b, L. Gardi^b, D. Tessier^b, A. Reznik^{c,d}, I. A. Cunningham^{a,b}, A. Fenster^{a,b}

^aDepartment of Medical Biophysics, Western University, London ON, Canada; ^bImaging Research Laboratories, Robarts Research Institute, London ON, Canada; ^cDepartment of Physics, Lakehead University, Thunder Bay, ON, Canada; ^dThunder Bay Regional Health Research Institute, Thunder Bay, ON, Canada

Introduction: Prostate cancer (PCa) is the most diagnosed cancer in men worldwide. Standard 2D transrectal ultrasound (TRUS)-guided biopsy is the gold standard for diagnosing PCa; however, it fails to directly visualize PCa, resulting in false-negative rates of 21–47% and frequent repeat biopsies¹. The transrectal biopsy approach also carries a notable infection risk. In contrast, the trans-perineal method reduces infection rates and improves access to anterior prostate zones, enhancing detection in hard-to-reach areas. Positron emission tomography (PET) is a valuable functional imaging tool for detecting and staging PCa. However, standard PET/CT and PET/MRI systems, designed for whole-body imaging, are suboptimal for prostate-specific applications, delivering higher radiation doses and limited accuracy for small lesions or recurrent PCa. The prostate-specific PET (P-PET) system, developed by Radialis Medical Inc. and Lakehead University, offers enhanced sensitivity and resolution tailored for prostate imaging². Despite its potential for detecting small PCa lesions, P-PET lacks anatomical guidance for precise biopsy. This project aims to integrate P-PET with 3D TRUS-guided biopsy to overcome these limitations.

Methods: Our goal is to develop and integrate 3D TRUS with P-PET-guided prostate biopsy system with advanced robotic technologies, including a motorized 3D TRUS mechanism and a mechatronic needle guidance system. To achieve this goal, we adapted a motorized 3D TRUS mechanism, based on our previously developed MRI fusion prostate biopsy and gynecological brachytherapy systems, for integration with the P-PET system and designed it specifically for trans-perineal prostate biopsies with a mechatronic needle guidance system for enhanced precision and accuracy³⁻⁴. The motorized 3D TRUS mechanism incorporates a side-firing ultrasound probe and a rotating mover for real-time 3D image reconstruction from 2D scans. The guidance system includes a needle guidance template with adjustable 2D movement and multiple holes, enabling precise alignment and targeting during trans-perineal biopsy. The coordinate system of the needle guidance template was integrated with the 3D TRUS image using a custom agar-based prostate phantom embedded with simulated tumor lesions, mimicking human tissue properties.

Results: First, the coordinate system calibration was conducted using in-house software, segmenting the prostate and inclusions and aligning the virtual needle template holes. Next, a software tool was developed showing the needle path through the aligned template hole targeting the inclusion, and the path was superimposed on the 3D US image. The target and insertion points were selected using the software. The created needle path in the 3D US image is shown in Fig. 2A. Finally, the biopsy needle was inserted through the selected template hole to the target point and tracked live on the 2D US image during the insertion. Figure 2C illustrates that the inserted needle is in the selected target in the 3D US image. The biopsy needle guidance error, defined as the distance between the needle track in the image and its planned position, was evaluated for five inclusions ($r=5\text{mm}$), resulting in a mean guidance error of $0.85 \pm 0.22\text{ mm}$.

Conclusions: We successfully developed and tested a 3D TRUS-guided prostate biopsy system with a newly designed needle guidance template using a tissue-mimicking phantom and in-house software. Once completed, this system, integrated with a P-PET system, is expected to reduce false-negative rates, minimize repeat procedures, and improve the detection and targeting of early-stage, high-grade PCa.

[1] Taira, A. V., et al., *Prostate cancer and prostatic diseases* 13.1 (2010): 71-77. [2] Stiles, Justin, et al., *Sensors* 22.13 (2022): 4678. [3] Cool, Derek W., et al., *Canadian Urological Association Journal* 10.9-10 (2016): 342. [4] Rodgers, Jessica Robin, et al. *Medical physics* 44.5 (2017): 1899-1911.

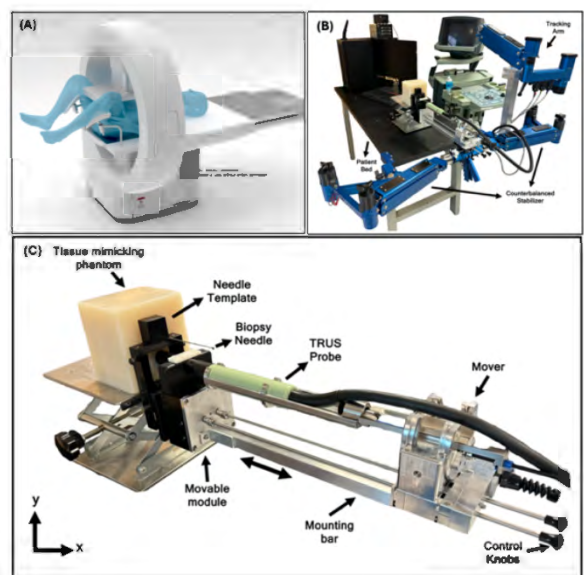


Figure 1: (A) The proposed P-PET system model with patient positioning for prostate biopsy. (B) Fully assembled 3D TRUS-guided biopsy system (C) Needle guidance system

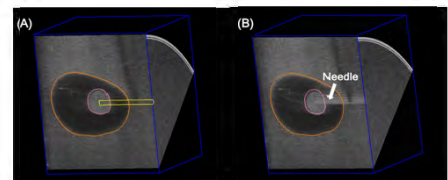


Figure 2: (A) Pre-needle placement: 3D US image with virtual needle path (yellow) aligned with the target; (B) Post-needle placement: 3D US image showing the needle in the target area.

Oral Presentations 10: Cardiac, Lung, and Musculoskeletal Imaging

Abstracts

Ultrasound 3D reconstruction of the lower spine for facet joint injection

Gaurav Ranjit¹, Tamas Ungi¹, Chris Yeung¹, Parvin Mousavi¹, Gabor Fichtinger¹

¹Queen's University, Kingston ON, Canada

INTRODUCTION: Facet joints are structures within the spine that connect adjacent vertebrae, enabling both stability and mobility. However, they can also be a source of significant pain due to conditions such as osteoarthritis, injury, or inflammation. In clinical practice, facet joint injections are a common treatment for managing such pain, often involving the injection of medication into the joint space. Traditionally, fluoroscopy is used for visualizing spinal anatomy and guiding needle placement in facet joint injections due to its high resolution and clear depiction of bony landmarks [1]. However, fluoroscopy involves exposure to ionizing radiation and its accessibility is limited. Ultrasound imaging is a radiation-free modality that offers real-time capabilities, enabling assessment of anatomical structures during procedures [2]. Despite its advantages, ultrasound presents challenges in accurately identifying anatomical structures due to limited resolution and signal artifacts. We hypothesize that ultrasound-based 3D reconstruction can reliably localize spinal landmarks for facet joint interventions, with accuracy comparable to CT-derived ground truth. By evaluating deviations between reconstructed and ground truth points across vertebral levels, this work aims to assess the feasibility of ultrasound as a safer and more accessible imaging modality for guiding spinal interventions.

METHODS: The dataset consists of anonymized tracked ultrasound and corresponding CT scans of the lower spine, obtained from 40 patients. The ultrasound data spans the L1 to L5 vertebrae and the L5-S1 junction, which are critical for guiding facet joint injections. U-net was trained to segment bones from the ultrasound scans. Segmentations were reconstructed to produce 3D volumes in 3D Slicer. A physician annotated points on the facet joints at the L1-L5 levels and the L5-S1 junction, using the reconstructed ultrasound volumes. These points were then compared to corresponding points placed on CT scans of the same spine, which were considered the ground truth for this analysis. The comparison was performed by calculating the distances between points in the two modalities.

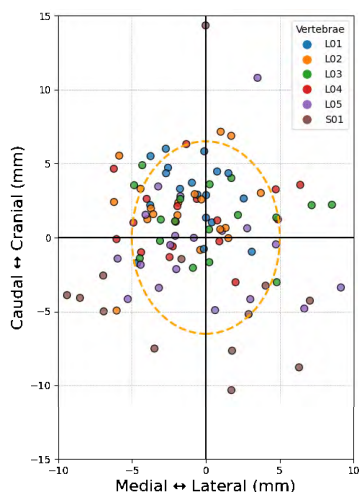


Figure 1. Scatter plot showing difference between US reconstruction and CT ground truth. The origin (0, 0) represents perfect alignment. The orange ellipse outlines the typical dimensions of a lumbar facet joint, providing a reference for acceptable positional deviations [3].

RESULTS: Analysis of point placements revealed variability in the deviations between reconstructed and ground truth landmarks across vertebral levels. Points were distributed both within and beyond the typical facet joint cross-sectional area (13 mm × 10 mm ellipsoid) [3]. 60% of the points fell within this target boundary. L01 and L02 vertebrae demonstrated the highest consistency, with 70% of fiducials located inside the ellipsoid. Conversely, L04 and L05 vertebrae displayed the greatest deviations, which could lead to reduced accuracy in needle placement during facet joint injections, increasing the risk of ineffective treatment or injury to surrounding structures. The largest outliers were observed at the S01 level, highlighting challenges in accurately segmenting sacral anatomy.

CONCLUSIONS: This study underscores the efficacy of ultrasound reconstructions in capturing vertebral facet joint dimensions, with most points aligning within the anatomical boundaries of the joint cross-section. However, increased deviations at lower lumbar (L04-L05) and sacral (S01) levels indicate potential improvements in handling anatomical complexity and curvature. Although these results lay the groundwork for using ultrasound reconstructions in clinical applications, the accuracy must dramatically increase to approach the

precision and reliability of fluoroscopy-guided techniques. Model accuracy will always be limited by the spatial resolution of the ultrasound probe. Future work will focus on refining the AI model to enhance segmentation accuracy, particularly for challenging vertebral levels.

REFERENCES: 1. Jacobson, J. A. (2018). *Fundamentals of musculoskeletal ultrasound*. Elsevier Health Sciences.

2. Srinivasan, S., & Moran, K. (2012). Ultrasound-guided interventions in pain management. *Ultrasound Clinics*, 7(3), 355-370.

<https://doi.org/10.1016/j.cult.2012.07.006>

3. Barry, M., & Livesley, P. (1997). Facet joint hypertrophy: the cross-sectional area of the superior articular process of L4 and L5.

European spine journal : official publication of the European Spine Society, the European Spinal Deformity Society, and the European Section of the Cervical Spine Research Society, 6(2), 121-124. <https://doi.org/10.1007/BF01358744>

Enhanced cardiac imaging using fixed-filter spectral imaging with anti-correlated noise correction

Lisa M. Garland and Ian A. Cunningham

Robarts Research Institute, Department of Medical Biophysics, Western University

Introduction: Cardiovascular disease (CVD) is the leading cause of death globally, claiming over 20 million lives in 2021.¹ To treat CVD, metal stents are often deployed under angiographic x-ray guidance at the site of stenosis to compress plaque, widen the vessel, and restore sufficient blood flow. For neurological and extremity angiography, digital subtraction angiography (DSA) is the gold-standard technique, enhancing vessel visibility by suppressing background anatomical structures. However, DSA is limited to stationary anatomy, as it relies on precise alignment of images captured before and after iodine contrast injection. Spectral imaging offers an alternative by exploiting energy-dependent attenuation differences in materials to suppress specific structures, such as soft tissue or bone. Unlike DSA, spectral imaging is not inherently constrained to stationary anatomy, making it a promising approach for partial background suppression in cardiac imaging. While soft tissue suppression could significantly improve cardiac angiography, clinical implementation remains challenging. Achieving the required separation of low- and high-energy exposures typically necessitates specialized hardware, such as a dual-layer detector or fast kV-switching generator. Previously, kV-switching dual-energy imaging required a rotating attenuation filter to enhance spectral separation by differentially attenuating the high-energy image.^{2,3} However, the rotating filter introduces additional complexity, complicating clinical adoption. To address this, we propose a novel approach using 1) a fixed attenuation filter for both low- and high-energy acquisitions, optimized through theoretical simulation. 2) To mitigate the associated signal-to-noise ratio (SNR) reduction, we incorporate an anti-correlated noise reduction algorithm to improve image quality. 3) Determine the detector requirements for successful spectral imaging

Methods: To optimize the protocol for fixed filter spectral imaging, a custom computational simulation was developed to quantify the iodine and nickel SNR for 12 varying x-ray parameters. An anti-correlated noise reduction algorithm was implemented on phantom images using a high pass filter convolved with the iodine suppressed version of the spectral images. Experiments were conducted using an anthropomorphic chest phantom with a custom 3-D printed simulated coronary artery modeled from clinical image data, as well as nickel stents. Experiment parameters were chosen closest to the 12 optimized parameters in the simulation as reasonably possible.

Results: An optimal fixed attenuation filter of 0.2mm of copper was chosen to optimize the patient entrance dose as well as the material specific SNR. When implemented experimentally, successful soft tissue suppression was achieved, and the noise reduction algorithm visibly reduced the image noise. Visible comparison with rotating filter spectral images showed negligible difference in material contrast. A quantum noise limit of 0.05 μ Gy or less is required for successful kV-switching spectral imaging, as well as reduced scatter via an air gap and high grid-ratio anti-scatter grid. Fixed filtering with 0.2mm of copper compared to the optimal rotating high/low filters reduced the SNR/\sqrt{dose} by on average 10%. This was considered minimal and could be offset by the noise reduction algorithm.

Conclusions: Soft tissue can be suppressed using spectral imaging to enhance the visibility of stents and contrasted vessels during cardiac angiography. To make clinical implementation feasible, a fixed attenuation filter was used rather than incorporating and calibrating a rotating filter with the kV-switching generator. Implementing a noise reduction algorithm assists in offsetting the SNR degradation introduced by the fixed filter. Successful spectral imaging requires high-end detector technology to meet the requirements of a cardiac spectral technique. Fast-kV switching and fast tube cooling rates are essential to ensure minimal motion occurs between the low and high energy image, while avoiding damage to the tube. This work demonstrated successful spectral phantom images with only the addition of a kV-switching generator for an optimized cardiac imaging protocol.

1) Di Cesare M. et al. Global heart (2024) 2) Van Lysel, MS. Et al. IJCI (1991) 3) McCollough, CH. et al. Med Phys (1989)

Development of a Tissue-Equivalent Lung Phantom Compatible for Proton Magnetic Resonance Imaging (MRI) for Evaluation of Airway Size

Razieh Enjilela¹, Brandon Zanette², Giles Santyr^{2,3}, Eric Da Silva¹, and Miranda Kirby¹

¹Physics Department, Toronto Metropolitan University, Toronto, ON, Canada, ²Translational Medicine Program, The Hospital for Sick Children, Toronto, Canada; ³Department of Pediatrics, University of Toronto, Canada; ³Department of Medical Biophysics, University of Toronto, Canada

Introduction: Computed Tomography is widely used to study airway morphology, but ionizing radiation limits its use for longitudinal monitoring. Ultra-short Echo Time (UTE) MRI offers a radiation-free alternative and shows promise for high-resolution airway imaging.¹ MR imaging of the lungs is challenging due to the lung's low water density (20–30%)² and short T_2^* (0.85ms)³, which limits signal detection. However, in normal human airways larger than 1 mm, the cartilage is composed of 80% water⁴ with a T_2^* of 20ms⁵, which provides a potential target for imaging. Commercial MRI-compatible airway phantoms do not exist, making it necessary to develop one to evaluate UTE MR accuracy and to determine the minimum measurable airway size. This study aims to develop materials and a phantom configuration to mimic human airway and lung parenchyma, providing a model to assess UTE MRI accuracy in airway size measurement.

Methods: Cylindrical materials were prepared separately for airway and parenchyma using agar as a gelling agent, copper sulphate (CuSO_4) as a T_2^* modifier if required, heavy water (D_2O) for signal intensity regulation, and distilled water. Mixtures were weighed before and after heating above 100°C, with adjustments for evaporation. Agar ranged from 0.25–1.5g, CuSO_4 from 0.5–1g, heavy water from 30–75g, and distilled water from 70–25g to simulate T_2^* and signal intensity of lung tissues. The material compositions and proportions were optimized through iterative adjustments. Several cylindrical holes were bored from the parenchyma, and segments with different wall thicknesses and lumen diameters were taken from the airway material and embedded in the parenchyma, mimicking the airway structure (Fig. 1a). A 3 Tesla multi-echo (0.05–40 ms) experiment mapped T_2^* and signal intensity. UTE MRI used $0.8 \times 0.8 \times 1 \text{ mm}^3$ resolution and a 5° flip angle. Signal-to-Noise Ratio (SNR) was measured as the ratio of mean MRI signal within a region-of-interest to the noise standard deviation. Contrast-to-Noise Ratio (CNR) was the difference between airway and parenchyma signal intensities, divided by noise standard deviation. Intra Class Coefficient (ICC) assessed agreement between MRI-derived and actual airway sizes.

Result: T_2^* values were $1.4 \pm 0.1 \text{ ms}$ for the parenchyma and $15.1 \pm 2 \text{ ms}$ for the airway, with airway signal intensity measuring 2.6 times higher than the parenchyma as expected based on theory. The phantom simulating parenchyma and airways were both visible and distinguishable on UTE MRI, allowing for segmentation (Fig.1b). CNR was 4.7 and SNR was 30 and 24 for airway and parenchyma, respectively. ICC analysis indicated agreement between lumen diameter measurements from UTE MRI and actual known airway dimensions (ICC = 0.99, 95% CI: 0.76–1.00, $p < 0.001$).

Conclusion: To the best of our knowledge, this is the first MRI-compatible lung phantom simulating parenchyma and airway structures. Using UTE MRI, airway lumen diameters were accurately measured, demonstrating its potential for advancing MRI-based lung studies. The phantom will further aid to optimize UTE MRI parameters for measuring airway sizes in diseases like Cystic Fibrosis (CF).

Sample	MRI Size		Actual Size	
	LD (mm)	WT(mm)	LD(mm)	WT(mm)
Cylinder 1	2.41	-*	2.50	0.75
Cylinder 2	4.94	1.72	5.00	2.00
Cylinder 3	2.25	-*	2.50	1.25
Cylinder 4	3.43	1.78	3.50	2.50

Table 1. Comparison of MRI measured and actual cylinder dimensions. LD = Lumen Diameter, WT = Wall Thickness. *: Not able to quantify.

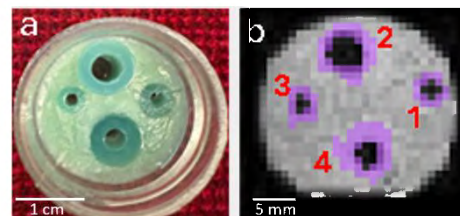


Figure 1. a) Photograph of a phantom containing four tubes that simulate different airway sizes. **b)** UTE MRI of the lung phantom (TE = 0.05 ms) showing segmented numbered tubes (purple regions) representing various airway sizes.

Reference: [1]. Dourmes et. al. Radiol, 2016. [2]. D. Alsop et.al, MRM, 1995. [3]. N. Gai et. al J Magn Reson Imaging. 2017. [4]. J. Shiguetoimi-Medina, J Orthop Traumatol, 2017. [5] T. Kim et.al, Skeletal Radiol, 2014.

Examining the Bilateral Loading Relationship in Thumb Osteoarthritis

Jennifer Villeneuve¹, Lauren Straatman², Assaf Kadar^{3,4}, Emily Lalone^{4,5}

Biomedical Engineering¹, Western University, London ON, School of Kinesiology and Health Sciences², University of Waterloo, Waterloo ON,

Department of Surgery³, Western University, London ON,

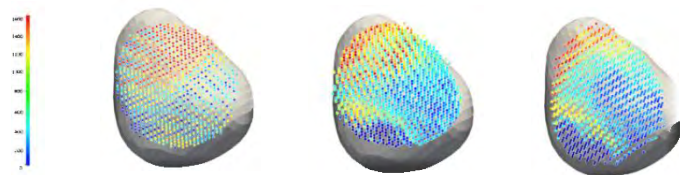
Roth | McFarlane Hand & Upper Limb Centre⁴, London ON, Mechanical and Materials Engineering⁵, Western University, London ON

Introduction: The carpometacarpal (CMC) joint is the most prominent location in the hand for osteoarthritis (OA), affecting 15% of adults older than 30, with a higher prevalence in women [1]. Patients with OA suffer from a lack of mobility, consistent pain, and diminished overall strength [2]. The study objective is to understand the correlation between the OA symptomatic thumb contact and subchondral volumetric bone mineral density (vBMD) compared to the healthy thumb. Joint contact area measures bone proximity within the articulation, while vBMD assesses density differences and structural integrity across regions. Previous research has shown that changes in subchondral bone is an early indicator of OA in the knee, which may also apply to the thumb [3]. This study will provide a relationship between the affected and healthy CMC joints regarding loading and contact suggesting a biomechanical reasoning as to why patients experience pain. This research is clinically relevant to determine what mechanical factors relate to the progression of OA.

Methods: Participants with CMC OA (n= 15) completed a static CT scan of their bilateral thumbs with a calibration phantom of known material densities. The average static contact area for the trapezium and first metacarpal were determined. The average subchondral vBMD for the first and third metacarpal were completed at three depths (increments of two and a half millimeters) while the trapezium was analyzed at five depths (increments of one and a quarter millimeter). The third metacarpal was used as a healthy vBMD frame of reference. The participants were also scanned completing various thumb movements (adduction-abduction, flexion-extension, and opposition-reposition) in the same 4DCT scanner with identical operating parameters. The total radiation dose was 0.2mGy from these scans. The kinematic contact maps will also be created for the first metacarpal and trapezium.

Results: Preliminary results (n=3) suggest a potential relationship between large contact area and the vBMD, within the deep regions of bone on the more symptomatic side. The joint contact maps are correlated with an increase in vBMD. Kinematic contact maps are still being completed which will be compared to the static vBMD and average contact area. These results are consistent with previous literature [4].

Conclusion: Preliminary results suggest that there is a correlation between subchondral bone mineral density and average contact area which may be related to the more symptomatic side. The large data set collected will provide insights into the progression of OA, how each region of subchondral bone reacts based on its contact area, and specific joint loading. These relationships can help identify important biological factors of OA progression, which may lead to early diagnosis and more specialized treatment options.



Depth (mm)	0 – 2.5	2.5 – 5.0	5 – 7.5
vBMD (mg/cm ³ K ₂ HPO ₄)	540.93	393.54	262.03

Figure 1: The first metacarpal subchondral volumetric BMD for a participant with CMC OA in the left thumb

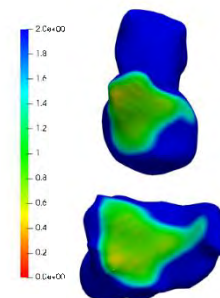


Figure 2: The static CT contact map for a participant with CMC OA in the left thumb

[1] M. M. HAARA *et al.*, "Osteoarthritis in the carpometacarpal joint of the thumb," *The Journal of Bone and Joint Surgery-American Volume*, vol. 86, no. 7, pp. 1452–1457, Jul. 2004.

doi:10.2106/00004623-200407000-00013

[2] L. Xu *et al.*, "Topography of the osteoarthritic thumb carpometacarpal joint and its variations with regard to gender, age, site, and osteoarthritic stage," *The Journal of Hand Surgery*, vol. 23, no. 3, pp. 454–464, May 1998. doi:10.1016/s0363-5023(05)80463-0

[3] W. D. Burnett *et al.*, "Patella bone density is lower in knee osteoarthritis patients experiencing pain at rest," *Osteoarthritis and Cartilage*, vol. 20, Apr. 2012. doi:10.1016/j.joca.2012.02.326

[4] L. Straatman *et al.*, "Use it or lose it: The relationship between two image-based biomarkers in better understanding osteoarthritis progression in the wrist," *Journal of Biomechanics*, vol. 161, p. 111849, Dec. 2023. doi:10.1016/j.jbiomech.2023.111849

Oral Presentations 11: Optical Imaging & Ultrasound Imaging

Abstracts

Deep Learning-Enabled 3D Fluorescence Imaging for Surgical Guidance: Assessing Surgical Margins

Hikaru Kurosawa,¹ Natalie Won,¹ Matthew Siracusa,¹ Rooaa Shanshal,¹

Mandolin Bartling,² Alessandra Ruaro,² Brian C. Wilson,¹ Jonathan C. Irish^{1,2} and Michael J. Daly¹

¹Princess Margaret Cancer Centre, University Health Network, Toronto ON

²Department of Otolaryngology – Head & Neck Surgery, University of Toronto

Introduction: Accurate assessment of 3D surgical margins remains a challenge after tumor resection. Fluorescence-guided surgery systems show promise to provide precise identification of residual tumor on the surface of resected tissue, but existing 2D fluorescence imaging systems lack the ability to quantify the 3D margin (i.e., thickness of healthy tissue surrounding the resected tumor). In oral cancer, a 5 mm pathologic margin has been identified as the prognostic cutoff by several studies¹, indicating the clinical significance to assess subsurface information of removed tissue. To quantify the 3D surgical margins in *ex vivo* tissue, our group has been developing a deep learning (DL)-enabled 3D fluorescence device. Here, we assess the topography of a simulated tumor submerged in healthy tissue (fig. a), predicting its fluorophore concentration and subsurface depth (fig. b).

Methods: A prototype spatial frequency domain imaging (SFDI) optical device has been developed to capture depth information and tissue optical properties by projecting varying structured patterns of light. *In silico* DL training used 10,000 synthetic tumors using composite spherical harmonics (CSH), created by merging four spherical harmonics of varying order, degree, and radius (width=5-40mm, height=5-10 mm, closest subsurface depth=1-10 mm). The tumor shapes were passed into a diffusion theory based SFDI light propagation model to produce optical property maps and synthetic fluorescence images (1 h simulation time). Those outputs were passed into a custom Siamese convolutional neural network (920,642 parameters), where optical property maps and fluorescence images were processed by convolutional layers, concatenated for further convolutional processing, and separated to predict the fluorophore concentration and subsurface depth (fig. c). The model performance was evaluated using CSH shapes with closest top surface at 0.5-10 mm (n = 1000) and 20 patient-derived tongue tumor shapes contoured using pre-operative MRI images with shifts of 1-10 mm applied to each shape (n = 200). The depth map was used to classify the margin as clear (0) or positive (1) using a cutoff of 5 mm thickness (fig. d).

Results: For CSH, the predicted depth and concentration over all points had a mean absolute error (MAE) of 0.59 ± 0.90 mm and 1.63 ± 1.26 $\mu\text{g/ml}$, respectively. The distance to closest top surface (“margin thickness”) had a MAE of 0.35 ± 0.25 mm and classified margin status with accuracy, precision, specificity and sensitivity of 94%, 90%, 88%, and 100% respectively. In patient-derived tumor shapes, the overall depth, overall concentration, and minimum depth MAE were 1.61 ± 1.96 mm, 2.16 ± 1.58 $\mu\text{g/ml}$, 0.35 ± 0.28 mm, respectively.

Conclusions: The DL system demonstrated accurate performance in predicting and classifying margin thickness. Testing in patient-derived tumor shapes increased the depth and concentration errors, but the quality of closest top surface distance prediction was retained. Future studies will advance tumor model complexity by considering tissue surface irregularity, optical heterogeneity, and variable tumor geometry including finger-like protrusions.

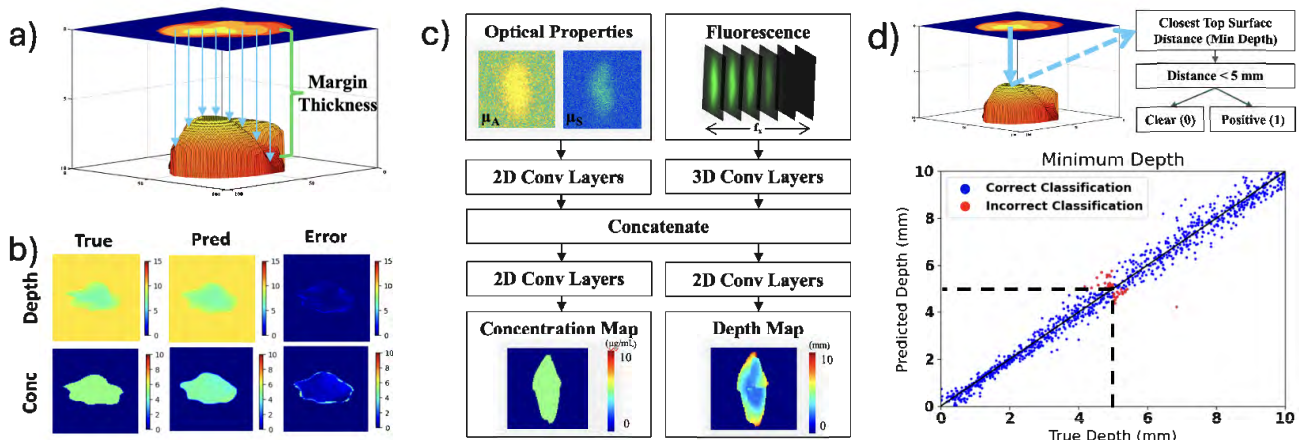


Figure: (a) 3D schematic of a submerged tumor. (b) Depth and Concentration prediction results (background depth assigned a value of 10 mm). (c) DL Architecture. (d) Minimum Depth graph for margin classification.

References: 1. Johnson et al. Head Neck 1998, Quantification of surgical margin shrinkage in the oral cavity

Three-Dimensional Ultrasound Synovial Blood Flow Volume Assessment in Thumb Osteoarthritis Patients

Megan Hutter^{1,2}, Clara Duquette-Evans^{1,2}, Randa Mudathir², Carla du Toit³, Assaf Kadar^{4,5}, Aaron Fenster^{1,2}, Emily Lalone^{4,6}

¹School of Biomedical Engineering, Western University, ²Robarts Research Institute, Western University, ³Faculty of Medicine, Dalhousie University, ⁴Roth | McFarlane Hand and Upper Limb Centre, St. Joseph's Health Care, ⁵Schulich School of Medicine and Dentistry, Western University, ⁶Department of Mechanical and Materials Engineering, Western University

Introduction: The basal thumb joint is a common site of osteoarthritis (OA), causing pain and reduced hand function. Inflammation of the joint lining, synovitis, contributes to pain and progression of OA.¹ This includes blood flow changes and increased stromal vascularization.² However, there is limited understanding of the role of angiogenesis in OA and its progression. Musculoskeletal ultrasound (US) can assess soft tissue features of synovitis and detect blood flow with Doppler technologies, including Power Doppler (PD) and the novel Superb microvascular imaging (SMI).^{3,4} These techniques are limited to 2D visualization, which are operator-dependent for image acquisition of 3D anatomy, thus limiting the assessment of the synovial vasculature. Therefore, this preliminary study aims to assess 3D US Doppler measures of synovial blood flow and investigate the association of blood flow measures with functional, pain, and existing radiographic measures of thumb OA.

Methods: A 3D US imaging device with Doppler capabilities was developed and used for this study. The device has a motorized assembly and translates a linear US transducer over the dorsal aspect of the thumb joint. Nineteen thumb osteoarthritis patients were recruited to investigate 3D US quantitative measures. 3D US B-mode, PD, and SMI images five centimeters in length were acquired. Synovial tissue volumes of all 3D US images were manually segmented every 0.25mm. PD and SMI blood flow volumes were automatically calculated with software counting the coloured voxels within each synovial tissue volume segmentation (Fig. 1). Functional and patient pain assessments, including pinch grip force, patient rated wrist evaluation (PRWE), and visual analog scale of pain pressing the fifth digit, were completed during the imaging session. A forward stepwise linear regression was performed to investigate associations between functional measures, pain measures, US synovial tissue volumes, 3D US phenotype, Eaton-Littler grades, and 3D US synovial tissue blood flow volumes measured using PD and SMI.

Results: Thumb osteoarthritis patients had an average synovial tissue volume of $280.4 \pm 161.7 \text{ mm}^3$ and average synovial blood flow volume of $4.71 \pm 7.72 \text{ mm}^3$ with PD and $1.97 \pm 2.96 \text{ mm}^3$ with SMI. The stepwise linear regression analysis showed the synovial tissue volume accounted for 22.8% of the variability in PD synovial blood flow volumes and 33.5% of the variability in SMI synovial blood flow volumes. Other variables of Eaton-Littler grade and pain measures were not retained in the models.

Conclusion: In this preliminary study, 3D US quantitative measures of synovial blood flow were determined, and predictors of these measures were analyzed. Synovial tissue volume, which represents the region and volume of inflammation, predicted a portion of the variability in the 3D US Doppler measures. These 3D US blood flow measures will be assessed in a cohort of thumb OA patients to investigate changes with disease progression and the clinical importance of blood flow assessment in OA. This novel quantitative measure of synovial blood flow may provide clinicians with a method to assess patients' inflammation and increase insight into the vascular changes associated with OA.

References: [1] Ashraf S, et al. (2008) *Curr Opin Rheumatol.* 20. [2] Prieto-Potin I, et al. (2015) *BMC Musculoskelet Disord.* 16. [3] Koski J, et al. (2006) *Ann Rheum Dis.* 65. [4] Gitto S, et al. (2020) *Radiol Med.* 125.

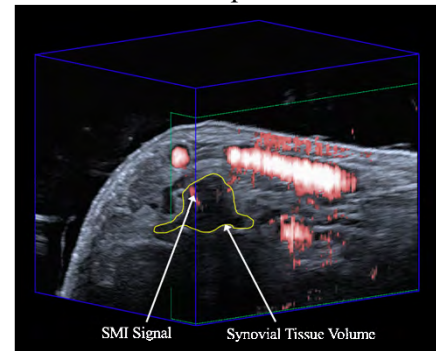


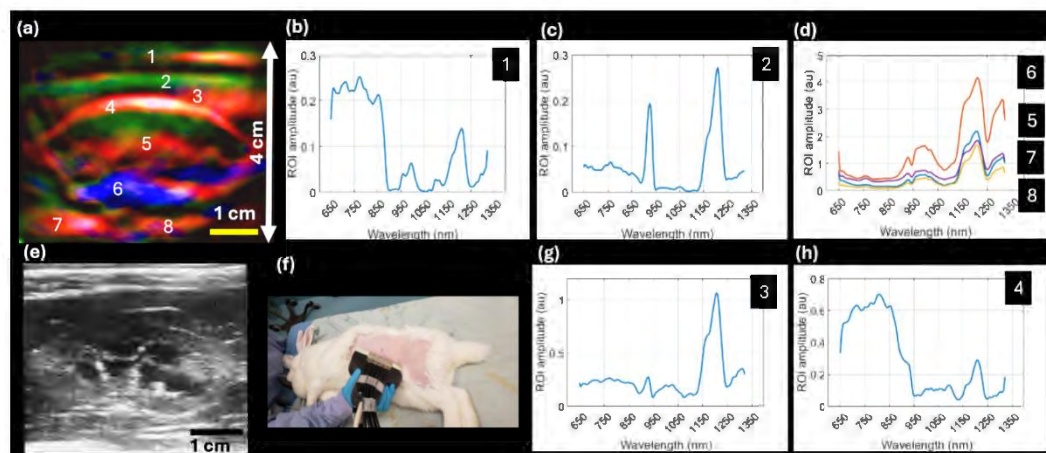
Figure 1. 3D US SMI image of thumb OA patient with outlined synovial tissue volume and SMI signal.

In vivo hyperspectral ultra-broadband sub-MHz photoacoustic imaging: volumetric optical contrast to 4 cm deep and beyond

Ivan Kosik¹, Robert Weersink^{2,3}, Margarete K. Akens^{1,3,4}, Fumi Yokote⁵, Gang Zheng^{1,3}, Brian C. Wilson^{1,3}

¹Princess Margaret Cancer Center, ²Institute of Biomaterials and Biomedical Engineering, Department of Radiation Oncology, University of Toronto, ³c, ⁴Department of Surgery, University of Toronto, ⁵Division of Thoracic Surgery, Toronto General Hospital/University Health Network, University of Toronto

Introduction: Optical imaging and sensing in the visible to near infrared (NIR) range is currently used for cancer diagnosis and surgical decision-making due to the molecular specificity and sensitivity of hyperspectral optical contrast¹. Disease onset and progression is frequently linked to biochemical and morphological disruption or rearrangement of tissue molecular composition, which are reflected in light-tissue interactions. Techniques using multiple disease-specific molecular dyes or nanoagents are increasingly investigated, including minimally invasive cancer therapies. These use multispectral information from techniques such as Raman and NIR spectroscopy, optical coherence tomography, fluorescence imaging, diffuse optical tomography and photoacoustic imaging (PAI). The latter two techniques provide the greatest imaging depth but still generally fail to achieve the urgently needed imaging scale and spectral sensitivity with adequate spatial resolution. PAI uses high-energy, low-power nanosecond laser pulses to rapidly modulate absorbed photon energy throughout a tissue volume thermally inducing pressure waves that can be detected at the tissue surface as ultrasound (US). The acoustic waves carry rich optical information with low attenuation.



Methods: We have designed and constructed a novel hyperspectral PAI system empowered by a specialized in-house built low-frequency (<1 MHz) US detector array with precisely-balanced bandwidth and sensitivity for maximum volumetric imaging performance at depth while

maintaining a spatial resolution ~ 1.5 mm. The detector sub-system is complemented by a tunable (650-1320 nm) Nd-YAG laser using a unique illumination scheme that achieves maximum illumination fluence at ~ 1 cm depth within the imaging slice. The system is packaged in an ergonomic hand-held format. Initial testing of the prototype consisted of controlled multispectral phantom studies and studies of the rabbit kidney as a model tissue, including image contrast using multifunctional porphyrin-lipid nanoparticles (Porphysomes) during interstitial injection².

Results: The above figure summarizes hyperspectral PAI of the rabbit kidney *in situ*: (a) PAI image with merged 800 nm (red), 930 nm (green), and 1200 nm (blue), indicating spectral-measurement sites, including skin (b), pararenal fat (c), hemoglobin-rich renal sinus, medulla, renal artery and vein, respectively (d). Major peaks are identified, including the deoxy hemoglobin peak at 760 nm, the lipid 3rd overtone at 930 nm, water near 980 nm, water/collagen/elastin at 1180 nm, and lipid 2nd CH overtone at 1210 nm. Panel (e) shows US, (g) shows spectra from perirenal fat and (h) the renal cortex.

Conclusions: To our knowledge, these results represent the deepest hyperspectral volumetric PA imaging achieved to date, implemented in a real-time, handheld device. We believe that this will have broad translational potential in diagnostics, surgical guidance and nanomedicine.

This work is supported by the Terry Fox Research Institute New Frontiers Program (#1137) and Canadian Cancer Society

1. B. C. Wilson, D. Eu, *Translational Biophotonics* 2022; 4(3) 2. E. Huynh, G. Zheng, *Nano Today* 2014; 9(2)

Deep Learning Architecture Optimization for 3D Optical Imaging in Early-Stage Oral Cancer Models

Rooaa Shanshal,¹ Hikaru Kurosawa,¹ Natalie Won,¹ Elise Schwarz,¹ Matthew Siracusa,¹
Alon Pener-Tessler,² Alessandra Ruaro,² Brian C. Wilson,¹ Jonathan C. Irish^{1,2} and Michael J. Daly¹

¹Princess Margaret Cancer Centre, University Health Network, Toronto ON
²Department of Otolaryngology – Head & Neck Surgery, University of Toronto

Introduction: Oral cancer progression is often associated with visually apparent changes in tissue composition (e.g., leukoplakia [white], erythroplakia [red]). “Optical biopsy” devices aim to provide low-cost, non-invasive modalities for reliable tumour delineation and depth of invasion assessment. To this end, our group is developing a deep learning (DL)-powered 3D optical imaging system based on spatial frequency domain imaging (SFDI) technology using structured illumination (Fig 1a). Here, we investigate the depth assessment accuracy of two convolutional neural network (CNN) architectures in *reflectance-only* simulation models of oral cancer.

Methods: To train the DL models, *in silico* reflectance images of 10,000 synthetic tumours (depths=0.5–3 mm, widths=3–30 mm) with randomized optical properties were generated using a diffusion theory (DT) light propagation model. The tumour-to-background ratio of free hemoglobin concentration ([fHb]) was set for higher tumour blood content ([B fHb]=0.5–2 g/L, [T fHb]=10xB g/L). This determined each sample’s absorption coefficient (μ_a) (B=0.0015–0.0060 mm⁻¹, T=0.0089–0.0583 mm⁻¹), while scattering coefficients (μ_s) were randomized (0.5–2 mm⁻¹). This reflectance data was fed into two CNNs to train two DL models (Figure 1b) to produce tumour infiltration depth maps; Res-Net uses 2D convolutions and residual blocks, while U-Net refines the data by downsampling and then upsampling data from previous layers. The models were evaluated using a testing dataset comprised of 100 synthetic tumours (depths=0.5–3 mm, widths=3–30 mm) with varying optical properties. Results assessed each architecture’s predicted tumour depth accuracy and qualitative delineation.

Results: Generating DT reflectance images for training took 2 hours. Training this data on the Res-Net-based and U-Net DL models took 1.25 and 4 hours, respectively. Res-Net produced depth maps with an average depth error of 0.25±0.22 mm, had artefacts surrounding the tumour region, and underestimated predicted depths greater than 2 mm. In contrast, U-Net had a lower average depth error of 0.15±0.17 mm, performed more consistently across varying depths, and demonstrated improved tumour delineation with no surrounding artefacts (Figure 1c).

Conclusions: The U-Net DL model yielded overall improved depth accuracy and tumour delineation. Given that the synthetic tumours range between 0.5-3 mm in depth, these results represent an improvement for non-invasive detection of early-stage oral cancer tumours. Next steps include evaluating depth prediction across a wider range of clinically realistic optical properties and surface topographies, in both simulations and phantom experiments.

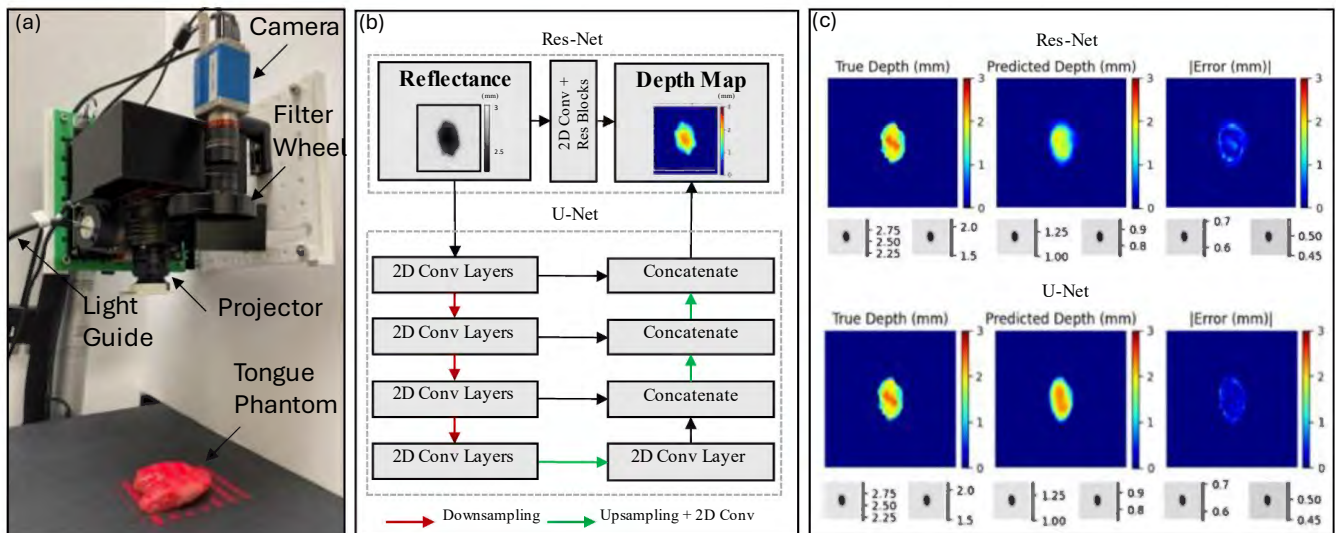


Figure 1. a) Portable SFDI system used to image tongue phantom b) Residual-Network-Based (Res-Net) and U-Net (U-Net) architectures c) Depth prediction results for Res-Net and U-Net models.

Oral Presentations 12: General 2

Abstracts

Evaluating the association between primary motor cortex metabolite levels and dexterity following spinal surgery for degenerative cervical myelopathy

Scott K. Wilson¹, Sarah A. Detombe¹, Alexander C. Friesen², Jennifer E. Murphy³, Pat Doyle-Pettypiece³, Neil Duggal³, and Robert Bartha^{1,4}

¹Centre for Functional and Metabolic Mapping, Robarts Research Institute, Western University, ²Schulich School of Medicine & Dentistry, Western University, ³Department of Clinical Neurological Sciences, London Health Sciences Centre, ⁴Department of Medical Biophysics, Western University

Introduction: Degenerative cervical myelopathy (DCM) can result in loss of finger dexterity, reduced sensation in the extremities, loss of balance, and urinary incontinence [1]. Decompression surgery aims to reduce spinal compression. Predicting which patients will regain functional dexterity post-surgical intervention is difficult. The purpose of this study was to determine whether metabolite levels in the motor cortex before surgery were associated with improved dexterity following surgery. Tissue metabolite levels in the brain can be measured non-invasively by magnetic resonance spectroscopy (MRS). Importantly, the metabolite *N*-acetylaspartate (NAA) is an indicator of neuronal density and mitochondrial function [2], [3]. Additionally, glutamate (Glu), is the primary excitatory neurotransmitter in the brain. We hypothesized that NAA/Creatine (Cr) and Glu/Cr levels at baseline would negatively correlate with post-surgical dexterity changes, as participants with low baseline NAA/Cr and Glu/Cr levels have greater potential to increase.

Methods: Twenty participants (13 male, 7 female; average age=61±13) were recruited during preoperative clinical visits after being diagnosed with DCM and identified as surgical candidates. All imaging and MRS was performed at baseline on a 3T Siemens (Erlangen, Germany) Magnetom Prisma FIT MRI scanner. Motor cortex metabolite levels were measured in participants using the Point RESolved Spectroscopy (PRESS) sequence (TE=135ms, TR=2s, number of transients = 192, 8 cm³ volume) and quantified using the fitMAN software [4]. Long echo-time reduced macromolecule signals. Dexterity was assessed using the Graded Redefined Assessment of Strength, Sensation, and Prehension Version Myelopathy (GRASSP-M) at pre-admission (baseline) and 6-week postoperative time points. Spearman correlations were used to test the associations between pre-operative NAA/Cr, Glu/Cr, and change in GRASSP-M scores 6 weeks following surgical intervention.

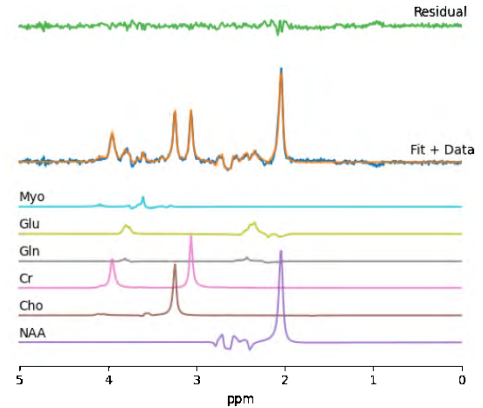


Figure 1: Typical MR spectroscopy data showing the processed in-vivo spectrum (blue), spectral fit overlaid (orange), and fit residual above (green). Below are metabolite components. Myo = myo-inositol, Glu = glutamate, Gln = glutamine, Cr = creatine, Cho = choline, NAA = *N*-acetylaspartate.

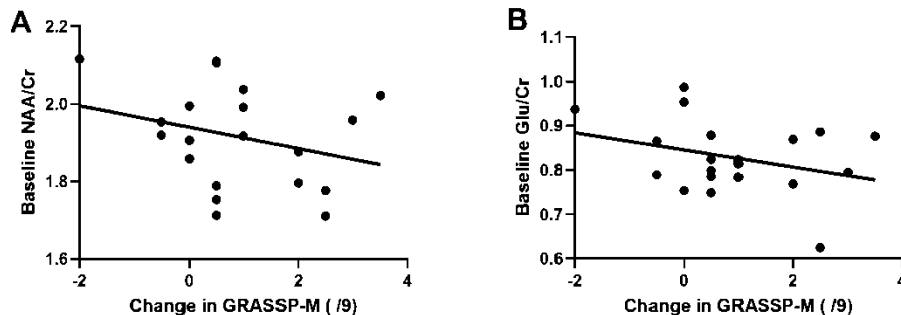


Figure 2: A) Correlation between NAA/Cr levels and change in GRASSP-M scores 6 weeks postoperatively. B) Correlation between Glu/Cr levels and change in GRASSP-M scores 6 weeks postoperatively. Trendlines are superimposed on both graphs.

Results: The average change in GRASSP-M score between 6 weeks after surgery and baseline was 0.9 ± 1.3 ($p < 0.05$; baseline average=4.3), on a scale of 0-9. No significant correlation was found between pre-operative NAA/Cr and change in GRASSP-M scores ($\rho = -0.22$, $p = 0.35$, Figure 2). There was also no significant correlation between pre-operative Glu/Cr and change in GRASSP-M scores ($\rho = -0.21$, $p = 0.37$, Figure 2).

Conclusions: The significant increase in GRASSP-M post-surgery validates the success of surgical treatment. The lack of significant correlation between baseline Glu/Cr and baseline NAA/Cr with change in GRASSP-M scores indicates that Glu/Cr and NAA/Cr are not viable predictors of successful spinal decompression surgery outcomes.

[1] R. J. Zhang *et al.*, *Spinal Cord*, vol. 56, no. 1, pp. 7–13, 2018. [2] T. E. Bates *et al.*, *Neuroreport*, vol. 7, no. 8, pp. 1397–1400, 1996. [3] N. De Stefano *et al.*, *Magn Reson Med*, vol. 34, no. 5, pp. 721–727, 1995. [4] R. Bartha *et al.*, *NMR Biomed*, vol. 12, no. 4, pp. 205–216, 1999.

Accelerating Monte Carlo Light Propagation Models for Deep Learning-Enabled Fluorescence-Guided Surgery

Matthew A. Siracusa,¹ Natalie Won,¹ Hikaru Kurosawa,¹ Rooaa Shanshal,¹ Christina Negus,¹ Brian C. Wilson,¹ Jonathan C. Irish^{1,2} and Michael J. Daly¹

¹Princess Margaret Cancer Centre, University Health Network, Toronto ON
²Department of Otolaryngology – Head & Neck Surgery, University of Toronto

Introduction: Accurate determination of tumor depth is essential for achieving clear margins during cancer surgery. Tumor-specific fluorescent contrast agents can help with surface delineation, but current optical devices do not measure sub-surface tumor depth. Our group is developing a deep learning (DL)-enabled 3D fluorescence system that uses spatial frequency domain imaging (SFDI) to quantify depth (Fig a). To leverage DL capabilities with limited patient data for training, we employ physics-embedded *in silico* training built on known light propagation models. To date, this uses an analytical diffusion theory (DT) method, which is fast, but limited in clinical realism. Monte Carlo (MC) is a stochastic method that can model a wider range of surgical scenarios than DT (Fig. b); however, MC requires significantly more computation. Here, we explore optimizing MC simulations for *in silico* DL training.

Methods: A prototype SFDI fluorescence system has been constructed to project a sequence (n=18) of structured illumination patterns across multiple spatial frequencies (n=6) and phase-shifts (n=3). Diffuse reflectance and fluorescence images are input into a custom Siamese convolutional neural network that outputs tumor depth and fluorescence concentration (Won et al. JBO, 2024). Monte Carlo eXtreme (MCX) (Fang et al. Optica, 2009), an open-source MC package, includes a ‘photon sharing’ option (PS-MC) that simulates multiple illumination patterns by scaling the detected photons from a single forward simulation by the illumination pattern weights. To compare simulation times and accuracy, PS-MC (“batch mode”) was compared with standard non-photon sharing (“sequential mode”) over a range of simulated photons (1e6, 5e6, 1e7, 5e7, 1e8). The validity of PS-MC as a method of generating DL training sets was assessed in a previously developed model of mucosal oral cancer (depths of invasion 1 – 10 mm). Using an in-house MATLAB tissue simulator, a set of 10,000 synthetic tumor meshes (composite spherical harmonics) were inserted into a voxelated volume (0.5 mm voxels) over randomized range of optical absorption ($\mu_a = 0.0015 - 0.015 \text{ mm}^{-1}$), scattering ($\mu_s' = 0.75-2 \text{ mm}^{-1}$) and fluorescence contrast (1–10 $\mu\text{g/mL}$).

Results: Using PS-MC, simulations of SFDI image sets were 4.1 times faster for total training time of n=10,000 tumor shapes (5.9 vs 24.6 hours at 1e7 photons) on average than standard MC simulations (Fig. c). The mean difference in pixel values between PS-MC and standard MC was $<1.5 \times 10^{-5} \%$. PS-MC training yielded mean (SD) tumor depth and fluorescence concentration errors of $0.71 \pm 0.70 \text{ mm}$ and $1.45 \pm 1.91 \text{ ug/mL}$, respectively (Fig. d).

Conclusions: MC-PS provides significantly faster SFDI simulations without sacrificing image quality to allow for practical generation of *in silico* training data. Initial results from MC-trained DL models validate depth accuracy, enabling future investigations over a wider range of cancer surgery scenarios.

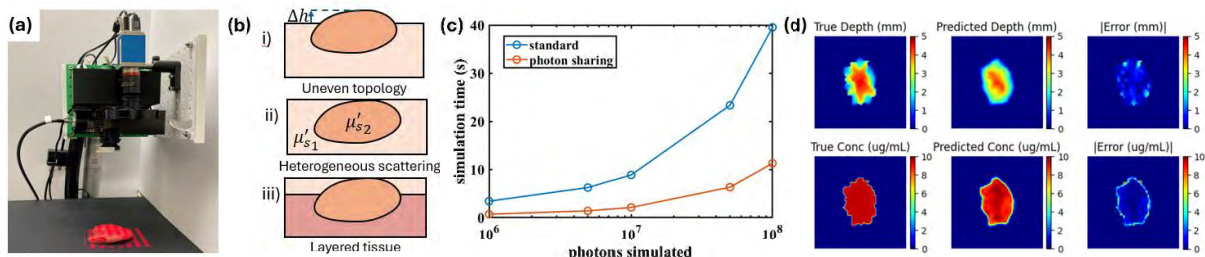


Figure. (a) Fluorescence imaging system. (b) Clinical cases enabled by MC. (c) Simulation time of standard vs PS-MC for n=1 tumor shape. (d) Tumor depth and concentration predictions from MC-trained DL model.

Role of Imaging Contrasts in the Volumetric Prediction of MT-NOE Attenuated Tumour Sub-Region

Céline Dubroy-McArdle^{1,2}, Wilfred Lam^{3,4}, Greg Stanisz^{3,4}, Dafna Sussman^{1,2,5}

¹Departments of Biomedical Physics & Engineering, Toronto Metropolitan University, ²Institute for Biomedical Engineering, Science and Technology (iBEST), Toronto Metropolitan University & St. Michael's Hospital, ³Sunnybrook Research Institute, ⁴Department of Medical Biophysics, University of Toronto ⁵Department of Obstetrics & Gynecology, University of Toronto

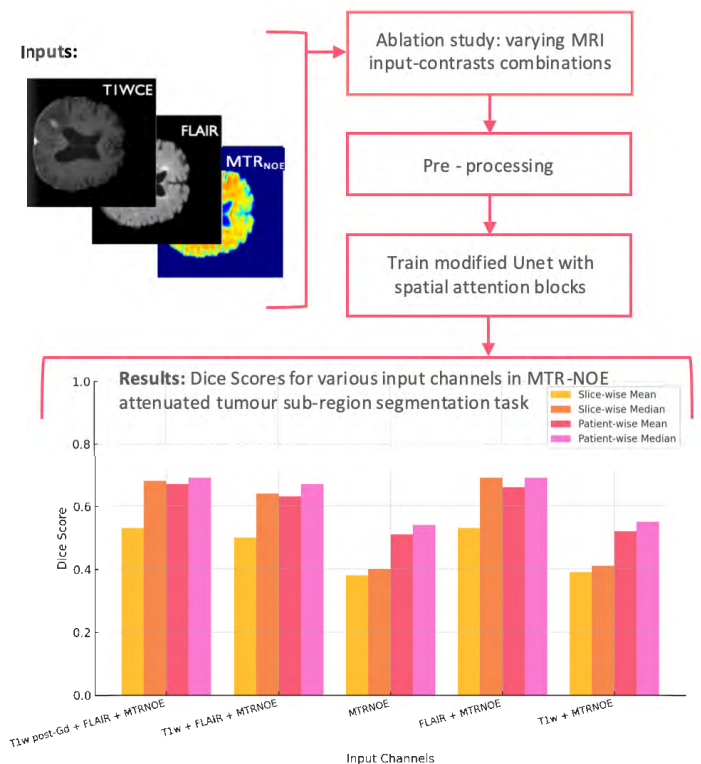
Introduction: Metastatic brain tumours affect approximately 20% of all cancer patients and rely on MRI- based segmentation for diagnosis and treatment planning [1]. Current protocols include T1-weighted (T1w) post-Gadolinium (Gd) images for assessing anatomical characteristics of the lesion, such as size and location, and fluid-attenuated inversion recovery (FLAIR) for evaluating the extent of edema [2]. Magnetization transfer ratio (MTR) images acquired at a frequency offset of -3.5 ppm, reflective of the nuclear Overhauser effect (MTR_{NOE}), provides a distinct contrast that may be valuable in identifying tumour microstructural and metabolic changes. Notably, the volume of the MT-NOE attenuated sub-region can extend beyond the region identified on T1w post-Gd images [3]. This study aims to assess the impact of various MRI input-contrasts on the automatic segmentation and volumetric prediction of the MT-NOE tumour sub-regions.

Methods: T1w post-Gd, FLAIR, and MTR_{NOE} images were acquired from 101 patients from Sunnybrook Health Sciences Centre. MT-NOE attenuated sub-regions were manually segmented using ITK-SNAP to establish the ground truth. All MRI contrast volumes were co-registered, and sliced into 2D transverse-plane images. MTR_{NOE} images were thresholded at the 99th percentile, and all images underwent normalization. The dataset was split patient-wise into a training set (75%) and a test set (25%). To address data imbalance, slices containing only background pixels in the training set were under-sampled. A modified U-Net with spatial attention blocks integrated into the encoder pathway, in order to have the model focus on the relevant parts of the image, was trained. An ablation study evaluated the contribution of different MRI contrast combinations. Predicted 2D masks were reassembled for each lesion for a volumetric comparison to the ground truth.

Results: For the MT-NOE segmentation task, the combination of T1w post-Gd, FLAIR, and MTR_{NOE} input-contrasts achieved the highest mean and median patient-wise Dice scores (0.67 ± 0.18 and 0.69 , respectively). Similar performance was observed with FLAIR and MTR_{NOE} (mean: 0.66 ± 0.20 ; median: 0.69). Additionally, the FLAIR and MTR_{NOE} combination also provided the most accurate volumetric predictions when compared to the computed ground truth, thus this combination of input-contrast proved to be essential in accurate segmentation of the MT-NOE attenuated sub-region.

Conclusions: This study demonstrates the feasibility of automatic segmentation of the MT-NOE attenuated tumour sub-regions, without the use of Gd contrast. The larger MT-NOE sub-regions reflect its utility in identifying abnormal tissue, however further research is required to explore the sub-regions' clinical value and integration into tumour treatment planning and monitoring.

References: [1] P. Sacks and M. Rahman, "Epidemiology of Brain Metastases," Oct. 01, 2020, W.B. Saunders. doi: 10.1016/j.nec.2020.06.001. [2] M. Martucci et al., "Magnetic Resonance Imaging of Primary Adult Brain Tumors: State of the Art and Future Perspectives," Feb. 01, 2023, MDPI. doi: 10.3390/biomedicines11020364. [3] J. H. Suh, R. Kotecha, S. T. Chao, M. S. Ahluwalia, A. Sahgal, and E. L. Chang, "Current approaches to the management of brain metastases," May 01, 2020, Nature Research. doi: 10.1038/s41571-019-0320-3.



Light-Based Pressure Monitoring Guidance in Neurosurgery Retraction: Development and Validation of an Optical Sensing Algorithm

Lee D. Sikstrom¹, David W. Holdsworth^{1,2,3}

¹Dept. of Medical Biophysics and Medical Imaging, ²School of Biomedical Engineering, ³Dept. of Surgery, University of Western Ontario

Introduction: In neurosurgery, retractors are used to displace healthy tissue, enabling access to deeper brain regions. However, the pressure this procedure puts on healthy tissue carries significant risk—with 40% of patients experiencing complications due to tissue retraction [1, 2]—highlighting the need for a retraction monitoring system to minimize harm. Our research addresses this challenge by developing a retractor equipped with miniaturized optical sensors and machine learning algorithms to alert surgeons to potentially harmful conditions. These sensors, embedded in the retractor and in contact with brain tissue, estimate applied pressure by emitting light into the tissue and measuring reflected signals. This study focuses on developing an algorithm to accurately estimate applied pressure using optical signals.

Methods: The MAXM86161 photoplethysmography (PPG) system, comprising three LEDs (530 nm, 660 nm, 880 nm) and a photodiode, was used to collect optical signals. The initial algorithm was built and tested on data collected from human fingertips before being evaluated on porcine brain tissue. To collect training data, the optical sensor was mounted on a translating platform to apply controlled pressure profiles to participants' index fingers, with simultaneous force measurements recorded using a load cell as ground truth. Pressure levels ranged from 0 to 320 mmHg, and data were collected across two sessions (n = 15, 47% male) separated by at least 24 hours. In addition, a validation set of 2,000 data points was collected from *in vivo* porcine brain tissue.

A Random Forest machine-learning model was employed to estimate applied pressure, with the light intensity (from three wavelengths), finger temperature, and blood pressure as the input features. The dataset from fingers was split into 90% training and 10% testing sets, with hyperparameter optimization conducted via random search. Feature importance in the model prediction was analyzed. Finally, the model's performance was evaluated when applied to the *in vivo* porcine brain tissue data.

Results: The optimized Random Forest model achieved an R² score of 0.98, a mean absolute error of 1.8 mmHg, and a root mean squared error (RMSE) of 4.5 mmHg (Figure 1). Green and infrared optical signals were the most influential features for pressure prediction. However, model performance on porcine brain tissue showed weak correlation with ground truth, with an R² value of 0.23 (Figure 2).

Conclusions: These results demonstrate the potential of optical sensors and machine learning for estimating applied pressure on vascularized tissue, achieving high accuracy on index finger data. However, the model's limited generalizability to porcine brain tissue underscores the need for further refinement. Future work will focus on improving model robustness, training algorithms directly with brain tissue data, and implementing principle component analysis of signal data to enhance performance in neurosurgical applications.

- [1] B. Konya, et al., "Brain retraction injury after elective aneurysm clipping: a retrospective single-center cohort study," *Acta Neurochir (Wien)*, vol. 164, no. 3, pp. 805-809, Mar 2022
- [2] Z. D. Travis, et al., "Surgically-induced brain injury: where are we now?," *Chin Neurosurg J*, vol. 5, no. 1, p. 29, 2019/12/16 2019

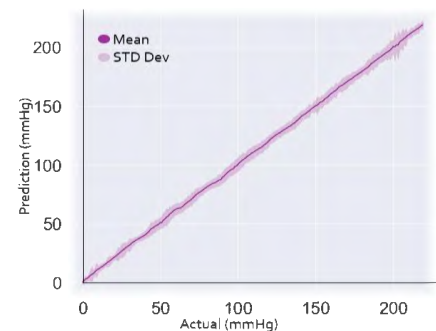


Figure 1: Performance of the machine learning model on human fingertip data. The actual data on the x-axis compared to the model's predictions on the y-axis.

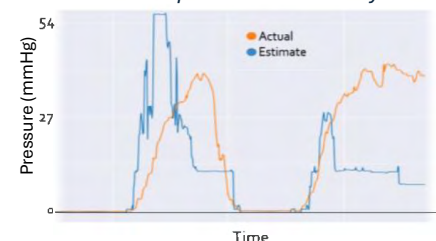


Figure 2: Performance of the model on *in vivo* porcine brain tissue.

Pitches 7: Optical Imaging & Ultrasound Imaging

Abstracts

Standardizing B-line annotation for reproducible lung ultrasound metrics

Maha Kesibi¹, Zhuoxin Guo¹, Gabor Fichtinger¹, Parvin Mousavi¹, Tamas Ungi¹

¹School of Computing, Queen's University, Kingston, Canada

INTRODUCTION: Lung ultrasound (LUS) is a widely used diagnostic tool for assessing pulmonary and cardiac conditions. B-lines are vertical, hyperechoic artifacts on ultrasound that extend from the pleural line to the bottom of the image and move synchronously with respiration. They serve as indicators of fluid overload in the lungs. However, traditional B-line counting is prone to interobserver variability, particularly in cases of confluent B-lines, where individual artifacts merge into continuous hyperechoic areas. Preliminary observations identified inconsistent annotation depths of B-lines as a source of variability in LUS analysis. To address these challenges, we developed a customizable visual depth guide and annotation tools to improve annotation. These annotations enable the calculation of a pleural B-line coverage percentage metric, proposed as a more standardized alternative to traditional B-line counting [1]. Pleural B-line coverage percentage quantifies hyperechoic area, reducing subjective counting errors. This study aims to improve B-line annotation consistency and reduce interobserver variability in lung ultrasound analysis.

METHODS: We developed tools within the 3D Slicer platform to support annotation tasks, such as adding/removing lines, toggling overlay guides, and navigating frames. Images were sourced from Brigham and Women's Hospital (Boston, MA). Four exploratory depth guide designs were implemented and evaluated based on user preference (Figure 1). Designs were created to balance clarity and minimize interference with the ultrasound image. A two-part evaluation was conducted to assess the options. First, a survey of 13 participants, including researchers with varying levels of experience in medical image annotation, ranked the four depth guide designs from best (1) to worst (4).

Rankings were analyzed using mean ranks and the Friedman test to assess statistical significance. Second, an interobserver variability assessment was conducted using Guide Mode 1 (dashed line). Two trained observers annotated 40 LUS scans under two conditions: with and without the depth guide. Observers marked B-line and pleural lines. Interobserver agreement was evaluated using the intraclass correlation coefficient (ICC).

RESULTS: The survey identified Mode 1 (dashed) as the most preferred depth guide, with a mean rank of 1.77, followed by Mode 4 (3.08), Mode 2 (2.23), and Mode 3 (2.92). The Friedman test revealed statistically significant differences ($p=0.033$), indicating that participants exhibited clear preferences for certain designs. The interobserver variability assessment demonstrated improved agreement with the use of the depth guide. The ICC improvement from 0.723 (moderate agreement) without the guide to 0.831 (good agreement) with the guide. The mean variability in the pleural coverage percentage metric decreased from 0.11 to 0.09.

CONCLUSION: Our proposed tools and depth guides demonstrate potential for reducing interobserver variability in B-line annotation. Survey results revealed Mode 1, a dashed line, as the most preferred depth guide, likely due to its simplicity and unobtrusive design, balancing clarity and usability. This finding emphasizes the importance of designing depth guides that align with user needs and enhance annotation consistency. Despite the small sample size (13 survey participants and 2 observers), the improved ICC scores and reduced mean variability indicate the method's promise for annotation reliability. However, these findings are preliminary, requiring further validation. Future work will assess interobserver variability with a larger user base, evaluate intra-observer variability, and validate the pleural B-line coverage percentage metric across more diverse datasets and clinical contexts.

REFERENCES: [1] Brusasco, C. et al. Quantitative lung ultrasonography: a putative new algorithm for automatic detection and quantification of B-lines. *Crit Care* 23, 288 (2019).

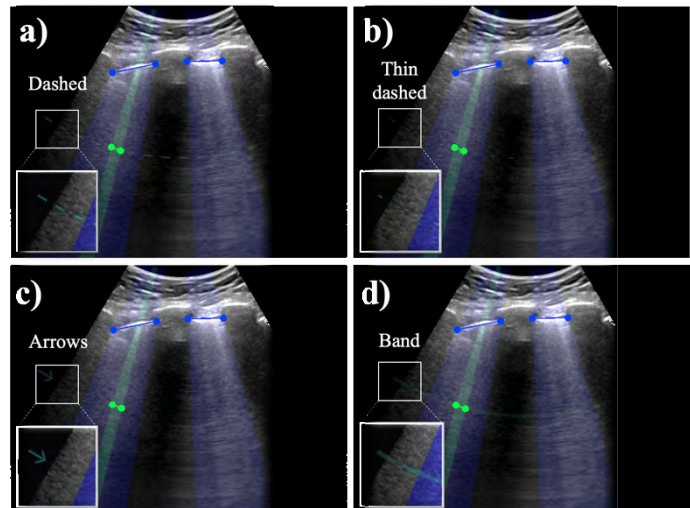


Figure 1. Comparison of Four Depth Guide Designs for B-Line Annotation in Lung Ultrasound, (a) dashed line, (b) thinner, more spaced-out dashed line, (c) side arrows, (d) translucent band.

Automated Liver Segmentation using Attention Models in Point-of-Care Ultrasound Images

Zachary Szentimrey¹, Miriam Naim Ibrahim², Ahmed El Kaffas^{2,3}, Eranga Ukwatta¹

¹School of Engineering, University of Guelph, Guelph, Ontario, Canada; ²Oncoustics, Toronto, Ontario, Canada;

³Department of Radiology, Stanford University, Stanford, California, USA

Introduction: Non-alcoholic fatty liver disease (NAFLD) is the most common chronic liver condition in Canada, affecting 20% of the population according to the Canadian Liver Foundation [1]. Approximately 5% of Canadians are estimated to have metabolic dysfunction-associated steatohepatitis (MASH), a more severe form of NAFLD characterized by liver inflammation and fat accumulation [2]. NAFLD causes a gradual stiffening of the liver, called fibrosis, that becomes permanent scarring if not intervened, termed cirrhosis. If left untreated, liver failure can result. Early detection of NAFLD is essential for implementing therapeutic strategies to prevent disease progression. Current diagnostic methods, such as liver biopsies, elastography, and magnetic resonance imaging/computed tomography (MRI/CT) scans are costly, and require specialized expertise. To this end, we propose a liver segmentation method utilizing point-of-care (POC) based ultrasound (US) imaging to support a cost-effective and accessible diagnostic alternative.

Methods: Our dataset includes 16,058 labelled POC US images from 231 patients with a wide range of liver stiffness scores, measured in kilopascals (kPa) using a FibroScan. Patients were categorized into four groups based on liver stiffness: <8 kPa, 8–12 kPa, 12–20 kPa, and >20 kPa. US images were acquired using Clarius C3 and C3HD3 probes, while liver

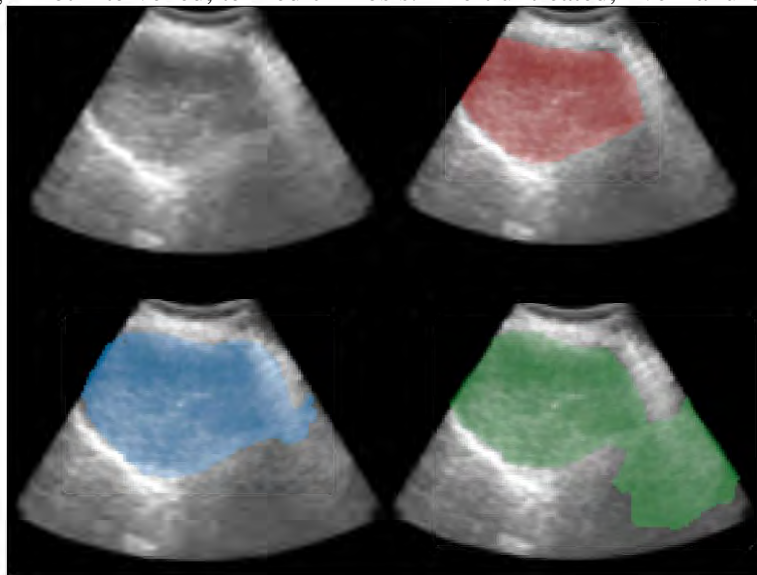


Figure 1: Example segmentation. Top left: US image. Top right: Ground Truth. Bottom left: Attention R2U-Net. Bottom right: 2D U-Net.

stiffness data were obtained via FibroScan. To ensure robust model evaluation, data were split into training, validation, and test sets at the patient level (185/22/24 patients) and image level (12,607/1,631/1,820 images). 106 patient images were captured using the C3 probe and 125 patient images captured using the C3HD3 probe. Manual liver segmentations by trained clinicians were used as ground truth for model comparison. We evaluated a baseline 2D U-Net model and an enhanced attention-based model, Attention R2U-Net [3], designed to improve the segmentation along object boundaries. The Dice Similarity Coefficient (DSC) was used as the primary evaluation metric, and the Wilcoxon signed-rank test (p -value < 0.05) was applied for statistical significance testing.

Results: Mean and standard deviation DSC scores on the test set are summarized in Table 1, with results stratified by liver stiffness groups. The Attention R2U-Net model outperformed the 2D U-Net with statistically significant improvements in DSC for all groups except the >20 kPa category. Example segmentations generated by both models, along with ground truth images, are presented in Figure 1.

Table 1: DSC results for each model tested and p -values between the models for each disease group.

Model	Mean DSC (%) for All Groups	Mean DSC (%) for <8 kPa	Mean DSC (%) for 8-12 kPa	Mean DSC (%) for 12-20 kPa	Mean DSC (%) for >20 kPa
2D U-Net	75.1 ± 17.7	78.8 ± 14.6	76.3 ± 16.6	80.2 ± 15.5	59.3 ± 19.3
Attention R2U-Net	75.9 ± 17.6	79.6 ± 14.5	77.9 ± 15.7	81.0 ± 15.5	58.4 ± 18.3
p-value	<0.001	<0.001	<0.001	<0.001	0.035

Conclusions: Our results demonstrate that the Attention R2U-Net model provides superior segmentation performance on POC US images, offering a promising approach for early NAFLD detection. This technique could serve as a practical, accessible diagnostic support tool, reducing reliance on invasive and costly procedures.

References: [1] Canadian Liver Foundation. Accessed Nov 2024. <https://www.liver.ca/patients-caregivers/liver-diseases/fatty-liver-disease/>. [2] Swain MG *et al.*, Burden of nonalcoholic fatty liver disease in Canada, 2019-2030: a modelling study. *CMAJ Open*. 2020. [3] Zuo Q *et al.*, R2AU-Net: Attention Recurrent Residual Convolutional Neural Network for Multimodal Medical Image Segmentation, *Security and Communication Networks*. 2021.

Influence of laser coherence length in polarization speckle-based tumour detection

Daniel C. Louie¹, Carla Kulcsar^{1,2}, Hector A. Contreras-Sanchez^{1,2}, W. Jeffrey Zabel^{1,2}, Alex Vitkin^{1,2,3}.

¹Princess Margaret Cancer Centre, University Health Network; ²Department of Medical Biophysics, University of Toronto;

³Department of Radiation Oncology, University of Toronto

Purpose/Background: Accurate and rapid tumour detection is among the foremost goals for optical imaging in cancer care. Within this context, the optical phenomenon of polarization speckle (PS) is an interesting non-invasive signal space to explore due to its sensitivity to scattering differences of tissues. Dispersion of a laser's coherent wavefront through tissue results in a backscattered stochastic interference pattern of fluctuating "salt-and-pepper" intensities and polarization states referred to as polarization speckle. PS is captured in a snapshot measurement without a lens, allowing for a technique with minimal hardware requirements that lends itself to wide accessibility and clinical integration. Previous studies [1] [2] have indicated cancer detection utility in the statistical properties of PS, such as speckle contrast and the degree of polarization. This study explores the differences between using a benchtop gas laser and a handheld laser diode pointer (more appropriate for clinical translation) as the illumination source for volumetric scattering polarization speckle measurements, towards determining the ideal optimal illumination characteristics for rapid tumour detection.

Methods: Polarization speckle patterns generated from a diode laser pointer (633 nm, coherence length <0.5 cm) were compared against the speckle generated from a HeNe laser (635 nm, coherence length > 20 cm). Each laser was used to interrogate scattering phantoms (titanium dioxide dispersions in resin), and excised tissues (murine dorsal skin flaps containing tumours growing from human-derived pancreatic cancer cells). A Stokes vector polarization state mapping of the resulting speckle pattern from the two light sources was derived using a custom polarization speckle measurement system, the results of which are shown in Fig 1. Sixty-six (66) statistical polarization and speckle-based metrics were extracted from these images for analysis.

Results and Conclusions: From the volumetric scattering phantoms, it was found that five PS metrics showed strong correlation to attenuation coefficient in both lasers. Speckle contrast metrics differed greatly between the two laser sources in absolute magnitudes (Mean $C = 0.65$ for HeNe and mean $C = 0.25$ for diode) but show similar sensitivity to different turbidities (slope $m=0.03$ for HeNe and diode). In tissue, differences in speckle contrast between human tumours and normal mouse skin were primarily visible with the lower coherence length laser diode ($p = 0.4$ for HeNe vs $p = 0.01$ by Kruskal-Wallis test). Results interpretation for both phantom and tissue experiments is currently ongoing. For now, these preliminary findings indicate that lower coherence length lasers can be equally effective for polarization speckle-based tumour detection.

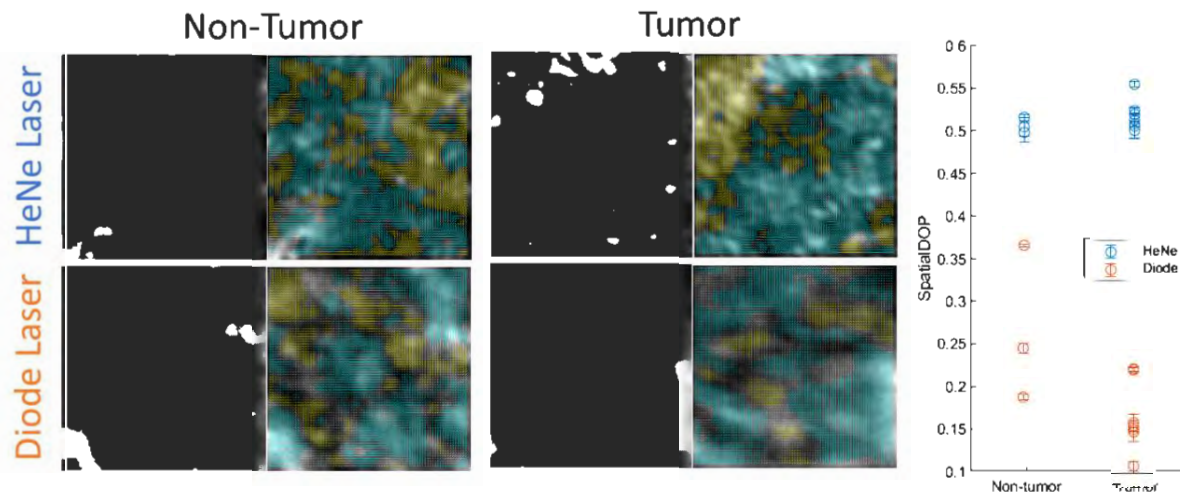


Figure 1. Left: Example speckle images with polarization overlays for non-tumor and tumor samples from two lasers. Right: Plot of PS metric 'Spatial DOP' showing separation between samples in Diode but not HeNe.

[1] Tchvialeva et. al. J. Biomed. Opt., 18 (6), (2012).

[2] Louie et. al. J. Biomed. Opt., 23 (12), (2018).

Quantifying Tendon Excursion in the Shoulder using a 3D-Ultrasound Musculoskeletal System

Marie Le¹, Aaron Fenster², George Athwal^{3,4}, Emily Lalone^{3,5}

¹School of Biomedical Engineering, Western University; ²Robarts Research Institute, Western University; ³Roth | McFarlane Hand and Upper Limb Centre, St. Joseph's Health Care; ⁴Schulich School of Medicine and Dentistry, Western University; ⁵Department of Mechanical and Materials Engineering, Western University

Background: Following reverse shoulder arthroplasty (RSA), a form of shoulder surgery where native biomechanics are reversed, some patients complain of anterior shoulder pain.¹ Although not fully understood, a potential etiology lies in the rotator cuff. The conjoint tendon, namely the coracobrachialis tendon originating at the coracoid process and extending down to the biceps—gets impinged between the coracoid process and the lesser tuberosity of the humerus.¹ Previous studies have employed the use of computed tomography (CT) to examine subcoracoid space¹. CT does not provide high resolution images of the soft tissue structures thereby, fails to capture what occurs at the site of impingement. Ultrasound (US) provides an accessible imaging modality allowing for the visualization of soft-tissue insertions, and bony structures. Conventional ultrasound is two-dimensional, which limits the comprehensive visualization of the entire three-dimensional (3D) joint. 3DUS allows for visualization of the whole joint and takes away some operator dependency by providing operators with an entire 3D volume rather than a slice. This work aims to quantify the distance between the conjoint tendon and the lesser tuberosity by using 3DUS to visualize impingement in healthy individuals and RSA patients.

Methods: A previously developed 3DUS system was used to acquire 3D volumes of the tendon and joint from healthy and RSA patients. The device consists of a tracked mechatronic arm that moves a 14L5 linear transducer to capture a series of 2D images. Using a guide, internal rotation and external rotation was measured in increments of 15° for neutral, abduction, elevation and behind the back positions. Following image acquisition, each 3D ultrasound volume was manually segmented and measured to obtain the distance between the lesser tuberosity and conjoint tendon. The distances across the various positions were statistically analyzed to determine most at-risk impingement sites and positions.

Results: Preliminary results demonstrate that healthy participants have varied conjoint tendon to humeral head distances and do not contact the lesser tuberosity at neutral and external rotation positions. The closest distance (0 mm) full contact is during behind the back positions in healthy populations, and the furthest away being during external rotation (11.3mm).

Conclusion: This study demonstrates the utility of 3DUS imaging to measure tendon-to-bone distances, enabling the investigation of shoulder impingement during internal and external rotation for various positions in healthy individuals and RSA patients. The study is currently in-progress, but we intend to quantify the distance between the conjoint tendon and lesser tuberosity of the humerus to provide a better understanding of the altered rotator cuff tendon path following RSA and to establish baseline biomechanics through these positions.

References: 1. Klosterman EL, Tagliero AJ, Lenters TR, et al. The subcoracoid distance is correlated with pain and internal rotation after reverse shoulder arthroplasty. *JSES International*. 2024;8(3):528-534. doi: 10.1016/j.jseint.2024.01.01

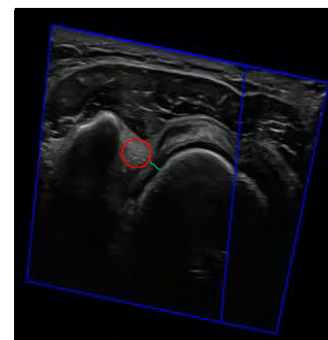


Figure 1: 3DUS image of conjoint tendon (in red). The green line depicts distance between the conjoint tendon and humerus.

Self-Supervised Learning for Retinal Disease Classification: Reducing Annotation Dependency with Transformation-Based Pretext Learning with Limited Labels

Pramit Dutta¹ and Eranga Ukwatta¹

¹School of Engineering, University of Guelph, Guelph, Ontario, Canada.

Introduction: Retinal diseases such as age-related macular degeneration (AMD) and diabetic macular edema (DME) are leading causes of vision impairment worldwide, significantly affecting quality of life. Subtypes of AMD, including choroidal neovascularization (CNV) and DRUSEN, along with DME-related complications, require precise detection for effective treatment. While manual classification of Optical Coherence Tomography (OCT) images demands specialized expertise, machine learning frameworks with automated detection capabilities can facilitate early diagnosis. This study proposes a self-supervised learning (SSL) approach to reduce reliance on labeled data by leveraging the intrinsic geometry of the data.

Methods: We introduce a self-supervised learning (SSL) framework that was implemented on a publicly available Optical Coherence Tomography (OCT) dataset where a transformation-based pretext learning method was leveraged to capture the undermined geometry of the dataset as well as the pattern of the images of different classes. The OCT dataset contains more than 100000 images divided into four classes- CNV(37,455), DME(11,598), Drusen(8,866), and Normal(51,390). In this approach labels were removed from 60% of the images for pretext learning, and the acquired representations were fine-tuned on the remaining 40% for classification. In the pretext learning, different transformation tasks (e.g.- flipping, 90° and 180° rotation, horizontal flipping, etc.) were performed and a ResNet-50-based architecture was used to predict the transformation. Later the learned features were used in the downstream model (based on ResNet-50 architecture) which used only 40% of the labeled data for fine tuning in final classification.

Result: The proposed framework achieved an average classification accuracy of 87.11% with a precision of 84% and an F1 score of 82%, demonstrating the model’s ability to learn intricate patterns and correlations using minimum labeled data. However, the model did not show a robust performance in classifying Drusen due to the low number of samples. An evaluation of the class-wise performance of the model is as follows:

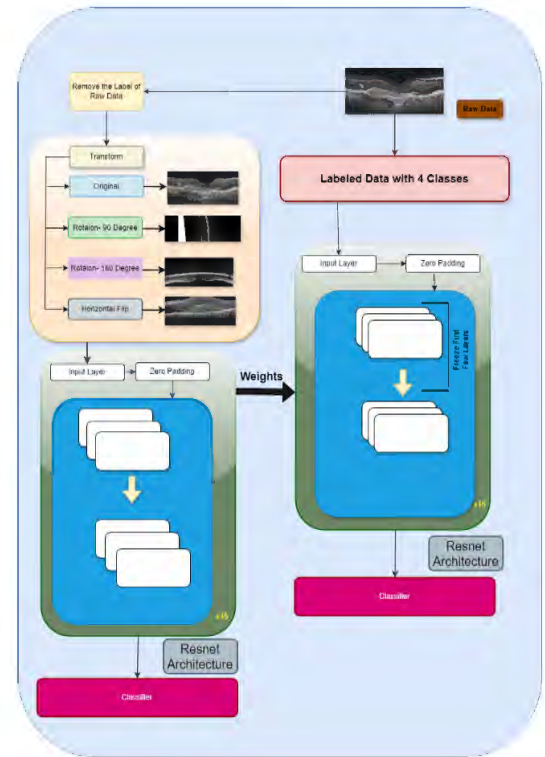


Figure 1: Self-Supervised Learning Framework utilizing Pretext Learning

Table 1: Classification Report (Class wise Performance)

Parameter	CNV	DME	DRUSEN	Normal
Precision	0.79	0.90	0.89	0.78
Recall	0.98	0.94	0.50	0.90
F1-Score	0.88	0.92	0.64	0.83

Conclusion: This study underscores the value of self-supervised learning in medical imaging, particularly in label-scarce scenarios. By effectively capturing the intricate geometry of the data, the proposed approach reduces annotation dependency while enhancing diagnostic performance. This SSL framework offers a scalable and data-efficient solution, making it well-suited for broader applications in medical imaging and other resource-constrained domains.

Polyvinyl Alcohol Cryogels (PVA-C): Fabrication Method for Homogeneous Multimodal Phantoms

Olivia Qi^{1,5}, Joeana Cambranis^{4,5}, Terry Peters^{2,3,4,5}, Elvis C.S. Chen^{1,2,3,4,5}

Department of Medical Biophysics¹, Department of Electrical and Computer Engineering², Department of Medical Imaging³, School of Biomedical Engineering⁴, Robarts Research Institute⁵, Western University, London, Ontario, Canada

Introduction: The development of accurate medical imaging phantoms is essential for evaluating applications under ultrasound (US), magnetic resonance imaging (MRI), and computed tomography (CT). Polyvinyl alcohol cryogel (PVA-C) mimics tissue properties after freeze-thaw cycles (FTC). However, for larger phantoms such as those representing liver and breast tissue, traditional methods often result in inhomogeneities between the core and outer layers due to uncontrolled FTC, as well as condensation of scattering agents caused by slow freezing and uneven stirring. These issues compromise mechanical and imaging quality.¹ This study proposes the use of an environmental chamber (EC) (TestEquity 1000 series, Fig. 1) to regulate FTC, enabling instant freezing and uniform thawing. The hypothesis is that this controlled approach will enhance phantom mechanical homogeneity and imaging quality by minimizing artifacts.

Methods: A 10% w/w PVA-C solution was prepared by mixing 100 g of PVA powder with 900 g of water, heated to 75–85°C, and maintained for 1.5 hours with constant stirring by placing a stirrer near the bottom to ensure homogeneity. The process was conducted in a fume hood for safety. After heating, 1 g of Germall germicide was added as a preservative, 2.5 % w/w talcum for CT and ultrasound², and 0.3 ml/kg gadolinium for MRI was added to 1 kg of PVA-c to enhance visibility. To avoid uneven mixing, talcum was mixed with drops of water before added to pva-c and mixed with turbine and degassed using a vacuum chamber (Fig. 1), PVA-C solution was poured into two molds (16 cm × 11 cm × 5 cm) and sealed to prevent vapor loss. FTC with each cycle consisting of freezing at –20°C for 20 hours followed by thawing in room temperature (22 °C) for 15 hours. In the traditional method, the mold was placed directly in a freezer for freezing and thawed at room temperature. The proposed method conducted FTC in an EC (Fig. 1) with instant freezing and uniform thawing at 0.05°C/min. Each phantom was scanned under US, CT, and MRI. MRI images were analyzed for uniformity by calculating the standard deviation (SD).

Results: The inhomogeneity is more visible under US and MRI, and not so much affected under CT. Core to periphery ratio(CTP) of traditional phantom and proposed phantom is 1.17 and 1.13.

Conclusion: The proposed method improved homogeneity and imaging results. The EC provided better control of FTC, enhancing uniformity. A lower CTP ratio confirmed reduced core-periphery deviation. Uniform mixing further contributes to phantom consistency and improved imaging quality.

References: [1] Cournane, S., et al. (2010). Assessment of ultrasound elastography liver scanning with a PVA-cryogel phantom. *Phys Med Biol*, 55(19), 5965–5983. [2] Cambranis, J., et al. (2024) Multimodal scattering agent for the development of training phantoms: Finding a substitution for Talc.



Figure 1. The beaker containing the PVA-C mixture after heating (top left). The “cooking” process took place in the fume hood (top right). The Vacuum Chamber with a pressure sensor on top of the lip, it is attached to a motor (bottom left). The Environmental Chamber with a piece of block placed in the center of the chamber (bottom right).

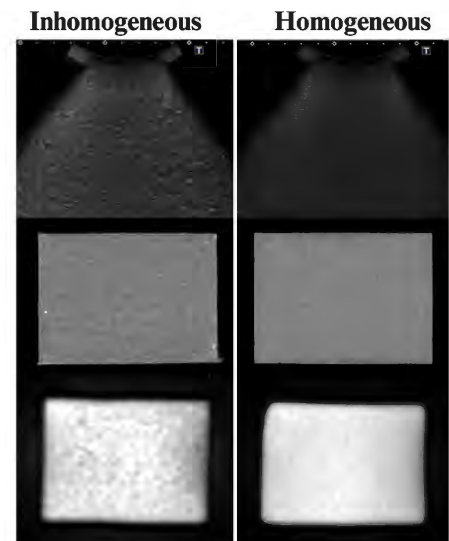


Figure 2: Top to bottom is US, CT, and MRI imaging results.

Spine ultrasound segmentation trained on registered CT as ground truth

Junhui Zong¹, Gabriella d'Albenzio¹, Tamas Ungi¹, Chris Yeung¹, Parvin Mousavi¹, Gabor Fichtinger¹

¹School of Computing, Queen's University, Kingston, Canada

INTRODUCTION: Spine imaging methods have various strengths and limitations. CT provides detailed images but involves high radiation, while X-ray offers 2D projections without volumetric data. Ultrasound is safe and cost-effective but traditionally limited by its narrow field of view. To address this, 3D tracked ultrasound reconstruction offers a safer volumetric imaging solution. Manual ultrasound annotation is resource-intensive, but registered CT scans, leveraging bone-specific Hounsfield Units, can serve as ground truth, reducing segmentation effort. This study compares ultrasound segmentation models trained on three ground truth types: manual annotations, CT-derived bone segmentations and posterior spinal contour segmentations visible in ultrasound.

METHODS: Data were collected from CT patients who volunteered for sagittal ultrasound scans, covering the spine from upper thoracic to lower lumbar levels at 10 frames per second over 2–3 minutes [1]. Scans were performed using a Clarius C3 HD3 system. Preprocessing involved exporting ultrasound frames using the Time Series Annotation module in 3D Slicer, converting curvilinear scan lines to linear representations, and extracting 2D slices. Ground truth segmentations were performed by trained students and reviewed by a physician experienced in ultrasound imaging. The training set included scans from 20 patients, and the validation set included 2 patients. Training was conducted on a PC with an RTX 4080 GPU, taking 3h 43min for manual segmentations and 7h 42min for the CT data. That is because not all frames were manually segmented, which results in less training data with manual segmentations. Three types of ground truth segmentations were used: (1) manual annotations, (2) bone segmentations from CT scans, and (3) posterior spinal contours filtered from CT scans. Attention U-Net models were trained using each type of ground truth segmentation and the volume reconstructions of the predicted spine segmentations were compared. To evaluate their performance, an Elo rating system was used to visually rank the three methods by one clinical observer [2]. Pixel-based metrics, such as IoU and accuracy, were excluded as three types of ground truths differed, making direct comparisons meaningless.

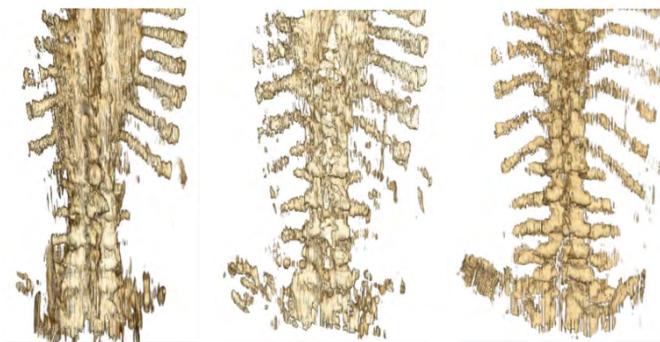


Figure 1. 3 ultrasound segmentation models trained on: CT-derived bone segmentations (left), filtered spinal contours (middle), manual annotations (right)

RESULTS: As expected, the model trained on manual annotations had the highest rating score from the clinical observer. This was followed by the model trained on posterior spinal contours, which provided a reasonable balance between anatomical detail and segmentation consistency. The model trained on bone segmentations yielded the lowest rating score.

CONCLUSIONS: This study demonstrates that the ultrasound segmentation model trained on manual annotations outperformed models trained on CT-derived segmentations, achieving the highest visual rating scores by the clinical observer. However, the

models trained on posterior spinal contours and bone segmentations derived from CT scans showed promise, indicating their potential as viable alternatives. Given the substantial reduction in manual effort that CT-derived ground truths offer, further refinement of these models could yield comparable segmentation accuracy while improving scalability and efficiency in clinical practice. Leveraging CT-derived segmentations thus remains a valuable avenue for future investigation to balance performance and resource utilization in spine imaging.

REFERENCES: [1] Ungi T, Greer H, Sunderland KR, et al. Automatic Spine Ultrasound Segmentation for Scoliosis Visualization and Measurement. *IEEE Trans Biomed Eng.* 2020;67(11):3234-3241.

doi:10.1109/TBME.2020.2980540 [2] Hashtrudi-Zaad, K., Ungi, T., Yeung, C., et al. (2024). Expert-guided optimization of ultrasound segmentation models for 3D spine imaging. *Proceedings of CCECE 2024*, 680–685. <https://doi.org/10.1109/CCECE59415.2024.10667291>

Ultrasound Based Evaluation of Stress Urinary Incontinence Pessaries on Bladder Neck, Bladder Descent, and Retrovesical Angle

Helena Kunic^a, Shufei Zhang^b, Goli Ameri^b, Eranga Ukwatta^a,

^aUniversity of Guelph, School of Engineering; ^bCosm Medical

^a50 Stone Rd E, Guelph, ON, Canada N1G 2W1. ^b101 College St, Toronto, ON, Canada M5G 1L7.

Introduction: Stress urinary incontinence (SUI), characterized by involuntary urine loss due to increased intra-abdominal pressure, negatively impacts both mental and physical health and affects approximately 30% of women. Treatment options include lifestyle changes, pelvic floor exercises, mechanical devices (e.g., pessaries), and surgery. While pessaries – devices inserted into the vagina to support vaginal tissue – provide a less invasive alternative, incontinence rings – a pessary type used for SUI – are not effective for all women. The probability of continued use of incontinence rings decreases to as low as 20% within 1 year. Since urethral hypermobility is linked to SUI, the objective of this study was to develop a novel technique for assessing pessary performance and mechanism of action in SUI patients using pelvic ultrasound measurements. Large differences in bladder neck position and retrovesical angle (RVA) between rest and the Valsalva maneuver indicate urethral hypermobility, which, along with significant bladder descent, is associated with SUI. A secondary objective was to assess if modifications made to pessaries for SUI affected urethral hypermobility.

Methods: Eight women with SUI participated in this study. Three-dimensional (3D) transperineal ultrasound volumes were acquired with no pessary, in the rest and Valsalva positions (Voluson E6 system, RAB6-D, GE Healthcare, IL, USA). The participants were fitted with a standard incontinence ring pessary and three new

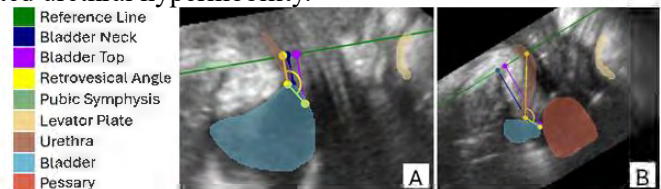


Fig. 1: 3D slicer midsagittal view of a patient on Valsalva with A) no pessary; B) a pessary

pessaries with modified knob configurations to assess their fit and comfort. The incontinence ring pessary and top two modified pessaries were taken home for one-week trials. After the at-home trials, patients returned for follow-up visits where 3D ultrasound images were obtained in the rest and Valsalva positions with the pessaries in place. In the midsagittal plane of the images, a reference line was drawn at the inferior border of the pubic symphysis¹. Bladder neck descent (labelled bladder top, the distance between the reference line and urethral sphincter), and bladder descent (the distance between the reference line and leading edge of the bladder) were measured¹. The RVA formed by the midline of the urethra and the tangent along the edge of the bladder base was also measured (Fig 1)¹.

Results: Fig. 1A and 1B show the midsagittal view of the pelvic anatomy in the Valsalva position with and without pessary, respectively. As shown by the grey columns in Table 1, 7 of 8 patients chose at least one pessary for long-term use, which was considered a successful outcome. The ultrasound

Table 1. Ultrasound Image Measurements. Grey columns indicate a patient wanted to continue wearing the pessary long-term, a successful outcome. Parentheses are (position, units) with R-V being rest minus Valsalva. Abbreviations are as follows: BN (bladder neck); RVA (retrovesical angle); BD (bladder descent); R (rest); V (Valsalva); NP (no pessary); B (incontinence ring); P1 (new pessary 1); P2 (new pessary 2); P3 (new pessary 3).

Patient ID	Patient 1				Patient 2				Patient 3				Patient 4			
Pessary Type	NP	B	P1	P2	NP	B	P3	P2	NP	B	P2	P1	NP	B	P3	P2
BN (R-V, mm)	-15.4	(3.8)	-5.2	(-2.7)	-4.0	(-4.2)	-1.7	(1.3)	-0.9	(-5.6)	-4.4	(4.5)	4.8	(1.8)	-13.0	(2.8)
RVA (R-V, deg)	-86.9	(24.5)	-56.3	(13.9)	-17.6	(4.2)	-21.2	(4.9)	-19.0	(3.7)	-10.6	(8.1)	-20.5	(4.2)	-6.2	(7.3)
BD (V, mm)	3.7	(-2.0)	-3.4	(-5.3)	-1.3	(-13.3)	-13.4	(-18.2)	-14.8	(-15.1)	-14.7	(-14.6)	-19.7	(-14.4)	9.4	(-15.0)
Patient ID	Patient 5				Patient 6				Patient 7				Patient 8			
Pessary Type	NP	B	P2	P1	NP	P1	B	P3	NP	B	P1	P2	NP	B	P1	P2
BN (R-V, mm)	-7.3	(-9.5)	0.0	(5.1)	-6.6	(-6.5)	1.5	(-1.0)	-10.5	(0.7)	5.7	(3.3)	3.3	(5.3)	6.3	(2.4)
RVA (R-V, deg)	-10.5	(18.8)	-13.6	(2.8)	0.7	(-1.7)	1.5	(7.9)	-7.8	(11.8)	9.9	(42.3)	27.8	(2.6)	-1.2	(-1.2)
BD (V, mm)	-13.5	(-9.3)	-23.1	(-25.6)	-12.1	(-18.2)	-18.2	(-17.1)	9.5	(-17.9)	-17.2	(-10.6)	20.9	(-11.5)	-14.2	(-14.2)

data from 1 patient was incomplete and not used for analysis. 8 patients had a reduction in magnitude in the difference between rest and Valsalva for the bladder neck, 6 patients had a reduction in magnitude in the difference between rest and Valsalva for the RVA, and 7 patients had reduced bladder descent in Valsalva, when wearing at least one of the pessaries. These reductions demonstrated decreased urethral hypermobility, but they did not correlate well with desired long-term pessary use; thus, no definitive conclusions were reached.

Conclusions: This study explored a novel methodology to evaluate the effect of SUI pessaries on urethral hypermobility through pelvic ultrasound measurements. While pessaries reduced urethral and bladder mobility in some cases, patients did not consistently choose to continue using them long-term, as they did not experience sufficient symptom improvement, or they experienced discomfort. Further research is needed to optimize pessary designs and better understand the relationship between urethral hypermobility and SUI symptoms.

References: [1] Dietz H.P. Am J Obstet Gynecol. 2010; 202(4):321–334

Polarization speckle analysis of volumetric scattering from controlled turbid phantoms and mouse skin tissues

Carla Kulcsar¹, Daniel Louie², Alex Vitkin^{1,2,3}

¹ Department of Medical Biophysics, University of Toronto, Canada

² Princess Margaret Cancer Research Tower, University Health Network (UHN), Canada

³ Princess Margaret Cancer Centre, Department of Radiation Oncology, UHN, Canada

Introduction: In this study, we explore the potential of laser polarization speckles to probe the optical properties of volumetric optical phantoms and establish a pathway for interrogating tissue pathologies through speckle analysis. Laser speckles are interference patterns arising from phase differences introduced into the initially coherent wavefront of a laser as it propagates through a scattering medium. These speckles manifest not only in the intensity but also the polarization state of scattered light, known as polarization speckle, and are intrinsically linked to the optical properties of the sample. To extend established intensity speckle theory, primarily focused on rough surface effects, to the generation of polarization speckle arising from volumetric scattering processes, we analyze the relationships between the scattering properties of controlled volumetric microsphere phantoms and polarization speckle metrics and interpret experimental findings with Monte Carlo simulations. Our methodology's biological relevance and feasibility are demonstrated in a proof-of-principle comparison of healthy skin and a melanoma tumor in a syngeneic mouse model.

Methods: Our cost-efficient setup consists of a HeNe laser illuminating the sample and a set of polarization cameras capturing each pixel's intensity and polarization state of backscattered light. The optical phantoms consist of polystyrene microspheres of varying sizes, suspended in water at different concentrations to achieve a range of strongly multiple scattering coefficients. A validated polarization-sensitive Monte Carlo simulation software, previously developed by our group, is used to measure photon propagation statistics through the medium.

Results: From the bulk turbid microsphere phantoms, we observe that a combination of the independent stochastic metrics speckle size and speckle contrast hold promise for predicting medium scattering properties. At constant turbidity, larger scatterers produce smaller speckles at higher speckle contrast, while an increased turbidity for a given scatterer yields larger speckles at lower speckle contrast (see Figure). Monte Carlo simulations of the path length and fluence patterns of backscattered light corroborate these experimental findings. The comparison with theoretical calculations indicates that the generation of polarization speckle patterns from volume scattering is not fully covered by established surface speckle theory, highlighting areas for further exploration. Proof-of-principle acquisitions from a syngeneic mouse model demonstrate a significant difference in speckle patterns obtained from healthy (speckle size: $93 \pm 3 \mu\text{m}$, contrast: 0.72 ± 0.02) and cancerous tissue (speckle size: $117 \pm 3 \mu\text{m}$, contrast: 0.75 ± 0.01). Expected speckle trends from pathology-related optical changes of the tissue are consistent with the relationships we established in the phantom study.

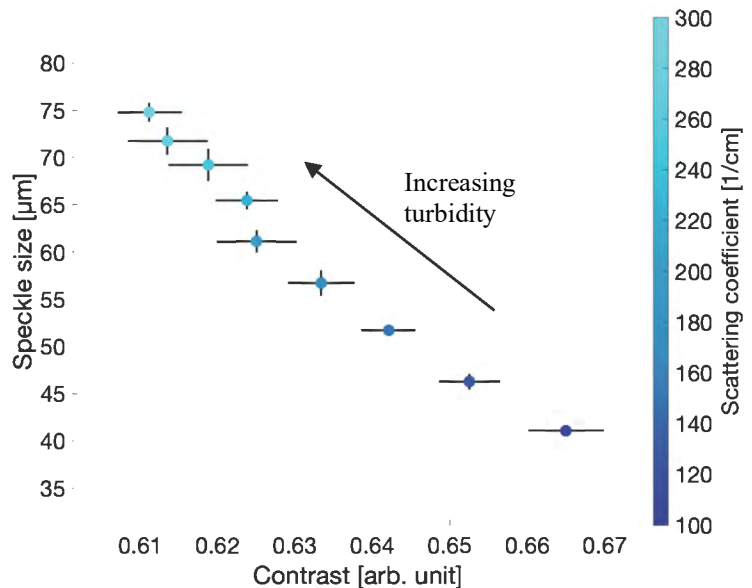


Figure: Combined plot of experimentally acquired speckle size and contrast for $0.58\mu\text{m}$ sized sphere suspensions at scattering coefficients of $\mu_s = 100\text{-}300\text{cm}^{-1}$

Conclusion: This study demonstrates the potential of speckle pattern analysis to interrogate the optical scattering properties of bulk samples. With the quantitative insights we gained by exploring changes in polarization speckle metrics in controlled optical phantoms and demonstrating initial results from tissue, we hope to provide a potential research avenue for future investigation of tissue pathologies using speckle analysis by the biomedical community.

Impact of Ambient Light on Spatial Frequency Domain Imaging for Surgical Guidance

Jack Wunder,¹ Rooaa Shanshal,¹ Matthew Siracusa,¹ Sujit Patil,¹
Alessandra Ruaro,² Jonathan C. Irish,^{1,2} and Michael J. Daly¹

¹Princess Margaret Cancer Centre, University Health Network, Toronto ON
²Department of Otolaryngology – Head & Neck Surgery, University of Toronto

Introduction: Spatial Frequency Domain Imaging (SFDI) is an innovative optical method under development for intra-operative guided resection and assessment of tumour margins. SFDI systems are comprised of a light source that projects structured illumination patterns on the surgical surface, along with a near-infrared camera to capture back reflected light. One challenge for intraoperative optical imaging systems can be the contaminating effects of ambient light in the operating room. Here, we investigate how SFDI, which inherently performs background subtraction, is affected by sources of ambient light.

Methods: SFDI is an amplitude-modulated imaging technique that involves collection of images at different spatial frequencies (f_x), each at 3 spatial phases, to compute the diffuse reflectance (R_d) of tissue. Using an in-house prototype system (Fig. a), we investigated the effect of two ambient light variables on SFDI reflectance data. In experiment 1, images of an optical calibration phantom (INO BioMimic) were captured at one camera exposure (24 ms), where environmental ambient light varied. Average reflectance values over a 50x50 pixel crop region were computed and observed as a function of total light intensity. In experiment 2, we investigated how room light sinusoidal fluctuations in intensity, known as “flickering,” may affect reflectance measurements taken at different camera exposure times. Reflectance images were captured at six spatial frequencies (0 to 0.25 mm^{-1} , in increments of 0.05 mm^{-1}), and camera exposure was varied over the range 16 to 36 ms in increments of 4 ms. Data was analyzed for variance in measurements using standardized (relative) standard deviation (RSDev).

Results: In experiment 1, the average reflectance decreased from 0.626 to 0.619 (Fig b), equating to only a 1.04% reduction, despite a 5114% increase in average pixel light intensity from 34.3 to 1789.6. In experiment 2, the average RSDev% across all spatial frequencies for exposure times from 16 ms to 36 ms (multiples of 4) were 0.91, 1.30, 1.01, 1.51, 0.61, 1.28, respectively (Fig c). The minimum RSDev% at 32 ms agreed with independent measurements of the room light flickering frequency. Across all exposure times, the spatial frequency with the lowest average RSDev was 0.25 mm^{-1} , equal to 1.02%, and highest was 0 mm^{-1} at 1.19%.

Conclusions: SFDI proved robust in computing reflectance values under various ambient light conditions. Flickering tests did prove slightly improved precision when captured at an exposure rate equal to ambient light flickering rates. Future testing will look at areas of specimens with steeper topography, where signal strength is reduced more than on flat surfaces. Testing will also be done in clinical settings, with clinicians that can elucidate how lighting environments can be set up and manipulated during operations.

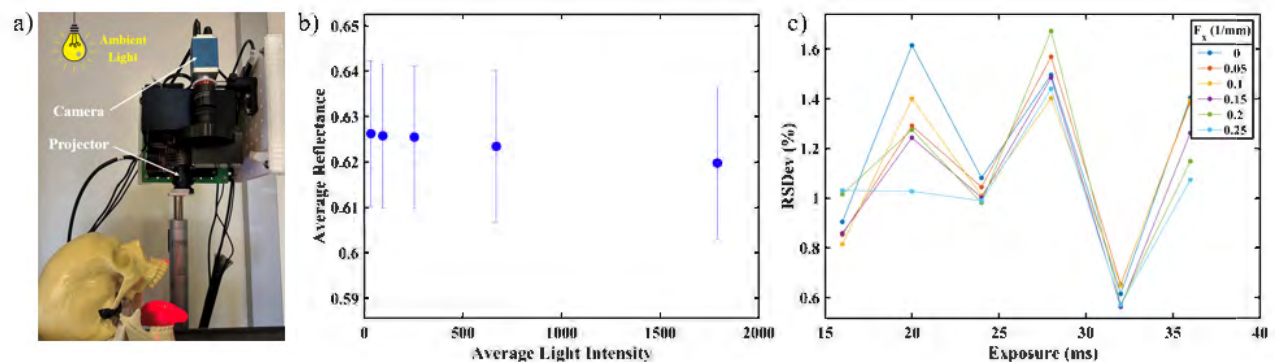


Figure: (a) SFDI portable system design. (b) Reflectance values, R_d , when increasing total ambient light. (c) Relative variance of reflectance values over different exposure times, at different spatial frequencies.

Tri-Modal Mosquito Bite Needle Endoscopy (MBNE) for Breast Cancer Diagnostics

Kate Dingle¹, Alex D'Ippolito¹, Dr. Vivianne Freitas², Dr. Alexandra Easson³, Dr. Alexandre Douplik^{4,5}

¹ Department of Biomedical Engineering, Toronto Metropolitan University

²Breast Imaging Division of the Toronto Joint Department of Medical Imaging, University Health Network, Sinai Health System, and Women's College Hospital

³ Division of General Surgery and Surgical Oncology, Mount Sinai Hospital & Princess Margaret Cancer Centre

⁴Department of Physics, Toronto Metropolitan University

⁵Institute for Biomedical Engineering, Science and Technology (iBEST), Keenan Research Centre of the Li Ka Shing (LKS) Knowledge Institute, St. Michael Hospital

Introduction: As of 2024, breast cancer was the most prevalent cancer among women worldwide, accounting for 25% of all cancer cases [1]. Recent clinical breast cancer detection methods include physical examinations and mammography. A biopsy is performed for diagnosis if a potential tumour is detected [2]. The US-guided needle biopsy method uses a 14-18G biopsy needle, the current gold standard. The procedure can cause patients discomfort, blood loss, and bruising due to the large needle size [3]. Inaccurate results and false negatives can arise from technical issues or poor sampling, often necessitating a follow-up biopsy. However, many patients avoid it due to fear of past painful experiences.

To lessen patient discomfort and improve breast cancer biopsy efficacy, a small, acupuncture-sized needle is proposed to be used for pre-biopsy screening by our group. The 200-micron needle with real-time imaging/detection capabilities can improve breast cancer detection accuracy and minimize unnecessary biopsies. The proposed project is a 34-gauge needle endoscope with built-in fiber optics, utilizing two-modal imaging and Raman spectroscopy to differentiate between cancerous and non-cancerous breast tissue.

Methods: WAR tri-modal imaging consists of white light RGB image (W), autofluorescence contrast imaging (A), and Raman spectra collection (R). Combined, these modalities present the ability to identify the optical properties associated with cancer development [4].

Results: A confocal microscope that utilizes the WAR tri-modal imaging techniques was designed with three major pathways: (1&2) white light reflectance and autofluorescence imaging via Thorlabs CS895MU CCD camera; (3) Raman collection via the Tornado HyperFlux Pro Raman Spectrometer, using the Thorlabs CLD1010LP laser driver with the LP785-SAV50 785 nm laser diode. The camera captures images and spectra in an ex-vivo setting. The 34G hollow needle, with an outer diameter comparable to an acupuncture needle (200 μm) and a lumen diameter of 90 μm , was combined with a novel 85-micron multi-core optic fibre threaded through the needle and used to collect the WAR data of the breast tissue at a resolution of ~ 1000 pixels.

Conclusions: A 34-gauge (G) acupuncture-sized needle endoscope offers a promising way to enhance comfort, reduce unnecessary 14-18G biopsies, and improve accuracy. The integration of tri-modal endomicroscopy enables accurate tissue classification and breast cancer detection through the WAR dataset, providing a less-invasive, efficient diagnostic tool to build a proper breast tissue database.

References:

- [1] "Breast Cancer." Accessed: Oct 11, 2023. [Online]. Available: www.who.int/news-room/fact-sheets/detail/breast-cancer
- [2] B. Salzman, S. Fleegle, and A. S. Tully, "Common Breast Problems," *Am. Fam. Physician*, vol. 86, no. 4, pp. 343–349, Aug. 2012.
- [3] J. H. Youk, E.-K. Kim, M. Kim, J. Lee, and K. Oh, "Missed Breast Cancers at US-guided Core Needle Biopsy: How to Reduce Them," *Radiogr. Rev. Publ. Radiol. Soc. N. Am. Inc*, vol. 27, pp. 79–94, Jan. 2007, doi: 10.1148/rg.271065029.
- [4] A. Douplik, W.-L. Leong, A. M. Easson, S. Done, G. Netchev, and B. C. Wilson, "Feasibility study of autofluorescence mammary ductoscopy" *Journal of Biomedical Optics*, vol. 14, no. 04, p. 1, Jul. 2009, doi: [10.1117/1.3210773](https://doi.org/10.1117/1.3210773)

Pitches 8: General

Abstracts

A Language-Audio Foundation Model for Characterization of Cancerous Tissue in Mass Spectrometry Images

Alon Gabriel¹, Amoon Jamzad¹, Mohammad Farahmand¹, Martin Kauffman¹, Natasha Iaboni¹, David Hurlbut¹, Kevin Yi Mi Ren¹, Christopher JB Nicol¹, John F Rudan¹, Sonal Varma¹, Gabor Fichtinger¹, Parvin Mousavi¹

¹Queen’s University, Kingston, ON, Canada

INTRODUCTION: Histopathology remains the gold standard for clinical cancer diagnosis, but emerging modalities like mass spectrometry imaging (MSI), particularly desorption electrospray ionization (DESI)-MSI, offer a fast and complementary approach to traditional methods. DESI-MSI enables direct molecular analysis from histology slides without the need for sample preparation, providing high-resolution spatial and spectral data that can enhance diagnostic precision. Despite its potential, the complex, high-dimensional data produced by MSI demands advanced computational techniques for effective interpretation. While foundation models excel in other domains, none address MSI data; however, spectral and audio data share notable similarities. Thus, we propose leveraging the audio arm of a language-audio foundation model (CLAP [1]) to characterize cancerous vs. non-cancerous tissue in MSI data.

METHODS: We use DESI-MSI data obtained from colorectal cancer (CRC) tissue samples from 10 randomly-selected patients undergoing surgical resection at Kingston Health Sciences Centre (KHSC), Canada [2]. Tumour cross-sections were affixed to slides, analyzed with MSI, and annotated by pathologists.

Annotations were grouped into binary classes (cancerous or non-cancerous) for this study. The annotated slides were

aligned with their corresponding MSI data using MassVision [3] software in Slicer 3D, and regions of interest were selected based on localized areas within each tissue type (Figure 1). This resulted in a labeled dataset consisting of 16,678 spectra; all remaining tissue regions were used to create an unlabeled dataset of ~147,000 spectra. The mass spectra were preprocessed with normalization, reduction to 900 most abundant ions and split patient-wise into train, test, and validation sets. We used the audio decoder of CLAP as a feature extractor for tissue classification, establishing it as a baseline. To enhance feature extraction,

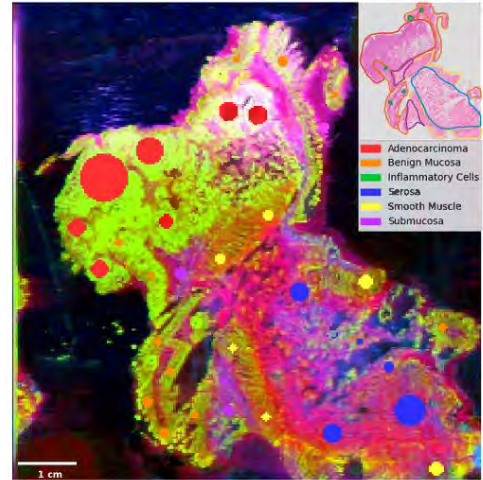


Figure 1: Visualization of histopathology mass spectral image with segmented regions of interest. Top right: corresponding histopathology slide.

	Sens.	Spec.	Bal. Acc.	AUROC
PCA-LDA	79.9	67.1	73.5	0.82
PLS-DA	96.3	39.5	67.9	0.94
SVM	88.4	73.7	81.0	0.92
CLAP	64.1	96.6	80.4	0.90
Our model	88.4	84.4	86.4	0.95

Table 1: Performance comparison of classification models.

we applied self-supervised pretraining to the audio decoder using SimCLR [4] on the unlabeled data. Traditional machine learning methods, PCA-LDA, PLS-DA, and SVM, were employed as benchmarks for comparison.

RESULTS: As seen in Table 1, our model outperformed all others, with the highest area under the receiver operating curve (AUROC) and statistically significant improvement in balanced accuracy (Bal. Acc.), whilst also having the best balance of sensitivity and specificity.

CONCLUSIONS: These results underscore the robustness of the model in accurately classifying cancerous tissue and demonstrates its potential for enhancing existing diagnostic workflows.

REFERENCES: [1] Y. Wu et al., ICASSP 2023. [2] M. Kaufmann et al., Metabolites 2023.

[3] <https://slicerdesi.readthedocs.io/en/latest/> [4] T. Chen et al., ICML 2020.

Histology hide-and-seek: visually navigating latent space clustering for pathology exploration

Phoenix Wilkie¹, Anne Martel^{1,2}, Kelvin Jok²

¹ University of Toronto, Medical Biophysics, Toronto, Canada,

² Sunnybrook Research Institute, Physical Sciences, Toronto, Canada

Background: Clustering is used to group similar images of tissue samples together. Unsupervised clustering allows for exploration of the latent space which is beneficial in digital pathology classification tasks. There exist new and improved methods for clustering pathology images. Yet, it remains difficult to assess which clustering method would be most effective for certain datasets when designing experimental research plans. Standard clustering evaluation typically quantifies the inter- and intra-cluster distances. However, in histology-based analysis, the variations in morphological features are subtle, necessitating labelled downstream tasks for cluster validation. Dunn's Index (DI) is useful for comparing clustering algorithms or parameter settings by assessing their ability to generate compact, well-separated clusters. In pathology images, DI often yields values of 0 due to sensitivity to noise and outliers. Significant overlap and poor cluster separation are common when assessing clustering in uncurated patch datasets. Furthermore, metrics such as the average Silhouette Coefficient (aSC) frequently approach 0, suggesting that many mixed tissue patches tend to reside near or on the decision boundary between neighboring clusters. Therefore, we propose a visual dimensionality reduction software pipeline. This will allow rapid, visual assessment of clusters.

Methods: A graphical user interface (GUI) application was developed to address histopathology clustering assessment challenges. This software pipeline facilitates rapid visual evaluation of clustering methods by enabling users to upload feature-extracted data and corresponding patches. Users can upload results from any clustering algorithm or utilize the built-in unsupervised clustering method provided by the program. The included unsupervised clustering method was pretrained on histology patches using the SIMCLR framework for contrastive self-supervised learning. This approach groups similar images while separating dissimilar ones. Hierarchical agglomerative k-means is then applied for further refinement. The software allows users to conduct the Elbow Test for optimal cluster number estimation and determine the minimum number of parent clusters in hierarchical clustering. It offers automated evaluation using established metrics and generates centroid patches as output. Internal validation metrics like aSC, DI, Davies-Bouldin Index (DBI), and Calinski-Harabasz Index (CHI) are available for users without ground truth labels. The GUI allows users to reduce dimensionality, orient plots, and access patches. Users can visualize patches in latent space using TSNE, PCA, Sammon, and UMAP in 2D or 3D. Interactive navigation enables users to right-click on data points to view associated images, facilitating manual inspection of clusters. This interactive visualization approach supports a comprehensive examination of clustered data.

Results: Two downstream tasks were conducted using public and private datasets. Firstly, patches containing cross-sectional views of complete tubules were identified with 98% (+/-1.7). This was done using the public BreCaHAD dataset [1]. Secondly, tissue classification, particularly adipose and blood patches, was performed on an unlabelled private dataset. Initial evaluation metrics included aSC = -0.02, DI = 0.0, DBI = 3.47, and CHI = 41.71. By retaining only the 60% of patches closest to centroids, metrics approached optimal values for aSC, DI, and DBI, indicating tighter clusters and increased separation between neighbors. Consequently, the remaining patches contained a single tissue type per patch.

Conclusion: Assessing latent space proximity involved examining patches from diverse tissue labels. Visual inspection revealed evident morphological similarities among patches within clusters. The GUI streamlines the selection of optimal clustering methods for experimental pipelines, enabling swift quantification using standard equations for assessing cluster quality. Moreover, qualitative assessment is facilitated through interactive exploration, i.e. clicking on points within graphical clusters displays corresponding histology patches. Additional evaluation metrics are currently being implemented and integrated into the GUI software.

References: [1] Aksaç, Alper et al. "BreCaHAD" BMC Research Notes 12 (2019).

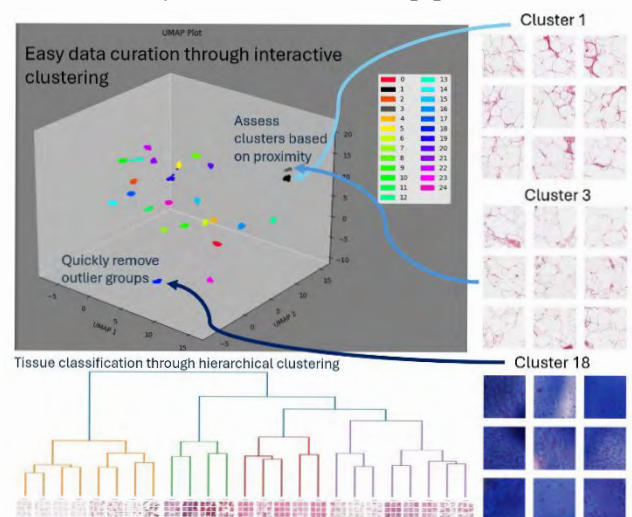


Figure 1: Collage of screenshots taken from the interactive GUI in a dataset curation task for tissue classification and quality control

A Comparison of Uncertainty Techniques on Basal Cell Carcinoma Mass Spectrometry Data

Tyler Elliott¹, F. Fooladgar², A. Jamzad¹, L. Connolly¹, M. Kaufmann¹, K. Ren¹, J. Rudan¹, D. McKay¹, G. Fichtinger¹, and P. Mousavi¹

¹Queen's University, Kingston, Canada, ²The University of British Columbia, Vancouver, Canada

INTRODUCTION: Basal cell carcinoma (BCC), a prevalent form of skin cancer, often occurs on the neck and face and is typically treated with surgical resection. Rapid evaporative ionization mass spectrometry (REIMS) can be used to determine the metabolic composition of tissue in real-time, deployed during surgery using the iKnife device [1]. Integrating machine learning models with REIMS data has the potential to improve diagnostic accuracy. However, in clinical applications, understanding the uncertainty associated with model predictions is vital to ensure reliability and interpretability. This study compares three uncertainty estimation techniques—ensemble methods, evidential deep learning, and Bayesian Neural Networks (BNNs)—to determine the most effective approach for analyzing BCC MS data.

METHODS: iKnife was used to collect 693 spectra of cancer and healthy samples acquired from 91 patients during basal cell carcinoma resection. Multiple deep neural network models were independently trained using different initial weights and data shuffling to implement ensemble methods. The ensemble's predictive mean and variance were calculated to estimate uncertainty, based on the diversity of predictions across models [2]. For the evidential model, a single deep neural network was modified to output parameters of a Dirichlet distribution, enabling the model to provide both prediction and uncertainty by modeling evidence supporting each class [3]. BNNs were implemented using variational inference, treating network weights as probability distributions. Monte Carlo sampling through dropout during inference allowed for the estimation of predictive uncertainty directly from the posterior distribution [4]. Performance metrics such as balanced accuracy, specificity, and sensitivity were used to assess the models. After training, the uncertainty calibration of each model was checked by removing predicted uncertain samples from the test set and re-checking balanced accuracy.

RESULTS: The ensemble model outperformed the other techniques, providing robust uncertainty estimates that closely correlated with misclassified samples. Evaluated on the full test set it achieved balanced accuracy of 72%, while removing the top 20%, 40%, and 60% of uncertain samples resulted in 77%, 81.5%, and 85.7% respectively. Ensemble and evidential methods exhibited similar uncertainty picking amongst samples, indicating consistency in detecting uncertain predictions as shown in Figure 1. The two techniques output the uncertain samples in ranked orders that shared a Spearman correlation coefficient of 0.53. The BNN achieved effective performance in terms of balanced accuracy starting at 74% on the full test set and rising to 83.8% after reducing the test set by 70% from the model's predicted most uncertain samples.

CONCLUSION: All three uncertainty techniques achieved effectively calibrated measures of uncertainty. However, the BNN model differed in identifying uncertain instances, assigning higher uncertainty to different samples compared to evidential and ensemble methods. This discrepancy suggests variability in how BNNs estimate uncertainty. The superior performance of the ensemble method is attributed to the aggregation of diverse models, capturing a broader representation of the data space and leading to more reliable uncertainty quantification in the context of BCC REIMS data analysis.

REFERENCES:

- [1] Connolly, L., et al.: ImSpect: Image-driven self-supervised learning for surgical margin evaluation with mass spectrometry. *Int J CARS* 19, 1129–1136 (2024)
- [2] Lakshminarayanan, B., et al.: Simple and scalable predictive uncertainty estimation using deep ensembles. In: *Advances in Neural Information Processing Systems*, vol. 30 (2017)
- [3] Sensoy, M., et al.: Evidential deep learning to quantify classification uncertainty. In: *Advances in Neural Information Processing Systems*, vol. 31 (2018)
- [4] Gal, Y., et al.: Dropout as a Bayesian approximation: representing model uncertainty in deep learning. *Proceedings of The 33rd International Conference on Machine Learning, PMLR 48:1050–1059* (2016)

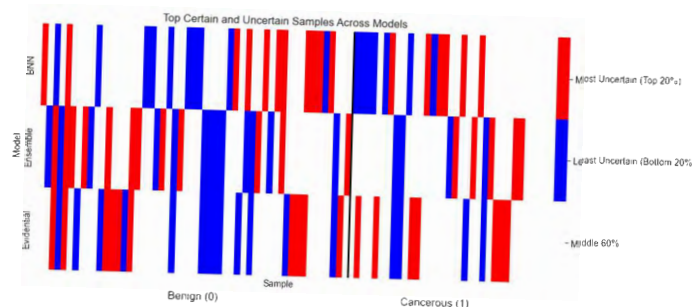


Figure 1: A comparison of uncertainty ranking by sample across techniques.

3D ABUS system with breast needle biopsy capability and integrated MRI-guidance lesion localization

Amal Aziz,^{a,c} C. K. Park,^b J. Bax,^c D. Tessier,^c L. Gardi,^c M. G. Kacen,^d P. Crivellaro,^d A. Fenster^{c,e}

^aSchool of Biomedical Engineering, Faculty of Engineering, Western University, London, Ontario, Canada,

^bDivision of Medical Physics and Biophysics, Department of Radiation Oncology, Brigham and Women's Hospital and Dana-Farber Cancer Institute, Harvard Medical School, Boston, Massachusetts, United States,

^cResearch Laboratories, Robarts Research Institute, London, Ontario, Canada, ^dDepartment of Medical Imaging,

Schulich School of Medicine and Dentistry, Western University, London, Ontario, Canada ^eDepartment of Medical Biophysics, Schulich School of Medicine and Dentistry, Western University, London, Ontario, Canada

Introduction: Breast cancer is the most common cancer among women worldwide, with two million diagnoses and 685,000 annual deaths. [1] Breast biopsy is the primary method to definitively confirm a breast cancer diagnosis, guided typically by ultrasound. [2] However, ultrasound-guided needle biopsies exhibit false-negative cases due to operator dependence. [3] Moreover, for women with dense breast tissue, where lesions are not visualized under ultrasound, MRI-guided breast needle biopsies are recommended instead. However, the MRI-based biopsy procedure is time-consuming, as it takes around 30 min, and inaccessible in some centers. [4] To address these challenges, we developed a 3D automated breast ultrasound (3D ABUS) system, compatible with any commercial ultrasound probe, to facilitate MRI-localized but 3DUS-guided breast needle biopsy procedures using an integrated needle biopsy mechanism.

Methods: We modified our previously developed 3D ABUS device to enable breast needle biopsy procedures, incorporating a custom 3D-printed wearable base conforming to the chest wall around the breast that can be customized to accommodate diverse anatomies, MR-compatible compression paddles with a biopsy needle template, and a motorized linear scanner for probe translation (Fig. 1). Although the system is compatible with any commercial US system, testing was performed using a Canon Aplio i700 and a 14L5 linear transducer. A custom workstation was developed to support real-

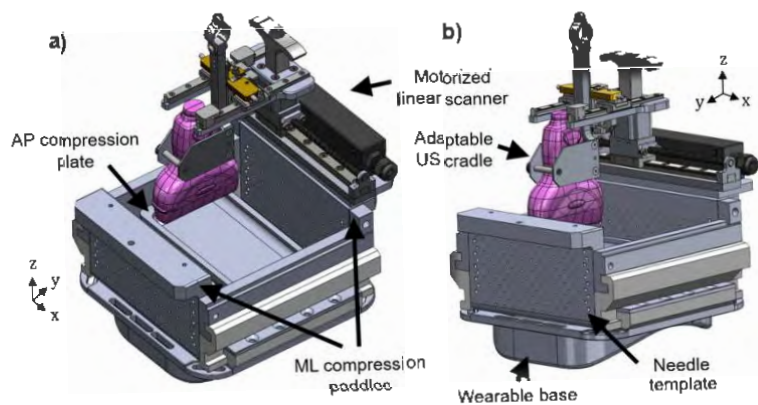


Figure 1. Computer-aided design illustration of the integrated 3D ABUS biopsy system with the wearable base, compression subassembly, and motorized-drive mechanism for the scanner.

time image acquisition and 3D reconstruction. [5] System registration was tested using a breast-mimicking phantom created with agar inclusions embedded in a gelatin-based background. Phantom imaging combined axial T2-weighted MRI and 3D ABUS images, with proof-of-concept co-registration analysis performed in 3D Slicer. Mean target registration error (TRE) and fiducial localization error (FLE) metrics were calculated using embedded inclusions.

Results: Inclusions were clearly visible and co-located in both 3D ABUS and MRI images at axial, coronal, and sagittal views. Additionally, the 3D ABUS images were able to be dynamically viewed at various oblique view planes. These results confirm that the phantom was able to be imaged in the same physical condition and level of compression for both acquisitions, which is necessary for enabling an integrated MRI-ABUS-guided needle biopsy protocol. The TRE and FLE were both found to be submillimeter, with values of 0.45 mm and 0.31 mm, respectively.

Conclusion: These results confirm the system's effectiveness in co-localizing lesions in MRI and 3D ABUS modalities. This advancement in integrating 3D ABUS with breast needle biopsy offers a more cost-effective and accessible solution, potentially improving breast biopsy procedure workflow and patient experience, particularly in women with dense breasts. Future work will involve developing automatic fiducial localization and experimenting with different breast phantom shapes.

[1] M. Arnold *et al.*, *Breast Off. J. Eur. Soc. Mastology*, vol. 66, pp. 15–23, Sep. 2022. [2] M. I. Nounou *et al.*, *Breast Cancer Basic Clin. Res.*, vol. 9, no. Suppl 2, pp. 17–34, Sep. 2015. [3] G. Schueller *et al.*, *Eur. Radiol.*, vol. 18, no. 9, pp. 1761–1773, Sep. 2008. [4] U. Bick *et al.*, *Insights Imaging*, vol. 11, no. 1, p. 12, Feb. 2020. [5] A. Fenster *et al.*, "System & method for oblique plane visualization in 3D ultrasound imaging," Patent 63/447,512.

Large Language Models are One-Shot Radiology Report Summarizers

Mahmoud Idlbi¹, Mohammad Hamghalam¹, Jianwei Yue¹, Richard Do², Amber Simpson¹

¹Queen’s University, Kingston, Ontario, Canada

²Memorial Sloan Kettering Cancer Center, New York, USA

Introduction: Radiology report summarization is a critical and high-stakes task due to its implications for patient safety and clinical workflows. Large language models (LLMs), while trained on diverse datasets, lack inherent design for radiology-specific tasks. Previous research [1, 2, 3, 4] has focused on summarizing the *Findings* section of individual radiology reports into concise *Impressions*. This study uniquely tackles summarizing the *Impressions* sections across a patient’s history of radiology reports, enabling radiologists to track disease progression over time. By highlighting key dates and information, this approach reduces cognitive load and enhances decision-making during follow-up visits and referrals.

Methods: We evaluated the performance of the instruction-tuned LLM, *Llama-3.2-3B-Instruct*, on summarizing the *Impressions* sections across a series of radiology reports. This model was selected based on its optimization for summarization tasks. Using a consistent prompt—concise, clear, and task-specific—we compared summaries generated without examples to those generated after the model was exposed to a one-shot example written by a radiologist. The prompt included the following key instruction: “*Below is a list of Impressions from a patient’s history of radiology reports. Provide a summary of them. Be very concise and highlight only significant information. Focus on key details such as organs with metastases, changes in metastases, and any new findings per new report.*” A consistent prompt ensured that differences in observed results were attributable to the one-shot example. Generated summaries were assessed against radiologist-provided references using ROUGE, BLEU, and BERTScore [5, 6], measuring overlap and semantic alignment.

Results: The one-shot example significantly improved alignment with radiologist summaries across 16 sampled test cases. ROUGE-1 increased from 0.43 to 0.63, and ROUGE-2 improved from 0.21 to 0.47. Similarly, ROUGE-L increased from 0.30 to 0.57. BLEU scores improved from 0.10 to 0.22, and METEOR scores increased markedly from 11.83 to 29.79. BERTScore F1, indicating semantic similarity, improved from 0.85 to 0.89. These results demonstrate the adaptability of LLMs to radiology-specific tasks when provided with relevant examples.

Conclusions: Incorporating a one-shot example significantly improves LLM performance on the task of radiology report summarization. This novel approach addresses the need for efficient, longitudinal tracking of disease progression, potentially saving radiologists time and reducing diagnostic errors. Limitations include model dependence on prompt quality and potential biases inherent in pretrained models. Future work will explore multi-shot learning, reinforcement-learning from human feedback (RLHF), direct preference optimization (DPO), and fine-tuned models to enhance reliability and expand clinical utility.

References

- [1] Cai et al. Chestxraybert: A pretrained language model for chest radiology report summarization. *IEEE Transactions on Multimedia*, 25:845–855, 2023.
- [2] Ma et al. An iterative optimizing framework for radiology report summarization with chatgpt. *IEEE Transactions on Artificial Intelligence*, 5(8):4163–4175, 2024.
- [3] Nishio et al. Fully automatic summarization of radiology reports using natural language processing with large language models. *Informatics in Medicine Unlocked*, 46:101465, 2024.
- [4] Van Veen et al. Radadapt: Radiology report summarization via lightweight domain adaptation of large language models. In *Proc. of the 22nd Workshop on Biomedical NLP and BioNLP Shared Tasks*, pages 449–460, 2023.
- [5] Zhang et al. Bertscore: Evaluating text generation with bert. *CoRR*, abs/1904.09675, 2019.
- [6] Chin-Yew Lin. Rouge: A package for automatic evaluation of summaries. In *Text Summarization Branches Out: Proceedings of the ACL-04 Workshop*, pages 74–81, Barcelona, Spain, 2004. Association for Computational Linguistics.

Accelerated 4D Flow with Respiratory Compensation and Cardiac View Sharing in Pediatric Congenital Heart Disease

Fatemeh Rastegar Jooybari^{1,2}, Christopher Huynh², Sharon Portnoy², Jonathan Voutsas³, Diana Balmer-Minnes², Ankavipar Saprungruang⁴, Shi-Joon Yoo⁵, Christopher Z Lam⁴, and Christopher K Macgowan^{1,2}

1 Department of Medical Biophysics, University of Toronto, Toronto, ON, Canada, 2 Translational Medicine, Hospital for Sick Children, Toronto, ON, Canada, 3 Queen's University, Kingston, ON, Canada, 4 Department of Diagnostic Imaging, Hospital for Sick Children, Toronto, ON, Canada, 5 Departments of Medical Imaging and Paediatrics, University of Toronto, Toronto, ON, Canada

INTRODUCTION: Conventional 4D flow MRI is limited in pediatric congenital heart disease (CHD) patients due to long scan times, leading to motion artifacts and reduced patient comfort.¹⁻³ This study validated an accelerated 4D flow MRI protocol that combines compressed sensing, respiratory soft-gating (SG), and cardiac view-sharing to improve imaging speed and quality, while maintaining accurate flow quantification.⁴

METHODS: Fourteen pediatric CHD patients (median age: 12 years [IQR: 3]) and four healthy adults (median age: 27 years [IQR: 5]) underwent a 5-minute free-breathing scan with a 3D radial trajectory. The reconstruction pipeline incorporated SG to reduce respiratory motion artifacts and cardiac view sharing for improved SNR.⁵⁻⁶ Flow measurements in major thoracic vessels were obtained using 4D flow MRI and validated against 2D phase-contrast MRI (2D PCMR), the reference standard. Internal flow consistency was assessed by comparing bifurcating vessel flow measurements.

RESULTS: Respiratory SG improved diaphragm sharpness and reduced motion blur (e.g., image quality scores: Healthy: 46.1 SG vs. 47.2 non-gated; CHD: 47.8 SG vs. 48.2 non-gated). Cardiac view sharing reduced undersampling artifacts and increased SNR (Healthy: +9.9%; CHD: +3.8%), consistent with qualitative improvements in reconstructed images. Flow quantification demonstrated strong correlations with 2D PCMR in healthy adults for mean flow ($R^2=0.94$, RMSE=6.4 ml/s) and peak flow ($R^2=0.90$, RMSE=40.9 ml/s). Similar agreement was observed in CHD patients for mean flow ($R^2=0.88$, RMSE=8.3 ml/s) and peak flow ($R^2=0.97$, RMSE=25.9 ml/s) (Figure 1). Internal consistency for 4D flow MRI in CHD cases showed mean percent differences of 6.1% for pulmonary arteries and 6.5% for the aorta.

CONCLUSION:

The accelerated 4D flow MRI method provides robust flow quantification and visualization in pediatric CHD patients, strongly correlating with 2D phase contrast MRI and completing scans in 5 minutes for clinical use.

REFERENCES:

- [1] Geiger J et al. "4D-MR flow analysis in patients after repair for tetralogy of Fallot." *Eur Radiol*, 2011.
- [2] Whitehead KK et al. "Systemic to pulmonary arterial collateral flow after Fontan." *Am J Cardiol*, 2015.
- [3] Powell AJ, Geva T. "Blood flow measurement by MRI in congenital heart disease." *Pediatr Cardiol*, 2000.
- [4] Bissell MM et al. "4D Flow CMR consensus statement: 2023 update." *J Cardiovasc Magn Reson*, 2023.
- [5] Jiang W et al. "Motion-robust free-breathing pulmonary MRI using self-navigators." *Magn Reson Med*, 2018.
- [6] Yang H et al. "GRASP reconstruction with KWIC filtering in pediatric CHD." *Magn Reson Med*, 2024.

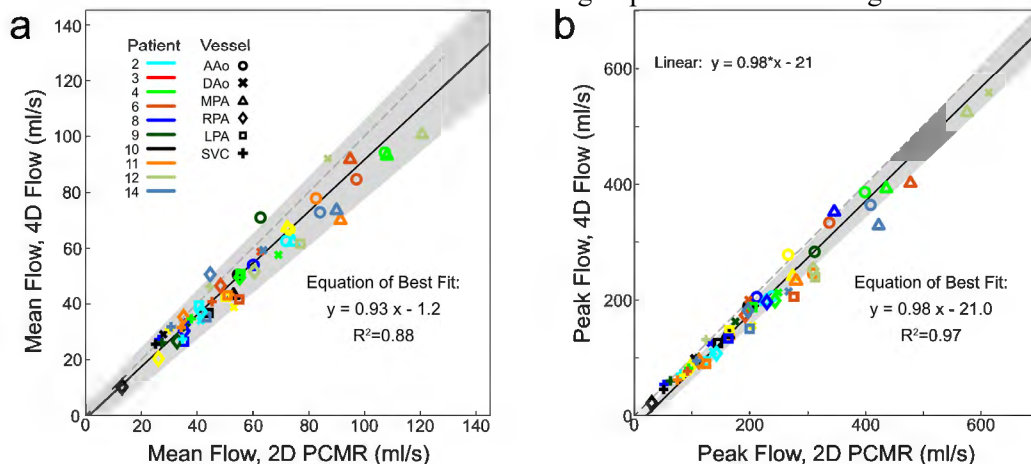


Fig. 1 Comparison of 4D flow vs. 2D PCMR (mean and peak flow rates) in pediatric congenital heart disease patients. Abbreviations: *AAo/DAo* ascending/descending aorta, *MPA/LPA/RPA* main/left/right pulmonary arteries, *SVC* superior vena cava.

Forecasting Movement Patterns in Stroke Patients Utilizing Time Series Foundation Models

Dharsan Ravindran¹, Faranak Akbarifar¹, Sean P. Dukelow², Stephen H. Scott¹, Parvin Mousavi¹

¹Queen’s University, Kingston, ON, Canada

²University of Calgary, Calgary, AB, Canada

INTRODUCTION: Stroke, a leading cause of disability, often results in permanent sensorimotor impairments requiring timely and accurate assessments for rehabilitation. Traditional assessments, such as the Chedoke-McMaster Stroke Assessment (CMSA) and Fugl-Meyer Assessment (FMA), rely on inaccurate subjective scoring [1][2]. Whereas interactive robot-based tasks like the Kinarm Standard Tests (KST) provide objective, quantitative evaluations [3]. KST comprehensively assesses post-stroke function, but its hour-long duration poses challenges for many patients. In the Visually Guided Reaching task, patients move their finger between targets while speed and position data are recorded [4]. This study investigated if foundation models can be used to predict future VGR trials based on 8 historic trials, potentially reducing patient load. **METHODS:** We chose 2 time series foundation models; Lag-Llama [5] and Chronos [6] to forecast position and speed signals. Foundation models in this study provide the ability to make accurate predictions based on large pre-trained knowledge sets, potentially overcoming the limited amount of data in this study. Initial testing was conducted with 150 control participants who had no history of stroke and 81 participants who had experienced a stroke prior to the study. All participants completed the VGR task across multiple trials. For this study we selected 8 trials as context and forecasted an additional 9th trial. All speed and positional signal readings were down sampled to 64 points, determined based on the optimal prediction length of the selected foundation models. Participants were divided into training and testing subsets using various randomized train-to-test ratios (80/20, 50/50, 30/70) to find optimal fine-tuning

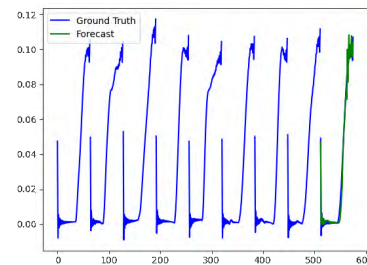


Fig 3. Position signal ground truth and prediction in best RMSE

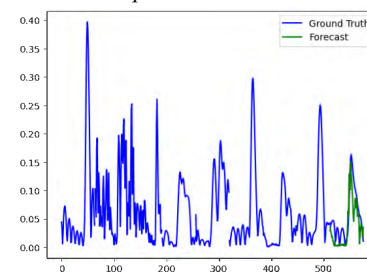


Fig 2. Velocity signal ground truth and prediction in best RMSE metric

Feature Type	Lag Llama Fine Tuned	Chronos Finetuned	ARIMA Forecasting
Speed	0.052 ± 0.025	0.0086 ± 0.002	0.0073 ± 0.003
Position	0.021 ± 0.009	0.0035 ± 0.001	0.0079 ± 0.001

Table 1. Average Forecasting RMSE for Chronos and Lag Llama in combined Stroke and Control Dataset

parameters. Each participant only had one data sample in the dataset, ensuring there is no data leakage when splitting. The forecasting and fine-tuning were completed in separate pipelines for the speed and position data stemming from the univariate nature of the models. Finally, a baseline prediction was established using the traditional ARIMA (autoregressive integrated moving average) forecasting method for comparative analysis. **RESULTS:** The best finetuning parameters for both models were located at the 80/20 train/test split. Root Mean Squared Error (RMSE) was used as the metric to analyze the accuracy between the ground truth and the prediction results of all models. The fine-tuned Chronos model showed substantially better performance with more consistent results over Lag Llama. Additionally, the prediction graphs (Fig 1. & Fig 2.) exhibited a closer fit to the ground trends underscoring the improved accuracy. However, the ARIMA approach outperformed both models in speed forecasting. **CONCLUSIONS:** This study shows promise in cutting patient assessment time while maintaining data quality. ARIMA's statistical capacity to predict stochastic processes may better capture the inherent variability in stroke patients' speed signals better. Although ARIMA and Chronos have comparable forecasting results, the utilization of foundation models has the advantage of incorporating additional contextual data, such as patient specific parameters to further refine forecasting. In future explorations multivariate foundation models will be used to investigate the potential of using speed and position signals together to improve the forecast accuracy. **REFERENCES:** [1] Gladstone et al., Neurorehabilitation and Neural Repair 2002. [2] Gowland et al., Stroke 1993. [3] Akbarifar et al., Research Square 2024. [4] Scott et al., Neurorehabilitation and Neural Repair 2023. [5] Ansari et al., Transactions on Machine Learning Research 2024. [6] Rasul et al., arXiv PrePrint.

Author Index

Name	Presentation(s)	Page(s)
Abolmaesumi, Purang	P1-2, P4-3, P4-5, P4-7, P5-6	41, 83, 85, 87, 117
Abraham, Leanna	O1-3, P1-7	32, 46
Addas, Shamel	P5-6	117
Akbarifar, Faranak	P8-7	169
Akens, Margarete K.	O1-3, P1-7, O11-3	32, 46, 143
Albweady, Ali	O9-1	131
Alexander, Sandra	O2-4	38
Alfieri, Joanne	P6-1	121
Alkins, Ryan	O1-1	30
Almasri, Eaman	O8-2	108
Alqaidy, Ghada	O9-1	131
Ameis, Stephanie H.	P2-7	59
Ameri, Golafsoun	P4-10, P7-8	90, 158
Assad, Lola	P6-2	122
Athwal, George	P7-4	154
Attarpour, Ahmadreza	O7-3	104
Au, Ryan	O1-4, P1-8	33, 47
Austin, Catherine	O4-4, P5-8, P6-4	69, 119, 124
Aydin, Serdar	P4-10	90
Aziz, Amal	O6-4, P8-4	100, 166
Babazadeh Khameneh, Nahid	P4-4	84
Bahig, Houda	P1-8	47
Balmer-Minnes, Diana	P8-6	168
Bang, Jin-Young	O1-2	31
Baranger, Jerome	O6-3	99
Barker, Kevin	P6-3	123
Baron, Corey A.	O2-3, P2-6	37, 58
Barr, Colton	O3-3, P6-7	63, 127
Bartha, Robert	P2-3, O12-1	55, 146
Bartling, Mandolin	O11-1	141
Battie, Michele	O7-1	102
Bauman, Glenn	O1-4	33
Baumgärtner, Timo	P6-2	122
Bax, Jeffrey	O9-4, P8-4	134, 166
Bernier, Martin L.	P6-1	121
Bierbrier, Joshua	P5-3, P5-5	114, 116

Bisleri, Gianluigi	O5-4, O6-2	95, 98
Black, Peter	P4-3	83
Boileau, Isabelle	P2-7	59
Bourbeau, Jean	P4-2, O7-2	82, 103
Braun, Michael	P6-2	122
Brown, Robert A.	P4-4	84
Calcada, Carla	P1-10	49
Cambranis Romero, Joeana	P7-6, O8-4	110, 156
Campbell, Maxwell	P3-7	77
Cardarelli-Leite, Leandro	O3-1	61
Carnahan, Patrick	O5-4, O6-2	95, 98
Castano, Yessica	P1-4	43
Catapano, Joseph	P3-3	73
Chang, Patrick Dong Min	P1-9	48
Chang, Silvia	P4-3	83
Charron, Danielle M.	P6-8	128
Chen, Elvis C. S.	P4-10, O5-4, O6-2, O8-4, P6-6, P7-6	90, 95, 98, 110, 126, 156
Chen, Juan	P1-5	44
Chen, Stephen	P1-4, P5-2	43, 113
Chiew, Mark	P5-7	118
Cho, N.	O7-3	104
Collins, Sophie	P4-2, O7-2	82, 103
Connell, Ian R. O.	P1-5	44
Connolly, Laura	O3-3, O4-1, P3-6, O6-1, P6-7, P8-3	63, 66, 76, 97, 127, 165
Contella, David	P6-3	123
Contreras-Sánchez, Héctor A.	P1-3, P7-3	42, 153
Cool, Derek W.	O1-4, P4-6	33, 86
Costanzo, Alejo	P2-2, P4-8	54, 88
Courtine, G.	O7-3	104
Crivellaro, Priscila	P8-4	166
Cunningham, Charles H.	P2-4	56
Cunningham, Ian A.	O3-1, P6-6, O9-4, O10-2	61, 126, 134, 137
d'Albenzio, Gabriella	P6-4	124
D'ippolito, Alex	P7-11	161
Da Silva, Eric	O10-3	138
Dai, Ling	O5-1	92
d'Albenzio, Gabriella	P7-7	157
Daly, Michael J.	O11-1, O11-4, O12-2, P7-10	141, 144, 147, 160
Danialy, Ava	O6-3	99

Daskalopoulou, Stella S.	P4-4	84
Davison, Colleen	P3-6, P3-8	76, 78
de Kort, Jessica	O4-3	68
Deguet, Anton	O6-1	97
Deisseroth, K.	O7-3	104
Desmond, Kim L.	P2-7	59
Detombe, Sarah A.	P2-3, O12-1	55, 146
Detsky, Jay	O8-2	108
DeVries, David	O9-1	131
Dickie, Erin W.	P2-7	59
Dinakaran, Deepak	O1-3	32
Dingle, Kate	P7-11	161
Dingwell, Dylan Archer	P2-4	56
Do, Richard	P8-5	167
Donovan, Adamo	O7-2	103
Donszelmann-Lund, Elise	P6-5	125
Douplik, Alexandre	P7-11	161
Doyle-Pettypiece, Pat	O12-1	146
Drake, James M.	O6-3, P6-5	99, 125
Drangova, Maria	O3-1	61
du Toit, Carla	O11-2	142
Du, Yong	P3-4	74
Dubovan, Paul I.	O2-3	37
Dubroy-McArdle, Céline	O12-3	148
Dueck, Andrew	P3-1	71
Duggal, Neil	P2-3, O12-1	55, 146
Duimering, Adrienne	P5-3	114
Dukelow, Sean P.	P8-7	169
Dunn, Alexander	O2-1, O3-2	35, 62
Duquette-Evans, Clara	P3-2, O11-2	72, 142
Durocher, Emma	O9-2	132
Dutta, Pramit	P7-5	155
Easson, Alexandra	P7-11	161
Eisenstat, Joshua	P2-2	54
El Kaffas, Ahmed	P7-2	152
Elghareb, Tarek	P1-2	41
El-Hamedi, Lynn	P6-1	121
Elkind, Emese	P3-6, P3-8	76, 78
Elliott, Tyler	P8-3	165
Eltahawi, Ahmed	P4-10	90

Engel, Cecil Jay	O8-3	109
Enjilela, Razieh	O10-3	138
Ertl-Wagner, Birgit	P2-2, P4-8, P5-4	54, 88, 115
Fakhari, Nikan	O6-3	99
Fakir, Hatim	O9-1	131
Farahmand, Mohammad	O4-1, P8-1	66, 163
Farvolden, Coleman	O3-3, P6-7	63, 127
Faul, James	O7-1	102
Fenster, Aaron	P3-2, P4-6, O5-1, O6-4, O8-1, P6-3, O9-4, O11-2, P7-4, P8-4	72, 86, 92, 100, 107, 123, 134, 142, 154, 166
Fichtinger, Gabor	O3-3, O4-1, O4-3, O4-4, P3-6, P3-8, O6-1, O8-3, P5-1, P5-3, P5-5, P5-8, P6-4, P6-7, O10-1, P7-1, P7-7, P8-1, P8-3	63, 66, 68, 69, 76, 78, 97, 109, 112, 114, 116, 119, 124, 127, 136, 151, 157, 163, 165
Finger, Elizabeth	P2-6	58
Fleshner, Neil	P1-11	50
Fong, Ching	P3-4	74
Fooladgar, Fahimeh	O4-1, P4-3, P8-3	66, 83, 165
Foussias, George	P2-7	59
Franz, Alfred M.	P6-2	122
Freitas, Vivianne	P7-11	161
Friesen, Alexander C.	O12-1	146
Gabriel, Alon	P1-2, P8-1	41, 163
Gadde, Suresh	O9-2	132
Gaede, Stewart	O1-2, O5-2	31, 93
Gammage, Alina	P3-8	78
Gardi, Lori	O9-4, P8-4	134, 166
Garland, Lisa M.	P6-6, O10-2	126, 137
Garvin, Gregory	P3-7	77
Genkin, Daniel	P4-2, O7-2	82, 103
Gerard, Ian J.	P6-1	121
Gilany, Mahdi	P4-3, P4-7	83, 87
Gilliland-Rocque, Rene	O3-4, P3-1	64, 71
Gokal, Mihir	P4-10	90
Goncalves, Vanessa	P2-7	59
Goubran, Maged	O7-3	104
Graham, Simon J.	P2-1, O5-3, P5-7	53, 94, 118
Grisaru Kacen, Maya	P8-4	166
Gu, Xijia	O3-4	64
Gulta, Dawit	P5-2	113
Guo, Zhuoxin	P4-3, P6-4, P7-1	83, 124, 151

Hajjar, Réna	P5-8	119
Hamghalam, Mohammad	P8-5	167
Hara-Lee, Kaito	P2-5	57
Hardisty, Michael	P1-4, P1-7, P5-2	43, 46, 113
Harmanani, Mohamed	P4-3	83
Hashtrudi-Zaad, Keyvan	O6-1	97
Hashtrudi-Zaad, Kian	O3-3, P6-7	63, 127
Hawkins, Cynthia	P6-8	128
Helfield, Brandon	O1-1	30
Hijal, Tarek	P6-1	121
Hisey, Rebecca	O4-4, P5-1, P5-3, P5-5, P5-8, P6-4	69, 112, 114, 116, 119, 124
Hofer, Stefan	P3-3	73
Hogg, Jim	P4-2	82
Holden, Matthew	P5-3, P5-5	114, 116
Holdsworth, David W.	O3-1, O6-4, O7-1, O12-4	61, 100, 102, 149
Hoover, Douglas	O8-1, P6-3	107, 123
Huang, Christine	P1-7	46
Huang, Xiaopei	P3-4	74
Hurlbut, David	P8-1	163
Husain, M. Omair	P2-7	59
Husby, Theodore	P1-5	44
Hutter, Megan	P3-2, O11-2	72, 142
Huynh, Christopher	P8-6	168
Iaboni, Natasha	P8-1	163
Ibrahim, George M.	P6-5	125
Idlbi, Mahmoud	P8-5	167
Irish, Jonathan C.	O11-1, O11-4, O12-2, P7-10	141, 144, 147, 160
Jabs, Doris	O8-3	109
Jamzad, Amoon	O4-1, P4-3, P4-7, O8-3, P8-1, P8-3	66, 83, 87, 109, 163, 165
Johnson, Carol	O1-4	33
Jok, Kelvin	P8-2	164
Kadar, Assaf	O10-4, O11-2	139, 142
Kahrs, Lueder A.	P6-5	125
Kalia, Vibhuti	O1-4	33
Karagulleoglu-Kunduraci, Sule	O9-4	134
Karim, Anisa	O4-2	67
Kaufmann, Martin	O4-1, O8-3, P8-1, P8-3	66, 109, 163, 165
Keshavarz, Mohammadmahdi (Sina)	O3-4, P3-1, P3-5	64, 71, 75

Kesibi, Maha	P7-1	151
Keun Park, Claire	P8-4	166
Khan, Ali	P2-6	58
Khan, Naimul	O2-1	35
Khan, Zardar	O4-2	67
Khoobani, Mohammad	O3-4	64
Kirby, Miranda	P4-2, O7-2, O10-3	82, 103, 138
Kitner, Nicole	O4-3	68
Klein, Geoff	P1-4, P5-2	43, 113
Klosa, Elizabeth	P5-8	119
Komposch, Jan	P6-2	122
Konermann, Sarah	P6-1	121
Kopek, Neil	P6-1	121
Kornecki, Anat	O1-4	33
Korzeniowski, Martin	O4-3, P4-1	68, 81
Kosik, Ivan	O11-3	143
Krishnan, Pradeep	O2-2	36
Kulcsar, Carla	P7-3, P7-9	153, 159
Kuling, Grey	O4-2	67
Kunic, Helena	P4-10, P7-8	90, 158
Kurosawa, Hikaru	O11-1, O11-4, O12-2	141, 144, 147
Laba, Joanna	O9-1	131
Lai, Meng-Chuan	P2-7	59
Lal, N.	O7-3	104
Lalone, Emily	P3-2, P3-7, O10-4, O11-2, P7-4	72, 77, 139, 142, 154
Lam, Christopher	P8-6	168
Lam, Matthew	P1-6	45
Lam, Wilfred	O12-3	148
Lang, Pencilla	P1-8	47
Lau, Angus	O8-2	108
Law, Christine	P5-3, P5-5	114, 116
Lawford-Wickham, Imogen	P4-5	85
Lawrence, Liam S. P.	O8-2	108
Le, Marie	P7-4	154
Learned, Noah	P3-8	78
Lee, Ting-Yim	O1-2	31
Lee, Yin Hau Wallace	P6-5	125
Leong, Iona	P1-12	51
Leung, Andrew	O9-1	131
Leveridge, Michael	P4-3, P4-7	83, 87

Liang, Libin	O5-1	92
Lim, Adam	P4-8	88
Lin, Hsiang-Yuan	P2-7	59
Little, Victoria	P2-3	55
Lo, Justin	P2-2, P5-4	54, 115
Long, Bining	O4-4, P5-3, P5-5	69, 114, 116
Louie, Daniel C.	P7-3, P7-9	153, 159
Macgowan, Christopher K.	P8-6	168
Maghsoodi, Nooshin	P5-6	117
Malik, Rubina	P2-6	58
Malthaner, Richard	O7-4	105
Mannina, Sophia	P5-6	117
Markel, Daniel	P1-8	47
Marshall, Harry	O1-4	33
Martel, Anne L.	P1-1, O4-2, P8-2	40, 67, 164
Martin, David	P6-9	129
Martinez, Diego	P1-5	44
Maslove, David	P5-6	117
Matsuura, Naomi	P1-9, O9-2	48, 132
Mattonen, Sarah A.	P1-8, P4-9, O7-4	47, 89, 105
Mccauley, Cole	P3-8	78
McGrath, Sean	O9-2	132
McKay, Douglas	O4-1, P8-3	66, 165
McLaurin, J.	O7-3	104
McNeil, Matthew	P1-1	40
Mehrez, Hatem	O5-2	93
Memari, Elahe	O1-1	30
Mendez, Lucas	O8-1, P6-3	107, 123
Meng, Lingjian	P3-4	74
Milantoni, Marcus	O7-4	105
Miller, Elka	O2-2, P5-4	36, 115
Mirfallah, Giselle	P2-7	59
Mirzaei, Mateen	P6-6	126
Mirzajavadkhan, Azin	O1-3, P1-7	32, 46
Modarai, Yasmin	P5-4	115
Mokhlesabadi, Mahsa	P6-8	128
Momeni, Nika	P2-2	54
Moore, John	O5-4, O6-2	95, 98
Mousavi, Parvin	P1-2, O4-1, O4-3, P3-6, P4-3, P4-5, P4-7, O6-1, O8-3, P5-6, O10-1, P7-1, P7-7, P8-1, P8-3, P8-7	41, 66, 68, 76, 83, 85, 87, 97, 109, 117, 136, 151, 157, 163, 165, 169

Mudathir, Randa	P3-2, O11-2	72, 142
Munawar, Adnan	O6-1	97
Murphy, Blake	P3-3	73
Murphy, Jennifer E.	O12-1	146
Music, Marina	P6-4	124
Myrehaug, Sten	O8-2	108
Naim Ibrahim, Miriam	P7-2	152
Nair, Viswam	P4-9	89
Nassar, Sarah	P5-6	117
Nasser, Jamiel	O8-1	107
Nayak, Rahul	O7-4	105
Near, Jamie	P2-1, P2-5, P5-7	53, 57, 118
Negus, Christina	O12-2	147
Ng, David	O3-1	61
Nguyen, Vivian	P4-7	87
Nicol, Christopher	P8-1	163
Nikolov, Hristo N.	O6-4	100
Nowak, Sydney	O6-3	99
O'Reilly, Meaghan A.	P6-8, P6-9	128, 129
Olding, Timothy	O4-3, P4-1	68, 81
Osmann, J.	O7-3	104
Ouyang, Zhonghua	P3-4	74
Patel, S.	O7-3	104
Pater, Piotr	P6-1	121
Patil, Sujit	P7-10	160
Pener-Tessler, Alon	O11-4	144
Pereira, Michael	P1-6	45
Peters, Terry M.	O5-4, O6-2, O8-4, P6-6, P7-6	95, 98, 110, 126, 156
Philp, Lauren	P1-10	49
Piorkowska, Karolina	O6-3	99
Piran Nanekaran, Negin	O9-3	133
Pires, Layla	P1-10	49
Policelli, Robert	O9-1	131
Portnoy, Sharon	P8-6	168
Prasses, Ioannis	P1-11	50
Prem, Alysha	P3-9	79
Psaromiligkos, Ioannis	P4-4	84
Purkey, Eva	P3-6, P3-8	76, 78
Qi, Olivia	P7-6	156
Qi, T.	O7-3	104

Qiabi, Mehdi	O7-4	105
Qin, Ansong	P3-4	74
Qiu, Jimmy	P3-3	73
Radcliffe, Olivia	P3-6, P4-5	76, 85
Raffiee, M.	O7-3	104
Randhawa, Shubreet	O1-4	33
Ranjit, Gaurav	O10-1	136
Rastegar Jooybari, Fatemeh	P8-6	168
Rastegarpoor, Maryam	P4-6	86
Ravindran, Dharsan	P8-7	169
Ray, Sengeeta	P3-4	74
Ren, Kevin Yi Mi	O4-1, P8-1, P8-3	66, 163, 165
Reznik, Alla	O9-4	134
Rezvanjou, Sara	P4-2	82
Rinaldi, A.	O7-3	104
Rios-Carrillo, Ricardo	P2-6	58
Robbins, Steven	P6-5	125
Rock, Jason	P2-1, P5-7	53, 118
Rodgers, Jessica R.	O4-3, P4-1	68, 81
Ross, Tayler D.	P1-4	43
Roskopf, Johannes	P6-2	122
Rozak, M.	O7-3	104
Ruaro, Alessandra	P1-5, O11-1, O11-4, P7-10	44, 141, 144, 160
Rudan, John F.	O4-1, O8-3, P8-1, P8-3	66, 109, 163, 165
Ruschin, Mark	O8-2	108
Rushlow, Ariana	O5-4	95
Sadanand, Siddharth	O2-1, O2-2, O2-4, O3-2	35, 36, 38, 62
Sadatamin, Saba	P6-5	125
Sahgal, Arjun	P1-4, O8-2	43, 108
Santiago, Christine A.	P4-9	89
Santyr, Giles	O10-3	138
Saprungruang, Ankavipar	P8-6	168
Schifani, Christin	P2-7	59
Schmitz, Bernd	P6-2	122
Schwarz, Elise	O11-4	144
Scott, Stephen H.	P8-7	169
Sewani, Alykhan	O3-4, P3-1, P3-5	64, 71, 75
Sgouros, George	P3-4	74
Shanshal, Rooaa	O11-1, O11-4, O12-2, P7-10	141, 144, 147, 160

Shehetila, Breana	P1-10	49
Shi, Kangdi	P1-11, P1-12	50, 51
Shinar, Shiri	O2-2	36
Sholzberg, Michelle	O2-1	35
Sibley, Stephanie	P5-6	117
Siemens, Robert	P4-3, P4-7	83, 87
Sikstrom, Lee D.	O12-4	149
Silic, Marina	O5-3	94
Simpson, Amber	P8-5	167
Singh, Davindra	O1-1	30
Siracusa, Matthew A.	O11-1, O11-4, O12-2, P7-10	141, 144, 147, 160
Smith, Benjamin	O7-2	103
Sobel, Mara	P1-6	45
Sojoudi, Samira	P4-3	83
Soleymani, Yasaman	P1-12	51
Soliman, Hany	O8-2	108
Sothynathan, Mayuri	O2-3	37
Squair, J.	O7-3	104
Stanisz, Greg	O2-2, O12-3	36, 148
Stefanovic, B.	O7-3	104
Stewart, James	O8-2	108
Stickland, Michael	P4-2, O7-2	82, 103
Stobbe, Rob	O2-2	36
Straatman, Lauren	O10-4	139
Stroian, Gabriela	P6-1	121
Surry, Kathleen	O8-1	107
Sussman, Dafna	O2-1, O2-2, O2-4, P1-6, P2-2, O3-2, P4-8, P5-4, O12-3	35, 36, 38, 45, 54, 62, 88, 115, 148
Szentimrey, Zachary	P7-2	152
Tabatabaei, Saleh	P1-4	43
Tahmasebi, Mohammadmahdi	O3-4	64
Tan, Wan-Cheng	P4-2, O7-2	82, 103
Tang, Terence	O9-1	131
Tavallaei, M. Ali	O3-4, P3-1, P3-5, P3-9	64, 71, 75, 79
Taylor, Edward	P1-3	42
Taylor, Russell H.	O6-1	97
Tessier, David	O9-4, P8-4	134, 166
Theriault, Aimee	O8-2	108
Thornton, Kanchana	P3-6, P3-8	76, 78
To, Minh Nguyen Nhat	P4-3	83

Townson, Jason	P1-5	44
Trumpour, Tiana	O8-1	107
Tseng, Chia-Lin	O8-2	108
Tun, Saw Aung Tin	P3-6, P3-8	76, 78
Tyc, Richard	P6-5	125
Ukwatta, Eranga	O9-3, P7-2, P7-5, P7-8	133, 152, 155, 158
Umoh, Joseph U.	O7-1	102
Ungi, Tamas	O4-3, O6-1, O8-3, O10-1, P7-1, P7-7	68, 97, 109, 136, 151, 157
Uribe, Carme	P2-7	59
Valencia, Nicole	P4-1	81
van der Kwast, Theodorus	P1-11	50
van Mieghem, Tim	O2-2, O6-3	36, 99
Vancer, Laura	P3-7	77
Varma, Sonal	P8-1	163
Vasdev, Neil	P2-7	59
Verdawala, Mustansir	O7-2	103
Vidarsson, Logi	P2-2, P4-8, P5-4	54, 88, 115
Vieira, Erica	P2-7	59
Villemain, Olivier	O6-3	99
Villeneuve, Jennifer	O10-4	139
Vitkin, Alex	P1-3, P7-3, P7-9	42, 153, 159
Voineskos, Aristotle N.	P2-7	59
Voutsas, Jonathan	P8-6	168
Wagner, Matthias W.	P2-2, P5-4	54, 115
Wang, Edward	P1-8	47
Wang, Tao	O6-3	99
Wangulu, Collins	P1-11	50
Ward, Aaron	O1-4, O9-1	33, 131
Wasim, Farhan	P1-6	45
Waspe, Adam C.	O6-3, P6-5	99, 125
Weersink, Robert A.	P1-5, O11-3	44, 143
Whyne, Cari M.	O1-3, P1-4, P1-7, P5-2	32, 43, 46, 113
Wilkie, Phoenix	P8-2	164
Williams, Stephanie	P3-3	73
Willis, Emma	P1-2	41
Wilson, Brian C.	P1-5, P1-10, O11-1, O11-3, O11-4, O12-2	44, 49, 141, 143, 144, 147
Wilson, Paul F. R.	P4-3, P4-5, P4-7	83, 85, 87
Wilson, Scott K.	O12-1	146
Wilson, Sydney	O6-4	100

Windover, Lauren	P3-8	78
Wisener, Kyla	P3-8	78
Wolkoff, Max	P3-8	78
Won, Natalie	O11-1, O11-4, O12-2	141, 144, 147
Wong, Aden	P5-1	112
Wong, Denise	O4-4	69
Wright, Graham	O3-4	64
Wright, Trinette	P3-3	73
Wunder, Jack	P7-10	160
Xia, Wenyao	O5-4	95
Xiao, Yuliang	P5-7	118
Yang, Can	P3-4	74
Yau, Timothy	O5-2	93
Ye, L.	O7-3	104
Yeung, Chris	O6-1, O8-3, O10-1, P7-7	97, 109, 136, 157
Yokote, Fumi	O11-3	143
Yoo, Shi-Joon	P8-6	168
Young, Dylan	O2-1	35
Yousef, George	P1-11	50
Yu, F.	O7-3	104
Yuan, Charles C. X.	O6-2	98
Yue, Jianwei	P8-5	167
Zabel, W. Jeffrey	P1-3, P7-3	42, 153
Zabihollahy, Fatemeh	P1-11	50
Zanette, Brandon	O10-3	138
Zaraska, Kat	P1-5	44
Zhang, Emma	O5-4	95
Zhang, Shufei	P4-10, P7-8	90, 158
Zheng, Gang	P1-5, P1-10, O11-3	44, 49, 143
Zhou, James	P3-5	75
Zong, Junhui	P7-7	157